

Magnetic hysteresis phenomena in electromagnetic actuation systems

Citation for published version (APA):

Vrijisen, N. H. (2014). *Magnetic hysteresis phenomena in electromagnetic actuation systems*. [Phd Thesis 1 (Research TU/e / Graduation TU/e), Electrical Engineering]. Technische Universiteit Eindhoven.
<https://doi.org/10.6100/IR780946>

DOI:

[10.6100/IR780946](https://doi.org/10.6100/IR780946)

Document status and date:

Published: 01/01/2014

Document Version:

Publisher's PDF, also known as Version of Record (includes final page, issue and volume numbers)

Please check the document version of this publication:

- A submitted manuscript is the version of the article upon submission and before peer-review. There can be important differences between the submitted version and the official published version of record. People interested in the research are advised to contact the author for the final version of the publication, or visit the DOI to the publisher's website.
- The final author version and the galley proof are versions of the publication after peer review.
- The final published version features the final layout of the paper including the volume, issue and page numbers.

[Link to publication](#)

General rights

Copyright and moral rights for the publications made accessible in the public portal are retained by the authors and/or other copyright owners and it is a condition of accessing publications that users recognise and abide by the legal requirements associated with these rights.

- Users may download and print one copy of any publication from the public portal for the purpose of private study or research.
- You may not further distribute the material or use it for any profit-making activity or commercial gain
- You may freely distribute the URL identifying the publication in the public portal.

If the publication is distributed under the terms of Article 25fa of the Dutch Copyright Act, indicated by the "Taverne" license above, please follow below link for the End User Agreement:

www.tue.nl/taverne

Take down policy

If you believe that this document breaches copyright please contact us at:

openaccess@tue.nl

providing details and we will investigate your claim.

Magnetic Hysteresis Phenomena in Electromagnetic Actuation Systems

PROEFSCHRIFT

ter verkrijging van de graad van doctor aan de Technische Universiteit
Eindhoven, op gezag van de rector magnificus, prof.dr.ir. C.J. van Duijn,
voor een commissie aangewezen door het College voor Promoties, in het
openbaar te verdedigen op maandag 27 oktober 2014 om 16.00 uur

door

Nilles Henricus Vrijsen

geboren te Eindhoven

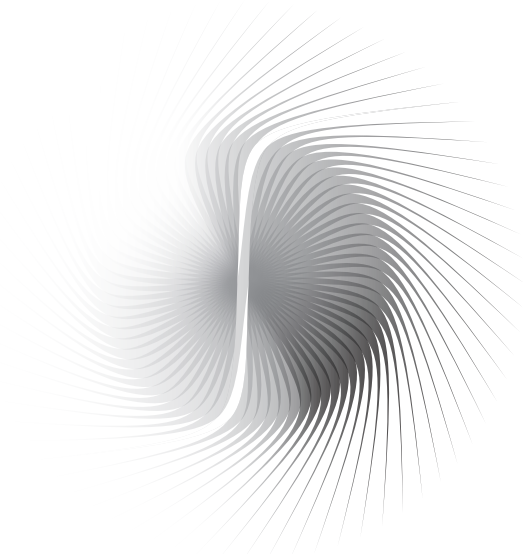
Dit proefschrift is goedgekeurd door de promotoren en de samenstelling van de promotiecommissie is als volgt:

| | |
|--------------------------|--|
| voorzitter: | prof.dr.ir. J.H. Blom |
| 1 ^e promotor: | prof.dr. E.A. Lomonova MSc |
| copromotor: | dr.ir. J.W. Jansen |
| leden: | prof.dr.ir. J.P.H. Benschop (Universiteit Twente / ASML) prof.dr. L.R.L. Dupré (Universiteit Gent) prof.dr.ir. M.G.D. Geers prof.dr.-ing. B. Ponick (Leibniz Universiteit Hannover) |
| adviseur: | dr.ir. R. Klaver (Heidenhain) |

Magnetic Hysteresis Phenomena in Electromagnetic Actuation Systems

Nilles Henricus Vrijsen

*Electromechanics and Power Electronics group, Department of Electrical
Engineering, Eindhoven University of Technology, The Netherlands*



This research is part of the Pieken in de Delta program and is funded by Rijksdienst voor Ondernemend Nederland (RVO), an agency of the Dutch Ministry of Economical Affairs, and the local governments of the South-East of the Netherlands.

Magnetic Hysteresis Phenomena in Electromagnetic Actuation Systems
by N.H. Vrijsen, Eindhoven University of Technology, 2014

A catalogue record is available from the Eindhoven University of Technology Library, ISBN: 978-90-386-3709-9

Reproduction: Ipskamp Drukkers B.V., Enschede, The Netherlands
Cover design: Johan Huijbregts
E-mail: nhvrijsen@gmail.com

Copyright © 2014 by N.H. Vrijsen. All rights reserved.

*To my wife - Suzanne
and to my family*

Summary

Magnetic hysteresis phenomena in electromagnetic actuation systems

The requirements on the force density and position accuracy for high-precision actuation systems are continuously increasing. Especially in the semiconductor lithography industry, the demands on the positioning systems are on the physical limits, because production speed is a major issue while nanometer accurate positioning is required. High accelerations are necessary to improve the wafer throughput, which determines the costs per chip. It is the force of electromagnetic actuators which defines the acceleration of a specific mass. To enhance the acceleration of future actuation systems, intrinsically different actuation techniques are investigated other than the often applied voice-coil actuators, which are expected to reach their limitations on force density. This research focuses on reluctance actuators for short-stroke applications, which are able to achieve a more than ten times higher force density than voice-coil actuators considering the moving mass. The major restriction for applying reluctance actuators for high-precision actuation systems is their non-linearity with respect to the current and position, and the presence of magnetic hysteresis and eddy currents in the ferromagnetic materials. This thesis aims to investigate the accuracy of the force prediction of reluctance actuators from a physical electromagnetic perspective.

Various electromagnetic modeling methods are evaluated for the determination of the force of reluctance actuators. The magnetic equivalent circuit (MEC) method and the finite element method (FEM) are selected to model the intrinsic non-linear force with respect to the current and the position. The analytical MEC method models the non-hysteretic force in the actuation direction with a high-accuracy, whereas it is not accurate for obtaining the forces perpendicular to the actuation direction. Besides the modeling of the evaluated reluctance actuators with the FEM, this numerical method is also used to investigate the influence of the homogeneity of the magnetic flux density in the actuator core related to the amount of magnetic hysteresis in the reluctance force. From this

analysis it is observed that the absolute magnitude of the magnetic hysteresis in the force in the actuation direction is directly related to the peak value of the magnetic flux density in the major part of the core of the reluctance actuator. The hysteresis in the force perpendicular to the actuation direction due to a misalignment of the stator and mover is negligible compared to the hysteresis in the actuation direction.

The physical magnetic hysteresis phenomena in ferromagnetic materials are explained, including the history dependency, the wiping-out property and rate-dependent effects, i.e. macroscopic eddy currents and excess losses. These aspects are important for the selection of a proper magnetic hysteresis model from commonly applied modeling methods. Furthermore, the most important properties for reluctance actuator design are discussed of regularly applied soft-magnetic material types, i.e. nickel-iron (NiFe), silicon-iron (SiFe), cobalt-iron (CoFe), ferrite and stainless steel. Moreover, the influence of annealing in the production process is considered and measurement methods to qualify ferromagnetic materials are elaborated.

The phenomenological Preisach model is selected to model the dominant ferromagnetic material properties, because the model incorporates the non-linearity of the magnetic hysteresis loop, the history dependency and arbitrary minor loops. The Preisach model is combined with the MEC method to describe the hysteretic behavior of reluctance actuators. A dynamic material model is used to describe the rate-dependent effects in the ferromagnetic materials. In addition to the Preisach model, a commercial available FEM and a complex impedance model are evaluated on their ability to model static and dynamic magnetic hysteresis effects.

The magnetic flux density obtained with the Preisach model is compared to quasi-static measurements for three different material samples, i.e. CoFe (Vacoflux 50), SiFe (M800-50A) and stainless steel (AISI 430). The dynamic material model is also evaluated for the laminated material samples with various lamination thicknesses of 0.10, 0.35 and 0.50 mm. The simulations show a maximum discrepancy of 10 % for most excitations ranging from a quasi-static magnetic flux density variation up to excitations with a sinusoidal magnetic flux density of 400 Hz.

The force prediction has been evaluated with the combined magnetic hysteresis and actuator model by an experimental verification on three E-core reluctance actuators, one has been manufactured from CoFe and two from SiFe, of which one has a pre-biasing permanent magnet and the other one has not. The force of the CoFe E-core actuator has been measured with an actuator test-rig, which consists of two linear voice-coil actuators to obtain the force. A nanometer accurate optical encoder has been used with a position feedback controller to maintain a constant airgap. The dynamic hysteresis phenomena in the reluctance force of the two SiFe actuators have been measured with

a piezoelectric load cell. The modeled magnetic hysteresis phenomena in the reluctance actuators show good agreement with the measurements for both, the absolute force and the amount of magnetic hysteresis in the force, including the history dependency, minor loops and dynamic effects.

Contents

| | |
|--|------------|
| Summary | vii |
| Contents | xi |
| Nomenclature | xv |
| 1 Introduction | 1 |
| 1.1 Background | 1 |
| 1.2 Research objectives | 4 |
| 1.3 Thesis outline | 6 |
| 2 Electromagnetic actuator modeling | 9 |
| 2.1 General electromagnetic theory | 10 |
| 2.2 Energy conversion | 11 |
| 2.2.1 Inductance | 12 |
| 2.2.2 Energy | 13 |
| 2.3 Force calculations | 14 |
| 2.3.1 Virtual work method | 14 |
| 2.3.2 Maxwell stress tensor method | 16 |
| 2.4 Reluctance actuator modeling | 17 |
| 2.5 Magnetic equivalent circuit method | 19 |
| 2.5.1 Equivalent network | 20 |
| 2.5.2 Permanent magnet model | 21 |
| 2.5.3 Airgap reluctances or permeances | 21 |
| 2.5.4 Analytical MEC expression for including hysteresis | 25 |
| 2.6 Nonlinearities in reluctance actuators | 27 |
| 2.6.1 Current-force relation | 28 |
| 2.6.2 Position-force relation | 29 |
| 2.7 Hysteresis in the reluctance force | 31 |
| 2.7.1 Evaluated E-core actuators | 32 |
| 2.7.2 Equal peak current-density | 34 |

| | | |
|----------|---|-----------|
| 2.7.3 | Equal peak force | 35 |
| 2.7.4 | Equal peak magnetic flux density | 35 |
| 2.7.5 | Cross-talk | 38 |
| 2.8 | Conclusions | 39 |
| 3 | Magnetic hysteresis | 41 |
| 3.1 | Magnetic constitutive law | 42 |
| 3.2 | Micromagnetic phenomena | 44 |
| 3.2.1 | Barkhausen effect | 46 |
| 3.2.2 | Anisotropy | 48 |
| 3.2.3 | Magnetostriction and elongation | 48 |
| 3.3 | Magnetic hysteresis loop | 50 |
| 3.4 | Soft-magnetic materials | 52 |
| 3.4.1 | Material evaluation | 52 |
| 3.4.2 | Material degradation | 54 |
| 3.5 | Measurement of magnetic hysteresis | 56 |
| 3.5.1 | Measurement methods | 57 |
| 3.5.2 | Applied measurement methods | 58 |
| 3.6 | Conclusions | 60 |
| 4 | Overview of hysteresis modeling methods | 63 |
| 4.1 | Preisach model | 64 |
| 4.2 | Jiles-Atherton model | 67 |
| 4.3 | Play and stop models | 68 |
| 4.4 | Positive-feedback model | 70 |
| 4.5 | Finite element method | 72 |
| 4.6 | Complex impedance method | 74 |
| 4.7 | Other models | 75 |
| 4.8 | Conclusions | 75 |
| 5 | Preisach hysteresis model | 79 |
| 5.1 | Classical Preisach model | 81 |
| 5.1.1 | Model properties | 83 |
| 5.1.2 | Numerical implementation | 88 |
| 5.1.3 | Congruency property | 90 |
| 5.1.4 | Degaussing of the Preisach model | 91 |
| 5.2 | Generalized scalar Preisach model | 92 |
| 5.2.1 | Neglected generalizations | 93 |
| 5.2.2 | Incorporated generalizations | 93 |
| 5.3 | Preisach distribution | 95 |
| 5.3.1 | Evaluated distribution functions | 98 |
| 5.3.2 | Distribution function correlated to constitutive relation | 100 |
| 5.3.3 | Optimization of the distribution functions | 101 |
| 5.4 | Simulation procedure | 102 |

| | | |
|----------|--|------------|
| 5.5 | Experimental verification | 103 |
| 5.6 | Conclusions | 106 |
| 6 | Dynamic magnetic material modeling | 109 |
| 6.1 | Statistical loss theory | 110 |
| 6.1.1 | Static hysteresis losses | 111 |
| 6.1.2 | Classical eddy current losses | 111 |
| 6.1.3 | Excess losses | 111 |
| 6.1.4 | Experimental verification | 112 |
| 6.2 | Field separation for instantaneous modeling | 116 |
| 6.3 | Eddy current model for magnetic materials | 117 |
| 6.3.1 | Rectangular shaped ferromagnetic material | 117 |
| 6.3.2 | Laminated material | 121 |
| 6.3.3 | Permanent magnet | 121 |
| 6.3.4 | Skin effect | 122 |
| 6.3.5 | Simulation procedure | 123 |
| 6.3.6 | Experimental verification | 124 |
| 6.4 | Hysteresis modeling in reluctance actuators | 131 |
| 6.4.1 | Hysteretic reluctance | 131 |
| 6.4.2 | Hysteresis in the MEC model of a reluctance actuator | 132 |
| 6.4.3 | Simulation procedure | 133 |
| 6.5 | Finite element method | 135 |
| 6.5.1 | Laminated structures with the 3d-FEM | 135 |
| 6.5.2 | Experimental verification | 136 |
| 6.5.3 | Simulation of reluctance actuators | 138 |
| 6.6 | Complex impedance method | 139 |
| 6.6.1 | Experimental verification | 139 |
| 6.6.2 | Simulation of reluctance actuators | 141 |
| 6.7 | Conclusions | 141 |
| 7 | Experimental verification | 143 |
| 7.1 | E-core actuator of cobalt-iron | 144 |
| 7.1.1 | Measurement instrument | 145 |
| 7.1.2 | Simulation results of the cobalt-iron E-core actuator | 147 |
| 7.2 | E-core actuators of silicon-iron | 156 |
| 7.2.1 | Measurement instrument | 157 |
| 7.2.2 | Simulation results of the unbiased E-core actuator | 160 |
| 7.2.3 | Simulation results of the pre-biased E-core actuator | 164 |
| 7.3 | Conclusions | 167 |
| 8 | Conclusions and Recommendations | 171 |
| 8.1 | Conclusions | 172 |
| 8.1.1 | Formulation and assessment of the reluctance actuator properties to be modeled | 172 |

| | | |
|----------|---|------------|
| 8.1.2 | Selection of models for the determination of the instantaneous force of high-precision reluctance actuators . . . | 174 |
| 8.1.3 | Experimental verification of the modeling methods . . . | 175 |
| 8.2 | Recommendations | 178 |
| 8.2.1 | Modeling of magnetic hysteresis | 178 |
| 8.2.2 | Electromagnetic actuator modeling | 179 |
| 8.2.3 | Actuator manufacturing | 179 |
| A | Airgap permeance methods | 181 |
| A.1 | Analytic permeance method | 181 |
| A.2 | Tooth contour method | 184 |
| B | Distribution function parameters | 187 |
| | Bibliography | 191 |
| | Samenvatting | 221 |
| | Dankwoord | 225 |
| | Curriculum Vitae | 229 |

Nomenclature

Table 1: Roman symbols

| Symbol | Unit | Description |
|---------------|-------------------|--|
| A | m^2 | Cross section area |
| \mathbf{B} | T | Magnetic flux density vector |
| \mathbf{D} | C m^{-2} | Electric flux density vector |
| d | m | Depth |
| \mathbf{E} | V m^{-1} | Electric field strength vector |
| E | - | Everett integral |
| f | Hz | Frequency |
| f | - | Preisach function |
| F | - | Integral over a subspace of the Preisach plane |
| \mathbf{f} | N m^{-3} | Volume force density vector |
| \mathbf{F} | N | Force vector |
| h | m | Height |
| \mathcal{F} | A | Magnetomotive force source |
| G | - | Eddy current constant |
| g | m | Airgap length |
| \mathbf{H} | A m^{-1} | Magnetic field strength vector |
| i | A | Instantaneous current |
| I | A | Constant current |
| \mathbf{I} | T | Magnetic polarization |
| \mathbf{J} | A m^{-2} | Current density vector |
| k_b | - | Boltzmann constant |
| K | - | Constant |

Continued on next page

| Symbol | Unit | Description |
|---------------|-------------------|---|
| k_ϕ | - | Flux leakage constant |
| L | H | Inductance |
| \mathbf{l} | m | Length vector |
| m | kg | Mass |
| m | - | Magnetic hysteresis operator |
| m | - | Minima of the Preisach model |
| m_B | J | Zeeman energy of a Bohr magneton |
| m_k | - | Mean of a distribution function |
| M | - | Maxima of the Preisach model |
| \mathbf{M} | A m ⁻¹ | Magnetization vector |
| n | - | Number of laminations |
| \mathbf{n} | - | Normal vector |
| N | - | Number of turns |
| P | - | Preisach distribution function |
| P | W | Power |
| \mathbf{P} | C m ⁻² | Polarization vector |
| \mathcal{P} | H | Magnetic permeance |
| q | C | Electric charge |
| Q | - | Trapezoidal area in the Preisach plane |
| R | Ω | Electric resistance |
| \mathcal{R} | H ⁻¹ | Magnetic reluctance |
| S | m ² | Surface area |
| S | - | Subspace of the Preisach plane |
| t | s | Time |
| T | - | Triangular subspace of the Preisach plane |
| T | K | Temperature |
| \mathbb{T} | N m ⁻² | Maxwell stress tensor |
| u | A m ⁻¹ | Preisach model input |
| v | V | Instantaneous voltage |
| v | V | Electric scalar potential |
| \mathbf{v} | m s ⁻¹ | Velocity vector |
| V | m ³ | Volume |
| V_0 | A m ⁻¹ | Excess loss constant |
| w | m | Width |
| W | J | Energy or work |

Continued on next page

| Symbol | Unit | Description |
|-----------|------|-----------------------|
| W' | J | Coenergy |
| x, y, z | - | Cartesian coordinates |

Table 2: Greek symbols

| Symbol | Unit | Description |
|--------------|-------------|---|
| α | - | Switching variable of the Preisach model |
| α | - | Weiss exchange-field coefficient in PFB model |
| α_L | K^{-1} | Thermal elongation coefficient |
| β | - | Switching variable of the Preisach model |
| β | - | Average number of aligned Bohr magnetons per domain width |
| γ | - | Hysteresis operator of the Preisach model |
| δ | m | Skin depth |
| δ | - | Signum function |
| Δ | - | Relative difference |
| ϵ | - | Discrepancy |
| ϵ | $F m^{-1}$ | Electric permittivity |
| ϵ_0 | $F m^{-1}$ | Electric permittivity of free space ($= 8.85 \cdot 10^{-12}$) |
| ϵ_r | - | Relative electric permittivity |
| λ | Wb | Flux linkage |
| μ | $H m^{-1}$ | Magnetic permeability |
| μ_0 | $H m^{-1}$ | Magnetic permeability of free space ($= 4\pi \cdot 10^{-7}$) |
| μ_r | - | Relative magnetic permeability |
| ρ_m | $kg m^{-3}$ | Mass density |
| ρ | $A m^{-2}$ | Electric charge density |
| σ | $S m^{-1}$ | Electric conductivity |
| σ | - | Standard deviation of distribution function |
| ϕ | Wb | Magnetic flux |
| Φ | - | Magnetic distribution function |
| χ | - | Magnetic susceptibility |
| φ | A | Magnetic scalar potential |

Table 3: Subscripts

| Subscript | Description |
|------------------|---|
| 0 | Room temperature (= 295 K) |
| <i>c</i> | Coercivity |
| <i>c</i> | Curie temperature |
| <i>cl</i> | Classical (loss term) |
| <i>conv</i> | Convection |
| <i>Cu</i> | Copper |
| <i>d</i> | Down switching |
| <i>e</i> | Electrical (energy term) |
| <i>eq</i> | Equivalent |
| <i>ex</i> | Excess (loss term) |
| <i>ex, inst</i> | Instantaneous excess (loss term) |
| <i>eye</i> | Loop-eye |
| <i>f</i> | Magnetic (energy term) |
| <i>fe</i> | Iron |
| <i>fr</i> | Friction (energy loss term) |
| <i>g</i> | Airgap |
| <i>h</i> | Hysteretic (loss term) |
| <i>hyst</i> | Hysteresis or hysteretic |
| <i>irr</i> | Irreversible |
| <i>k</i> | Variable |
| k | Index number |
| <i>l</i> | Leakage component |
| <i>m</i> | Mean |
| <i>m</i> | Mechanical (energy term) |
| <i>mag</i> | Permanent magnet |
| <i>max</i> | Maximum |
| <i>meas</i> | Measured |
| <i>nom</i> | Nominal |
| <i>o</i> | Hysteretic component in MEC model |
| <i>O</i> | Point of operation |
| <i>past</i> | Past or history |
| <i>q</i> | Quantum-mechanical (field contribution) |
| <i>rev</i> | Reversible |

Continued on next page

| Subscript | Description |
|------------------|-----------------------|
| rms | Root mean square |
| s | Saturation |
| T | Total |
| u | Up switching |
| z | z -direction |
| Ω | Resistive (loss term) |

Table 4: Abbreviations

| Abbreviation | Description |
|---------------------|-----------------------------|
| 1d/2d/3d | One/two/three-dimensional |
| ac | Alternating current |
| BEM | Boundary element method |
| CIM | Complex impedance method |
| CoFe | Cobalt iron |
| dc | Direct current |
| DoF | Degree of freedom |
| emf | Electromotive force |
| FEM | Finite element method |
| GO | Grain oriented |
| HT | Hysteresis transducer |
| J-A | Jiles-Atherton |
| MEC | Magnetic equivalent circuit |
| mmf | Magnetomotive force |
| MST | Maxwell stress tensor |
| NiFe | Nickle iron |
| NO | Non-oriented |
| P&S | Play and stop |
| PFB | Positive feedback |
| P-M | Preisach model |
| rms | Root mean square |
| SiFe | Silicon iron |
| TCM | Tooth contour method |

Continued on next page

| Abbreviation | Description |
|---------------------|--------------------|
| VAC | Vacoflux |
| VW | Virtual work |
| WP | Working point |

Introduction

1.1 Background

The ambition of humanity to improve itself and its environment has resulted in several industrial revolutions, which improved the production efficiency of factories. Each revolution is originated by a specific scientific breakthrough, resulting in a major technical improvement years later. Halfway the eighteenth century, the invention of steam power started the first industrial revolution with the transition from manual labor to mechanical labor. Another major industrial change was the introduction of electricity at the end of the nineteenth century. Slowly, steam power was interchanged by electrical power. Decades later, the digital era started by the invention of the transistor, which resulted in 1954 in the first silicon based transistor. Several years later the semiconductor industry was born.

The evolution of integrated circuits has resulted in our modern society, wherein computers are indispensable. The numerous possibilities of current computers are a direct consequence of the continuous improvement of integrated circuits. Already in 1965, Gordon E. Moore predicted that the number of components on a commercially available integrated circuit would double each year [184], which he adjusted in 1975 to doubling each two years [185]. This statistical prediction is often differently interpreted as explained by Gordon Moore in [186]. His findings are currently known as Moore's law, which turned out to be a self-fulfilling prophecy that is still being used as a road map for chip manufacturers [51].

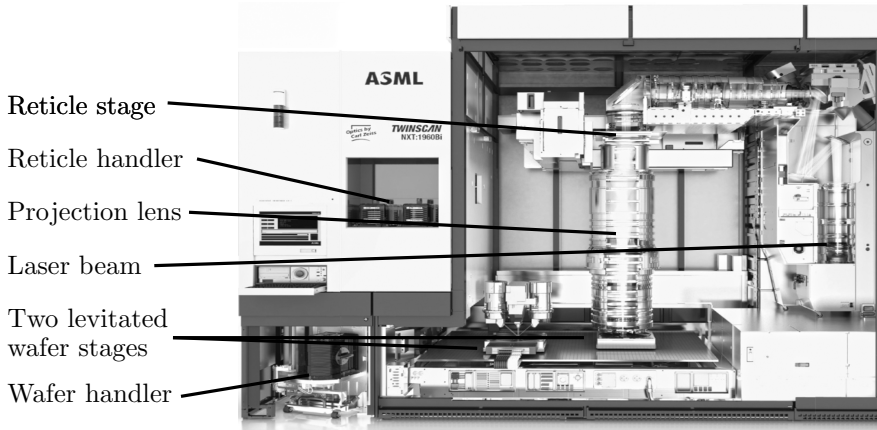


Fig. 1.1: ASML's NXT 1960Bi dual stage immersion lithography system (wafer scanner) [258].

The continuous improvement of computer chips is amongst others achieved by the enhancement of numerous parts of semiconductor lithography systems (wafer scanners) [243]. The most important subsystems of a wafer scanner are indicated in Fig. 1.1. The evolution of the lithography process can be attributed to the improvement of three crucial technologies, i.e. the optical system [243] (light source, mirrors and projection lens), the metrology [51] (the measurement of e.g. overlay, material properties and contamination) and the positioning systems (reticle stage and wafer stage). Improvement of the positioning systems is the major goal of this research.

The positioning accuracy of both the reticle stage and the wafer stage determines the overlay of two subsequent exposure steps [157, 222], but also their speed, acceleration and reliability are of major importance. The accelerations of the positioning stages affect the productivity (throughput) and hence, the production costs per chip. In this perspective, research on high-precision actuation systems is performed to achieve a sub-nanometer position accuracy with a speed and acceleration in the order of 5 m/s [204] and 50 m/s² [222], respectively.

An example of a wafer scanner produced in 2013 is shown in Fig. 1.1. This NXT 1960Bi is used for the exposure step of the production process of 300 mm diameter wafers. The wavelength of the light beam is 193 nm, the resolution of the lithography system is 38 nm, the throughput is larger than 230 wafers per hour and the achieved overlay is below 2.5 nm.

This extreme position accuracy of lithography systems is achieved by a hybrid

concept of the positioning stages, which consist of a long-stroke and a short-stroke stage [36, 112, 266]. The bottom stage (long-stroke) of the wafer stage is a planar motor, which is a moving-coil planar actuator [53]. On top of the long-stroke motor, a short-stroke stage is stacked to achieve the nanometer positioning accuracy. Hence, the short-stroke stage achieves the final positioning by compensation for the floor vibrations coupled into the system and disturbances introduced by the long-stroke stage.

To enhance the productivity of future semiconductor lithography systems, research is performed on increasing the wafer size from a diameter of 300 mm to 450 mm [51]. This increases the wafer area by a factor 2.25, whereas the effective area is increased even more, because a wafer with a larger radius has effectively less unused edges with respect to the total wafer area. To meet future productivity and overlay requirements, also the moving mass has to be reduced significantly. This is essential for future 450 mm wafer stages, and this is also required to stretch current 300 mm technology [266]. The reduction of the moving mass, combined with an increased wafer size, increases the demands for the positioning systems. Specifically, the actuation and control of flexible stage structures or non-rigid bodies are challenging. Research has been performed on the control of non-rigid body modes by applying over-actuation and over-sensing for the short-stroke positioning system [113], for which the number of actuators should be increased. Moreover, a higher actuator bandwidth is required, because a lower mass and stiffness have intrinsically a higher sensitivity to disturbances.

Because of both changes, i.e. the increasing size of the wafer stage and the over-actuated stage concept, the requirements on the actuators are significantly increased regarding the force density. Especially, the moving mass of the electromagnetic actuation system is important to meet the future acceleration requirements. Therefore, intrinsically different actuation techniques are investigated for short-stroke positioning rather than the currently applied voice-coil actuators. This research focuses on reluctance actuators, which can achieve a substantial higher force density compared to voice-coil actuators [260, 270]. Major challenges for applying reluctance actuators for high-precision applications are their nonlinearity with current and position, hysteresis and saturation effects due to the use of ferromagnetic materials, and the stiffness in the actuation direction as well as parasitic forces due to misalignment in the plane perpendicular to the actuation direction (cross-talk). These issues are the subject of this thesis and are considered and assessed in the following chapters.

1.2 Research objectives

The requirements on the force density and position accuracy of high-precision actuation systems are tightened up every year. Therefore, the physical limits of actuation systems are continuously explored. For the next step in the short-stroke high-precision actuator technology, reluctance actuators are investigated. The high force-density of reluctance actuators could result in a decreased actuator mass or the force could be increased to enhance the accelerations of the positioning systems.

The essential difference between voice-coil and reluctance actuators is the inherent use of soft-magnetic materials with respect to the variation of the magnetic flux density. In voice-coil actuators the approximately constant flux of hard-magnetic materials (permanent magnets) could be guided by soft-magnetic materials, while the actuation is based on the interaction of moving charged particles (current) with the nearly constant magnetic flux density produced by the permanent magnets. The force can be calculated with the Lorentz force law and hence, the voice-coil actuator is also called Lorentz actuator. In reluctance actuators a large variation of the magnetic flux density occurs in the soft-magnetic materials, because the reluctance force is a direct result of interaction of the magnetic field with the soft-magnetic material.

Generally, short-stroke reluctance actuators are advantageous for achieving a high force density, but nothing comes for free. The most significant disadvantages of strongly varying magnetic fields in ferromagnetic materials for electromagnetic systems are nonlinearities, magnetic hysteresis, eddy currents and saturation. These ferromagnetic material properties are challenging subjects to incorporate in the analysis of reluctance actuators. This thesis aims to investigate the accuracy of the force prediction of reluctance actuators from a physical electromagnetic perspective. From this perspective, the following goals are addressed and researched:

1. **Formulate and assess the intrinsic reluctance actuator properties to be modeled.** The variety of the aforementioned challenges for applying ferromagnetic materials in electromagnetic devices requires an adequate analysis of all of these phenomena. The phenomena that occur in reluctance actuators are divided into two categories, i.e. the electromechanical actuator properties and the ferromagnetic material phenomena. The most important properties of both categories are qualitatively and/or quantitatively assessed.
2. **Selection of models for the determination of the instantaneous force of high-precision reluctance actuators.** Based on the formulated reluctance actuator properties, various modeling methods are evaluated on their applicability to predict the force of reluctance actuators

accurately. Because electromechanics and magnetism are often considered as different fields of science, proper combinations of existing models from both fields are examined.

- (a) **Choice of the electromechanical modeling method for reluctance actuators.** Electromechanical actuation systems can be modeled with various methods, but each of these methods has its restrictions on e.g. geometry, materials, complexity, computational effort. The major consideration for a method to be applicable to model reluctance actuators is to which extent soft-magnetic materials can be incorporated. More specifically, the methods are assessed on the following two criteria:

- The ability to model the magnetic fields inside and outside soft-magnetic structures.
- The possibility to include hysteretic actuator behavior.

- (b) **Evaluation of magnetic material modeling methods for incorporating magnetic hysteresis phenomena in reluctance actuator models.** Numerous magnetic material modeling methods are qualitatively compared on their ability to incorporate magnetic hysteresis phenomena in the force prediction of reluctance actuators. The examination of the magnetic material modeling methods is performed based on the following criteria:

- The ability to be combined with existing reluctance actuator modeling methods.
- The ability to have arbitrary current excitations as model input.
- The ability to incorporate rate-dependent magnetic material effects.

3. **Experimental verification of the selected modeling methods.** Besides the experimental verification of the reluctance actuator models including magnetic hysteresis phenomena, the modeling of magnetic materials is evaluated separately.

- (a) **Examine the prediction of static and dynamic magnetic hysteresis phenomena for three different ferromagnetic materials.** The ferromagnetic material models are discussed and experimentally verified by a comparison with measurements of the magnetic flux density. The static analysis is conducted for three different soft-magnetic materials, i.e. cobalt iron (CoFe), silicon iron (SiFe) and stainless steel. The dynamic magnetic hysteresis phenomena are modeled for the laminated materials and compared to measurements for a frequency of $0 < f \leq 400$ Hz.

- (b) **Assess the combined electromagnetic and magnetic hysteresis models on the instantaneous force prediction of three reluctance actuators.** Eventually, it is essential to examine the modeling accuracy of reluctance actuators, and to assess their ability to predict the instantaneous force of reluctance actuators for high-precision actuation systems. Force measurements are performed for three reluctance actuators on two measurement instruments. Two SiFe reluctance actuators are experimentally verified for sinusoidal excitations at a frequency of 320 Hz. One of the two actuators is pre-biased with a permanent magnet. The third reluctance actuator is manufactured of CoFe. This actuator is only examined for low frequencies, whereas a wider force range is measured than for the other two actuators and various arbitrary waveforms are examined.

1.3 Thesis outline

In this thesis two interconnected research topics are considered, i.e. electromagnetic actuators and hysteretic magnetic material phenomena. The analysis of both research subjects is discussed separately throughout the work. Eventually, the modeling methods of both topics are combined and experimentally verified by a comparison with force measurements.

In Chapter 2, the modeling of electromagnetic actuators and more specifically of reluctance actuators is discussed. The most significant reluctance actuator properties are considered, which are used to assess various electromagnetic modeling methods on their applicability to model reluctance actuators (**research objectives 1 and 2(a)**). The magnetic equivalent circuit (MEC) method is selected for analytical reluctance actuator modeling and a 2d/3d finite element method (FEM) is selected which can include magnetic hysteresis in its analysis. The modeling of the position dependency of the reluctance force is investigated with both, the MEC method and 2d FEM. The amount of magnetic hysteresis in the force of reluctance actuators is investigated by an evaluation of the force of several E-core reluctance actuators topologies with 2d FEM simulations.

In Chapter 3, the hysteretic phenomena in ferromagnetic materials are summarized and their impact on the force of reluctance actuators is elaborated on (**research objective 1**). Accordingly, various soft-magnetic materials are qualitatively compared on their suitability for reluctance actuators. The discussed ferromagnetic materials are: pure iron, nickel-iron, ferrite, stainless steel, silicon-iron and cobalt-iron. The influence of manufacturing processes on the magnetic material properties are considered. Furthermore, various measurement techniques for obtaining the magnetic properties of ferromagnetic

materials are evaluated, with a more detailed explanation of the applied measuring method.

In Chapter 4, a variety of magnetic hysteresis modeling methods is discussed. The history of the modeling methods is described, which gives an impression of the evolution and the acceptance of the methods by the scientific community. The hysteresis models are qualitatively evaluated to determine their applicability to reluctance actuators (**research objective 2(b)**).

In Chapter 5, the generalized scalar Preisach model is explained, which is applied for the modeling of magnetic materials. Four analytical distribution functions are optimized for three different magnetic materials. The accuracy of the prediction of the magnetic flux density with the static Preisach model is experimentally verified by a comparison to dc-measurements with various peak excitations for each soft-magnetic material (**research objective 3(a)**).

In Chapter 6, the dynamic phenomena of ferromagnetic materials are analyzed. The statistical loss theory is assessed and used to describe the magnetic field separation method. Moreover, the analytical eddy current model is described for laminated and non-laminated ferromagnetic materials. The combination of the eddy current model with the generalized Preisach model is presented. The results of the combined magnetic material modeling methods are compared to the measured material losses and to the instantaneous $B-H$ characteristics of Vacoflux 50 and M800-50A, for lamination thicknesses between 0.10 mm and 0.50 mm (**research objective 3(a)**). Additionally, the incorporation of the (dynamic) Preisach model for reluctance actuators is described. Besides the Preisach model, the 3d FEM and the complex impedance method are assessed on their predictions of various dynamic magnetization curves of the SiFe material, M800-50A (**research objective 3(a)**).

In Chapter 7, the discussed modeling methods are experimentally verified on the prediction of the hysteresis in the reluctance force of three E-core reluctance actuators (**research objective 3(b)**). The first reluctance actuator, manufactured of CoFe (Vacoflux 50) with a 0.10 mm lamination thickness, is examined for various arbitrary (low frequency) current excitations. The second SiFe (M800-50A) reluctance actuator is evaluated for dynamic excitations up to 320 Hz. The third reluctance actuator manufactured of the same SiFe is pre-biased with a NdFeB permanent magnet, which significantly increases the force range. The pre-biased E-core is also examined for sinusoidal current excitations up to 320 Hz.

In Chapter 8, the conclusions, contributions and recommendations are given.

Electromagnetic actuator modeling

The documented history about magnetism dates back to the ancient times around 200 B.C., in which the Greeks and Chinese experienced the force of a magnetic lodestone interacting with the magnetic field of the earth [50, 173]. The mathematical formulation of the observed electromagnetic phenomena started centuries later with a major contribution of Charles-Augustin de Coulomb in 1785. The understanding of electromagnetism improved substantially around the year 1820, by the research of Hans-Christian Oersted, André-Marie Ampère and Michael Faraday, who separately revealed the theory of electrical and magnetic phenomena. Years later in 1861, James Clerk Maxwell formulated the unified theory of electricity and magnetism [164], which he extended three years later by including light as an electromagnetic wave [165, 166]. The whole theory was covered in eleven equations, which were reformulated by Oliver Heaviside [189]. This resulted in the four differential equations, which are currently known as Maxwell's equations.

Besides the general theory, the origin of electrical machines is assigned to the invention of the iron-cored electromagnet [50]. It was a horseshoe-shaped core energized by a coil build by William Sturgeon in 1824 [242]. This electromagnet proved to be more effective in that time than the available natural permanent magnets. This invention is actually equivalent to the C-core reluctance actuator discussed in this work, although back then, the magnetic materials and electric isolation were far from optimal. The first voice-coil actuator dates back to the year 1874, when a patent was filed by Ernst Werner von Siemens [234]. The

voice-coil actuator is also known as the Lorentz actuator, because it is based on the Lorentz force. The Lorentz force equation was formulated in the modern form in 1892 by the Dutch scientist Hendrik Lorentz [189].

This chapter describes the modeling of electromagnetic actuators in general and more specifically, the modeling of reluctance actuators is discussed. Various modeling techniques are qualitatively compared on their suitability for the modeling of reluctance actuators. An analytical modeling method is selected, which is further explained for the modeling of (pre-biased) reluctance actuators. In Section 2.6, this analytical modeling method is used to discuss the most important properties of reluctance actuators related to short-stroke high-precision positioning systems, i.e. the nonlinearity of the force with current and position, and the parasitic forces due to misalignment of the stator and the mover. Additionally, simulations have been performed with a 2d FEM to investigate the amount of magnetic hysteresis in the force of reluctance actuators as presented in Section 2.7. The contributions of this chapter have been published in [261, 268, 270, 277].

2.1 General electromagnetic theory

The general electromagnetic analysis is based on Maxwell's equations, which are derived for the quasi-static case at a macroscopic scale in differential form, as

$$\nabla \times \mathbf{H} = \mathbf{J} \qquad \text{Ampère's law} \qquad (2.1)$$

$$\nabla \cdot \mathbf{B} = 0 \qquad \text{Gauss's law for magnetism} \qquad (2.2)$$

$$\nabla \times \mathbf{E} = -\frac{\partial \mathbf{B}}{\partial t} \qquad \text{Faraday's law} \qquad (2.3)$$

$$\nabla \cdot \mathbf{D} = \rho \qquad \text{Gauss's law} \qquad (2.4)$$

where \mathbf{J} and ρ are the source terms, i.e. the free current density and the free electric volume charge density, respectively. The electromagnetic fields are defined as follows: \mathbf{H} is the magnetic field strength, \mathbf{E} is the electric field strength, \mathbf{B} is the magnetic flux density and \mathbf{D} is the electric flux density. These four differential equations are only valid for relative low frequencies, typically below 1 MHz, which is more than three orders of magnitude higher than the dynamic effects in reluctance actuators and the typical control bandwidth of approximately 200 Hz in high-precision systems [36].

The Maxwell's equations are combined with the following constitutive relations

to describe the electromagnetic fields in a specific medium

$$\mathbf{B} = \mu_0(\mathbf{H} + \mathbf{M}) \quad (2.5)$$

$$\mathbf{D} = \epsilon_0\mathbf{E} + \mathbf{P} \quad (2.6)$$

where μ_0 and ϵ_0 are the magnetic permeability and the electric permittivity in free space, respectively. Additionally, \mathbf{M} is the magnetization and \mathbf{P} is the polarization. Hence, the relation between the magnetic flux density and the magnetic field strength in vacuum is $\mathbf{B} = \mu_0\mathbf{H}$, because $\mathbf{M} = 0$. However, when ferromagnetic materials are involved the magnetic constitutive relation is nonlinear and hysteretic, as explained in detail in Chapter 3. Similarly, the electric flux density and the electric field strength are related to the electric polarization, \mathbf{P} , which is substantially present in e.g. piezoelectric or ferroelectric materials [253].

In the classical linear theory of homogeneous, isotropic, stationary materials, the current density in conducting materials is given by the following constitutive relation

$$\mathbf{J} = \sigma\mathbf{E} \quad (2.7)$$

where σ is the electric conductivity. This expression relates Ampère's law (2.1) to Faraday's Law (2.3), which is later applied for the derivation of the eddy currents in ferromagnetic materials.

2.2 Energy conversion

The energy conversion of electromagnetic systems is discussed for the analysis of reluctance actuators. Generally, electric motors are intended to convert the electrical- and magnetic energy to mechanical energy in the most efficient manner. Usually, the generated thermal energy is undesired and, hence, it is considered as energy loss. Losses occur in all the three energy states i.e. the ohmic losses, the iron losses and the friction losses.

In electrical machines and hence, also in reluctance actuators the conservation of energy is given by [42]

$$W_e - W_\Omega = W_f + W_{fe} + W_m + W_{fr} \quad (2.8)$$

where W_e , W_f and W_m correspond with the three lossless energy components, i.e. the electrical energy, the stored magnetic energy and the mechanical energy, respectively. The other three components are defined as follows: W_Ω is the resistive energy dissipation, W_{fe} is the dissipated magnetic energy in the ferromagnetic material, and W_{fr} is the energy dissipation due to mechanical

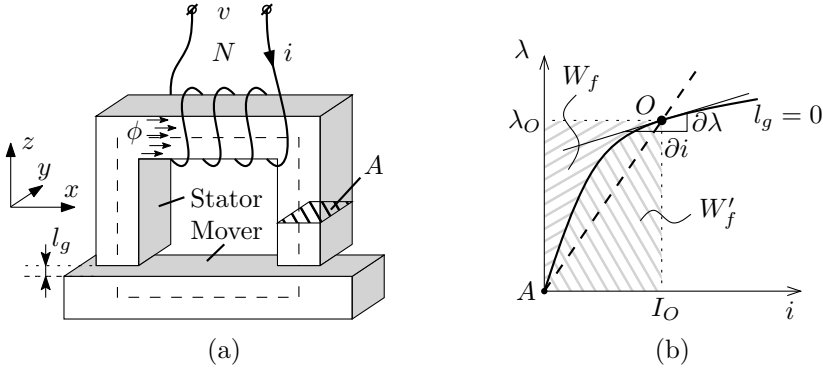


Fig. 2.1: An illustration of a ferromagnetic C-core actuator (a), and the relation between the flux linkage and the current (b).

friction. In this section, the energy conversion is discussed for a lossless system, in which all three loss components are neglected. The dissipated magnetic energy in the ferromagnetic material, also known as iron losses, are thoroughly evaluated by the analysis of magnetic hysteresis phenomena in this thesis.

The energy conversion principle in (2.8), is generally applicable for electromagnetic systems. In this section, the method is discussed for the C-core actuator as shown in Fig. 2.1(a). A ferromagnetic C-shaped stator and a mover are illustrated, with a coil of N turns around the stator. The coil is excited by a current, i , which results in a magnetic flux, ϕ , in the magnetic circuit. The flux linked with the turns of the coil is called the flux linkage, which is for this magnetic circuit defined as, $\lambda = N\phi$. For a C-core actuator with a nonlinear non-hysteretic ferromagnetic material the flux linkage-current characteristic, $\lambda-i$, is shown in Fig. 2.1(b). From this characteristic the coil inductance, L , is obtained, which relates the magnetic circuit components to the electric circuit.

2.2.1 Inductance

The inductance of the magnetic structure is given by the slope of the $\lambda-i$ plot in the point of operation, O , as

$$L(i, z) = \left. \frac{\partial \lambda(i, z)}{\partial i} \right|_O \quad (2.9)$$

which is also known as the incremental inductance. This expression for the inductance can be simplified when a magnetically linear material is assumed. In this case, the inductance is only dependent on the airgap length, l_g , which

is equal to the position of the mover in the negative z -direction. Therefore, for linear materials the inductance is expressed as

$$L(z) = \frac{\lambda(z)}{i} = \frac{N\phi(z)}{i} \quad (2.10)$$

which corresponds with the slope of the dashed line in Fig. 2.1(b) from the origin through the point of operation. This inductance is also known as the apparent inductance.

2.2.2 Energy

The electrical energy in a circuit, as shown in Fig. 2.1(a), is given for a lossless coil, by [40]

$$W_e = \int_0^T i(t)v(t)dt = \int_0^T i(t) \frac{d\lambda(i, z)}{dt} dt \quad (2.11)$$

where v is the coil voltage. The resistive energy losses can easily be incorporated as $W_\Omega = Ri(t)^2$. The electrical energy is equal to the energy stored in the magnetic fields in the system at a constant position. When the current is increased from 0 to I_O , the stored magnetic energy is given by

$$W_f = \int_0^{\lambda_O} i d\lambda(i, z) \quad (2.12)$$

which corresponds with the area on the left hand side of the λ - i characteristic, as shown in Fig. 2.1(b). The stored magnetic energy can also be derived from the magnetic flux density and magnetic field strength. Considering a closed magnetic circuit with magnetic length, l , cross-section area, A , and additionally, assuming a homogeneous magnetic field distribution in the ferromagnetic material, the stored magnetic energy is derived from (2.12) as

$$W_f = \int_0^{B_O} \left(\frac{Hl}{N} \right) NAdB = lA \int_0^{B_O} HdB \quad (2.13)$$

where B_O is the magnetic flux density corresponding to the flux linkage, λ_O . For a non-homogeneous magnetic field distribution, e.g. an open reluctance actuator, the magnetic fields have to be integrated over the whole volume including the entire air surrounding the actuator, to obtain the stored magnetic energy in the system from the magnetic fields. Therefore, in more general form, the stored magnetic energy is written as

$$W_f = \int_V \int_0^{B_O} HdBdV \quad (2.14)$$

where V is the volume of the electromagnetic converter, which consists of the actuator, the airgap, and the region in the surrounding of the actuator having a considerable magnetic field that could be influenced by a small position variation. Additionally, it is convenient to define the coenergy, which is the area under the $\lambda-i$ characteristic and is obtained as

$$W'_f = \lambda_O I_O - W_f = \int_0^{I_O} \lambda(i, z) di \quad (2.15)$$

or

$$W'_f = \int_V \int_0^{H_O} B dH dV. \quad (2.16)$$

2.3 Force calculations

Two methods are described to obtain the force of reluctance actuators, i.e. the virtual work (VW) method and the Maxwell stress tensor (MST) method. The force obtained from the VW method is derived from the previously discussed energy conversion analysis.

2.3.1 Virtual work method

The virtual work (VW) method is derived from the conservation of energy in a lossless system. The VW method is explained for a C-core reluctance actuator as shown in Fig. 2.1(a) with an airgap length, l_g . The VW method is derived for the $\lambda-i$ characteristic of Fig. 2.2. Equivalent to the energy equation (2.8), the sum of the change of each energy component is zero, such that

$$dW_e = dW_f + dW_m \quad (2.17)$$

where an infinitesimal change of energy is considered, such that it can be written in differential form. It is convenient for the analysis to maintain the current or to have a constant flux linkage during motion. In this analysis the current is maintained at a constant value.

For an infinitesimal position variation of the mover the change of the mechanical energy is related to the force as

$$dW_m = F_z dz \quad (2.18)$$

Moreover, the change of the electrical energy is derived from (2.11) as

$$dW_e = id\lambda \quad (2.19)$$

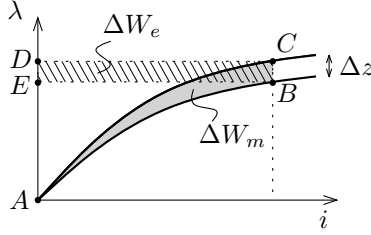


Fig. 2.2: The change of energy in relation with the λ - i characteristic.

and by combining the previous three equations, the following expression is obtained

$$F_z dz = -dW_f + i d\lambda \quad (2.20)$$

As can be seen in Fig. 2.2, the flux linkage is a function of the independent variables current, i , and position, z . The constant current during a position variation, Δz , is indicated by the vertical line, BC . Using the fact that the current and the position are two independent variables whereas the flux linkage is dependent on both variables, the force is obtained for a constant current as [42]

$$F_z = -\frac{\partial W_f(i, z)}{\partial z} + i \frac{\partial \lambda(i, z)}{\partial z}. \quad (2.21)$$

Using (2.15), the force is obtained from the coenergy as

$$F_z = \frac{\partial W'_f}{\partial z}. \quad (2.22)$$

When a magnetically linear case is considered, the energy and coenergy are equal, and the force is easily obtained from the coil inductance (2.10) as

$$W_f = W'_f = \frac{1}{2} i^2 L(z) \quad (2.23)$$

and hence, the force is obtained as

$$F_z = \frac{1}{2} i^2 \frac{dL(z)}{dz} \quad (2.24)$$

The analysis of the derivation of the force from the stored magnetic energy and coenergy is also illustrated by the gray area in Fig. 2.2. Using (2.12), the change of the stored magnetic energy is given by

$$\begin{aligned} \Delta W_f &= \int_0^{\lambda_D} i d\lambda - \int_0^{\lambda_E} i d\lambda \\ &= \text{Area}(ACD) - \text{Area}(ABE) \end{aligned} \quad (2.25)$$

Additionally, the change of the electrical energy (2.19) corresponds with the rectangle $BCDE$. Hence, using (2.17) the mechanical energy change is given by

$$\begin{aligned}\Delta W_m &= -\Delta W_f + \Delta W_e & (2.26) \\ &= \text{Area}(ABE) - \text{Area}(ACD) + \text{Area}(BCDE) \\ &= \text{Area}(ABC) \\ &= \Delta W'_f\end{aligned}$$

2.3.2 Maxwell stress tensor method

The Maxwell stress tensor (MST) method can be derived from either the VW method or from the Lorentz force. Here, the MST method is derived from the Lorentz force [212]. The Lorentz force is acting on a charged particle with charge, q , in an electric field, \mathbf{E} , and on a charged particle with a velocity, \mathbf{v} , in a magnetic field with a local flux density, \mathbf{B} . The Lorentz force is given by

$$\mathbf{F} = q\mathbf{E} + q\mathbf{v} \times \mathbf{B} \quad (2.27)$$

In a coil conductor, there is no net charge as the sum of the moving electrons and the stationary positive charges is zero and hence, the first term is zero. Additionally, the force on the negative charges in the electric field is transferred to the coil conductor by collisions with the atoms and hence, the net force due to this effect is zero. However, these collisions do result in Joule losses also known as Ohmic losses.

In this case, the Lorentz force only acts on the moving negative charges in the magnetic field. Considering the electric charges per volume, ρ , the current density in the coil is obtained as, $\mathbf{J} = \rho\mathbf{v}$. The Lorentz force density on a current density in a magnetic field is then defined as

$$\mathbf{f} = \mathbf{J} \times \mathbf{B} \quad (2.28)$$

The force is obtained as

$$\mathbf{F} = \int_V \mathbf{J} \times \mathbf{B} dV \quad (2.29)$$

where V is the volume of the whole system, but when the coil is the only current carrying volume it is sufficient to integrate over the coil only.

Using the same reasoning as for voice-coil actuators, no net charge is present in the coil of reluctance actuators and hence, also (2.28) can be applied. If a substitution is made for the current density, \mathbf{J} , by using Ampère's law (2.1), the force density is derived from (2.28) as [156]

$$\mathbf{f} = \left(\nabla \times \frac{\mathbf{B}}{\mu_0} \right) \times \mathbf{B} \quad (2.30)$$

As described in [88, 156, 183], this can be expressed in tensor form as

$$\mathbf{f} = \nabla \cdot \mathbb{T} \quad (2.31)$$

where the complete Maxwell stress tensor is given by

$$\mathbb{T} = \frac{1}{\mu_0} \begin{bmatrix} \left(B_x^2 - \frac{|B|^2}{2} \right) & B_x B_y & B_x B_z \\ B_y B_x & \left(B_y^2 - \frac{|B|^2}{2} \right) & B_y B_z \\ B_z B_x & B_z B_y & \left(B_z^2 - \frac{|B|^2}{2} \right) \end{bmatrix} \quad (2.32)$$

The stress tensor provides the local values of all magnetic stress components along each coordinate axis. This force density expression is valid for a volume and using Stoke's theorem, this can be reduced to a surface integral as follows

$$\mathbf{F} = \int_V \nabla \cdot \mathbb{T} dV = \oint_S \mathbb{T} \cdot \mathbf{n} dS \quad (2.33)$$

where S is the bounding surface and \mathbf{n} is the normal vector on S .

In e.g. a C-core reluctance actuator as shown in Fig. 2.1(a), the magnetic field that contributes to the force is located mostly in the airgap between the mover and the stator teeth. Therefore, under the condition that the magnetic field is homogeneous and perpendicular to the mover and stator surface, the force obtained with the MST method can be approximated by

$$F_z = \frac{B_z^2 A_T}{2\mu_0} \quad (2.34)$$

where A_T is the sum of the cross-section area of all teeth, and B_z is the magnetic flux density in the airgap. Using the same assumptions, this is equivalent to the force expression obtained with the VW method (2.22) using (2.14).

It should be noted that the force obtained with the VW method is only valid for a lossless system. Hence, no hysteresis can be included as it is previously presented. Whereas the force calculation with the MST method is based on the magnetic flux density distribution, in which the magnetic hysteresis phenomena could be included as explained later in Chapter 6.

2.4 Reluctance actuator modeling

This section focuses on the modeling of attracting reluctance actuators with and without a pre-biasing permanent magnet. An analytical and a numerical modeling method are selected from various electromagnetic modeling methods,

based on a qualitative comparison of their applicability for the modeling of reluctance actuators.

As mentioned in the introduction of this chapter, the first reluctance actuator is almost two centuries old. Since that time, numerous variants have been investigated and, therefore, it is not the intention of this work to propose a new design or topology. Basically two reluctance forces can be distinguished, based on the alignment [88, 120, 270] and attracting [18, 150, 202, 233, 283] principle, which can also be combined [19, 20]. Additionally, various attracting designs exist with a pre-biasing permanent magnet [148, 149, 192]. Furthermore, motors based on the alignment principle are the linear [91, 198, 287], planar [200, 201] or rotary [282] switched reluctance motors which are also named in literature as variable reluctance motors. General overviews of various actuator principles are given in [30, 114].

Numerous modeling techniques are developed over the years to analyze the electromagnetic phenomena in arbitrary geometries. These modeling methods are used to provide an accurate and/or fast description of the magnetic field distributions. For electromagnetic actuation systems the prediction of the magnetic fields is of major importance, to be able to obtain the force accurately.

A thorough overview of commonly applied actuator modeling techniques is given in e.g. [135]. A variety of analytical techniques is discussed, i.e. the equivalent current and charge methods [88], the harmonic method [99, 137], the conformal mapping method [108] and the magnetic equivalent circuit (MEC) method [39, 197, 221, 254]. In addition, the following numerical techniques are considered, i.e. the finite difference [88], finite element [125] and boundary element methods [92].

Generally, each one of these methods is suitable for a range of problems, but they also have their restrictions on e.g. geometry, materials, complexity, computational effort. The major consideration for a modeling method to be applicable to reluctance actuators is to which extent soft-magnetic materials can be incorporated. More specifically, the models are assessed on the following two criteria:

- The ability to model the magnetic fields inside and outside soft-magnetic structures.
- The possibility to include hysteretic actuator behavior.

The aforementioned modeling methods are subsequently discussed.

The equivalent current and charge method are applicable for obtaining the magnetic flux density from permanent magnets in air. Therefore, the charge modeling method is often applied for the analysis of voice-coil actuators. Ferromagnetic materials can only be analytically incorporated with a constant

magnetic permeability (mirroring) for flat surfaces [54] or numerically for specific shapes [41, 133]. The harmonic model and conformal mapping method are especially applicable for obtaining magnetic fields in air regions, where special boundary conditions are used to include the magnetic materials. However, these models cannot cope with nonlinear materials. From the analytical modeling methods, only the MEC method can incorporate nonlinear and hysteretic materials in its analysis, by applying an iterative solving procedure. Hence, the MEC model is further discussed in the following section.

From the numerical modeling methods, the boundary element method can only include linear materials, while the finite difference and finite element method (FEM) are able to iteratively solve magnetic field distributions in nonlinear materials. The FEM is the most commonly applied numerical method for the simulation of electromagnetic actuators, because of its flexibility and numerical stability [135]. One of the only commercially available FEM packages that can incorporate magnetic hysteresis in its analysis, Opera-Vector Fields [49], is evaluated on the simulation of reluctance actuators. The applied FEM is further discussed in Sections 4.5 and 6.5.

2.5 Magnetic equivalent circuit method

The magnetic equivalent circuit (MEC) method (also called network reluctance method, lumped parameter model or permeance network method) is a widely applied model for various electromagnetic problems where magnetic fields are modeled in structures mainly consisting of soft-magnetic materials. The soft-magnetic materials are usually applied in electromagnetic machines to concentrate the magnetic fields in a desired location. MEC models are applied for the modeling of transformers [295], synchronous machines [235], linear [136] and rotary flux switching motors [139, 190, 250], double salient permanent magnet machines [115], turbo generators [206], stepping motors [240, 241] and reluctance actuators [159, 261].

In general, the MEC model shows good agreement with measurements for closed magnetic structures with a high magnetic permeability, while only a fraction of the elements is needed in comparison with the finite difference, FEM or even the boundary element method. However, the modeling of magnetic fields in the air is more challenging with the MEC method and, hence, the MEC model is often extended with numerical or analytical approaches, e.g. the analytical representation of Roters [159, 221] or the tooth contour method [139, 205]. Both methods are briefly discussed in Section 2.5.3.

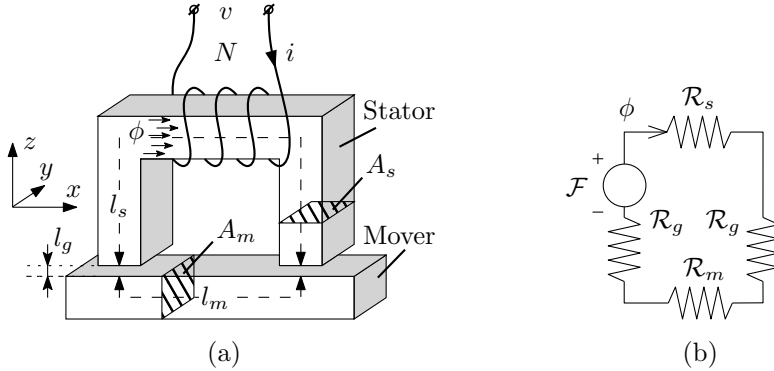


Fig. 2.3: Illustration of a C-core actuator (a), and the corresponding MEC model with reluctances (b).

2.5.1 Equivalent network

The MEC is the magnetic analogy of Ohm's law defined for electric circuits, which is also known as Hopkinson's law. This method models magnetic reluctances or permeances similarly as resistances or conductances, and a magnetomotive force (mmf) source in a magnetic circuit is the equivalent of a voltage source in an electric circuit. The reluctances incorporate the magnetic properties and shape of the modeled structure in so called flux tubes. These flux tubes are based on the expected magnetic flux paths in the considered space.

An example of a magnetic structure (a C-core actuator) is shown in Fig. 2.3(a). The C-core actuator is modeled with four flux tubes (the stator, the mover and two airgaps) represented by the four reluctances shown in Fig. 2.3(b). Equivalent to Kirchhoff's voltage law for an electric circuit, Ampère's law can be applied to a magnetic structure, as shown in Fig. 2.1(a). The integral over a closed flux path in a certain magnetic structure with n different material sections, results in

$$\oint_C \mathbf{H} \cdot d\mathbf{l} = \sum_n H_n l_n = Ni \quad (2.35)$$

where l is the length of the flux tube, N is the number of turns and i is the current through the coil. The source term, in this case the current multiplied by the number of turns, is the magnetomotive force (mmf) given by, $\mathcal{F} = Ni$. Rewriting (2.5), using the magnetic permeability, μ , the B - H relation is given as, $B = \mu H$, and (2.35) is rewritten as

$$\mathcal{F} = \sum_n \frac{B_n}{\mu_n} l_n = \sum_n \phi_n \frac{l_n}{\mu_n A_n} \quad (2.36)$$

where A is the cross-section area of a flux tube. In air, $\mu = \mu_0$, whereas for a ferromagnetic structure $\mu = \mu_0\mu_r(H)$ with a nonlinear or even hysteretic relative permeability. Assuming a continuous flux which is directed perpendicular to the cross-section area of each flux tube, (2.36) can be written as

$$\mathcal{F} = \phi \sum_n \frac{l_n}{\mu_n A_n} = \phi \sum_n \mathcal{R}_n \quad (2.37)$$

where \mathcal{R} is the magnetic reluctance. The permeance is defined as

$$\mathcal{P} = \mathcal{R}^{-1} = \frac{\mu A}{l} \quad (2.38)$$

which is used for solving complex MEC networks, as the magnetic fluxes in the network are in this case defined by a matrix multiplication of the permeances with the source vector.

2.5.2 Permanent magnet model

Permanent magnets can be included in a MEC model by the combination of a reluctance or permeance in series with an mmf-source or in parallel with a flux-source. The reluctance of the permanent magnet is derived from (2.38). In the following analysis the permanent magnets are described by an mmf-source given by

$$\mathcal{F}_{mag} = H_c l_{mag} \quad (2.39)$$

where H_c is the absolute value of the coercive field strength (as defined in Section 3.1) of the hard magnetic material and l_{mag} is the length of the permanent magnet in the magnetization direction.

2.5.3 Airgap reluctances or permeances

For obtaining the force of reluctance actuators it is essential to describe the airgap magnetic flux density with a high accuracy. When the force is obtained with the MST method, the magnetic flux density in the airgap determines the force directly (2.34). When the force is derived with the VW method, the changing magnetic energy in the system due to the change of the airgap length is used, i.e. (2.21) or (2.22). Because the energy is proportional to $\mathbf{H} \cdot \mathbf{B}$, most energy is located in the airgap of a reluctance actuator. Hence, the accuracy of the force prediction is highly dependent on the modeling of the magnetic fields in the airgap.

The accurate modeling of airgap reluctances with a MEC is rather challenging due to the fringing fluxes on the boundary between the relatively high magnetic

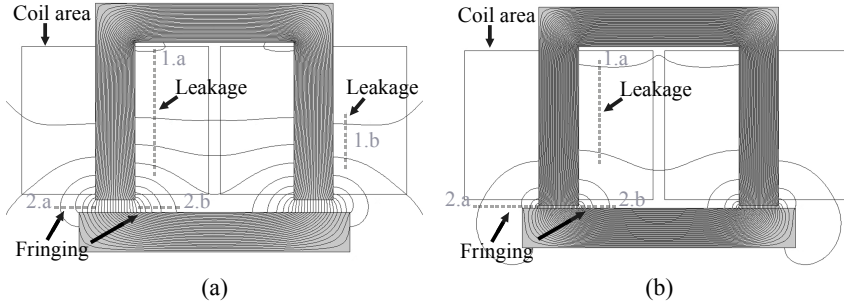


Fig. 2.4: The flux lines of a C-core reluctance actuator with an airgap of 2.5 mm (a), and 0.5 mm (b).

Table 2.1: Dimensions of the C-core reluctance actuator as shown in Fig. 2.5(a).

| Parameter | Symbol | Value | Unit |
|---------------------|---------------|-------|---------|
| Magnetomotive force | \mathcal{F} | 739 | A-turns |
| Stator width | sw | 42.9 | mm |
| Stator height | sh | 35.5 | mm |
| Tooth width | tw | 7.1 | mm |
| Tooth depth | td | 7.1 | mm |
| Mover width | mw | 48.9 | mm |
| Mover height | mh | 7.1 | mm |

permeability of the soft-magnetic material ($\mu_r \approx 10^3$) and the low relative permeability of air ($\mu_r = 1$). Besides fringing, also leakage occurs in the air region. The major difference between leakage and fringing is that leaking fluxes do not couple between the stator and mover and, hence, do not contribute to the force, while the fringing fluxes link the stator and the mover and, therefore, these do contribute to the force on the mover.

The fringing and leakage fluxes are shown in Fig. 2.4(a) and (b) for a C-core actuator with an airgap, $l_g = 2.5$ mm and $l_g = 0.5$ mm, respectively. The geometric parameters are given in Table 2.1 as indicated in Fig. 2.5(a). In both simulations shown in Fig. 2.4(a) and (b), the current density and the coil size are equal. In both cases 20 flux lines are drawn and hence, the number of lines leaking from one tooth to the other is a measure for the percentage of leakage for both airgap lengths. It can be noted that the fringing fluxes are majorly dependent on the airgap length.

In the C-core actuator on the left hand side, the gray-dashed line, 1.a, indicates the area where leakage occurs. Additionally, two flux lines are leaving at the outer surface of the actuator (dashed line 1.b) and leak around the actuator, since the bottom flux line does not couple with the mover in the simulation. Moreover, it can be noted that more fringing occurs with a larger airgap as indicated with the horizontal dashed lines, 2.a and 2.b, beside the left stator tooth. The density of the flux lines is proportional to the magnetic flux density and hence, it can be seen that the homogeneity and the level of the flux density in the airgap decrease with an increasing airgap length.

Two methods are considered for the modeling of the airgap permeances of reluctance actuators. Firstly, an analytical modeling method is discussed [221] and secondly the numerical tooth contour method (TCM) is evaluated [139, 205]. Both modeling methods are examined on the prediction of the force in the actuation direction and on the force perpendicular to the actuation direction (referred to as the parasitic force). The parasitic force is orders of magnitude smaller than the force in the actuation direction and is highly dependent on the fringing fluxes, as shown later in Section 2.6. This parasitic force cannot be controlled with the actuator producing it and, hence, this force results in undesired cross-talk between actuators in positioning systems.

Analytical permeance method

The 2d representation of the analytical permeance network is illustrated in Fig. 2.5(b). The airgap permeances of the third dimension are incorporated in the model as well. These 3d flux tubes are modeled with (parts of) cubical, cylindrical and spherical shapes [159, 221]. The applied leakage and fringing permeances are given in Appendix A.1. The reluctance network illustrated in Fig. 2.5(b) is further referred to as, model 1, which consists of 11 analytically obtained airgap reluctances.

The analytical method has its limitations, because not all the flux paths can be analytically described as the flux does not confine itself to particular predictable paths, e.g. the flux tubes that enter the mover from the side or from the bottom. Moreover, the flux leakage at the outside of the stator, and in the top corners are not incorporated. Therefore, obtaining the force perpendicular to the actuation direction is impossible with this model, because these forces are majorly dependent on the fringing fluxes that enter the mover from the side.

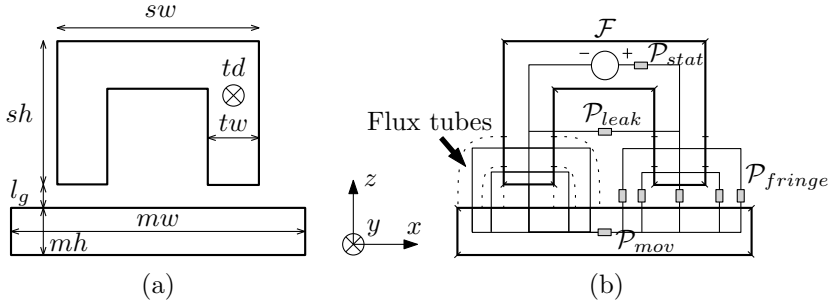


Fig. 2.5: C-core reluctance actuator corresponding with Fig. 2.4, its geometric parameters (a), and the MEC model with analytically determined airgap permeances (model 1) (b).

Numerical tooth contour method

The tooth contour method (TCM) gives a more general representation of the airgap permeances. The airgap permeances are obtained either with numerical [136, 181] or analytical methods [116, 205]. The analytical methods can describe the airgap permeances only in closed structures or periodic structures by applying boundary conditions. Because reluctance actuators are non-periodic and unbounded, a numerical method is applied to obtain the airgap permeances.

Generally, the airgap permeances are obtained by the simulated potential difference between two soft-magnetic boundaries of the specific problem. The analogy between the electric scalar potential and the magnetic scalar potential is used, as described in Appendix A.2. The potential drop between two selected boundaries is obtained, which is proportional to the equivalent permeance between these surfaces. Only the discretization of the ferromagnetic structure and the number of surface combinations have to be chosen.

The boundary element (BEM) software (ELECTRO2D) [280] is used to determine the permeance values from an electrostatic simulation. The permeances are obtained for each discrete mover position. In this analysis two models are evaluated, i.e. model 2 and model 3, which are shown in Fig. 2.6(a) and (b), respectively. It is chosen to incorporate 11 airgap permeances in model 2 and 73 airgap permeances in model 3, although, dependent on the available simulation time, any finite number of airgap permeances can be taken into account. In Section 2.6 is discussed how the modeling accuracy improves by adding complexity to the MEC model.

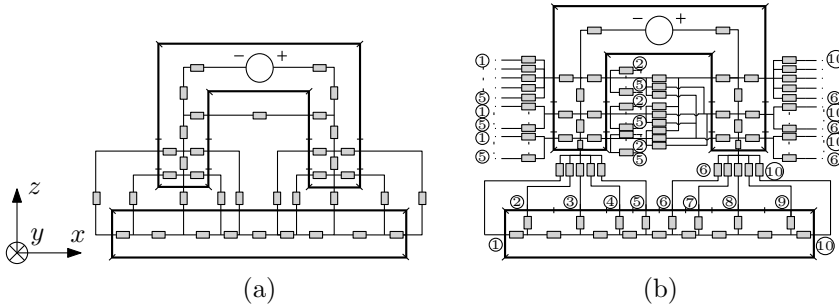


Fig. 2.6: C-core reluctance actuator and two MEC models. Model 2 with 11 airgap permeances and 27 iron permeances (a). Model 3 with 73 airgap permeances and 37 iron permeances (b).

2.5.4 Analytical MEC expression for including hysteresis

Generally, a MEC network can either be solved by applying Kirchhoff's voltage or current law. The relative complex reluctance networks, i.e. model 2 and 3, are solved by applying Kirchhoff's current law, where a linear equation is obtained for each node in the network. These equations are solved using a permeance matrix and vectors for the magnetic potentials and magnetic fluxes as described in [135]. This method is only applied for linear magnetic materials, because the analysis with nonlinear and hysteretic ferromagnetic materials significantly increases the complexity. For the case that a nonlinear or hysteretic material is considered, each iron reluctance or permeance has to be solved iteratively.

The analytical MEC expression, is derived for a pre-biased E-core reluctance actuator, as illustrated in Fig. 2.7(a). The major difference between the previously discussed C-core actuators and an E-core actuator is the geometry. Both actuators are considered equivalent from an electromagnetic modeling point of view. The applied MEC model of the E-core actuator, is shown in Fig. 2.7(b). This MEC representation is comparable to the MEC model of an unbiased E-core actuator, whereas in this case the mmf source of the permanent magnet is, $\mathcal{F}_{mag} = 0$ A-turns, and the corresponding reluctance is, $\mathcal{R}_{mag} = 0 \text{ H}^{-1}$, which is equivalent to a short-circuit in an electric network. The following analysis is not only applicable to reluctance actuators, but also to coils and transformers with an airgap as has been presented in [273].

In Fig. 2.7(b), \mathcal{F}_{el} , is the mmf source, \mathcal{R}_g , is the airgap reluctance, \mathcal{R}_{fe} , is the reluctance of the ferromagnetic material, and, \mathcal{R}_l , is the leakage reluctance. The three airgap reluctances have been modeled with a single equivalent reluctance, either based on the analytical permeance model (similar to model 1) or

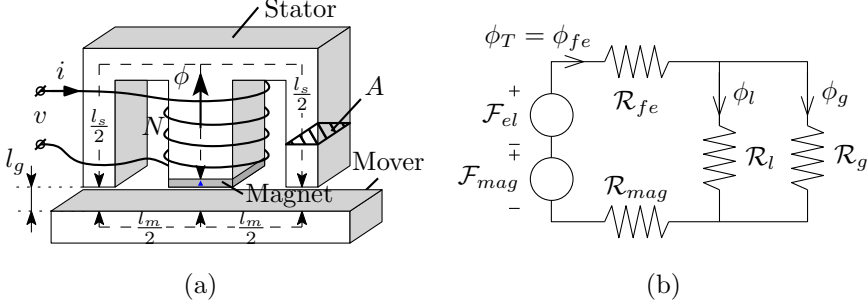


Fig. 2.7: Schematic view of the pre-biased E-core actuator (a), and the corresponding magnetic equivalent circuit (MEC) model (b).

the TCM (similar to model 2 or 3). The airgap flux, i.e. ϕ_g , and the leakage flux, i.e. ϕ_l , are related to the total flux, i.e. ϕ_T , as follows

$$\phi_g = k_\phi \phi_T \quad (2.40)$$

$$\phi_l = (1 - k_\phi) \phi_T \quad (2.41)$$

where k_ϕ is an airgap dependent coupling coefficient, defined as

$$k_\phi = \frac{\mathcal{R}_l}{\mathcal{R}_l + \mathcal{R}_g}. \quad (2.42)$$

Applying Ampère's law to the magnetic circuit of Fig. 2.7(b), results in

$$\mathcal{F}_{el} + \mathcal{F}_{mag} = H_{fe} l_{fe} + H_g l_g + H_{mag} l_{mag} \quad (2.43)$$

where the mmf-source of the permanent magnet is $\mathcal{F}_{mag} = H_c l_{mag}$ and the mmf over the permanent magnet is given by $H_{mag} l_{mag}$. Using (2.36) and (2.40), this is rewritten as

$$Ni + H_c l_{mag} = \phi_T (\mathcal{R}_{fe} + \mathcal{R}_{mag} + k_\phi \mathcal{R}_g) \quad (2.44)$$

from which the total flux is derived as follows

$$\phi_T = \frac{Ni + H_c l_{mag}}{\mathcal{R}_{fe} + \mathcal{R}_{mag} + k_\phi \mathcal{R}_g} \quad (2.45)$$

which is used to obtain the force of the reluctance actuator using either the VW method or the MST method. The force with the VW method can be obtained from the coenergy (2.22) using the inductance (2.10) and the energy change of the permanent magnet with a mutual term is incorporated as follows

$$F = \frac{1}{2} i^2 \frac{dL(z)}{dz} + \frac{1}{2} H_c \cdot l_{mag} \frac{d\phi_{mag}(z)}{dz} + Ni \frac{d\phi_{mag}(z)}{dz}. \quad (2.46)$$

This expression can be divided into three force components. The first term is the force resulting from the coil, the second term is the force from the permanent magnet and the third contribution is the mutual force resulting from both the coil and the permanent magnet. The flux of the permanent magnet depends on the position, and is derived from (2.44) as

$$\phi_{mag}(z) = \frac{H_c l_{mag}}{\mathcal{R}_{fe} + \mathcal{R}_{mag} + k_\phi \mathcal{R}_g(z)} \quad (2.47)$$

For obtaining the force with the MST method, the magnetic flux density in the airgap is derived from the total flux (2.45). The force is then obtained using (2.34) by applying an equivalent airgap cross-section area, A_{eq} , of the parallel connected airgap reluctances.

$$F_z = \frac{B_z^2 A_{eq}}{2\mu_0} \quad (2.48)$$

where

$$B_z = \frac{k_\phi \phi_T}{A_{eq}} \quad \text{and} \quad A_{eq} = \frac{l_g}{\mathcal{R}_g \mu_0}. \quad (2.49)$$

By applying the MST method, the magnetic hysteresis in the magnetic flux density is automatically incorporated in the force. But in case a hysteretic force is derived using (2.46), the obtained force is incorrect, because this derivation is based on the VW method which is only valid for a lossless system.

2.6 Nonlinearities in reluctance actuators

As discussed in Chapter 1, the challenges of reluctances actuators for short-stroke high-precision applications are the intrinsic nonlinearities of the actuator. The non-hysteretic actuator nonlinearities are discussed in this section. More specifically, the nonlinear current-force relation, and the nonlinear position-force relation in the actuation direction and perpendicular to the actuation direction. The amount of magnetic hysteresis in the reluctance force is assessed in the following section. The presented analysis is valid for attractive reluctance actuators in general, because the applied C-core and E-core actuators used in the analysis are considered equivalent from an electromagnetic perspective.

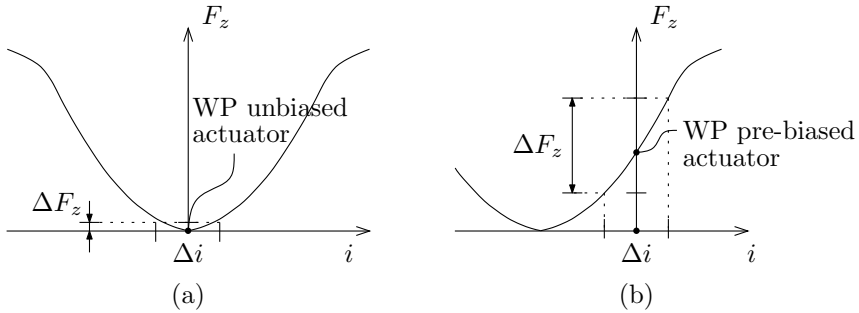


Fig. 2.8: Current-force characteristic in the working point (WP) for an unbiased reluctance actuator (a), and for a pre-biased reluctance actuator (b).

2.6.1 Current-force relation

The nonlinear current-force relation of an unbiased reluctance actuator is shown in Fig. 2.8(a). The current force relation is approximately proportional to the current squared, as derived with the VW method for linear materials in (2.24). For low current excitations the airgap reluctance is dominant. When the magnetic material approaches its saturation magnetization the value of the iron reluctance increases. This is illustrated in Fig. 2.8(a), by the decreasing slope of the current-force characteristic at a high current level. This is a physical limit of the reluctance actuator, because increasing the current excitation will not significantly increase the force when the ferromagnetic material approaches its saturation magnetization.

The inclusion of a permanent magnet in a pre-biased reluctance actuator shifts the working point, WP, in the current-force characteristic, as illustrated in Fig. 2.8(b). In practice, this is not exactly true, because the permanent magnet has a low relative permeability and, hence, the effective airgap length is slightly increased in this case. By including a permanent magnet, the force variation, ΔF , due to a current variation, Δi , significantly increases around the working point. On the one hand, this increases the efficiency of the actuator and a more linear current-force relation is achieved. On the other hand, the static force results in a high stiffness for zero current and additionally, a relatively high current is needed to decrease the force to zero.

2.6.2 Position-force relation

The nonlinear position-force relation of reluctance actuators is assessed for the force in the actuation direction (z -direction) due to a position variation in the z -direction and the parasitic force due to a movement perpendicular to the actuation direction (cross-talk). The airgap modeling methods presented in previous section are assessed on their suitability for modeling these position dependent forces of the C-core actuator, depicted in Fig. 2.4(a) and (b). The dimensions are given in Table 2.1. It can be noted that the mover width exceeds the stator sizes with 6 mm, which significantly reduces the parasitic forces due to misalignment in comparison to an equally sized stator and mover.

Firstly, the force in the actuation direction (z -direction) with a position variation in the actuation direction is investigated with the three previously presented MEC models, which are an analytical model (model 1) and two models based on the tooth contour method (model 2 and 3), which are illustrated in Figs. 2.5(b), 2.6(a) and 2.6(b), respectively. The simulation results are also compared to 2d BEM and 2d FEM simulations, as shown in Fig. 2.9(a). All three MEC models show similar accuracy compared to the FEM and BEM simulations regarding the force, due to a position variation in the actuation direction. The three MEC models show good agreement with the 2d FEM simulation. A maximum discrepancy of 1 N is obtained for all three models, which corresponds with a maximum force error of 2.7 % when the mover is positioned 0.5 mm below the stator. This discrepancy is a result of the changing fringing and leakage fluxes dependent on the airgap length as previously discussed in Section 2.5.3. For a constant airgap the force is modeled with a significantly higher accuracy as shown by a comparison to FEM simulations in next section.

Secondly, Fig. 2.9(b) shows the parasitic force which is simulated with the two MEC models that are based on the TCM (model 2 and 3), and which are compared to the FEM and BEM simulation results. The analytical MEC model is not compared because it is not suitable for obtaining the parasitic forces. The parasitic force variation obtained with model 2, with 11 airgap permeances is 57 times higher than the simulation results obtained with the FEM and BEM. MEC model 3 with 73 airgap permeances predicts the perpendicular force much better than model 2, although still a discrepancy of 56.2 % is obtained.

The accuracy of the parasitic force prediction can be improved by adding more complexity to the MEC model with an increasing number of (airgap) permeances. However, the accuracy of the force prediction of reluctance actuators in the direction perpendicular to the actuation direction is limited with the TCM, because it is highly dependent on the number of the selected fringing paths. A similar analysis with the TCM has been presented in [261] for an E-core reluctance actuator. In this case, 161 airgap permeances are applied

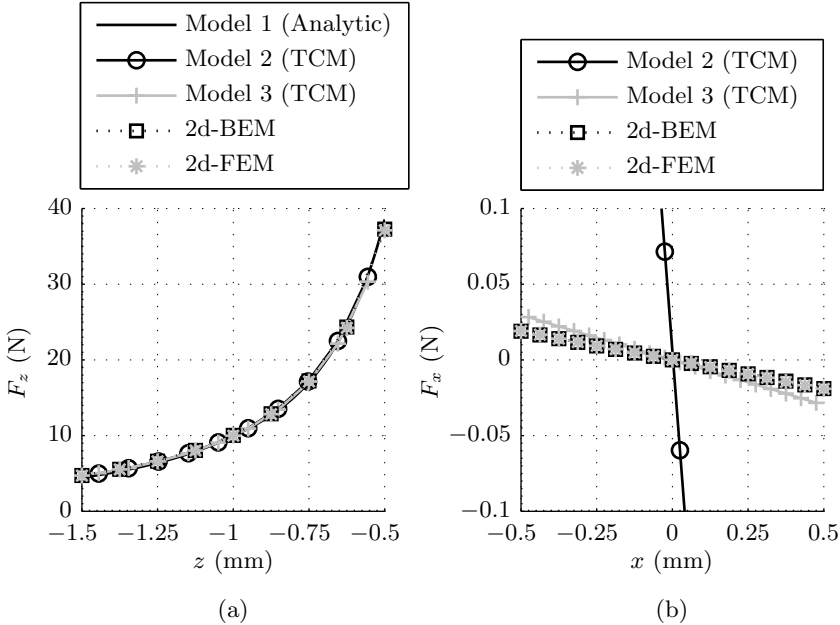


Fig. 2.9: Simulation of the force of a C-core actuator with five simulation methods, in the actuation direction (z -direction) (a), and perpendicular to the actuation direction (x -direction) (b).

and a simulation accuracy of the parasitic force was obtained of approximately 17 %, for a problem with more fringing and leakage than presented here.

Based on this analysis it is concluded that the TCM is not effective for modeling the parasitic forces of reluctance actuators for two reasons. Increase the number of permeances will eventually lead to a permeance network approaching the complexity of a FEM model, to achieve a reasonable accuracy. Furthermore, the permeances should be determined for each configuration and position with a numerical BEM or FEM, whereas the forces can also be obtained directly from these methods which is more efficient.

The modeling accuracy of the reluctance force in the actuation direction is important, because its quadratic relation to the position results in a high (negative) stiffness. In high-precision actuation systems, a high-stiffness is undesired, because in this case the disturbances are directly transferred, e.g. between wafer-stages or between the floor and the moving mass, as discussed in Chapter 1. These disturbances have to be actively compensated when reluctance actuators are applied, while the disturbances are significantly better decoupled

with voice-coil actuators, which have a relatively low-stiffness.

The determination of the force perpendicular to the actuation direction due to misalignment is also important. These parasitic forces are undesired because the actuator itself cannot compensate for any force in the direction perpendicular to the actuation direction. For reluctance actuators this is a so called positive stiffness, whereas for voice-coil actuators this is a negative stiffness or zero stiffness dependent on the direction of the misalignment. The amount of the parasitic force variation due to a misalignment of a reluctance actuator and a voice-coil actuator are similar, as has been presented in [270]. Therefore, it is concluded that the parasitic force of reluctance actuators is no limiting issue.

2.7 Hysteresis in the reluctance force

Besides the previously discussed forces in the actuation direction and perpendicular to the actuation direction, the magnetic hysteresis in the force is important for high-precision applications. In cases where a nanometer accurate positioning is required, an accuracy of 99.99 % is necessary for the applied feed-forward force [36]. This high-accuracy specification for the force prediction, can only be achieved for reluctance actuators when magnetic hysteresis is taken into account, as shown in this section.

Magnetic hysteresis is a highly nonlinear and history dependent effect in ferromagnetic materials, which will be thoroughly discussed in Chapter 3. Due to magnetic hysteresis in the soft-magnetic material, the force of reluctance actuators is also nonlinear and history dependent. The most evident effect of hysteresis in the force is the difference between the force resulting from an increasing or a decreasing current. A slightly higher force occurs for a decreasing excitation compared to the increasing current. In this section, the amount of hysteresis in the reluctance force is investigated with a 2d finite element method (FEM), which can incorporate magnetic hysteresis in its analysis. The applied FEM is later discussed in Sections 4.5 and 6.5.

Besides investigating the amount of the magnetic hysteresis in the force of a standard reluctance actuator, the 2d FEM is used to investigate the possibility of minimizing the magnetic hysteresis in the force by a comparison of various E-core actuator topologies. These other three reluctance actuators are adjusted with the intention to increase the homogeneity of the magnetic flux density in the actuator core. The four reluctance actuator topologies are based on the results of the topology optimization described in [153, 154].

The hysteresis in the reluctance force of four E-core topologies is examined for the force in the actuation direction (z -direction), for equal peak amplitudes of the current, force and magnetic flux density in the middle tooth. Additionally,

the hysteresis and the force variation due to a position variation perpendicular to the actuation direction are evaluated.

2.7.1 Evaluated E-core actuators

The amount of hysteresis in the force is evaluated for the four E-core actuator topologies, as shown in Fig. 2.10. The actuators are referred to as (a)-(d) corresponding with the order in this figure. All four actuators have an equal actuator depth (ad), stator height (sh), stator width (sw), tooth height (th), tooth width (tw), mover height (mh), mover width (mw), coil size and airgap length ($l_g = 0.5$ mm). Additionally, all four actuators are simulated with SiFe (M800-50A) core material. The sizes of the four actuator topologies are given in Table 2.2.

The shape of the actuators is altered to increase the force density by removing material with minimal magnetic flux density. Additionally, the force is enhanced by applying tooth tips, which increases the width of the teeth. It should be noted that the manufacturing of the actuators with the tooth tips is more difficult, because a pre-wound coil cannot be easily inserted. Besides these four topologies, intermediate topologies have been considered (which are not depicted), where stator and/or mover material is removed without applying tooth tips. These topologies show that removing material with a low magnetic flux density only improves the force density but not the force. Additionally, the amount of hysteresis in the force is not significantly influenced by only removing the iron material in the corners.

The coil size is equal for each topology and, hence, the magnetomotive force (mmf) is the same for a given current density. However, the magnetic circuit determines the resulting magnetic flux (density) and the output force. The tooth tips decrease the airgap reluctance, and as a result, the flux is increased for the same mmf. Additionally, the shape of the stator teeth and the mover width influence the disturbance forces due to position variations perpendicular to the actuation direction considerably.

The comparison on the amount of hysteresis in the force is performed with the 2d FEM for equal peak amplitudes of the current, force and magnetic flux density, subsequently. Each quasi-static simulation is performed with a sinusoidal current excitation. The first simulation with equal current density has a peak amplitude of 5.63 A/mm². The second and third simulation are performed with an equal peak force of approximately 35 N and a magnetic flux density of 0.55 T, respectively. Finally, the cross-talk is simulated with two periods of a sinusoidal position of the mover in the x -direction with a stroke of ± 3 mm and a dc current density of 15 A/mm².

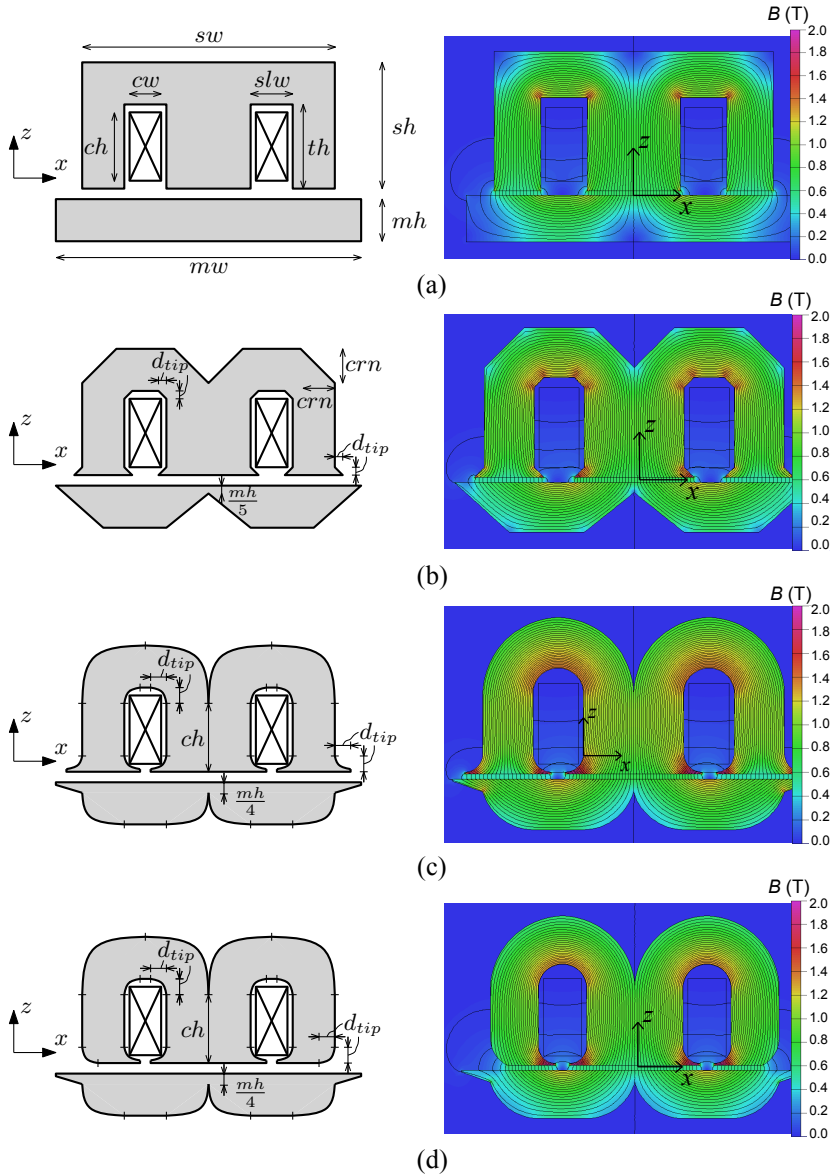


Fig. 2.10: The four E-core reluctance actuator topologies with geometric parameters and the magnetic flux and flux density distribution for a current density of 15 A/mm^2 . A standard E-core actuator with increased mover length (a), with removed corners and added tooth tips (b), with rounded stator and mover corners (c), and with round inner tooth tips (d).

Table 2.2: Dimensions of the four E-core actuators illustrated in Fig. 2.10.

| Parameter | Symbol | Topology | | | | Unit |
|----------------|-----------|----------|-----|-----|-----|------|
| | | (a) | (b) | (c) | (d) | |
| Actuator depth | ad | 30 | 30 | 30 | 30 | mm |
| Mover width | mw | 36 | 36 | 36 | 36 | mm |
| Mover height | mh | 5 | 5 | 5 | 5 | mm |
| Stator w. | sw | 30 | 30 | 30 | 30 | mm |
| Stator h. | sh | 15 | 15 | 15 | 15 | mm |
| Tooth w. | tw | 5 | 5 | 5 | 5 | mm |
| Tooth h. | th | 10 | 10 | 10 | 10 | mm |
| Coil w. | cw | 4 | 4 | 4 | 4 | mm |
| Coil h. | ch | 8 | 8 | 8 | 8 | mm |
| Slot w. | slw | 5 | 5 | 5 | 5 | mm |
| delta tip | d_{tip} | - | 1 | 2 | 2 | mm |
| Corner w./h. | crn | - | 4 | - | - | mm |

2.7.2 Equal peak current-density

Actuators are usually optimized on the force density, in which case only the current-force relation is considered, as shown in Fig. 2.11(a). The rms-current is directly proportional to the copper losses and, hence, to the actuator temperature (for equal outer surface and coil area). Therefore, the highest force related to volume or mass gives immediately the optimal design. From this point of view the best topology is clearly actuator (c) with round corners and tooth tips, as shown in Fig. 2.11(b). The force density of actuator (b), (c) and (d) is 44 %, 69 % and 39 % higher than the force density of the standard actuator (a), respectively.

The goal of this analysis is to investigate the amount of magnetic hysteresis in the force, which is first examined for an equal current excitation. The magnetic hysteresis in the force is not directly visible in the figures showing the current-force relation (Fig. 2.11(a) and (b)), because the amount of magnetic hysteresis is relatively small compared to the peak force. Therefore, the hysteresis in the force is graphically shown by the subtraction of the non-hysteretic force obtained with the proposed analytical actuator model (2.46). Moreover, the hysteresis in the force is normalized as a percentage of the peak force, because the peak force is different for each actuator. This results in the loops as shown in Fig. 2.11(c), in which the maximum opening is called the loop-eye and corresponds with the error of the force when it is predicted with a

non-hysteretic actuator model.

In Fig. 2.11(c), it is shown that the maximum magnetic hysteresis in the force occurs for actuator (c) with the round corners, which is 0.81 % of its peak force. The larger loop-eye due to magnetic hysteresis is a result of the higher magnetic flux (density) in the center of the middle actuator tooth, as shown in Fig. 2.11(d) and Table 2.3. In addition to the relative loop-eye, the absolute loop-eye is given which is also significantly larger for actuator (c).

In addition, the total iron losses in the actuators due to magnetic hysteresis are deducted from the simulation, which is obtained by the integral over the magnetic field strength with respect to the flux density as described in (2.13). This integral is the energy dissipated in the material in one period of the applied current, and is also a measure for the hysteresis in the force.

2.7.3 Equal peak force

It is not clear from previous analysis, which actuator encounters minimal magnetic hysteresis as the peak force and magnetic flux density is different for each topology. Therefore, the magnetic hysteresis in the reluctance force is investigated for an equal peak force of approximately 35 N. In Fig. 2.12(a), it is shown that the maximum loop-eye varies between 0.63 % and 0.94 % for actuators (a) and (c), respectively. The results are similar to the previous analysis for an equal current density, as the magnetic flux density in the middle tooth is again significantly higher for actuator (c) compared to actuator (a).

2.7.4 Equal peak magnetic flux density

A sinusoidal current is applied for all four topologies, which corresponds with an approximately equal peak magnetic flux density of 0.55 T in the middle tooth. The percentage of magnetic hysteresis in the reluctance force of the four E-core actuators is similar to the results of the other current profiles, as shown in Fig. 2.12(b). However, the absolute loop-eye is approximately 0.28 N for all four actuators with an equal peak magnetic flux density, as given in Table 2.3. Moreover, Table 2.3 shows that the total hysteresis losses in the actuators are directly related to the peak magnetic flux density in the middle tooth.

From the previous analysis, it can be concluded that the amount of magnetic hysteresis in the reluctance force as percentage of the peak force is lower for the standard E-core actuator shown in Fig. 2.10(a). However, the absolute magnetic hysteresis in the force and the iron losses due to magnetic hysteresis are directly proportional to the peak magnetic flux density in the major part (bulk) of the actuator. Based on these two observations, it is concluded that it

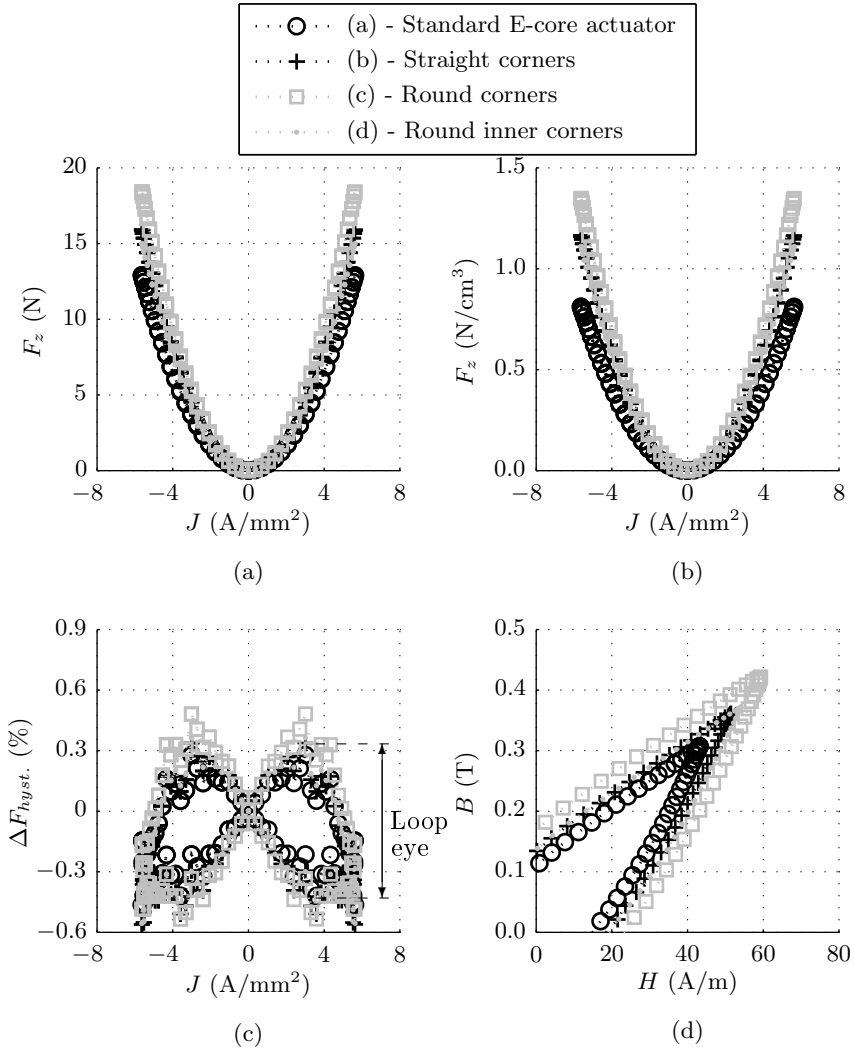


Fig. 2.11: Comparison of the four actuator topologies with 2d FEM simulations of the current-force relation (a), the current-force density (b), the percentage hysteresis in force (c), and the $B-H$ loops in the center of the middle tooth (d). All the results are obtained for an equal peak current density of 5.63 A/mm².

Table 2.3: Simulation results of the four actuator topologies.

| | Quantity | Topology | | | | Unit |
|---------------------|-------------------------|----------|------|------|------|-------------------|
| | | (a) | (b) | (c) | (d) | |
| Equal J_{\max} | J_{\max} | 5.63 | 5.63 | 5.63 | 5.63 | A/mm ² |
| | F_{\max} | 12.9 | 15.9 | 18.4 | 15.0 | N |
| | B_{\max} | 307 | 361 | 422 | 372 | mT |
| | absolute loop-eye | 0.06 | 0.10 | 0.15 | 0.10 | N |
| | relative loop-eye | 0.49 | 0.64 | 0.81 | 0.66 | % |
| | $W_f = lA \oint H(B)dB$ | 0.15 | 0.23 | 0.34 | 0.25 | mJ |
| Equal F_{\max} | J_{\max} | 9.22 | 8.29 | 7.70 | 8.54 | A/mm ² |
| | F_{\max} | 34.8 | 34.7 | 34.6 | 34.7 | N |
| | B_{\max} | 505 | 534 | 578 | 566 | mT |
| | absolute loop-eye | 0.22 | 0.27 | 0.32 | 0.28 | N |
| | relative loop-eye | 0.63 | 0.77 | 0.94 | 0.80 | % |
| | $W_f = lA \oint H(B)dB$ | 0.49 | 0.57 | 0.70 | 0.65 | mJ |
| Equal B_{\max} | J_{\max} | 10.10 | 8.55 | 7.33 | 8.31 | A/mm ² |
| | F_{\max} | 41.5 | 36.9 | 31.4 | 32.8 | N |
| | B_{\max} | 552 | 551 | 550 | 551 | mT |
| | absolute loop-eye | 0.28 | 0.29 | 0.29 | 0.27 | N |
| | relative loop-eye | 0.66 | 0.78 | 0.92 | 0.81 | % |
| | $W_f = lA \oint H(B)dB$ | 0.60 | 0.61 | 0.62 | 0.61 | mJ |

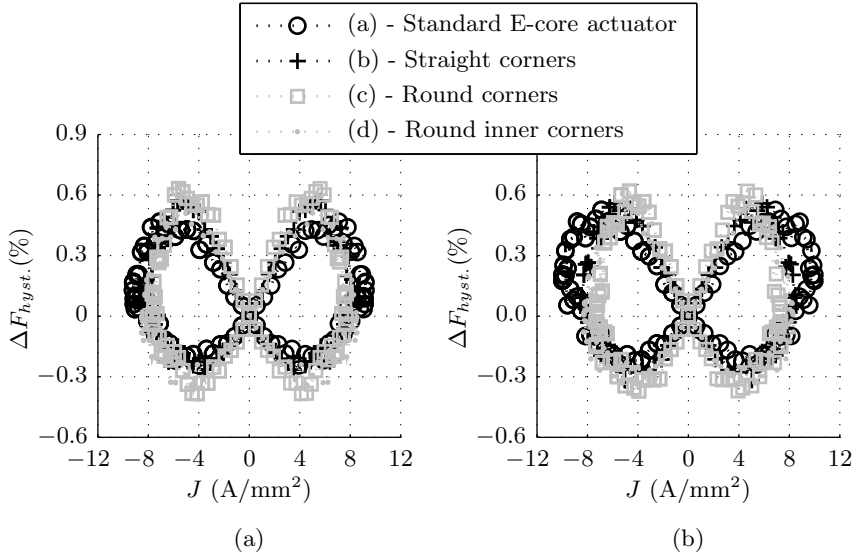


Fig. 2.12: 2d FEM simulations of the percentage hysteresis in force of the four actuator topologies, for a peak force of 35 N (a), and a peak magnetic flux density in the middle tooth of 0.55 T (b).

should be sufficient to model the magnetic hysteresis in the bulk of the actuator only. Henceforth, a single hysteretic reluctance should be enough to model the hysteresis in the force of reluctance actuators. The maximum magnetic hysteresis in the force of all reluctance actuators is between 0.5 % and 1.0 % of the peak force.

2.7.5 Cross-talk

Additionally, the hysteresis in the reluctance force due to a position variation is evaluated for the four actuators. The position dependent forces are shown in Fig. 2.13(a) and (b) for the force in the z - and x -direction, respectively. Both forces (ΔF_x and ΔF_y) are normalized to the peak force in the z -direction at the aligned position, $\delta_x = 0$ mm. The hysteresis in the cross-talk is negligible with maxima at the center position below 0.1 % for all topologies, which corresponds approximately to 1 % of the peak value of the cross-talk. This is in the same order of magnitude as the magnetic hysteresis in the force in the actuation direction.

The cross-talk is highly dependent on the symmetry and overlap of the mover and stator with respect to the position. Hence, a larger mover width, topol-

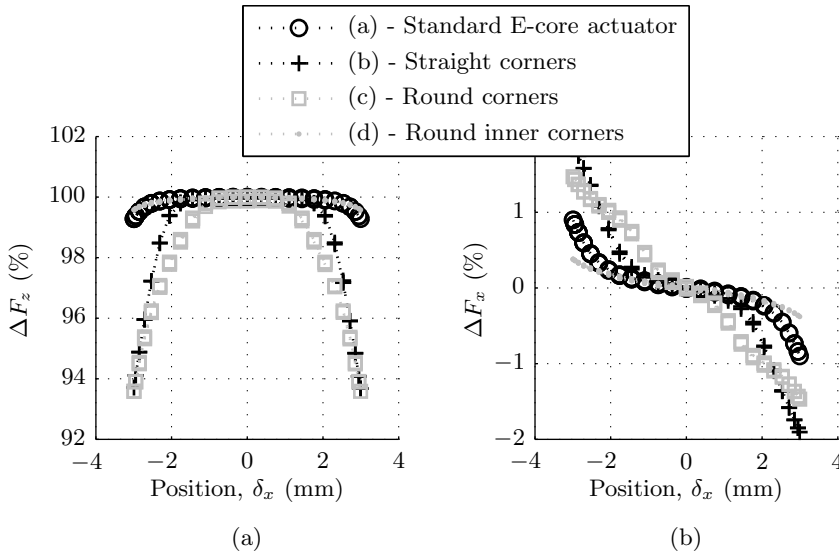


Fig. 2.13: 2d FEM simulations of the relative force in the z -direction (a) and of the relative force in the x -direction (b), both caused by a position variation, δ_x , in the x -direction for the four actuator topologies.

ogy (a), and a smaller stator tooth-tip at the sides, topology (d), decrease the cross-talk significantly. The actuator with round inner corners (d), shows minimal cross-talk of 0.42 % and 0.38 %, for the force in the z - and x -direction, respectively. Actuators (b) and (c) with straight and round corners show a cross-talk larger than 6.3 % and 1.5 % for the force in the z - and x -direction, respectively.

2.8 Conclusions

This chapter concerns the modeling of reluctance actuators based on a general electromagnetic analysis. The most important properties of reluctance actuators are discussed related to short-stroke high-precision positioning systems, i.e. the nonlinearity with current and position, the stiffness due to misalignment of the stator and the mover, and the amount of hysteresis in the reluctance force. The analytical magnetic equivalent circuit (MEC) modeling method and a commercially available finite element method are selected from various modeling techniques, because of their ability to include magnetic material properties in

their analysis. The MEC model is explained for the modeling of (pre-biased) reluctance actuators.

It is concluded that the force in the actuation direction obtained with the MEC model at a constant airgap length, can be modeled with an accuracy such that only a force error due to magnetic hysteresis remains. Accurately modeling of parasitic forces with the MEC model is inefficient for two reasons. Firstly, it costs much effort to increase the number of permeances, which eventually leads to a permeance network approaching the complexity of a FEM model to achieve the required accuracy. Secondly, the permeances should be determined for each configuration and position with a numerical BEM or FEM, whereas the forces can also be obtained directly from these methods.

Apart from modeling reluctance actuators, the amount of magnetic hysteresis in the reluctance force of four E-core topologies is investigated with 2d FEM simulations. The static hysteresis in the force as percentage of the peak force is between 0.5 and 1.0 % for the evaluated reluctance actuators. It is concluded that the absolute amount of hysteresis in the force and the hysteresis losses are directly related to the peak value of the magnetic flux density in the bulk of the actuator. Based on these two observations, it is also concluded that it should be sufficient to model the hysteresis in the bulk of the ferromagnetic material with a single hysteresis operator. Modifying the tooth tips of a standard E-core actuator shows an increased force density up to 69 %, but these actuators experience more magnetic hysteresis as percentage of the peak force. The analysis of magnetic hysteresis phenomena in ferromagnetic materials is the major subject in the following chapters, which eventually leads to the static and dynamic modeling of hysteresis phenomena in the reluctance force.

The cross-talk is highly dependent on the tooth shape of the stator and the extension of the mover width with respect to the outer stator dimensions, which is true for both, the force in the actuation direction and perpendicular to the actuation direction. The amount of magnetic hysteresis in the cross-talk is negligible and, hence, the magnetic hysteresis in the cross-talk is not considered further.

Magnetic hysteresis

Magnetic phenomena in ferromagnetic materials, such as magnetic hysteresis and eddy currents, originate from micromagnetic quantum effects at the atomic level. Although the discussed magnetic phenomena in electromagnetic actuation systems are mainly macroscopic effects, the microscopic origin is also addressed. In principle, the macroscopic material phenomena should be the physical outcome of the micromagnetic analysis. However, apart from a few ideal cases, no one knows exactly how to relate them [28].

In this chapter, magnetic materials are primarily discussed regarding their magnetic properties. Also some electrical, mechanical and thermal properties are discussed, because they affect the magnetic material phenomena. Among these magnetic material properties, magnetic hysteresis* is one of the most significant macroscopic effects, which is attributed to various microscopic material properties.

A worthy formulation explaining the complexity of ferromagnetism is given by Edmund C. Stoner in 1947 [239]: “*The rich diversity of ferromagnetic phenomena, the perennial challenge to skill in experiment and to physical insight in coordinating the results, the fast range of actual and possible applications of ferromagnetic materials, and the fundamental character of the essential theoretical problems raised have all combined to give ferromagnetism a width of interest which contrasts strongly with the apparent narrowness of its subject matter, namely, certain particular properties of a very limited number of substances.*”

*From the Greek word *hysterein* = to be behind or later, to come late

In this chapter, the most significant magnetic hysteresis phenomena in ferromagnetic materials are explained. Firstly, the commonly used terms and magnetic material properties are introduced. Followed by a theoretical explanation of the fundamental hysteresis phenomena in Section 3.2, i.e. magnetic domains, the Barkhausen effect, magnetic hysteresis loops, congruency, accommodation and anisotropy. This explanation of the micromagnetic phenomena is based on a literature survey obtained from [28, 29, 57, 183]. In Section 3.3 more detailed effects related to the magnetic hysteresis loop are discussed. In Section 3.4, more practical subjects related to ferromagnetic materials are considered, such as the variety of available soft-magnetic materials and the influence of manufacturing processes on the magnetic material properties. Finally in Section 3.5, various measurement techniques for obtaining the magnetic properties of ferromagnetic materials are evaluated, with a more detailed explanation of the applied measurement methods.

3.1 Magnetic constitutive law

The most important properties of ferromagnetism are the existence of a saturation magnetic flux density and hysteresis. Ferromagnetic substances cannot be characterized by any simple constitutive law, because an infinite set of history dependent magnetic hysteresis loops can be observed. The constitutive law $\mathbf{B}(\mathbf{H})$ (2.5) describes the material on a gross scale, larger than that of domains, such that the material appears to be homogeneous. For hard-magnetic materials (permanent magnets), the constitutive relation is often represented by the magnetic polarization, $\mathbf{I} = \mu_0 \mathbf{M}$, (also referred to as J) which is measured in Tesla. The magnetization is written as

$$\mathbf{M} = \frac{\mathbf{B}}{\mu_0} - \mathbf{H} \quad (3.1)$$

This constitutive relation should be represented in vector form because most magnetic materials are anisotropic. However, in practice and for non-oriented materials often the scalar representation is applied. In the following chapters, in which the modeling of magnetic materials is discussed, magnetic materials are assumed to be homogeneous, isotropic, nonlinear and stationary. When the magnetic constitutive relation of materials is considered linear as well, this expression is simplified to

$$\mathbf{M} = \chi \mathbf{H} \quad (3.2)$$

or

$$\mathbf{B} = \mu_0(1 + \chi)\mathbf{H} \quad (3.3)$$

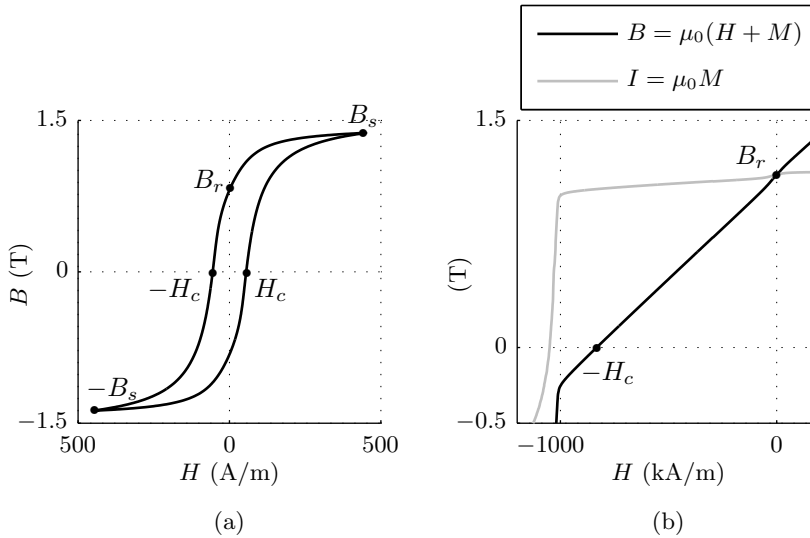


Fig. 3.1: Typical constitutive relations of a soft-magnetic (a), and a hard-magnetic ferromagnetic material (b).

where $\mu = \mu_0(1 + \chi)$, and hence $\mu_r = 1 + \chi$, where χ is the magnetic susceptibility.

In this thesis, the nonlinear scalar representation of magnetic hysteresis is described by hysteresis loops, as shown in Fig. 3.1(a), for a soft-magnetic material. In Fig. 3.1(b), the typical characteristic of the magnetic flux density and the magnetic polarization of a hard-magnetic material (permanent magnet) are shown, in the second quadrant. This magnetic behavior is considered stationary, although, the magnetic hysteresis phenomena are history dependent and highly dependent on the environment, e.g. temperature variations and stresses. The environment is considered constant in the analysis, and the history dependency is related to the variation of the magnetic field strength in stead of the time.

A typical hysteresis loop of a soft-magnetic material is shown in Fig. 3.1(a), which is obtained by applying a cyclic magnetic field strength, H , while measuring the change of the magnetization, M , or the magnetic flux density, B , which is also known as magnetic induction. A few characteristic points are indicated in Fig. 3.1(a), i.e. B_s is the saturation magnetic flux density, B_r is the remanent magnetic flux density, and H_c is the coercivity or coercive field strength. The saturation magnetic flux density is defined as a finite limit of the magnetic material at which the magnetic flux density increases proportional with $\mu_0 H$ [33]. However, this occurs for extremely high magnetic fields

only. Therefore, in this thesis, the term saturation magnetic flux density is used as the highest magnetic flux density, as indicated in Fig. 3.1(a). The remanent magnetic flux density and the coercivity are more precisely defined as, $B_r = B(H)|_{H=0}$ and $H_c = H(B)|_{B=0}$, respectively. Because both have an equal positive and negative value in a symmetric $B-H$ curve, only the positive values are used throughout this thesis.

In soft-magnetic materials the coercive field strength is typically between, $0.1 < H_c < 200$ A/m, whereas hard-magnetic materials typically have a coercivity between, $5 \cdot 10^3 < H_c < 1 \cdot 10^7$ A/m [50]. This is also the reason why usually only the $B-H$ curve is shown for soft-magnetic materials, while for hard-magnetic materials the $M-H$ curve is often shown as well. In contrast to soft-magnetic materials in which B and $\mu_0 M$ have a similar magnitude, the hard-magnetic materials have a magnetic field strength, H , and a magnetization, M , of a comparable order of magnitude. Thus, in hard-magnetic materials there is a significant difference between the $B(H)$ and $M(H)$ loops, as shown in Fig. 3.1(b). Similarly, the susceptibility of a hard-magnetic material is of the order of $0.03 - 50$, whereas for soft-magnetic materials, $10^1 < \chi < 1 \cdot 10^6$, ranging from powder core materials to Metglas.

3.2 Micromagnetic phenomena

The source of magnetization originates from the property of atomic particles to have a so called “spin”. These particles move along a circular orbit, which results in an angular momentum. If this spinning particle is an electron, this circular motion is also a current that behaves like a magnetic dipole having a magnetic moment. Hence, a spinning electron has both an angular momentum as well as a magnetic moment. In non-ferromagnetic (paramagnetic, $\chi \ll 1$) materials, the magnetic moments do not interact with each other, but have random orientations due to the thermal energy. Hence, the electrons cancel out any net magnetization alignment except for strong external magnetic fields in the order of 10^8 A/m. In ferromagnetic materials the electron spins tend to spontaneously align, and they do produce a net magnetic moment, already by external magnetic field strengths in the order of $10 - 10^2$ A/m [28, 183]. Note that this effect only occurs below a material specific critical temperature, the Curie’s temperature, T_c .

In 1907 [279], Weiss ascribed the alignment of magnetic moments in ferromagnetic materials to the Weiss molecular field that interacts between the magnetic moments. This molecular field is an internal field proportional to the magnetization of the order of 10^9 A/m for iron, which is among other material properties related to the Curie temperature. This spin-spin interaction is also known as exchange. The exchange forces between electron spins are not discussed here

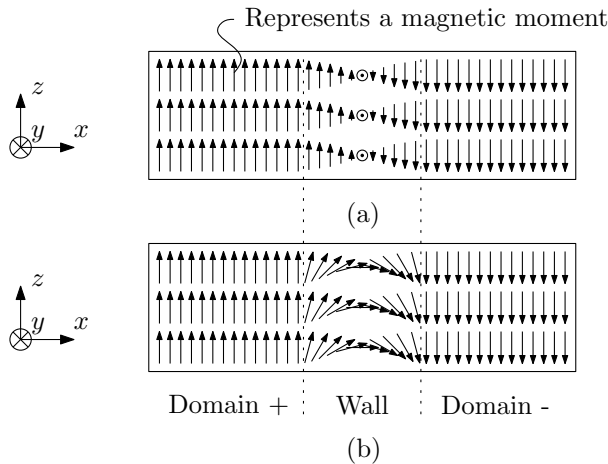


Fig. 3.2: Representation of 180° domain wall movement parallel to the plain (rotation around the x -axis), i.e. the Bloch wall (a), and perpendicular to the plane (rotation around the y -axis), i.e. the Néel wall (b) [29].

but these problems are often described by the Heisenberg Hamiltonian [57].

The eight orders of magnitude difference between the atomic internal fields and an external field of e.g. 10 A/m , which can be enough to change the magnetization direction, are resolved by Weiss through the introduction of regions, called magnetic domains. The neighboring atoms only align themselves over a certain number of atoms, after which the alignment changes direction as shown in Fig. 3.2(a) and (b). Each region of aligned magnetic moments is a domain. The transition between domains has been described in 1932 by Bloch, who introduced the moving Bloch walls, where the aligned magnetic moments move parallel to the plain of the wall (out of the page). In this case the rotation of the magnetic moments in the domain wall is around the x -axis, as illustrated in Fig. 3.2(a). Additionally, Néel walls occur where the rotation is perpendicular to the plain of the wall [142, 191], in which case the magnetic moments rotate around the y -axis, as shown in Fig. 3.2(b). Besides, the 180° domain alignment, as shown in Fig. 3.2, the domain walls can be oriented in any other direction, in which case the domain wall angle is less than 180° and is called a 90° -domain wall.

An example of a macroscopic $B-H$ curve, starting from its demagnetized state with the initial magnetization curve, followed by a demagnetization curve back to $B = 0$ and hence, $H = -H_c$, is shown in Fig. 3.3(a). The corresponding domain representation is shown in Fig. 3.3(b). In a demagnetized ferromag-

netic material, the internal domains have a random magnetization direction and hence, the net magnetization is zero. In Fig. 3.3(b) this is represented by rectangle 1, in which the vertical gray line is a 180° -domain wall and the other domain walls are exactly 90° -domain walls, because these walls separate domains with a 90° difference in the magnetization direction. This representation is far from reality, because the domains are randomly oriented in nature, but it is useful to explain the domain wall movement due to an externally applied magnetic field strength.

When an external magnetic field is applied and H grows from point 0 to 2, the domains that are (more) aligned with the field can grow at the expense of those which are not aligned, as shown in Fig. 3.3(b) (block 2). The approximately linear line segment from point 0 to 1 is still reversible, while the section 1-3 is irreversible. Reversibility means that the initial magnetic flux density is recovered when the magnetic field strength is returned to its initial value, which is not the case for an irreversible section. Increasing the magnetic field strength further, a single domain is formed which points along its preferred direction. The reversible region of the magnetic hysteresis curve is reached. The saturation magnetic flux density is reached when all the domains are aligned in the direction of the applied field, as shown in block 4 of Fig. 3.3(b). When the magnetic field strength is decreased, the original magnetization direction of the domain is restored (block 5). Decreasing the magnetic field strength further, the irreversible region is entered, and a domain is formed with an opposite magnetization direction. The negative coercive field strength is reached when the net magnetization is zero again, as shown in Fig. 3.3(b) (block 6).

3.2.1 Barkhausen effect

The magnetic constitutive relation, as shown in Fig. 3.1(a), is the result of macroscopic hysteresis effects for a relatively large ferromagnetic piece of material. This figure shows an average $B-H$ characteristic over a volume containing many domains and, hence, it does not contain information of local domains. In a macroscopic magnetic system, there is always a substantial amount of structural disorder. Such as, the presence of grains in poly-crystals, dislocations and lattice deformations, fluctuations of composition, presence of inclusions, surface roughness in thin films and thin sheets, random variations of particle shapes etc. [28]. These sources of disorder are coupled to the magnetic flux density through so called exchange interaction, anisotropy, and magneto-static interactions. This results in a complicated energy landscape, with a huge number of local minima and saddle points. The states with minimum energy in ferromagnetic materials jump from one stable state to the other with variation of the applied field, which is called the Barkhausen effect. The randomness of Barkhausen jumps on the macroscopic scale is described with statistical

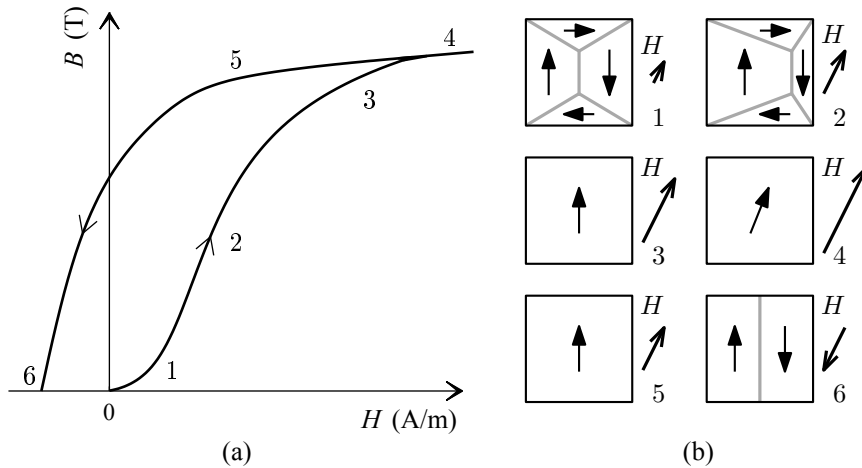


Fig. 3.3: Initial magnetization curve followed by a demagnetization curve (a), and a representation of the domain movement (b), due to an alternating magnetic field strength out of alignment with the preferred magnetization direction of the domains [50].

methods to analyze magnetization processes and domain structures.

Until now hysteresis effects have been considered as rate-independent. However, eddy currents occur at Barkhausen jumps when domain walls are moving. These eddy currents result in iron losses (heat), which is a rate-dependent effect. A high rate-of-change of the external applied field, results in more Barkhausen jumps and hence, there is more energy converted to thermal energy. The related macroscopic effect is the increase of the hysteresis loop area, which represents the amount of energy irreversibly transformed into heat during one hysteresis loop. Rate-independent hysteresis is an approximation for absolute zero-temperature, at which the system remains at the local free energy minimum initially occupied. For any other temperature, the minimum free energy of the system is determined by Boltzmann statistics [29]. Barkhausen jumps are thermally activated, and the magnetic system moves toward states of lower energy until an equilibrium is reached. These energy states can be seen as numerous bistable systems, which change by temperature variations or by an external magnetic field. As a result of the addition of thermal energy, the iron losses and the relative permeability of magnetic materials decrease [248], whereas the iron losses and the permeability increase for a decreasing temperature [179]. Henceforth, rate-independent hysteresis is an approximation of numerous processes that are intrinsically rate-dependent. Hysteresis is the whole set of connected phenomena resulting from metastable states, thermal

energy and dissipation mechanisms with certain time scales.

In the remainder of the thesis, rate-independent hysteresis is considered for measurements at which the rate of change of the magnetic flux density is limited to 30 mT/s as explained in Section 3.5. Moreover, the discussed rate-dependent effects are attributed to two effects, i.e. macroscopic eddy currents and excess losses.

3.2.2 Anisotropy

Anisotropic properties of magnetic materials are a result of the applied manufacturing process. For the production of thin sheets for laminations, the ferromagnetic material is rolled to a specific thickness. The direction parallel to the axis of rolling, shows the lowest values of total losses and the highest magnetic permeability. The lattice structures are deformed and are oriented in the rolling direction. Consequently, the lattice structure has a direction with minimal energy that is favored, named as anisotropy. Besides anisotropy, the magnetic materials can be grain oriented (GO) or non-grain oriented (NO/NGO). The magnetic materials discussed in this thesis are considered non-grain oriented materials.

3.2.3 Magnetostriction and elongation

Magnetostriction is the change of the dimensions of a material substance exposed by a magnetic field. The change in length of a volume, in the direction of the applied magnetic field strength, is the most dominant effect [33]. Other magnetostriction phenomena are the change in dimensions perpendicular to the direction of the magnetic field strength, the change in magnetic flux density due to longitudinal and/or transverse stress, the change in Young's modulus or shear modulus due to a magnetization, the change in volume due to a magnetization, the twist or bending of a magnetic material due to longitudinal fields or its reciprocal effect [183].

Magnetostriction is a result of two processes, the domain-wall motion and domain rotation, of which the later one is more dominant. Domain rotation does not change the volume of the material and hence, an increased length parallel to the applied field must be accompanied by a contraction in the plain perpendicular to the field. Magnetostriction occurs in all materials, although, even in strong magnetic materials, which experience the most magnetostriction, the effect is relatively small [183].

The various magnetostriction effects are caused by the interaction of physical material properties, i.e. magnetic flux density, stress and temperature [24].

These interacting aspects of magnetostriction make the measurement of magnetostriction rather challenging, especially, when the elongation and shear in more directions are considered. A study is performed on building a measurement setup to investigate the magnetostriction of Invar in 3d [61]. It has been shown that among others, minimizing the external forces, positioning of the material sample with a high accuracy as well as distinguishing the shear from the measured elongation, are challenging.

The relative elongation in the direction of the applied magnetic field is typically in the order of 10^{-5} , for the saturation magnetic flux density of a soft-magnetic material. Which means that for reluctance actuators with a tooth length of 50 mm, a maximum airgap variation due to magnetostriction of $5 \cdot 10^{-7}$ m occurs, which is two orders of magnitude smaller than the thermal elongation, which is approximately equal to $1 \cdot 10^{-6}$ m for a temperature difference of 10 K. The force variation due to magnetostriction is calculated with the analytical MEC model described in previous chapter, and is expected to be approximately equal to 0.2 % of the peak force at an airgap of 0.5 mm. The deviation of the force due to a temperature variation of the ferromagnetic material is approximately equal to 0.45 % K^{-1} .

Another magnetostriction effect, is the change in Young's modulus due to magnetic fields. The Young's modulus is the elasticity of materials defined as the ratio of linear stress to strain. The change of the Young's modulus due to the presents of a magnetic flux density is relatively small, since it is approximately 1 % for iron and 6 % for nickel [183].

The elongation of the ferromagnetic material due to the force of the actuator itself, is also related to the Young's modulus. The maximum force on the surface of the mover of the evaluated reluctance actuators in Chapter 7 is 300 N, which corresponds with a force density (pressure) of approximately $4 \cdot 10^5$ N/m^2 . Using the Young's modulus of steel of approximately $200 \cdot 10^9$ N/m^2 [50], the maximum elongation of a tooth of 50 mm is obtained as $1 \cdot 10^{-7}$ m. The force difference of the actuator due to this effect at an airgap of 0.5 mm is approximately 0.04 % of the applied force.

These effects are not taken into account in this thesis, because magnetic hysteresis is more significantly present in the force of reluctance actuators. It should be noted that the temperature is kept constant during the measurements performed in this thesis.

3.3 Magnetic hysteresis loop

The most significant macroscopic effect measured in soft-magnetic materials is the hysteresis curve, of which a typical example is shown in Fig. 3.1(a). Besides this measured $B-H$ loop any point in the interior of the major loop can be reached as shown in the $B-H$ characteristic of Fig. 3.4(a). The most important properties regarding magnetic hysteresis loops are defined according to this figure.

Often two typical cyclic loops are distinguished, i.e. the major loop and the minor loop. The major loop is defined as the outer most loop possible, reaching from positive to negative saturation. In theory, this sounds like a clear definition. However, it is difficult to have a uniform definition for the saturation magnetic flux density as this definition differs per field of application. Several definitions are (i) the magnetic field strength at which the upward and downward magnetic flux density are equal, (ii) the magnetic field strength at which the relative magnetic permeability is unity, or (iii) the saturation is specified for a certain value of the magnetic field strength. The first two definitions are basically equal but unrealistic, because a relative permeability of one means that all the magnetic moments and domains are aligned in the direction of the applied magnetic field strength. Hence, any increase of the magnetic field strength will result in an increased magnetic flux density proportional to $\mu_0 = 4\pi \cdot 10^{-7}$. It means that the incremental inductance (2.9) of the coil is equal to the same coil in air. Generally, this magnetic field strength is difficult to apply, due to the high currents needed which are often limited by the temperature that should be constant for a single measurement. Other definitions of the saturation magnetic flux density which are not so harsh are related to the fractional decrease of the magnetic permeability or the coil inductance. In this thesis, the term major loop is used for the largest loop shown in a specific figure and any of the other loops are called minor loops.

The minor loops shown in Fig. 3.4(a) that are directly connected with the major loop are the first-order minor loops, whereas the minor loop closest to the origin is an example of a second-order minor loop. Except for the largest displayed minor loop, all others have an equal variation of the magnetic field strength of, $\Delta H = 60$ A/m. It can be seen that the size of the minor loop is dependent on the offset in the magnetic field strength, when the top three minor loops are considered in the zoomed view of Fig. 3.4(b). The two minor loops on the right side are cycling between two equal values of input magnetic field strengths, i.e. $H = 40$ A/m to $H = 100$ A/m. They have the same shape whereas the magnetic flux density is different due to a different history. These two minor loops are called congruent, because these are equally shaped. However, many experiments show that such minor loops may substantially deviate from this property [29], which are therefore called non-congruent [126].

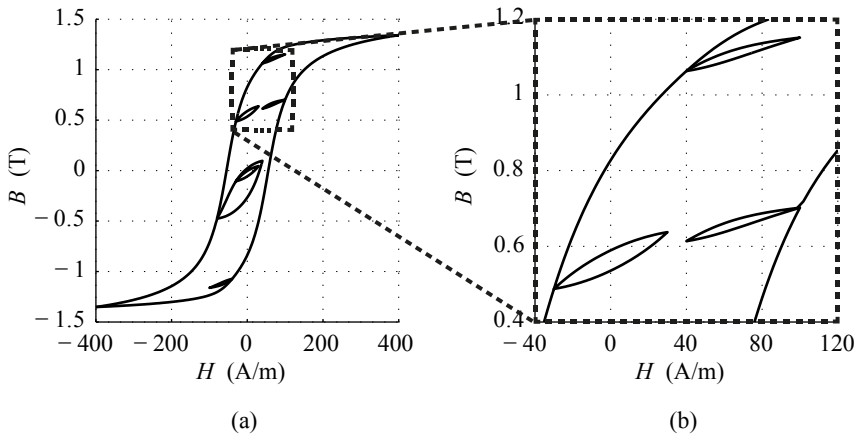


Fig. 3.4: Example of first- and second-order reversal curves (minor loops) and the wiping-out property. A full $B-H$ curve (a), and a zoomed (magnified) view around the upper three minor loops (b).

Additionally, it is often assumed that the minor loops close after one cycle in exactly the same point as where the minor loop has started, which is called the wiping-out property. However, experiments show that under repeated cycling, the system progressively adjusts its domain configuration [66]. The slow stabilization process requires generally a large number of cycles to achieve a stable minor loop. This ferromagnetic property is called an accommodation or a reptation process [29]. Typically, the percentage of error in the prediction of the magnetic flux density due to accommodation is between one and five percent of the peak magnetic flux density, i.e. 1.5 % [23], 2 % [256], 2.8 % [160] and 4.4 % [289].

Both ferromagnetic properties, i.e. the non-congruency and the accommodation, are considered insignificant for the analysis because the magnetic material models have a limited accuracy compared to the measurements which is in the same order of magnitude. Moreover, a three percent error of the predicted hysteresis will result in a discrepancy of the force of approximately 0.03 %, because the maximum amount of hysteresis in the force is approximately 1 % of the peak force, as shown in previous chapter. Therefore, the more dominant actuator behavior and the global hysteretic phenomena are considering more important for reluctance actuators.

3.4 Soft-magnetic materials

Numerous ferromagnetic materials exist, which are often named by its chemical composition or by a name given by the manufacturer. Various books [85, 172] summarize the properties of these materials and manufacturers specify the most relevant physical properties. In this section, an overview is given of commonly applied soft-magnetic materials, which are discussed on their applicability for reluctance actuators.

The desired properties of soft-magnetic materials for high-precision reluctance actuators should be linked to the application. Firstly, the actuators should have a high force density related to both its volume and its mass. Considering the force density per unit mass, \mathbf{f}_m [N/kg], and the fact that the force is related to the square of the magnetic flux density, $F \sim B^2$ (2.34), the soft-magnetic material should have a high saturation magnetic flux density.

Besides the force density of the reluctance actuator the amount of magnetic hysteresis in the force is important to achieve the desired positioning accuracy and for minimizing the iron losses. Therefore, the coercivity and the peak magnetic flux density are important parameters for a static analysis. The conductivity in combination with the lamination thickness determines the dynamic eddy current effects. Except for ferrites, all materials are available in various lamination thicknesses and hence, also the conductivity is, besides magnetic hysteresis, an important parameter for the material evaluation.

3.4.1 Material evaluation

The soft-magnetic materials to be evaluated are listed in Table 3.1, i.e. ferrites, stainless steel, nickel-irons, silicon-irons, cobalt-iron and pure iron. The presented magnetic material properties are defined as follows: B is the saturation magnetic flux density, μ_r is the initial relative magnetic permeability, σ is the electric conductivity and H_c is the coercive field strength. The material compositions are given in wt%, which is defined as the mass fraction as percentage of the total mass. The material properties of these materials are mainly obtained from the IEC standard 60404-1 [118], complemented by [85, 172] and an additional verification is performed by an inspection of the specifications of the manufacturers. The material properties should be considered as typical values, because commonly the experimentally obtained values are lower than the specified values.

The first category materials are the ferrites, which are often applied in inductors (coils). Ferrites are also known as ferromagnetic oxides, which have the general formula $M^{2+}Fe^{3+}O^{4+}$ where M is a bivalent metallic ion such as Fe^{2+} , Ni^{2+} , Mg^{2+} , Cu^{2+} and Zn^{2+} or mixtures of these ions. Here, only the following

Table 3.1: Typical properties of the discussed magnetic materials [85, 172].

| Soft-magnetic material | B_s (T) | μ_r (10^3) | σ (S m ⁻¹) | H_c (A m ⁻¹) | ρ_m (kg dm ⁻³) |
|----------------------------------|--------------|-----------------------|----------------------------------|-------------------------------|------------------------------------|
| NiFe ₂ O ₄ | 0.34 | 3 | $6 \cdot 10^{-5}$ | 20 – 80 | 5.38 |
| CoFe ₂ O ₄ | 0.53 | 3 | $\approx 1 \cdot 10^{-5}$ | 20 – 80 | 5.29 |
| MgFe ₂ O ₄ | 0.15 | 3 | $\approx 1 \cdot 10^{-5}$ | 20 – 80 | 4.52 |
| MnFe ₂ O ₄ | 0.50 | 3 | $5.3 \cdot 10^{-7}$ | 20 – 80 | 5.00 |
| X6Cr17 | 1.55 | 1.3 | $1.67 \cdot 10^6$ | 250 | 7.7 |
| Ni36-Fe64 | 1.30 | 2 | $1.33 \cdot 10^6$ | 40 | 8.15 |
| Ni50-Fe50 | 1.60 | 15 | $2.22 \cdot 10^6$ | 7 | 8.25 |
| Ni80-Fe20 | 0.75 | 150 | $1.67 \cdot 10^6$ | 0.4 | 8.7 |
| Si3-Fe97 GO | 2.03 | 80 | $2.0 \cdot 10^6$ | 5 | 7.8 |
| Si3-Fe97 NO | 2.03 | 5 | $4.35 \cdot 10^6$ | 55 | 7.8 |
| Si7-Fe93 GO | 1.8 | 23 | $1.2 \cdot 10^6$ | 30 | 7.5 |
| Co50-Fe50 | 2.35 | 8 | $2.27 \cdot 10^{-6}$ | 80 | 8.12 |
| Fe | 2.15 | 5 | $1.33 \cdot 10^6$ | 70 | 8.15 |

ferrites are considered, NiFe₂O₄, CoFe₂O₄, MgFe₂O₄ and MnFe₂O₄. Ferrites, are typically applied in the kHz-GHz range because of the low conductivity in the order of $1 \cdot 10^{-5}$ S/m and below. The conductivity is rarely specified, because mainly the losses at various frequencies are of major interest. The relatively low saturation magnetic flux density is the reason why ferrites are rarely used for reluctance actuators, because a low flux density results in a low force density.

Secondly, a stainless steel (also named inox steel) is considered with a 17 % chromium content. Stainless steels can be divided in three categories, of which the ferritic and martensitic steels are magnetic, and the austenitic stainless steels are non-magnetic. The most important property of stainless steels is their resistance against corrosion from water, like ordinary steel. In Table 3.1, X6Cr17 is considered, which is a ferritic steel alloy also known as AISI 430 or 1.4016. The saturation magnetic flux density of 1.55 T and the relative permeability are moderate, as both are lower than for silicon-iron and cobalt-iron. Additionally, the coercivity is rather high, which results in high static iron losses.

The third category are the nickel-irons; Ni36-Fe64, Ni50-Fe50 and Ni80-Fe20. Ni36-Fe64 is also known as Invar, which name comes from its invariance with temperature related to its elongation. Invar has a low saturation magnetic flux

density. Ni80-Fe20 is a Mu-metal because of the high-magnetic permeability and its low coercive field strength, but its saturation magnetic flux density is limited. The percentage of nickel majorly determines the magnetic permeability, coercivity and mass density.

The fourth category are the silicon irons, with a 3 % silicon content and a silicon content of 6.5 %. The 3 % silicon-irons are subdivided in grain oriented (GO) and non-oriented (NO) materials. The high magnetic flux density level is advantageous for reluctance actuators, whereas the high conductivity results in significant eddy currents and hence, iron losses.

Fifthly, the cobalt-iron, Co50-Fe50, is considered (Vacoflux 50). The high saturation magnetic flux density and relatively high magnetic permeability are beneficial for reluctance actuators. This cobalt-iron is the most expensive material of all, because raw cobalt is far more expensive than raw iron.

Lastly, the properties of pure iron are considered as a reference, where pure means an iron content of more than 99 %. Pure iron is not applied because the mechanical properties are improved by a factor thousand with only a few percent of carbon.

Samples of three commonly used materials are selected for further analyses in this thesis, i.e. stainless steel (AISI 430), non-oriented silicon-iron (M800-50A) and cobalt-iron (Vacoflux 50). Measurements are performed on these material samples to obtain the $B-H$ characteristic. The stainless steel is a solid ring sample, which is only statically analyzed. The M800-50A and Vacoflux 50 are evaluated both statically and dynamically. Two of the experimentally verified reluctance actuators are manufactured of M800-50A. The index 800 in its name, corresponds with the maximum amount of iron losses of 8.00 W/kg at 50 Hz with a peak magnetic flux density of 1.5 T. The index 50 is the lamination thickness of 0.50 mm and 'A' indicates that it is a non-oriented material sample. Vacoflux 50 is investigated for two lamination thicknesses of 0.10 mm and 0.35 mm, which are named in this thesis as Vacoflux 50-10 and Vacoflux 50-35, respectively. One of the three discussed reluctance actuators is manufactured of Vacoflux 50-10.

3.4.2 Material degradation

The manufacturing processes to obtain the shape of reluctance actuators deteriorate the magnetic properties significantly. Local and global stresses, distortions and temperature differences in the material influence the magnetic permeability and the magnetic saturation level. First of all, due to cold or hot rolling of materials to create thin sheets for laminations, stresses are applied to the material lattice. Other commonly applied production steps for shaping

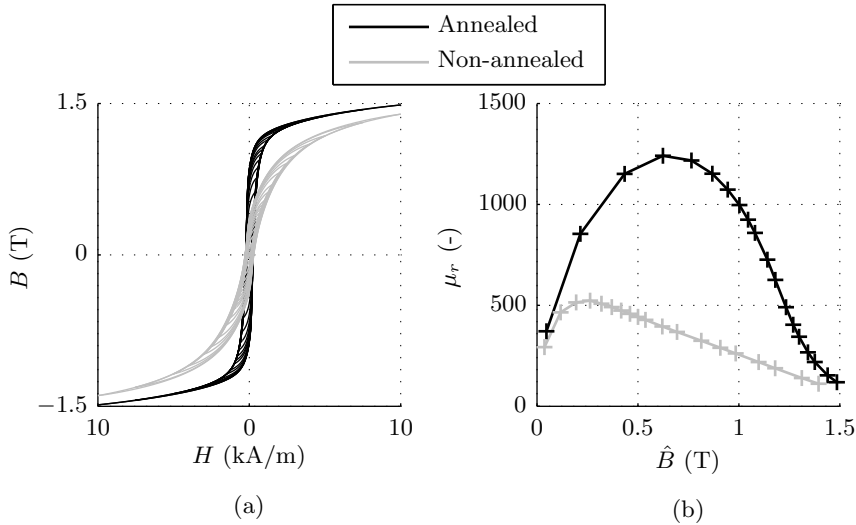


Fig. 3.5: Measurements on an annealed solid stainless steel (AISI 430) ring sample versus a non-annealed one, under a dc-excitation, the $B-H$ characteristics (a), and the relative permeability (b).

magnetic materials are stamping, laser cutting, water cutting and electric discharge machining (EDM) which is also known as wire cutting. Additionally, welding, interlocking and shrink fitting are used to fix lamination stacks of electrical machines. These production steps introduce stresses and local heating, which influences besides the magnetic properties also the eddy current losses of the laminated stacks [140, 141].

The effects of local stresses and heating can be significantly reduced by a heat treatment, also known as annealing. Annealing brings the material back to its original energy state, by restoring the defects in the lattice due to deformation and stresses. The optimal annealing procedure differs per material. Except for the applied temperature, also the time and the speed with which the temperature is increased and decreased, are parameters that should be optimized for a specific material. The magnetic material properties are enhanced substantially by the annealing procedure, as shown in Fig. 3.5(a). These measurements are performed on two solid stainless steel (AISI 430) ring samples with a cross-section area of $4 \times 5 \text{ mm}^2$ and an inner and outer diameter of 70 mm and 80 mm, respectively. The $B-H$ characteristic clearly shows the degradation of these solid ring samples due to the cutting process and the effect of annealing on the magnetic properties. The saturation level of the non-annealed sample has decreased by 6 %. Additionally, the relative permeability of both ring samples

is obtained as shown in Fig. 3.5(b). The relative permeability is decreased approximately by a factor of 2.4 due to the manufacturing process. These results are comparable to the research results performed for different edged geometries in [56, 263, 265]. Furthermore, comparable material deterioration is seen when lamination stacks are welded [134].

Besides the effects of the actuator production and shaping, global stresses on the material have a significant impact on the magnetic material properties. The impact of these stresses is highly dependent on the material, as shown for different nickel and carbon contents in [262]. Additionally, the direction of the stress influences the magnetic permeability substantially [59].

From this analysis it can be concluded that it is essential to identify the magnetic properties of a material sample to know the properties of the reluctance actuator. Obviously, it is important that the material sample is obtained from the same batch as the actuator, and it should be made using the same production method with a similar cross-section area as the actuator teeth (to have similar edge effects).

3.5 Measurement of magnetic hysteresis

The magnetic characterization of materials concerns the intrinsic material properties, such as saturation magnetic flux density, magnetic anisotropy, Curie temperature, the magnetic constitutive relation, which consists of the hysteresis loops and the related hysteresis phenomena. This section focuses on the measuring techniques of the magnetic flux density in soft-magnetic materials to obtain the $B-H$ characteristics.

A large number of possible techniques to determine hysteretic phenomena are summarized in [87]. The so-called fluxmetric techniques and the magnetometric techniques are discussed in this section. The fluxmetric techniques concern the analysis with a primary coil linked with the test sample to apply a magnetomotive force, which results in a varying magnetic field strength in the magnetic material, and hence also, a changing magnetic flux density which is measured by an induced voltage in a secondary coil. The magnetometric techniques are based on the measurement of magnetic fields in an open structure, such as the airgap of a reluctance actuator. All the discussed methods analyze the macroscopic material effects, which originate from an extremely complex sequence of microscopic processes as previously discussed in Section 3.2.

The large variety of possible states of the magnetic material, requires that the measurements should start from a reference state. The only two possibilities are the saturation magnetic flux density, where all domains are oriented in the

direction of the applied field, or the demagnetized state where both the magnetic field strength and the magnetic flux density are zero ($\mathbf{H} = \mathbf{B} = 0$). The demagnetized state can be reached by either starting from the saturation level and slowly reducing the amplitude of an applied alternating field to zero, or by cooling down the sample from its Curie temperature without any applied field. The magnetization curve after the demagnetization process with the decreasing alternating field gives the so called initial magnetization curve, whereas the magnetization curve after thermal demagnetization is called the virgin curve, which can be different from the initial magnetization curve. Additionally, a so called normal magnetization curve can be obtained, which coincides with the tips of the symmetric minor loops as shown in Fig. 3.5(a). This curve is practically the same as the initial magnetization curve.

3.5.1 Measurement methods

Methods to characterize the magnetic hysteresis curve of soft-magnetic materials are given in [3, 85, 87]. Some of the most commonly applied methods are the measurement of the induced electromotive force on ring samples, the Epstein frame, the double C-core for single sheets (single strips/sheet tester (SST)), the rotational SST (RSST) in a cross-configuration or with hexagonal symmetry to investigate anisotropy. Local induction measurements of sheets can be performed with the magnetoresistive sensor or with needle probes. Microscopic material properties are investigated with quantum methods using electron and nuclear magnetic moments in magnetic materials. The quantum methods are applied for the analysis of thin films e.g. the nuclear magnetic resonance (NRM) or electron spin resonance (ESR) [85].

The most commonly applied method for identifying the magnetic properties of soft-magnetic materials is the measurement of the flux density variation with a coil around a material sample, i.e. directly around a ring samples or around strips in an Epstein frame. The most commonly applied method to obtain the magnetic fields in open structures is the Hall sensor. In this thesis, the B - H characteristics are obtained from a ring sample (toroid).

The magnetic flux density is obtained from a ring sample by a secondary coil around the magnetic material, as defined in the international standard IEC 60404-6 [117]. The changing magnetic flux density causes an induced electromotive force resulting in a varying coil voltage, as given by Faraday's law (2.3). The induced coil voltage is given as

$$U_c = -N_2 A \frac{dB}{dt}. \quad (3.4)$$

where N_2 is the number of turns of the (secondary) sensing coil and A is the cross-section area of the magnetic material. This induced voltage is integrated

to obtain the magnetic flux density in the material sample. The magnetic field strength is applied with a primary coil with N_1 turns, and according to Ampère's law (2.35) the applied field strength is given by

$$H = \frac{N_1 I}{l_m} \quad (3.5)$$

where I is the current applied to the primary coil and l_m is the mean magnetic path length.

For this measurement, there has to be a change of the magnetic field in the coil to have an induced voltage. Therefore, the measurement of dc fields is more challenging, but these can be measured by integrating the induced voltage upon coil flipping or by the rotation or the displacement to a region without magnetic fields (Helmholz coil).

The most easy and flexible measurement method to obtain the magnetic field strength in free air is the Hall probe measurement. The sensor consists of semi-conducting plates, typically of GaAs or InAs crystals, which use the interaction of a dc current with the magnetic field (Lorentz force) that causes a voltage perpendicular to the current and the magnetic fields. Besides the Hall probe, the local fields can be determined with a fluxgate sensor, a Ragowski-Chattcock potentiometer which is a bent coil measuring a scalar potential difference [1] or a flat H-coil that can be placed at the surface of a magnetic material. The most accurate measuring methods for obtaining the magnetic field strength is the Hall probe, which does not require any integration, amplification or filtering [2]. For all measurements in open magnetic structures, the positioning of the sensor is crucial to perform accurate measurements [2, 273].

3.5.2 Applied measurement methods

In this work measurements are performed on ring samples (toroids) with the Brockhaus GmbH MPG 200 soft-magnetic steel tester. These toroidal structures are taped with Kapton foil for electric insulation. Firstly, the secondary coil is wound around the specimen, which can be a thin wire because a voltage is induced but no current is circulating during the measurement. Secondly, a primary coil with a sufficient cross-section area is also uniformly distributed to achieve homogeneous magnetic fields in the magnetic material. Examples of measured ring samples are shown in Fig. 3.6. Before each measurement the material sample is demagnetized with a sinusoidal decreasing magnetic field strength, from the saturation magnetic flux density level to zero.



Fig. 3.6: Example of one solid toroid and two toroids with the applied primary and secondary coils.

Dc measurement on a ring sample

The hysteretic characteristic of the soft-magnetic material samples is obtained with a quasi-static excitation. As previously discussed, this so called dc-measurement is in reality impossible, because the applied field must change with time. Hence, inside the material Barkhausen jumps occur due to flipping magnetic moments and moving domains. Due to the change of the magnetic flux density, dynamic effects occur that thermally activate the material.

The applied quasi-static measurements approach a dc-excitation by controlling the change of the magnetic flux density such that $\frac{\partial \mathbf{B}}{\partial t} < 30 \text{ mT/s}$. Before and during the measurement the drift of the integrators is monitored, for which is compensated after a full measurement cycle.

Ac measurement on a ring sample

The performed ac-measurements on the ring samples are also performed with the MPG 200. The measurement instruments controls the applied current, such that the voltage and hence also the magnetic flux density are sinusoidal. During a measurement the MPG 200 continuously controls the current, such that the measured hysteresis curve is symmetric with an equal positive and negative peak magnetic flux density. The obtained hysteresis loop is a mean curve from multiple cycles and, hence, the noise from the Barkhausen jumps is averaged out. For the same reason, the accommodation effect of minor loops cannot be measured with this measurement instrument as such.

Ac measurement on a reluctance actuator

Additionally, the magnetic flux density is obtained in two E-core reluctance actuators as discussed in section 7.2.1. The magnetic flux density is obtained in the stator of the E-core actuator with a measurement coil around one of the actuator teeth. By integration with a low-noise high-bandwidth operational amplifier (NE5534) the magnetic flux density is obtained from the sensing voltage using the cross-section area of the tooth. The measurement of the magnetic flux density in the stator core of two E-core reluctance actuator is performed under a sinusoidal current excitations between 40 and 320 Hz. Hence, only a dc error has to be compensated for, whereas the drift of a few cycles is negligible.

3.6 Conclusions

This chapter introduces the theory of magnetic hysteresis from a microscopic level up to the macroscopic magnetic hysteresis phenomena. Magnetic domains, the Barkhausen effect, anisotropy and magnetostriction are described, which influence the macroscopic $B-H$ characteristic. Furthermore, the differences between soft-magnetic and hard-magnetic materials are discussed.

The influence of magnetostriction and the elongation due to the actuator force are considered insignificant, as their value is at least two orders of magnitude smaller compared to the elongation due to temperature variations. The non-congruency and accommodation phenomena in magnetic materials are only a few percent of the total magnetic flux density variation in reluctance actuators and hence, these are not incorporated in the magnetic material models either.

Various commonly applied soft-magnetic materials are discussed on their applicability for high-precision reluctance actuators. The level of the saturation magnetic flux density and the relative permeability are important for obtaining a high-force density, as well as the conductivity of which the level of importance is dependent on the frequency of operation. Based on these aspects are silicon-irons and cobalt-irons considered as the most applicable materials for reluctance actuators. Available ring samples of stainless steel (AISI 430), silicon-iron (M800-50A) and cobalt-iron (Vacoflux 50) are selected for the experimental verification of magnetic hysteresis modeling methods in the following chapters.

The importance of the manufacturing processes for the magnetic properties of reluctance actuators is assessed. The effects of material cutting methods are discussed and fixing methods for laminated electrical machines are addressed. An example is given for the influence of annealing on the magnetic material properties of a stainless steel ring sample. The saturation magnetic flux density

is decreased by 6 % while the maximum relative permeability is reduced by a factor 2.4. Therefore, it is concluded that it is essential to identify the magnetic material properties of a sample obtained from the same manufacturing process as the reluctance actuator to know its material properties.

Finally, measurement methods are given for obtaining the magnetic flux density inside and outside magnetic materials. The applied measurement method to obtain the $B-H$ characteristic of ring samples is discussed in more detail. This measuring method is used for dc- and ac-measurements on various magnetic material samples in the remainder of this thesis.

Overview of hysteresis modeling methods

Magnetic hysteresis has been studied and modeled since the end of the 19th century by Rayleigh (1887) [216] a decade after the contributions of Maxwell (1873) [166]. The next significant research was from Madelung who published in 1905 [158] his study on the behavior of magnetic hysteresis loops. In 1907, Weiss proposed the mean field theory of ferromagnetism [279], based on the Langevin theory of paramagnetism [143] and introduced the fundamental concept of magnetic domains and spontaneous magnetization, which is explained in 1928 by Heisenberg in terms of quantum mechanics. From the year 1935 until now, many phenomenological mathematical models have been developed [106, 110, 123, 132, 213, 236, 238].

In this thesis magnetic hysteresis phenomena in ferromagnetic materials are concerned. Various other fields of science experience nonlinear hysteresis phenomena, e.g. ferroelectric hysteresis, mechanical hysteresis, superconducting hysteresis, adsorption hysteresis, optical hysteresis, electron beam hysteresis, economic hysteresis, etc. [151]. The research on these different types of hysteresis phenomena has resulted in numerous mathematical models. An overview is given of the available modeling methods for ferromagnetic materials.

Generally, magnetic hysteresis models can be divided into physical and phenomenological models, which have its origin in two different disciplines of research within magnetic hysteresis modeling. On the one hand, magnetic materials are modeled on microscopic scale (thin films) by chemists and physicists,

in e.g. material research and magnetic recording. On the other hand, hysteresis is researched and modeled on macroscopic scale within, e.g. transformers, motors and (piezoelectric)actuators.

The physical based models tend to describe micromagnetic effects on one or a few particles. These models describe the domain wall movement, which is orders of magnitudes smaller than the macroscopic behavior that is observed in e.g. toroids or strips. The models can only be solved numerically for very simple magnetic systems in magnetic fields, and become computationally expensive when being applied for macroscopic magnetic phenomena [151]. Nevertheless, many properties of the various phenomenological hysteresis models, attribute their behavior to micromagnetic material phenomena.

In the following sections, an overview of six commonly applied phenomenological hysteresis models is given, namely, Preisach model [26, 64, 167, 213], Jiles-Atherton model [123, 124], play and stop model [132], positive-feedback model [102], finite element method [49], and complex impedance method [269]. The history of these modeling methods is discussed and the models are qualitatively compared on their applicability for the modeling of reluctance actuators. The hysteresis models are evaluated on the following three criteria:

- (a) The hysteresis model can be combined with the proposed magnetic equivalent circuit (MEC) method for the modeling of reluctance actuators.
- (b) It should be possible to have an arbitrary current excitation as model input and hence, arbitrary minor loops should be modeled as function of the magnetic field strength $B(H)$.
- (c) Rate-dependent magnetic material effects should be possible to incorporate.

The modeling methods are discussed and finally an overview is given, which summarizes the model properties related to these three criteria. The modeling methods are qualitatively evaluated on their applicability for the modeling of magnetic hysteresis in reluctance actuators.

4.1 Preisach model

History

The classical Preisach model (CPM), described in 1935 by Preisach [213], is originally a purely intuitive model concerning the physical mechanisms of magnetization. In those times the model was considered as a physical model of hysteresis with the hysteresis operators as representation of switching domains,

the so called Barkhausen jumps. However, years later the local magnetic behavior could not be explained with the Preisach models [267]. Nevertheless, the mathematicians Krasnosel'skiĭ and Pokrovskiĭ [132] developed a mathematical description of the Preisach hysteresis model, such that it could be applied in various systems with hysteresis.

The Preisach model has been extended over the years with various generalizations. The classical Preisach model is improved with a reversible part, which resulted in the generalized Preisach model (GPM) [171]. The non-congruency of magnetic materials is modeled with the moving Preisach model [64] (MPM), the product Preisach model [127], the nonlinear Preisach model [171] and the average Preisach model [4]. The generalized moving Preisach model (GMPM) is described in [16] and the moving and product models are compared in [126] and [255]. Incorporation of a dynamic (rate-dependent) excess loss component is introduced by Mayergoyz [169] and Bertotti [27] (DPM/GDPM). Accommodation is included as an extension to the moving Preisach model by an additional input dependent term [66, 67, 169]. Finally, magnetostriction [169] and vector Preisach models [168] are also discussed by Mayergoyz.

Afterwards, Basso and Bertotti (1995) [21] succeeded to connect the macroscopic Preisach model and its generalizations to the physical microscopic magnetization mechanisms in soft-magnetic materials. Others described how the micromagnetic magnetic material phenomena are related to the macroscopic Preisach model from an energy point of view [257]. Nevertheless, the Preisach model is considered as a phenomenological model, which is able to include numerous physical properties with the many generalizations.

Model characteristics

Although the evolution of the Preisach model has dominantly been in the research on magnetic media, this model is also considered suitable in other fields of research, e.g. in finite element implementations [63, 109, 207], in transformer models [12], in piezoelectric actuator models [94, 155] and in reluctance actuator models [178]. This broad applicability is one of the major advantages of the Preisach model.

The magnetic hysteresis representation of the Preisach model is given by

$$M(t) = \iint_{H_u \geq H_d} \Phi(H_u, H_d) \hat{m}(H_u, H_d) H(t) dH_u dH_d \quad (4.1)$$

where $M(t)$ is the magnetization, Φ is the weight function, \hat{m} is the hysteresis operator, as illustrated in Fig. 4.1, $H(t)$ is the magnetic field strength, and H_u and H_d are the 'up' and 'down' switching decision variables describing the width and offset of the hysteresis operator. The hysteresis as shown in Fig. 4.1

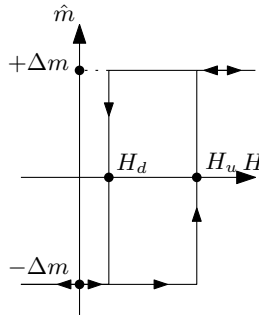


Fig. 4.1: Rectangular loop of the simplest magnetic hysteresis operator for the Preisach model.

is the most simple hysteresis operator, of which an infinite set is incorporated in the model as thoroughly explained in the following chapter.

The Preisach model is the most applied magnetic hysteresis model in literature, and the model has been extended to describe most magnetic phenomena. Moreover, continuous analytical distribution functions can be applied, which are preferred for the stability of the modeling method, while a numerical Everett function can be used as well. A disadvantage of the Preisach model is that it is relatively complicated to invert the Preisach model [68], which is necessary to obtain the magnetic field strength, H , from the magnetization, M , for control purposes or for the implementation in FEM simulations [60, 247]. In this thesis, inversion is not considered.

For the qualitative comparison of the modeling methods, the three criteria for the modeling of reluctance actuators are subsequently discussed. Firstly, the Preisach model can be combined with the magnetic equivalent circuit (MEC) method [12]. Secondly, the Preisach model inherently describes minor loops and first-order-reversal-curves [69], which is a necessity for the simulation of arbitrary currents in actuators. Thirdly, the modeling of dynamic effects is not included, but this can be incorporated as one of the generalizations. Therefore, the Preisach model is considered as an appropriate candidate to predict magnetic hysteresis effects in reluctance actuators.

4.2 Jiles-Atherton model

History

The Jiles-Atherton (JA) model is a more recent model obtained by Jiles and Atherton in 1984 [123], in which they relate their findings to the pinning sites of domains [131] and domain wall motion. The shape of the Jiles-Atherton hysteresis loop is obtained from micromagnetic behavior as discussed by Tebble and Craik in 1969 [251]. In this way, the creators tried to bring forth a physical based magnetic hysteresis model.

Despite their efforts, the model is not considered as a physical model for several reasons. Most parameters of the Jiles-Atherton model cannot be measured directly and hence, must be obtained by functional fitting. An example is the anhysteretic part of the Jiles-Atherton model, which is obtained by applying the Langevin function [143] as the only anhysteretic function. Additionally, according to Zirka *et al.* [296], “the non-physicality of the Jiles-Atherton model manifests itself in practical errors when it is extended to a dynamic hysteresis model.”

More recently, the Jiles-Atherton model is evolved by changing the Langevin function with the original Brillouin function [32, 34]. In addition, Chwastek [46, 48] generalized the Jiles-Atherton model such that it is stable in modeling minor loops and rate-dependent hysteresis effects [47]. The inclusion of dynamic hysteresis phenomena shows resemblance to that presented for the Preisach model by Dupré [75], likewise the non-congruency property is included similarly as the product model [127] implementation applied to the Preisach model.

Model characteristics

The reason that the Jiles-Atherton model has become one of the most commonly applied models is that it is originally based on micromagnetic properties in contradiction to the already evolved Preisach model. In addition, the Jiles-Atherton model is defined by analytical functions, which are described by five parameters only. Hence, functional fitting algorithms can easily be applied to obtain the optimal Jiles-Atherton model for a specific material and the simulation is relatively fast.

A disadvantage of the Jiles-Atherton model is that the shape of the constitutive relation is partly defined, because the Langevin function describes the anhysteretic part of the $B-H$ curve. Furthermore, negative slopes of the differential permeability can occur in the Jiles-Atherton model [72, 296], which leads to instability in simulations.

In principle, the Jiles-Atherton model can be combined with the MEC method for the modeling of reluctance actuators. However, with the Jiles-Atherton model it is intrinsically impossible to model physically-reasonable arbitrary minor loops [106]. Minor loops can only be modeled under the condition that a priori both, the maximum and minimum values of the minor loop are known. The dynamic material properties can be incorporated similarly as presented in Chapter 6. Nevertheless, the Jiles-Atherton model is considered not suitable for the modeling of reluctance actuators.

4.3 Play and stop models

History

The history of the play- and/or stop-type models have its origin in the description of ferromagnetic hysteresis by Rayleigh in 1887 [216], which model is equivalent to the Prandtl-Ishlinskiĭ model of the play-type. In 1928, Prandtl introduced a more general hysteresis model applied for elastoplastic materials, obtained by composing a family of linear stops. This model was studied by Timoshenko (1930) and Ishlinskiĭ (1944). The evolved model is named after Ishlinskiĭ in Russian literature, but in this work the model is called the Prandtl-Ishlinskiĭ model, as in most western publications.

In 1970, Krasnosel'skiĭ and other mathematicians proposed a mathematical formulation of the Prandtl-Ishlinskiĭ model in terms of hysteresis operators. Their research in the following decade resulted in the book of Krasnosel'skiĭ and Pokrovskiĭ [132]. This work was the mathematical basis for the description of hysteresis with elementary hysteretic operators, i.e., 'relay', 'play' and 'stop' operators. As previously discussed, a similar relay representation is also used by Mayergoyz to describe the Preisach model [169], which boosted the popularity of that model in the nineties. Simultaneously, the popularity of the Prandtl-Ishlinskiĭ (stop) and Krasnosel'skiĭ-Pokrovskiĭ (play) models diminished. The monographs of Visintin in 1994 [267] and of Brokate and Sprekels in 1996 [35] returned the interest of researchers in the play and stop models again.

Nowadays, the play- and stop-type models are often used for modeling nonlinear hysteretic behavior of piezoelectric [70], piezoceramic [7], magnetostrictive [11, 249] and shape memory alloy (SMA) actuators [5, 6, 9, 286]. Generalizations of the play and stop models are also applied for the prediction of magnetic hysteresis [31, 161, 162] with an envelope function similar to the Preisach distribution functions.

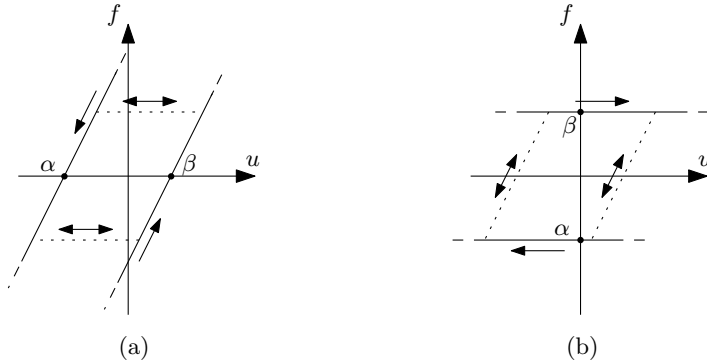


Fig. 4.2: The hysteresis diagram of the play-type model (a), and the stop-type model (b).

Model characteristics

The play mechanism, as described by the play-type model, is known in engineering as a friction-controlled backlash, from which the hysteresis diagram is shown in Fig. 4.2(a). The second mechanism, described by Prandtl, is the stop-type model based on elasto-plasticity. It describes the behavior of a mass connected to a spring, while the body encounters friction. The corresponding hysteresis operator is shown in Fig. 4.2(b) [267]. It is clear from these figures that both, the play-type model and the stop-type model are variants of the hysteresis operator used in the Preisach model. The differences between each of these three hysteresis operators, i.e. ‘relay’, ‘play’ and ‘stop’ operators, is discussed in [119] from a control perspective.

Intrinsically, the play and stop models are rate-independent just as the classical Preisach model. An other disadvantage is the inability to model saturation effects present in magnetic materials in its classical formulation. This aspect explains the popularity in modeling piezoceramic and magnetostrictive actuators, in which limited saturation occurs in the working range of the actuator [8]. Nevertheless, generalizations are developed for both drawbacks as elaborated in [35]. In [5, 6], the hyperbolic tangent function is proposed as envelope function to incorporate saturation effects and a generalized Prandtl-Ishlinskiĭ model is proposed that incorporates rate-dependent effects. In [163], Matsuo describes several identification methods to obtain the optimal envelope function.

The elementary advantage of combining the play- and stop-type models is their duality, as the stop-type model is appropriate to represent the inverse of the play-type model [9, 31]. Play- and stop-type models that can be set up by both operators, are referred to in the literature as Prandtl-Ishlinskiĭ models [132]. It is shown in [31] that the numerical inverse of both $B = B(H)$ and $H = H(B)$

can be applied complementary, which is also useful for control theory and FEM modeling. Recently, the Prandtl-Ishlinskiĭ model is even analytically inverted [286], in contradiction to the Preisach model and the Krasnosel'skiĭ-Pokrovskii model, which inverse is obtained numerically with the Everett function (as discussed in Section 5.3).

The characteristics of the play- and stop-type models including the generalizations are similar to the Preisach hysteresis model. The model can be combined with the MEC method, arbitrary inputs can be applied and the model can be extended to include the dynamic effects. Hence, the models are considered suitable for the modeling of reluctance actuators.

4.4 Positive-feedback model

History

The positive-feedback (PFB) model is one of the most recent hysteresis models. The model is introduced by Harrison in 2003 [102], and is based on micromagnetic hysteresis phenomena as described in 1935 by Landau and Lifshits [142]. The model is presented as a full physically-based magnetic hysteresis model, which can be applied to macromagnetic phenomena by normalization to the specific magnetic fields.

Harrison extended the model to include the initial-magnetization from its demagnetized state [103]. Later first-order reversal curves [104] and higher-order reversal curves (minor loops) [105, 106] are included, which lead to the generalized positive-feedback theory (G-PFB). Finally, Harrison succeeded to determine the Curie temperature with the positive-feedback theory [107], all based on micromagnetic material properties, which underlines that it is a physically-based modeling method.

Model characteristics

The positive-feedback model consists, similarly as the Jiles-Atherton model, of an anhysteretic part and a hysteretic part. As in the Jiles-Atherton model, the anhysteretic part is derived with the physically-based Langevin function [143], although any mathematical (or tabulated) function can be applied for the anhysteretic part to describe non-Langevin behavior [106]. The hysteretic mechanism occurs at the mesoscopic scale of the domains, which act like classical-physics particles.

The origin of the hysteretic part is the quantum mechanics based Brillouin function [34, 45, 57], which describes the atomic magnetization of Bohr mag-

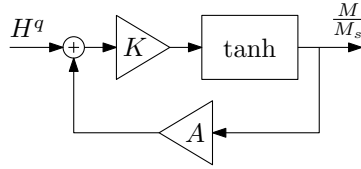


Fig. 4.3: Positive-feedback mechanism corresponding to Equation (4.2) with $A = \alpha M_s$ and $K = \frac{\mu_0 \beta m_B}{k_b T}$.

netons. This effect is scaled up to the size of domains by the scalar, β , which is defined as the average number of Bohr magnetons aligned in the direction of its magnetization. In this theory, all instances of the irreversible magnetization are due to the quantum-mechanical positive-feedback mechanism of magnetic hysteresis [106], which is also described by Visintin [267] and Bertotti [28]. The hysteretic positive-feedback part of the model is illustrated in Fig. 4.3 and can be expressed as,

$$\frac{M}{M_s} = \tanh \left[\frac{\mu_0 \beta m_B}{k_b T} (H^q + \alpha M) \right] \quad (4.2)$$

where M and M_s are the magnetization and saturation magnetization, respectively, μ_0 is the permeability of vacuum, m_B is the Zeeman energy of the Bohr magneton, k_b is the Boltzman constant, T is the temperature, H^q is the quantum-mechanical field contribution, and α is the Weiss exchange-field coefficient.

Additionally, a demagnetizing field contribution must be incorporated for hard-magnetic materials. The demagnetization is linearly related to the magnetization and all the contributions are scaled to the atomic magneton scale and added. The summation of the contributions is equivalent to the linear energy summation and similar to the addition of field contributions. The total magnetic field strength is obtained by multiplication with the average number of magnetons in the material.

Modeling of first-order reversal curves and higher-order reversal curves is discussed in [105] and [106], respectively. The history dependency and wiping-out property are incorporated by memorizing the pre- and post-reversal points. In addition, the model incorporates the non-congruency of magnetic materials and the whole theory is contained in four algebraic equations. The positive-feedback model is validated for a wide range of soft- and hard-magnetic materials with a coercive field strength, H_c , ranging from 18 A/m to $1.35 \cdot 10^6$ A/m [106], but no rate-dependent effects are incorporated.

A disadvantage of the positive-feedback model is that the output is the magnetic field strength, H , for a given magnetization, M . This input-output rela-

tion of the positive-feedback model makes it incompatible for the applied MEC model, whereas, this input-output relation is advantageous for FEM models and control purposes. The positive-feedback model can describe minor hysteresis loops due to arbitrary current excitations. Up to now, no dynamic effects are incorporated, and it cannot be combined with the later proposed dynamic material model in Chapter 6. It can be concluded that the positive-feedback model is not applicable for reluctance actuators. Nevertheless, the physical based derivation of the model is promising for further research on magnetic materials.

4.5 Finite element method

History

The history of magnetic hysteresis modeling in finite element methods (FEMs) is limited, because computers are only recently capable to include the computational expensive hysteresis models in their simulations. The first known 2d FEM implementation including magnetic hysteresis is from Ossart and Meunier (1991) [196], where a polynomial model is used to incorporate some magnetic hysteresis phenomena. Shortly after that, the first Preisach implementation followed by Henrotte *et al.* [109]. From that time on, the Preisach model became the most popular hysteresis model for FEM simulations and hence, these implementations improved over the years [63, 207]. The 2d FEMs have been further extended with dynamic eddy current effects [175], or vector implementations [76, 81]. Simultaneously, the 3d FEM has been combined with the scalar Preisach model [147], and the vector Preisach model has been implemented for the 3d BEM [215]. Meanwhile, other researchers improved the convergence of the FEM computations including magnetic hysteresis [13, 217, 228].

Besides the Preisach implementations, neural networks are applied for hysteresis modeling in the FEM [229, 230], the Jiles-Atherton model is applied in 2d FEM [146, 226], and the rate-dependent vector play model is discussed [177]. Nevertheless, none of all above mentioned hysteresis implementations are incorporated in a commercial available FEM package.

The first implementation of magnetic hysteresis in commercial 2d FEM software has been presented in 2001 [218], although it never became commercially available. Generally, FEM software packages include nonlinear materials and the iron losses can be obtained in the post-processor. For example in Flux [43] it is an option to calculate the iron losses according to the Bertotti loss model, as described by (6.6).

One of the few commercial software packages that include magnetic hysteresis

in its 2d- and 3d-simulations, is Opera from Vector Fields [49]. Recently, this FEM package has been used for electromechanical systems [176]. 2d FEM simulations including hysteresis have been performed for a four-pole permanent magnet generator and 3d FEM simulations have been performed for a hysteresis motor. Additionally, in [219], 2d FEM simulations are evaluated in a transient analysis including magnetic hysteresis on a solenoid valve.

Model characteristics

The simulation software of Vector Fields uses only the left part of the major hysteresis curve as model input. The data points of the inserted major loop are approximated with a cubic spline fitting method to reduce the number of points. The software uses this tabulated data to create a hysteresis model based on transplantations [246, 288]. The behavior of minor loops is obtained by empirical Madelung rules. A list of turning points is memorized and updated during the simulation for each finite element [176]. The detailed algorithm of the finite element software is unknown because of commercial interests.

The geometry of the actuator is described in the FEM as well as the magnetic hysteresis in the core of the ferromagnetic material. Furthermore, arbitrary current excitations can be applied to model minor loops of magnetic materials, both for static and dynamic simulations. However, rate-dependencies for arbitrary currents in laminated structures are challenging, due to two orders of magnitude difference in mesh elements between the laminations and the isolation. An anisotropic conductivity can be incorporated to model a stack of laminations with a solid structure [100], but this is only valid for a fixed excitation frequency.

A major disadvantage of the 2d/3d FEM analysis is the long simulation time, especially when besides magnetic hysteresis also eddy currents are taken into account. The 2d FEM simulations are in the order of hours, while the 3d FEM simulations can take one to four days, depending on the complexity of the actuator model and convergence of the iterative solver [219, 278]. It is concluded that it is very interesting to examine the FEM package including magnetic hysteresis on its suitability for the modeling of magnetic hysteresis phenomena in reluctance actuators.

4.6 Complex impedance method

History

One of the first applications of the complex impedance method for magnetic hysteresis dates back to Steinmetz in 1900 [237]. He thoroughly studied magnetic hysteresis phenomena and wrote his monograph to complement his earlier research on describing hysteresis losses with the Steinmetz equation (1892) [236], as discussed later in Section 6.1.

Years later in 1934, Gall and Sims [90] extended this analysis with the complex permeability, $\mu = (a - jb)$, and described it in a vector diagram. Furthermore, the shape of the elliptic hysteresis model was altered by the addition of higher order sinusoidal $B-H$ relations.

The representation of magnetic hysteresis with a phase lag between the magnetomotive force and the flux, which is equivalent to a complex permeability, is also often applied for the analysis of hysteresis motors. The elliptic hysteresis curve was introduced for the hysteresis motor in 1965 by Miyairi and Kataoka [180], which is further analyzed in the seventies and eighties [187, 195, 231, 285]. Nowadays, elliptic models are applied for modeling magnetic hysteresis in piezoelectric actuators [95, 96] and magnetostrictive actuators [252].

Model characteristics

The complex impedance method is an easy and fast model to describe some magnetic hysteresis effect. The elliptic behavior of minor loops in a non-saturated actuator can be translated to a complex impedance. The resultant of the complex impedance method is a rate-dependent phase delay between the current and the voltage or equivalently H and B , respectively.

This hysteresis model does not model any physical representation of magnetic hysteresis. The analogy of magnetic hysteresis with an elliptic model is based on the fact that non-saturated minor loops have an elliptic shape and that eddy currents intrinsically result in a phase delay between the current and the magnetic flux density.

The complex impedance method is considered rate-dependent in case the phase delay is adjusted with the frequency. The phase delay can e.g. be obtained from measurements, and it can be modeled by a magnetic reluctance with a complex magnetic permeability

$$\mathcal{Z}_{fe} = \frac{l_{fe}}{\mu_0 \mu_r A_{fe}} \quad (4.3)$$

where l_{fe} and A_{fe} are the magnetic path length and the cross-section of the ferromagnetic material, respectively. The complex relative permeability is given by

$$\mu_r = \mu_r \cos(\delta) - j\mu_r \sin(\delta) = \mu_r' - j\mu_r'' \quad (4.4)$$

The complex impedance method can easily be incorporated in the reluctance actuator model and can describe dynamic material effects. A disadvantage is that it can only model sinusoidal excitations and hence, the model is unable to cope with arbitrary current inputs. Despite that the complex impedance method does not have all desired model characteristics, it is evaluated for the modeling of magnetic hysteresis because of its speed and simplicity.

4.7 Other models

Besides the previously discussed hysteresis representations, it is worthwhile to acknowledge three other models, i.e. the Stoner-Wohlfarth [238], Coleman-Hodgdon [52, 110] and Takács [245] model. From which the first model is a vector based hysteresis model, describing domain size magnetization with an ellipsoid pointing in the magnetization direction. Because of the applied reluctance actuator model (the MEC method) only a scalar hysteresis model is applicable. The second model, is an extension of the differential Duhem model [71], and is often applied to model piezoelectric actuators [82, 174], but it is less applied for hysteresis modeling in ferromagnetic materials. The third model is an hysteresis model based on fitting the hyperbolic tangent function. Its mathematical formulation incorporates minor loops, but more importantly the inverse function is rather easily obtained analytically [246]. However, no literature has been found on the verification of the model on measured magnetic hysteresis loops.

4.8 Conclusions

An overview has been given on the evolution of hysteresis modeling in general, and specifically for six hysteresis modeling methods. The history of these methods shows their acceptance by the scientific community in time, and discusses the major contributors. Additionally, the hysteresis models have been qualitatively discussed on three criteria to stipulate their ability to model magnetic hysteresis in reluctance actuators, which is summarized in Table 4.1. The three criteria are subsequently discussed for the six modeling methods.

Table 4.1: Hysteresis model comparison, based on the three criteria for hysteresis modeling in reluctance actuators.

| Method | P-M | J-A | P&S | PFB | FEM | CIM |
|---------------------|-----|-----|-----|-----|-----|-----|
| (a) Actuator model | + | + | + | - | + | + |
| (b) Arbitrary input | + | - | + | + | + | - |
| (c) Rate-dependency | o | o | o | o | o | + |

- (a) The hysteresis model can be combined with the proposed MEC method for the modeling of reluctance actuators.

Considering the first criterion for the evaluation of the modeling methods on their applicability for reluctance actuators, only the positive-feedback model (PFB) is considered incompatible, as indicated in Table 4.1. This is the only model with, instead of the magnetic flux density, the magnetic field strength as modeling output, which is necessary for the applied MEC method. The other models can be combined with the MEC model, except for the FEM which intrinsically incorporates the magnetic geometry of the reluctance actuator.

- (b) It should be possible to have an arbitrary current excitation as model input and, hence, arbitrary minor loops should be modeled as function of the magnetic field strength $B(H)$.

The Jiles-Atherton (J-A) model and the complex impedance method (CIM) are the only two hysteresis modeling methods from the evaluated methods, that are not capable of modeling arbitrary current inputs. The Jiles-Atherton model can only incorporate minor loops when the maximum and minimum magnetic field strengths are a priori known. The complex impedance model, as it is evaluated here, uses a constant phase delay, which is only applicable for sinusoidal excitations. The other modeling methods do incorporate minor loops due to an arbitrary input.

- (c) Rate-dependent effects should be incorporated with the combination of hysteresis and actuator models.

Only the complex impedance method can incorporate dynamic effects in its analysis, when a frequency-dependent phase delay is applied. The FEM has the option to give a conductivity to the material, which results in the incorporation of the rate-dependent effects. However, reluctance actuators are often manufactured of stacked laminated sheets of magnetic material, which is modeled with an anisotropic conductivity. This anisotropic conductivity is frequency-dependent and hence, no dynamic effects of arbitrary excitations can be incorporated in this case. The other modeling methods do not incorporate

rate-dependent effects, but these methods can be extended with a dynamic magnetic material model as presented in Chapter 6.

Based on the qualitative comparison it can be concluded that the Preisach model (P-M), the play- and stop-type models (P&S) and the FEM are qualified equally well regarding all three criteria for hysteresis modeling in reluctance actuators. The Preisach model and the play- and stop-type models are both applicable and can be similarly combined with the MEC method. The Preisach model is selected, because it has a long history with numerous improvements and is widely accepted in the scientific community.

Additionally, the FEM is selected, because it is the most applied analysis tool for electromagnetic systems. The major disadvantage of the FEM is the high computational effort, which is in the order of hours to several days, compared to milliseconds to seconds for the other methods. The limited computational effort and the simplicity of the complex impedance model are the major reasons for selecting this modeling method.

In the following chapters, the Preisach model is extensively elaborated and experimentally verified with measurements. Additionally, the FEM and the complex impedance method are further examined on the prediction of magnetic hysteresis phenomena in the force of reluctance actuators.

Preisach hysteresis model

As discussed in the previous chapter, the scalar Preisach model has evolved over the years from the classical form [213] to the moving model [55, 64], generalized model [65] and generalized dynamic Preisach model [73], which are all scalar models. Additionally, these models have been extended and described in vector form [77, 169]. Recent contributions of vector hysteresis models [37] and benchmark problems [22, 38] express the ongoing interest in this field. In this chapter, the generalized scalar Preisach model is elaborated, and the dynamic effects of eddy currents and excess losses are incorporated in Chapter 6. As previously discussed in Chapters 2 and 3, the scalar representation of magnetic hysteresis is considered sufficient for reluctance actuators. Besides the fact that vector hysteresis cannot be measured with the available soft-magnetic material tester, it is assumed that the vector properties of the applied non-grain oriented laminations are small.

The most general representation of any hysteresis, is illustrated in Fig. 5.1(a) with an arbitrary input, $u(t)$, the hysteresis transducer, HT, and a variable output, $f(t)$ [132, 168, 171]. The hysteresis transducer is defined in [169] as follows, “. . . it is called a hysteresis transducer if its input-output relationship is a multi-branch non-linearity for which branch-to-branch transitions occur after input extrema.” Similarly, hysteresis can be expressed as, $f(t) = \text{HT}(u, u_{past})u(t)$, where the hysteresis transducer incorporates a nonlinearity with a memory based on the past input extrema, u_{past} , that determines the branches/transition curves. As a consequence, for each point in the $f - u$ characteristic an infinite number of curves exists which results in the specific values of the corresponding input and output.



Fig. 5.1: Elementary model of hysteresis with, the hysteresis transducer (HT) (a), and the magnetic equivalent with the Preisach model (P-M) (b).

The magnetic equivalent of the hysteresis representation with the Preisach model, is shown in Fig. 5.1(b), where the input is the magnetic field strength, $H(t)$, the transducer is for example the Preisach model (P-M), and the output is the magnetization $M(t)$. In case this same representation is used for mechanical hysteresis, the input, $u(t)$, is the force in Newtons and the output, $f(t)$, is the displacement in meters.

In the analysis of magnetic systems (with or without) magnetic hysteresis, the magnetic field strength is often unknown. The local magnetic field strength has to be determined by the interaction with other elements in the system, e.g. coils, permanent magnets, the particular shape, airgap length, etc. In this thesis, the magnetic equivalent circuit (MEC) method, as explained in Section 2.5, is used to calculate the local magnetic field strength as input for the Preisach model.

Only for a closed magnetic circuit with a homogeneous magnetic flux density, the magnetic field strength is unambiguously obtainable from the dimensions, the number of coil turns and the applied current. For that reason, the scalar Preisach implementations are first examined on the prediction of the magnetic flux density in closed, toroidal, soft-magnetic samples in Section 5.4. Thereafter, the implementation of the generalized Preisach model as part of a magnetic system is discussed in combination with a MEC model in Section 6.4.

In Section 5.1, the classical Preisach model is elaborated, the implementation of which is mainly based on the work of Mayergoyz [169], Bertotti [28], and their mutual publication [29]. For completeness of this work, the applied Preisach model is fully explained with an example of an arbitrary input signal, which is similar to the example in [169]. In Section 5.2, the generalizations of the Preisach model are discussed. The applied Preisach distribution functions are introduced in Section 5.3. The simulation procedure is discussed and finally simulations are compared to measurements performed on four ring samples, in Section 5.5. The contributions of this chapter have been published in [272, 273].

5.1 Classical Preisach model

The classical Preisach model can describe rate-independent hysteretic behavior, which means that the hysteretic nonlinearity is only determined by the past extreme values of the input and the evolution of the output does not depend on the speed of the input changes. The mathematical description of the classical Preisach model consists of an infinite set of simple hysteresis operators, $\hat{\gamma}_{\alpha\beta}$, as illustrated in Fig. 5.2. In this representation, it is assumed that $\alpha \geq \beta$ and the values of these switching variables are different for each hysteresis operator. The only two outputs of these two-position relays are $\hat{\gamma}_{\alpha\beta}u(t) = +1$ and $\hat{\gamma}_{\alpha\beta}u(t) = -1$, which depends on the current, $u(t)$, and past, u_{past} , input value.

As the input, $u(t)$, monotonically increases, the ascending branch *abcde* is followed. When the input is decreased the descending branch *edfba* is followed. Hence, this simple hysteresis operator already models a nonlinearity with local memory. To complete the hysteresis model a weight function is inserted in the Preisach plane $P(\alpha, \beta)$, which is also known as the Preisach function. The resulting classical Preisach model follows as

$$f(t) = \iint_{\alpha \geq \beta} P(\alpha, \beta) \hat{\gamma}_{\alpha\beta} u(t) d\alpha d\beta \quad (5.1)$$

with switching variables α and β . This model can be interpreted as a discrete but continuous, analog system of n parallel connected relays, as illustrated in Fig. 5.3. Each single branch has its own hysteresis operator that functions as decision variable and weight function, which determine the steepness of the hysteresis function. Although magnetic hysteresis phenomena are considered, the general hysteresis form (5.1) is used to describe the properties of the classical Preisach model in this chapter, instead of the magnetic representation (4.1), given in previous chapter.

The infinite number of hysteresis relays of the continuous hysteresis model are distributed over a triangular Preisach plane, as shown in Fig. 5.4. The Preisach plane is a triangle limited by the line $\alpha = \beta$ and the coordinates α_0 and β_0 with $\beta_0 = -\alpha_0$. The hysteresis operator $\hat{\gamma}_{\alpha\beta}$ is directly related to the point (α, β) on the Preisach plane by the past extrema of the input, $u(t)$.

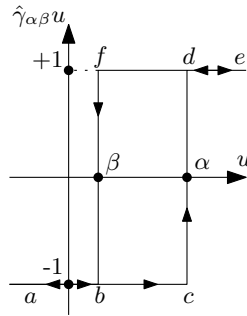


Fig. 5.2: Rectangular loop of the simplest magnetic hysteresis operator for the Preisach model.

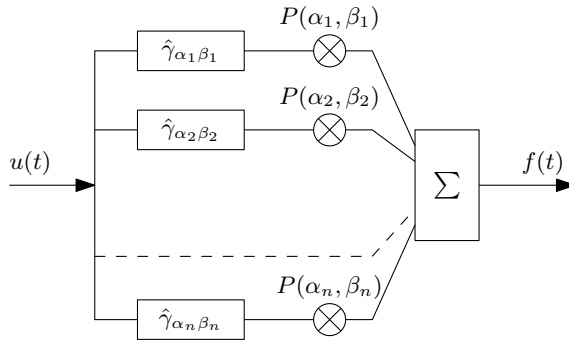


Fig. 5.3: Continuous analog discrete block diagram of parallel connected hysteresis operators.

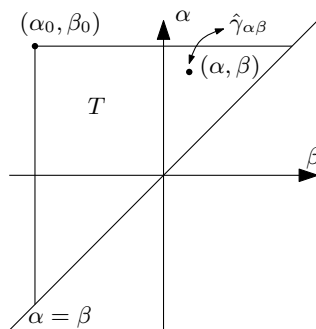


Fig. 5.4: Representation of the Preisach plane.

5.1.1 Model properties

The hysteresis properties of the classical Preisach model are discussed by an example with an arbitrary input sequence, which shows similarities with the interpretation of Mayergoyz [169] pp.7-17. The specific properties of the Preisach model which are discussed are the following: the major and minor loops, reversal points, history dependency, the wiping-out property, and congruency. The properties of the classical Preisach model are explained with a normalized constant distribution in the Preisach plane, because the discussed properties are independent of the Preisach distribution, $P(\alpha, \beta)$. The Preisach distribution includes the shape of the material specific hysteresis loop, and is elaborated on in Section 5.3.

Example: An arbitrary input signal is generated and separated into five sections as shown in Fig. 5.5(a)-(e), which are discussed subsequently. For the rate-independent classical Preisach model, the excitation speed is irrelevant and hence, the saw-tooth signal of Fig. 5.6(a) results in the same input-output characteristic as the arbitrary input shown in Fig. 5.5(e). The corresponding input-output characteristic, $u - f$, is shown in Fig. 5.6(b), where the dots a - h represent the specific points that are discussed and explicitly visualized in Fig. 5.7(a)-(h) and Fig. 5.8.

The first part of the arbitrary input, as shown in Fig. 5.5(a), starts at t_0 from m_0 , which corresponds with $\beta_0 = -1$, in the normalized Preisach plane. Hence, at t_0 the outputs of all $\hat{\gamma}$ -operators are equal to -1 , which corresponds with negative saturation of the hysteresis model. When the input increases, the horizontal line $\alpha = u(t)$ moves upward to the point $\alpha_1 = M_1$, as graphically illustrated by the arrow on the line $\alpha = \beta$ in Fig. 5.7(a). At this instance of time, the triangle is geometrically divided into two sets, $S^+(t)$ and $S^-(t)$ in which the $\hat{\gamma}$ -operators are equal to $+1$ and -1 , respectively. The hysteretic output is then obtained by the Preisach integral (5.1) which can be partitioned over the positive and negative sets as

$$f(t) = \iint_{S^+(t)} P(\alpha, \beta) \hat{\gamma}_{\alpha\beta} u(t) d\alpha d\beta + \iint_{S^-(t)} P(\alpha, \beta) \hat{\gamma}_{\alpha\beta} u(t) d\alpha d\beta. \quad (5.2)$$

Hence, an instantaneous output depends on the subdivision of the Preisach plane and can be written as

$$f(t) = \iint_{S^+(t)} P(\alpha, \beta) d\alpha d\beta - \iint_{S^-(t)} P(\alpha, \beta) d\alpha d\beta \quad (5.3)$$

since $\hat{\gamma}_{\alpha\beta} u(t) = +1$ in set $S^+(t)$, and $\hat{\gamma}_{\alpha\beta} u(t) = -1$ in set $S^-(t)$.

After reaching the first maximum, M_1 , the input is decreased to the value $\beta_1 = m_1$, which is modeled in the Preisach plane by a vertical line, $\beta = u(t)$,

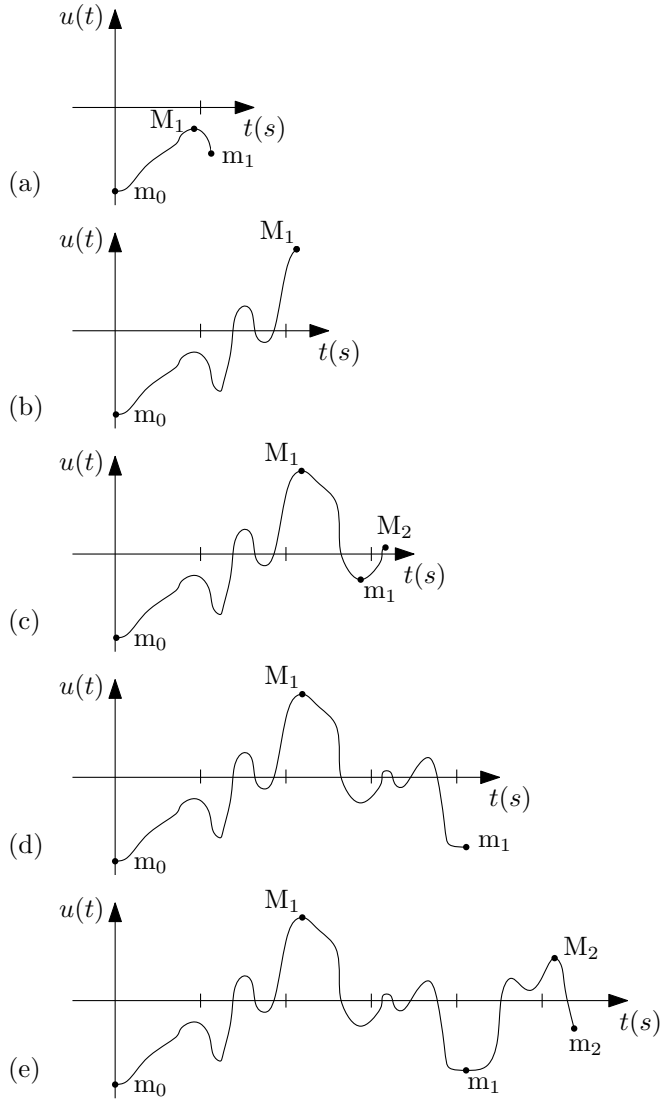


Fig. 5.5: Evolution of the history dependent maximum and minimum values dependent on the random input signal (a)-(e).

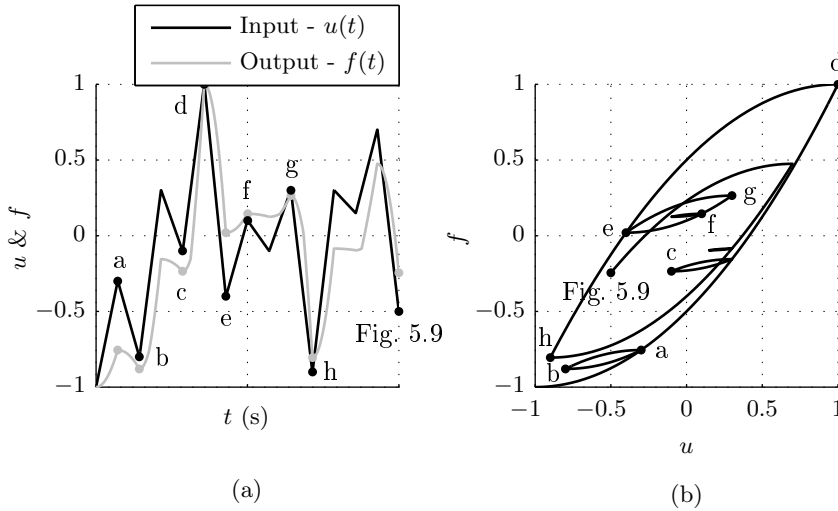


Fig. 5.6: Saw-tooth excitation with an equivalent sequence of the minima and maxima of the input signal of Fig. 5.5(e) (a), and the corresponding normalized input-output relation (b). In both figures, the points a - h are related to Fig. 5.7(a)-(h) and Fig. 5.8.

and is also illustrated by the arrow in Fig. 5.7(b). This procedure divides the Preisach plane by horizontal and vertical lines, which follow from the past extreme values of the input. The resulting input-output relation of the Preisach model for the input of Fig. 5.5(a) is graphically shown in Fig. 5.8(a). The first part of the curve up to the first maximum follows the major loop of the hysteresis model and the second part of the decreasing input is called a first-order reversal curve/branch.

The adjacent random input interval is shown in Fig. 5.5(b), where the input is increased to a value larger than the previous maximum, which closes the first minor loop and wipes-out both, the first maximum M_1 and the minimum m_1 of this minor loop. Afterwards, the input is slightly decreased to $\beta_1 = m_1$, and the corresponding Preisach plane is illustrated in Fig. 5.7(c). Increasing the input up to, or beyond α_0 completes the lower limiting branch of the major loop, as shown in Fig. 5.8(b). At this point, positive saturation is reached and all previous minima and maxima are wiped out, as this is the largest possible input value. This is illustrated in the Preisach plane in Fig. 5.7(d).

Next, the input is decreased from positive saturation to a new minimum m_1 , as shown in Fig. 5.5(c), which results in the upper part of the major loop, as shown in Fig. 5.8(c). The corresponding Preisach planes for the new minimum and maximum are shown in Fig. 5.7(e) and (f), respectively. The following

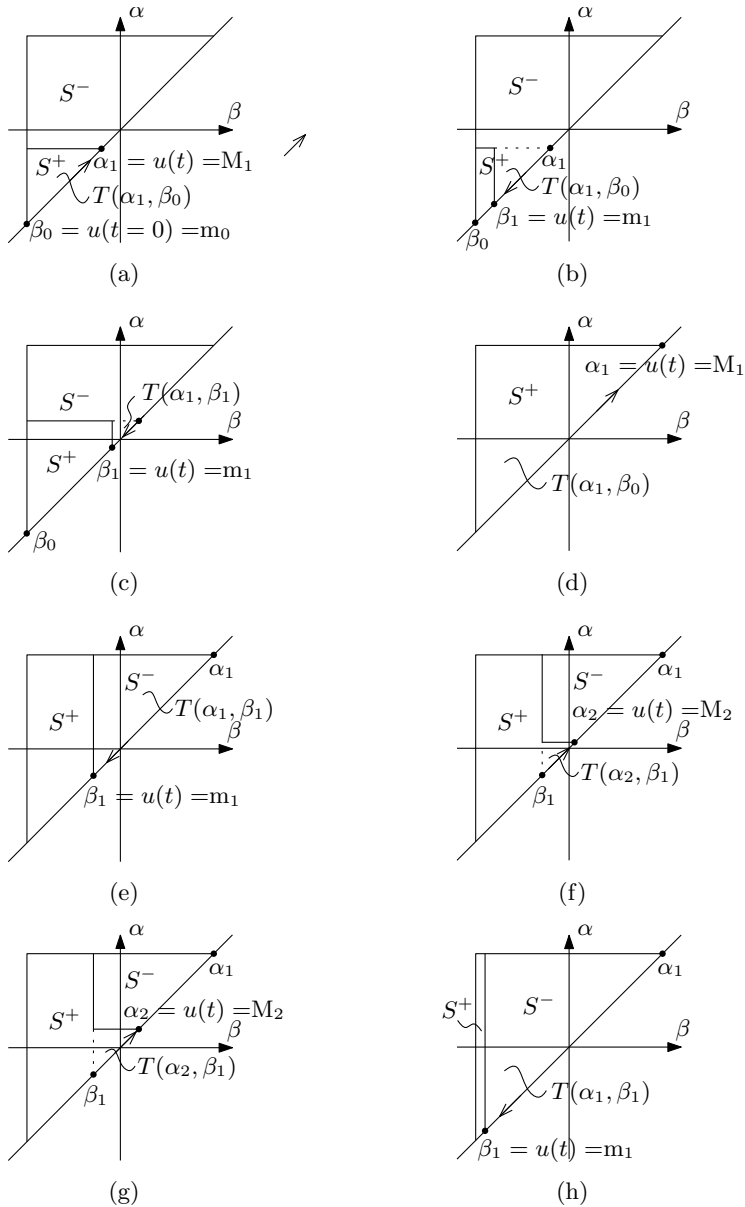


Fig. 5.7: The Preisach planes resulting from arbitrary input signal of Fig. 5.5 and 5.6. The corresponding input-output relations are shown in Fig. 5.8.

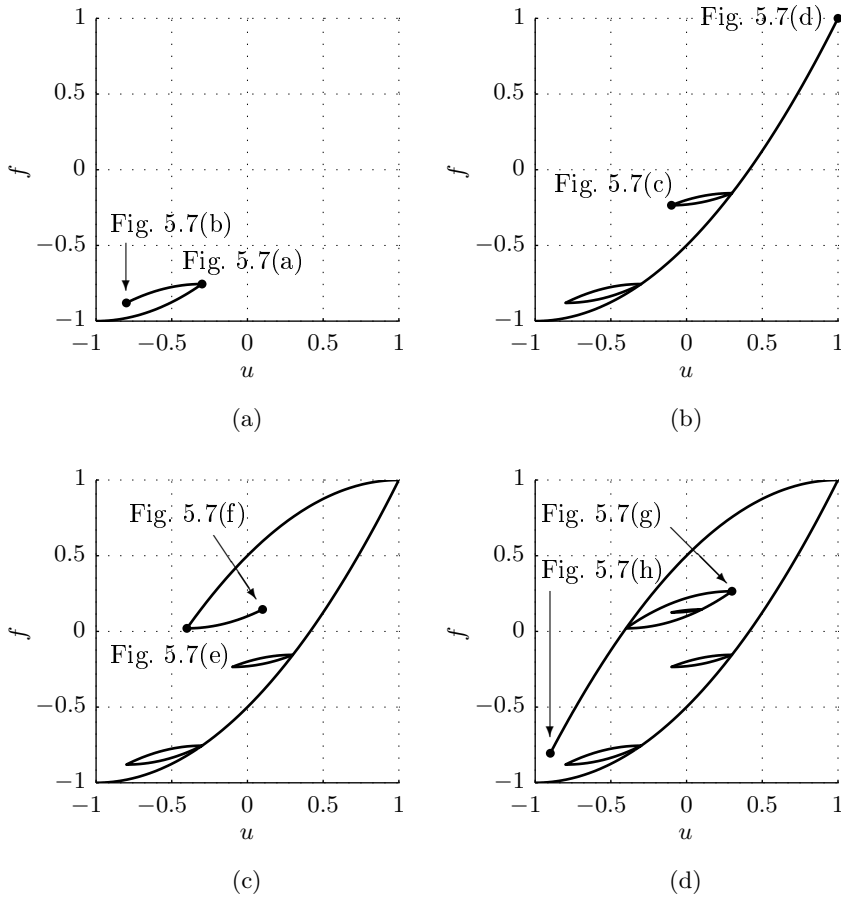


Fig. 5.8: Input-output relation of the classical Preisach model at the various time instances of the arbitrary input as shown in, Fig. 5.5(a) (a), Fig. 5.5(b) (b), Fig. 5.5(c) (c), and Fig. 5.5(d) (d).

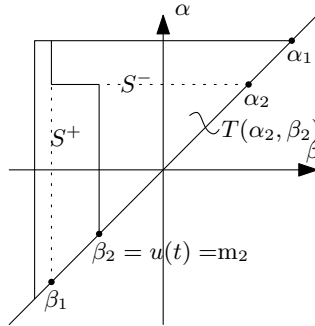


Fig. 5.9: The Preisach plane corresponding with the input of Fig. 5.5(e), the hysteretic input-output relation is shown in Fig. 5.6(b).

input (shown in Fig. 5.5(d)) introduces a second order minor loop, after which the input is further decreased, wiping-out the previous minima, as shown in Fig. 5.8(d). The two intermediate Preisach planes are shown in Fig. 5.7(g) and (h).

The concluding part of the arbitrary excitation as shown in Fig. 5.5(e) introduces an extra second order minor loop as shown in Fig. 5.6(b) and the corresponding Preisach plane is shown in Fig. 5.9.

5.1.2 Numerical implementation

The classical Preisach model can be implemented in various procedures resulting eventually in the same input-output relation. In this section the implementation of the Preisach model is explained based on [169]. By rewriting (5.3) such that, instead of calculating the area of both sets, $S^+(t)$ and $S^-(t)$, it is sufficient to obtain only the positive set, as it is given that the sum of $f_{S^+}(t)$ and $f_{S^-}(t)$ is equal to the limiting triangle, $T(\alpha_0, \beta_0)$. Hence, the Preisach model can be rewritten as

$$f(t) = -F(\alpha_0, \beta_0) + 2 \iint_{S^+(t)} P(\alpha, \beta) d\alpha d\beta \quad (5.4)$$

where the surface integral of the limiting triangle is written as $F(\alpha_0, \beta_0)$, which corresponds with positive saturation. Because of the symmetry of magnetic hysteresis, negative saturation is defined as, $-F(\alpha_0, \beta_0)$. Next, the positive set of the Preisach plane is subdivided into n trapezoidal parts with area Q_k as shown in Fig. 5.10. For a certain instant of time the area of the positive set,

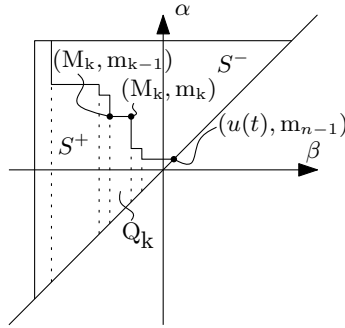


Fig. 5.10: The Preisach plane divided in n trapezoidal parts, Q_{1-n} , which are dependent on the past extrema.

$f_{S^+}(t)$, can be derived as

$$f_{S^+} = \iint_{S^+} P(\alpha, \beta) d\alpha d\beta = \sum_{k=1}^n \iint_{Q_k} P(\alpha, \beta) d\alpha d\beta. \quad (5.5)$$

Each of these trapezoids is obtained by the difference of the two triangles, $T(M_k, m_{k-1})$ and $T(M_k, m_k)$ such that

$$\begin{aligned} \iint_{Q_k} P(\alpha, \beta) d\alpha d\beta &= \iint_{T(M_k, m_{k-1})} P(\alpha, \beta) d\alpha d\beta \\ &\quad - \iint_{T(M_k, m_k)} P(\alpha, \beta) d\alpha d\beta \end{aligned} \quad (5.6)$$

$$= F(M_k, m_{k-1}) - F(M_k, m_k) \quad (5.7)$$

where $F(M_k, m_{k-1})$ is the surface integral over the triangle $T(M_k, m_{k-1})$. For a monotonically decreasing input the positive set can be divided in, n , trapezoidal sections, Q_k , and for a monotonically increasing input the final section is the triangle $T(u(t), m_{n-1})$, as shown in Fig. 5.10. Hence, the expression for the implemented classical Preisach model is given by

$$\begin{aligned} f(t) &= -F(\alpha_0, \beta_0) + 2 \sum_{k=1}^{n-1} [F(M_k, m_{k-1}) - F(M_k, m_k)] \\ &\quad + 2 [F(M_n, m_{n-1}) - F(M_n, u(t))], \end{aligned} \quad (5.8)$$

$$\begin{aligned} f(t) &= -F(\alpha_0, \beta_0) + 2 \sum_{k=1}^{n-1} [F(M_k, m_{k-1}) - F(M_k, m_k)] \\ &\quad + 2F(u(t), m_{n-1}) \end{aligned} \quad (5.9)$$

for an decreasing and increasing input, respectively.

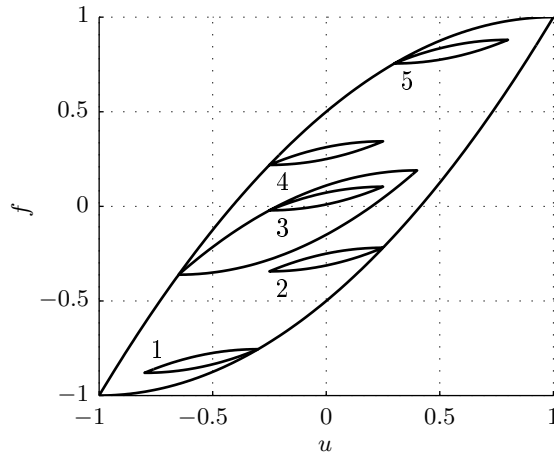


Fig. 5.11: Congruency property.

5.1.3 Congruency property

The congruency property of the classical Preisach model can be useful for many hysteretic applications, while e.g. magnetic hysteresis is non-congruent. Congruency in the hysteresis model means that all minor loops are equal in size and shape, for any back-and-forth input value between the same two consecutive extreme values independent of the history. The congruency of minor loops is shown in Fig. 5.11, where the loops 2, 3 and 4 are congruent, with equal input extrema and different history. The loops 2 and 4 are first-order minor loops of the increasing and decreasing limiting branch, respectively. Loop 3 is an example of a second-order minor loop, because it is a minor loop in a minor loop. The loops 1 and 5 are congruent due to symmetry. In this case, all five minor loops have a back-and-forth extremum with a distance of $\Delta u = 0.5$, and all are congruent, since all are identically shaped.

The distribution functions, which will be introduced in Section 5.3, result in unequal minor loops dependent on the offset of the input u or H . Hence, the distribution functions will change the shape of the minor loops 1 and 5, while the loops 2-4 will remain congruent. It is assumed in this thesis, that the non-congruency is insignificantly present in the evaluated magnetic materials, as discussed in Section 3.3. Furthermore, this effect is not observed in any of the performed measurements. This non-congruency can be modeled by the moving- and product Preisach model with an output dependent offset, which are not implemented in this work. These generalizations are discussed in [29]

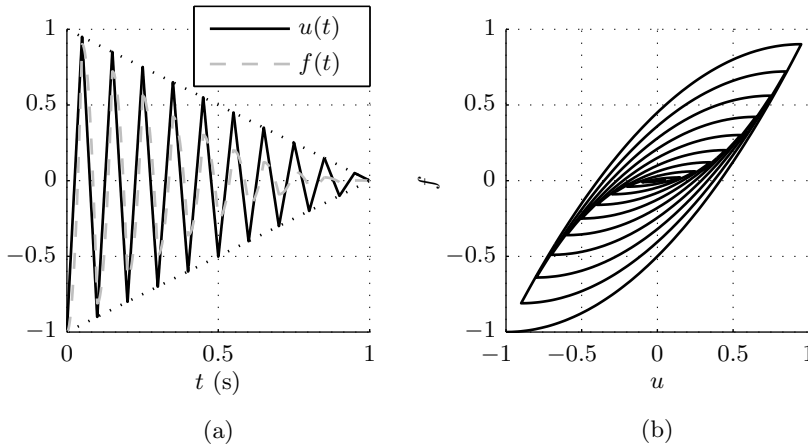


Fig. 5.12: The degaussing of the Preisach model to create the history of a material sample in its demagnetized state, input and output signal (a), and the resulting hysteretic relation (b).

and could be implemented as [126, 127].

5.1.4 Degaussing of the Preisach model

Before the Preisach model can be applied, a check should be performed on the input, to examine if the input starts at positive or negative saturation. In one of those cases, all the history of the model is wiped out. In all other cases, the history is unknown, and for that reason the models starts at the demagnetized state with zero input and zero output.

The demagnetized state of the Preisach model is obtained for the line $\alpha = -\beta$, where $S^+(t) = S^-(t)$. This state can be approximated by an oscillating input, from which the amplitude decreases slowly from saturation to zero, as illustrated in Fig. 5.12(a). The input-output relation of the degaussing process is shown in Fig. 5.12(b) and the corresponding Preisach plane is shown in Fig. 5.13.

The actual demagnetized state of the Preisach model cannot be obtained, because there is always a finite number of horizontal and vertical lines that approximate the straight line dividing the triangular plane into two equal halves. In further simulations, the magnetic material is assumed to be demagnetized. The demagnetization is modeled by the Preisach model with a rate-independent

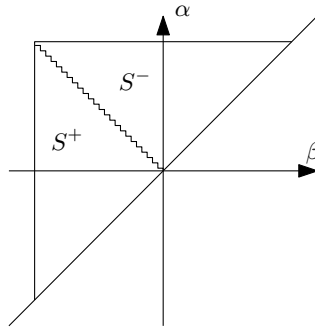


Fig. 5.13: The Preisach plane corresponding to the demagnetized Preisach model.

excitation, with a decreasing input with a thousand extrema (instead of twenty as shown in Fig. 5.12).

5.2 Generalized scalar Preisach model

Many generalizations of the scalar classical Preisach model have been developed to model the experimentally obtained magnetic hysteresis effects in soft-magnetic materials. From these generalizations the most important extensions are selected to obtain a satisfactory hysteresis model that incorporates the most dominant phenomena present in reluctance actuators. The generalizations as described by Mayergoyz [169] involve,

1. non-zero magnetic permeability at the reversal points,
2. unbounded magnetization,
3. non-congruency,
4. accommodation,
5. rate-dependency,
6. magnetostriction,
7. vector representation.

In this work the three most apparent hysteretic properties are considered. Namely, the non-zero permeability at the reversal points, the unbounded magnetization outside the limiting Preisach plane and the rate-dependency. The rate-dependency of magnetic hysteresis is discussed in Chapter 6, where the

dynamic effects are modeled separately instead of incorporating them in the Preisach model.

5.2.1 Neglected generalizations

As discussed in Section 3.3, the non-congruency and accommodation properties, are considered insignificant for the analysis, because the expected discrepancy in the prediction of the magnetic flux density, caused by either one of them, is in the same order of magnitude as the simulation error of the typical symmetric (minor) loops (approximately 3 % of the peak magnetic flux density). Besides that, the generalizations which include these hysteresis phenomena, adjust the hysteresis model according to the observed effects in the measured minor loops. Since both effects, i.e. the non-congruency and accommodation, are not observed in the performed measurements, it is not possible to take these effects into account.

Magnetostriction is not considered in this thesis, because it is expected to induce a maximum force error of approximately 0.2 %, as explained in Section 3.2.3. Additionally, magnetostriction is beyond the scope of this thesis, because it is a research subject on itself, as experienced in an attempt to measure this effect in six degrees of freedom [61]. Moreover, none of these three discussed phenomena in ferromagnetic materials are recognized from the force measurements on three reluctance actuators, as presented later in Chapter 7.

Vector hysteresis is not considered in this analysis for three reasons; (i) it cannot be measured in ring samples with the available soft-magnetic material tester, (ii) it is assumed that the vector properties of the applied non-grain oriented laminations are small, (iii) in this thesis, reluctance actuators are modeled with one-dimensional reluctances in a magnetic equivalent circuit (MEC) method and, hence, only scalar magnetic fields are modeled.

5.2.2 Incorporated generalizations

The first two generalizations of the Preisach model, the non-zero magnetic permeability at the reversal points and the unbounded magnetization are incorporated by the extension of the classical model with a reversible part [171]. The hysteretic constitutive relation between the magnetic flux density and the magnetic field strength in the soft-magnetic material is obtained as [72, 208]

$$B(H) = B_{rev}(H) + B_{irr}(H, H_{past}) \quad (5.10)$$

where the reversible part, $B_{rev}(H)$, is only dependent on the current magnetic field strength, while the irreversible part, B_{irr} , is also dependent on the past input extrema.

Table 5.1: Fitting parameters for the analytical reversible magnetization.

| Material | a | b | c | d |
|-------------|-------|------------------------|-------|------------------------|
| Vacoflux 50 | 1794 | $-2.051 \cdot 10^{-3}$ | 5.074 | $1.251 \cdot 10^{-4}$ |
| M800-50A | 717.8 | $-6.114 \cdot 10^{-3}$ | 75.67 | $-3.187 \cdot 10^{-4}$ |
| AISI 430 | 152.8 | $-1.627 \cdot 10^{-3}$ | 43.19 | $-1.297 \cdot 10^{-4}$ |

The reversible part is modeled with a variable magnetic permeability, $\mu_{rev}(H)$, which is obtained by the slope, dB/dH , at the reversal points of a finite set of measured quasi-static minor loops. The reversible magnetic permeability (also called differential permeability) is obtained for three different soft-magnetic materials, CoFe (Vacoflux 50), SiFe (M800-50A) and stainless steel (AISI 430) and is shown in Fig. 5.14(a). The reversible magnetic permeability is not the same as the relative permeability, which is obtained by $\mu_r = \frac{B}{\mu_0 H}$. The relative permeability is shown in Fig. 5.14(b) and is significantly different from the reversible permeability shown in Fig. 5.14(a).

The measured reversible permeability is modeled by an analytical exponential function

$$\mu_{fit} = ae^{(bH)} + ce^{(dH)}. \quad (5.11)$$

The coefficients, $a - d$, of the obtained differential permeability are given in Table 5.1. There is only a small discrepancy between the measured and fitted reversible permeability for the Vacoflux 50 material at low magnetic field strengths, as shown in Fig. 5.14(a).

The reversible and irreversible part, $B_{irr}(H)$, are obtained from the measurements by

$$B_{rev}(H) = \frac{1}{\mu_0} \int_0^H \mu_{rev}(H) dH, \quad (5.12)$$

$$B_{irr}(H) = B_{meas}(H) - B_{rev}(H) \quad (5.13)$$

where $B_{meas}(H)$ is the measured magnetic flux density for the applied magnetic field strength, H . The reversible permeability is analytically described by (5.11), which is integrated with respect to the applied magnetic field strength corresponding with the experimental measurement. The measured-, reversible- and irreversible $B-H$ relations, are shown in Fig. 5.15, for the three materials. As the irreversible part is modeled with the classical Preisach model its maximum magnetic flux density is limited by the area of the Preisach triangle. By including the reversible part of the generalized Preisach model, magnetic field strengths above the saturation level of the classical model are also simulated.

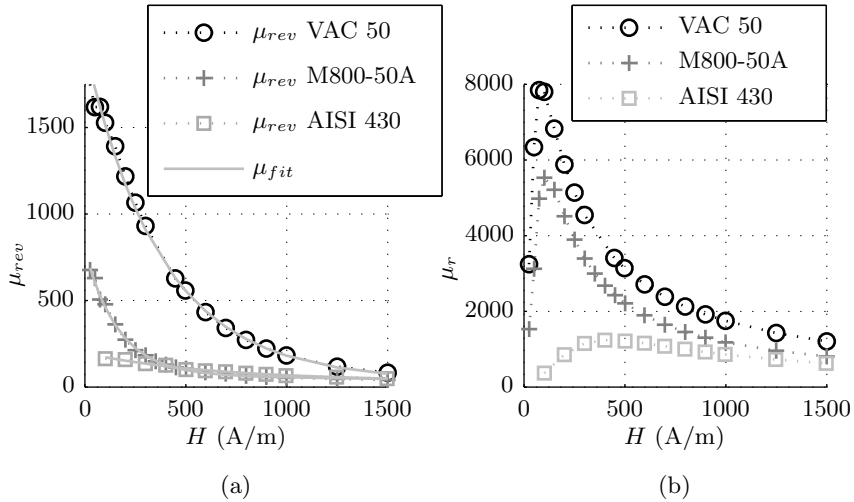


Fig. 5.14: The measured and fitted reversible magnetic permeability, $\mu_{rev}(H)$ (a), and the relative permeability, $\mu_r(H)$ (b), of Vacoflux 50 (VAC 50) with a lamination thickness of 0.35 mm, M800-50A and solid AISI 430.

5.3 Preisach distribution

As previously discussed, the classical Preisach model describes the general hysteretic behavior. However, the soft-magnetic material properties are modeled by the Preisach distribution. This Preisach distribution determines the shape of the irreversible part of the modeled magnetic hysteresis curve. Although much research on magnetic hysteresis has been performed, only two generally accepted methods to identify the Preisach distribution exist, the Everett distribution and the implementation of continuous analytical distributions [244].

The Everett distribution function [62, 72, 84, 97, 169] is determined by the analysis of a set of measured first-order reversal curves, obtained for a low-frequency excitation. This analysis results into a two-dimensional Everett map $E_{irr}(\alpha, \beta)$, from which the Preisach distribution is obtained by the partial differentiation with respect to α and β

$$P(\alpha, \beta) = -\frac{\delta^2 E_{irr}(\alpha, \beta)}{\delta\alpha\delta\beta}. \quad (5.14)$$

Due to the congruency property of decreasing and increasing first-order reversal curves (symmetry), a set of one of both is enough for material identification

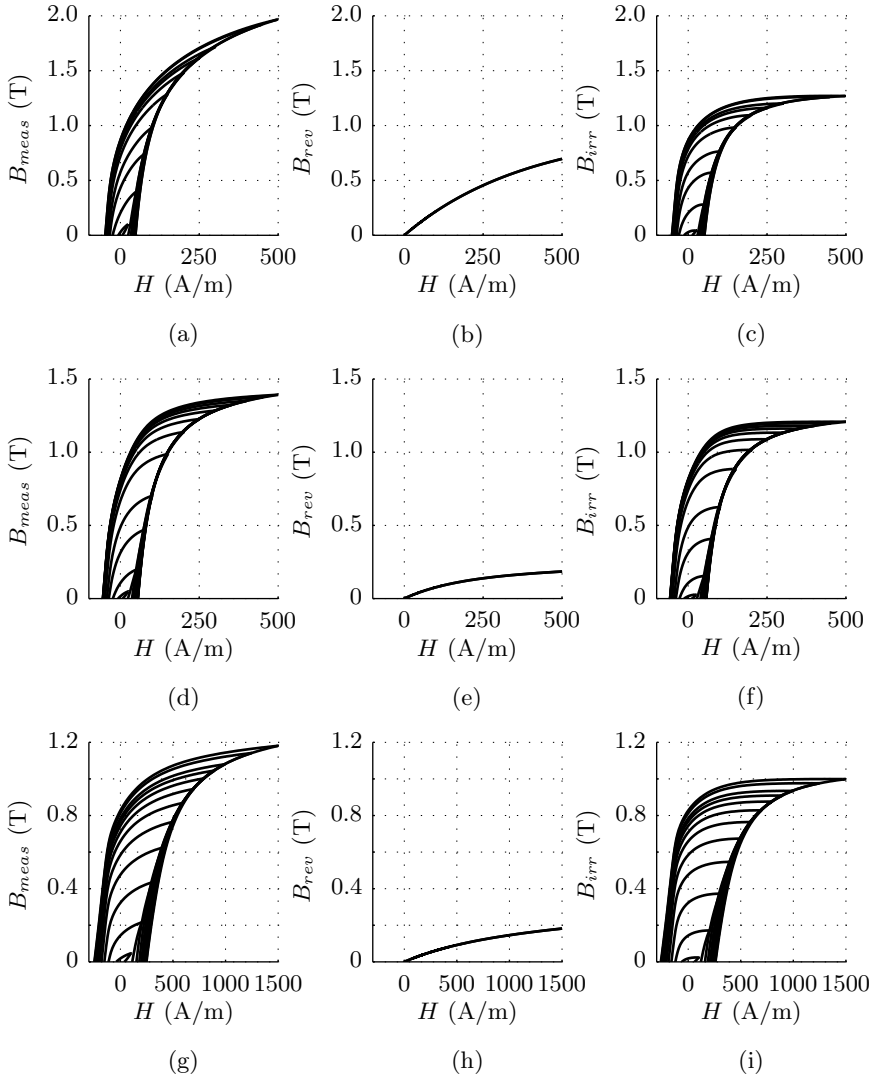


Fig. 5.15: The measured symmetric hysteresis loops for a dc excitation, the corresponding reversible curve and, the irreversible $B-H$ curves, for Vacoflux 50-35 (a)-(c), for M800-50A (d)-(f), and for AISI 430 (g)-(i).

[170]. Unfortunately, the second-order partial derivative of a measured contour map results in amplification of the measurement noise and, consequently, in numerical discontinuities in the Preisach distribution [14, 89]. A smooth Preisach plane is desirable for convergence, as the Preisach model is often part of a larger electromagnetic system. In this thesis, the Preisach model is implemented in a MEC model as later discussed in Section 6.4, but the same holds for the implementation in any FEM. Therefore, analytical continuous Preisach distributions are applied, which directly describe the magnetization and its derivative with respect to the magnetic field strength in analytical closed form.

Besides the numerical stability of the continuous defined distribution functions, it is not necessary to measure the reversal curves for model identification. Only three quasi-static loops are used as input for the parametric identification of a satisfactory distribution for the irreversible part of the generalized Preisach model. The major weakness of continuous distributions is the fact that these functions are never exactly equal to the measured major loop. Furthermore, only a finite set of distribution functions can be evaluated for each material, which will always be an approximate model of the genuine irreversible part of the constitutive relation. Generally, the distribution functions are selected such that the cumulative distribution function mimics the sigmoid* shape of the hysteresis loop.

As previously discussed, the Preisach model consists of an infinite set of rectangular hysteresis operators, as shown in Fig. 5.2(b). These operators are directly coupled to the Preisach plane by its 'up' and 'down' switching operators, α , and β , respectively. The Preisach plane is formed by the product of two independent distributions represented as

$$P(\alpha, \beta) = P(\alpha) \times P^*(\beta). \quad (5.15)$$

In the rectangular hysteresis operator, $h_c = (\alpha - \beta)/2$ is the coercive field and, $h_m = (\alpha + \beta)/2$ is the interaction field. The coercive field corresponds with the standard deviation and the interaction field with the mean of the specific distribution function, both normalized to the maximum magnetic field strength. Furthermore, the distributions P and P^* are both normalized to one, such that the saturation magnetic flux density can be scaled linearly to the derived saturation magnetization of the irreversible part.

*A sigmoid function is a bounded differential real function that is defined for all real input values and has a positive derivative in each point [101].

5.3.1 Evaluated distribution functions

Four candidate distribution functions are evaluated. The analyzed distributions are the hyperbolic tangent function, the Gaussian or Normal distribution, the Cauchy-Lorentz distribution [182], and the Langevin distribution [143]. The corresponding normalized 3d-distribution functions are shown in Fig. 5.16(a)-(d).

The hyperbolic tangent distribution is selected because some magnetic hysteresis models are based on tangential functions, e.g. Coleman-Hodgdon's model [52], Positive-Feedback model [106], and Takács model [194, 246]. The Gaussian distribution is frequently applied, especially in statistics, but also in magnetism [14, 89, 214]. According to Pruksanubal et al. [214] the Cauchy-Lorentz distribution is the best fit for many ferromagnetic materials and, hence, this distribution is also commonly applied [12, 13, 17, 89, 273]. Finally, the Langevin function is part of the original Jiles-Atherton model [123, 124], in which it represents the anhysteretic part of the magnetic hysteresis curve. The Langevin function is a simplification of the Brillouin distribution [34], which is based on microscopic magnetic quantities. The Langevin function is equal to the Brillouin function in the classical limit, where the total angular momentum quantum number of the magnetic moments is assumed infinite, such that all the moments continuously align with the magnetic field [45, 57, 58].

The four discussed distribution functions are expressed by

$$P_{tanh}(k) = \frac{1}{\sigma_k} \operatorname{sech}^2 \left(\frac{k - m_k}{\sigma_k} \right), \quad \text{Hyperbolic tang.} \quad (5.16)$$

$$P_G(k) = \frac{1}{\sigma_k \sqrt{2\pi}} \exp \left(-\frac{(k - m_k)^2}{2\sigma_k^2} \right), \quad \text{Gaussian} \quad (5.17)$$

$$P_{CL}(k) = \frac{1}{\sigma_k \pi} \frac{1}{1 - ((k - m_k)/\sigma_k)^2}, \quad \text{Cauchy-Lorentz} \quad (5.18)$$

$$P_L(k) = \frac{\sigma_k}{(k - m_k)^2} - \frac{1}{\sigma_k} \operatorname{csch}^2 \left(\frac{k - m_k}{\sigma_k} \right) \quad \text{Langevin} \quad (5.19)$$

where, k , is substituted by, h_m , or, h_c , depending on the distribution function, m_k is the mean and σ_k is the standard deviation of the specific distribution function. Each 3d-distribution function has only four parameters, which are determined for each material by curve fitting with a least square method of the cumulative distribution function. The cumulative distribution function is the

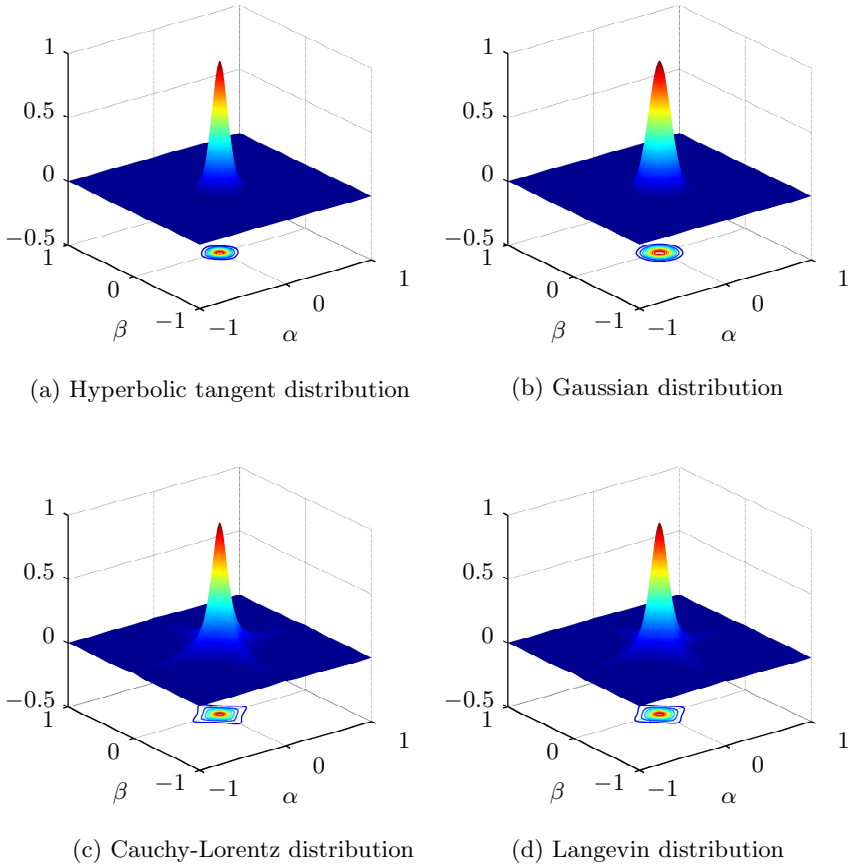


Fig. 5.16: The four considered normalized distribution functions (a)-(d).

integral of the distribution function, which are analytically defined as

$$D_{\tanh}(k) = \tanh\left(\frac{k - m_k}{\sigma_k}\right), \quad \text{Hyperbolic tangent} \quad (5.20)$$

$$D_G(k) = \frac{1}{2} \left(1 + \operatorname{erf}\left(\frac{k - m_k}{\sigma_k \sqrt{2}}\right)\right), \quad \text{Gaussian} \quad (5.21)$$

$$D_{CL}(k) = \frac{1}{2} + \frac{1}{\pi} \tan^{-1}\left(\frac{k - m_k}{\sigma_k}\right), \quad \text{Cauchy-Lorentz} \quad (5.22)$$

$$D_L(k) = \coth\left(\frac{k - m_k}{\sigma_k}\right) - \frac{\sigma_k}{k - m_k}. \quad \text{Langevin} \quad (5.23)$$

Often two equally defined distribution functions are combined to obtain the Preisach plane, although any combination can be formed as shown in [89] with the Cauchy-Lorentz and Gauss distribution, and in [214] for any combination of the Cauchy-Lorentz, Gaussian and Lognormal distribution. Note that the Lognormal distribution is not considered in this work, because it is similar to the Gaussian distribution.

5.3.2 Distribution function correlated to constitutive relation

The implementation of the distribution functions in the scalar Preisach model represents the irreversible part, B_{irr} , of the constitutive relation (5.10). The four distribution functions are implemented to show the differences in the modeled $B-H$ relation. The simulations are performed for a saturation magnetization of the irreversible part, $B_{s,irr} = 1.23$ T at a magnetic field strength, $H_s = 600$ A/m, which corresponds with the experimentally obtained $B-H$ curve of M800-50A.

The mean and standard deviation of the distribution functions are optimized for each material (Section 5.3.3), but for a first impression the following parameters are chosen, $m_k = \sigma_k = H_c/H_s = 9.26 \cdot 10^{-2}$, with $H_c = 55.6$ A/m. The simulated $B_{irr} - H$ curves of the distribution functions are compared in Fig. 5.17. The differences in the distribution functions can be distinguished in the slope of the curve, which is dependent on both, the function and its standard deviation, σ_k . Additionally, the coercive field strength of the irreversible part is influenced by the mean, m_k , of the distribution function. Nevertheless, it is obvious from Fig. 5.17 that the specific distribution determines the slope before saturation is reached.

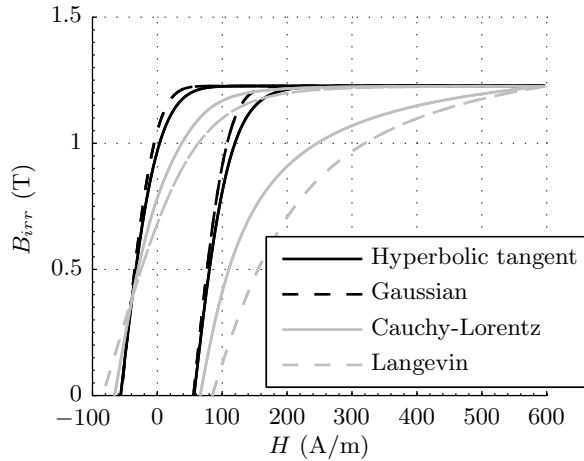


Fig. 5.17: The modeled $B_{irr} - H$ curves obtained for the four distribution functions.

5.3.3 Optimization of the distribution functions

The four parameters of the distribution functions are optimized for each material. In this work, the four distribution functions are optimized for three materials. The constraint minimization algorithm in Matlab is used to optimize the fitting parameters for each distribution function. The objective of the algorithm is the minimization of the rms error, ϵ_{rms} , between the simulated and the irreversible part of the measured $B-H$ curves. The optimal parameters are verified with a parametric sweep over the distribution function parameters to find the global minimum.

In each simulation the rms error is obtained for the simulation of the major loop and two minor loops with the scalar Preisach model, while often only the measured major loop is used to obtain the optimal distribution function [138]. By incorporating the minor loops in the optimization algorithm, it is attempted to obtain the optimal distribution for the whole Preisach plane. In addition to the rms error, the maximum error, ϵ_{max} , is obtained and compared for each simulation. The simulation results for the optimized distribution function parameters are compared to measurements for the three evaluated materials in Section 5.5.

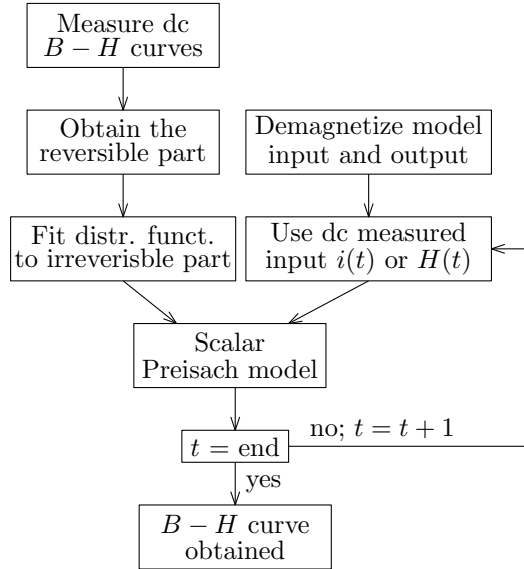


Fig. 5.18: Procedure to obtain the $B-H$ characteristics in the ferromagnetic material of a closed toroidal structure under dc-excitation.

5.4 Simulation procedure

The simulation of the Preisach hysteresis model with the various distribution functions corresponding with the specific materials is summarized in this section. The block diagram of Fig. 5.18 illustrates the procedure to simulate a static $B-H$ curve with the scalar Preisach model, which can be summarized by the following steps,

- Various symmetric $B-H$ curves are measured for maximum magnetic field strengths over the full simulation range.
- The reversible part is obtained by obtaining the slope of the $B-H$ loop at the reversal points of the measured curves.
- The irreversible part is obtained by subtraction of the reversible relation from the measurement and the distribution function is fitted to three irreversible symmetric (minor) loops.
- The demagnetized state of the Preisach model is obtained in thousand steps by a decreasing alternating input.
- A measured current or equivalent magnetic field strength is used as input

for the simulation.

- The Preisach model is executed until the end of the input sequence.

The presented simulation procedure is extended to an iterative procedure with the dynamic magnetic material model in Chapter 6 and is further extended with the MEC model in Section 6.4 to simulate the force in reluctance actuators.

5.5 Experimental verification

The simulation results of the static, generalized, scalar Preisach model are compared to dc-measurements on a closed toroid. The applied measurement method and the definition of a dc-measurement are discussed in Section 3.5. The model parameters of the optimized distributions corresponding with the evaluated materials are given in Table 5.2 as well as the optimized rms- and maximum errors.

The optimized distribution function is compared to measurements for each material, as shown in Fig. 5.19-5.22. Besides positive magnetic flux density of the minor loops, the error between the simulated and measured magnetic flux density, B_{err} , is shown for each material sample. The horizontal axes of the error-plots are normalized to one cycle of each minor loop. The cycle starts at the maximum magnetic field strength, H_{max} . From 0 to 0.5 cycle the discrepancy of the upper branch is shown, 0.5 cycle corresponds with $-H_{max}$, and the last half cycle is the bottom branch of the specific minor hysteresis loop.

An overview of the optimized parameters of each distribution and the model accuracy for each material is presented in Appendix B. The maximum error between the measured and modeled magnetic flux density as a percentage of the peak flux density of Vacoflux 50 is equal to 11.15 % and 5.88 % for 0.10 mm and 0.35 mm laminations, respectively. Moreover, the percentage of rms error for 0.10 mm and 0.35 mm laminations is equal to 2.08 % and 1.77 %, respectively. The Preisach model predicts the magnetic flux density of M800-50A more accurately with a maximum error of 4.43 % and an rms error of 1.66 %. The fit of the distribution functions is less accurate for AISI 430 as the maximum error is equal to 12.48 % and the rms error is equal to 2.98 % of the maximum magnetic flux density.

The Cauchy-Lorentz distribution is the most applicable distribution function (out of the four evaluated functions) for all the examined ferromagnetic materials. The curvature of the $B-H$ characteristic of Vacoflux 50-10 approaches its saturation magnetization more gradually than the Cauchy-Lorentz distribution can model, which results in the relatively large discrepancy. On the

Table 5.2: Optimized distribution function parameters and the corresponding rms and maximum error, for the four examined material samples.

| Material sample | Vacoflux 50 | | M800-50A | AISI 430 |
|-----------------------|----------------|----------------|----------------|----------------|
| | 0.10 mm | 0.35 mm | | |
| Distribution function | Cauchy-Lorentz | Cauchy-Lorentz | Cauchy-Lorentz | Cauchy-Lorentz |
| H_s (A/m) | 800 | 500 | 500 | 1500 |
| h_m | -0.0602 | -0.0935 | -0.0882 | -0.1625 |
| h_c | 0.0600 | 0.0934 | 0.0886 | 0.1664 |
| σ_m | 0.0667 | 0.0663 | 0.0613 | 0.0917 |
| σ_c | 0.0652 | 0.0656 | 0.0613 | 0.0967 |
| ϵ_{rms} (T) | 0.042 | 0.035 | 0.024 | 0.035 |
| ϵ_{rms} (%) | 2.08 | 1.77 | 1.66 | 2.98 |
| ϵ_{max} (T) | 0.223 | 0.116 | 0.063 | 0.147 |
| ϵ_{max} (%) | 11.15 | 5.88 | 4.43 | 12.48 |

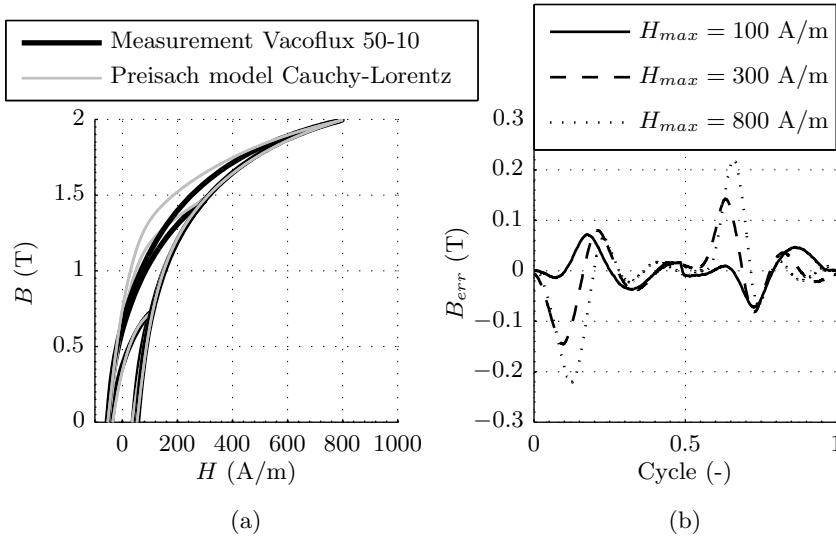


Fig. 5.19: Comparison of the modeled and measured $B-H$ curves of Vacoflux 50 with 0.10 mm laminations (a), and the modeling error for each minor loop (b) (normalized to one cycle).

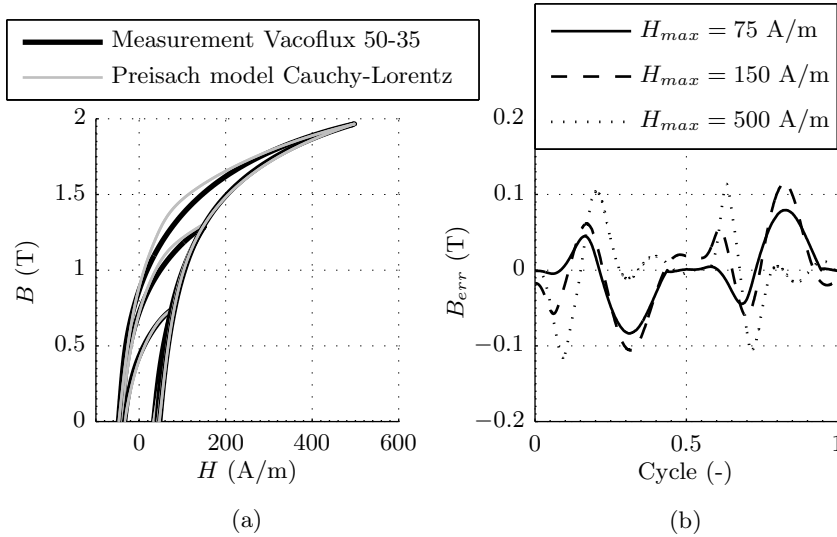


Fig. 5.20: Comparison of the modeled and measured B – H curves of Vacoflux 50 with 0.35 mm laminations (a), and the modeling error for each minor loop (b) (normalized to one cycle).

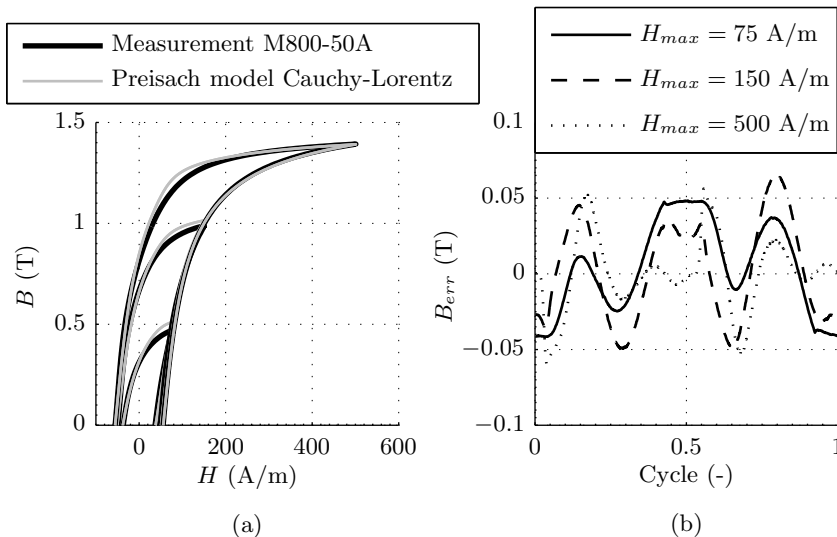


Fig. 5.21: Comparison of the modeled and measured B – H curves of M800-50A (a), and the modeling error for each minor loop (b) (normalized to one cycle).

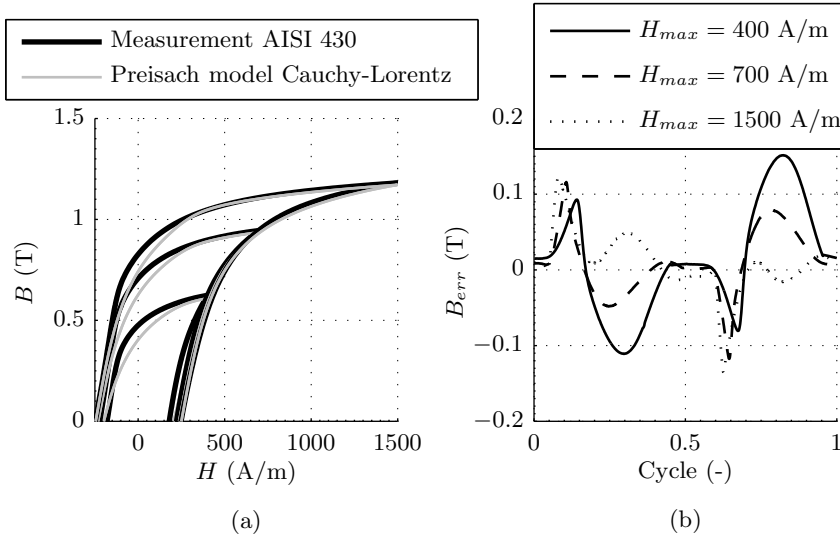


Fig. 5.22: Comparison of the modeled and measured $B-H$ curves of AISI 430 (a), and the modeling error for each minor loop (b) (normalized to one cycle).

contrary, the $B-H$ curve of the AISI 430 sample shows a more abrupt transition between the linear and saturated region than the optimized distribution function. It can be concluded from this analysis, that the discrepancy between the magnetic flux density simulated with the Preisach model and the measured $B-H$ characteristic is highly dependent on the suitability of the evaluated distribution functions. Besides evaluating other distribution functions, the numerical Everett distribution could be derived (5.14) to obtain a more accurate Preisach distribution for these two materials.

5.6 Conclusions

The scalar Preisach model is extensively elaborated including its generalizations, from which the three most significant hysteretic properties are considered. The numerical implementation of the classical Preisach model and the model properties are explained using an example of an arbitrary excitation. Additionally, four analytical distribution functions are optimized for three different soft-magnetic materials.

The four Preisach distribution functions are assessed on the estimation of the

magnetic flux density in three different materials. The simulation results are compared to dc-measurements with various excitation amplitudes. The scalar Preisach model shows that it is able to predict the instantaneous magnetic flux density in a closed toroid with a maximum discrepancy of 11.2 %, 5.9 %, 4.4 % and 12.5 % for Vacoflux 50-10, Vacoflux 50-35, M800-50A and AISI 430, respectively. The rms errors of the simulated magnetic flux density of three hysteresis loops are at least a factor 3 smaller than the maximum discrepancies, for all four ring samples.

The effect of these static modeling errors, is discussed for the dynamic analysis of magnetic materials in the following chapter, followed by the influence on the determination of the magnetic hysteresis in the force of reluctance actuators in Chapter 7.

Dynamic magnetic material modeling

Modeling of dynamic effects in magnetic materials has been intensively investigated in the last decades. The analysis is generally based on the separation of the losses in static and dynamic contributions. This loss separation is often based on the statistical loss theory of Bertotti [25, 26], which is an extension of the Steinmetz law of hysteresis [236]. This statistical loss separation is also combined with static hysteresis models, e.g. the Jiles-Atherton model [122] and the Preisach model [28].

The static hysteresis losses are usually described by the static magnetic hysteresis models, as discussed in Chapter 4. The dynamic losses consist of two contributions, the classical losses and the excess losses. The classical losses are due to eddy currents (Foucault currents) and are analytically obtainable for rectangular structures, as explained in Section 6.3. The excess losses or anomalous losses contributed to domain wall motion, which are generally obtained by a functional model fit to the residual of the measured losses.

Besides the derivation of the excess loss component with the statistical loss theory, the excess losses can be incorporated in the generalized dynamic Preisach model. In the dynamic Preisach model, the physical domain wall motion is represented by gradually switching of the Preisach relay [27, 74, 78, 209]. This model has been thoroughly elaborated on by Dupré in [73, 75, 79].

Concerning the iron losses in electrical machines, often finite element methods are applied to determine the non-hysteretic magnetic flux density in the mesh

elements. These simulation results are then used in the post-processor to obtain the iron losses in the machine by applying the statistical loss theory [15, 203, 227, 284]. The higher harmonics in the local magnetic flux density waveform are sometimes incorporated by the technique proposed by Lavers [144].

Most dynamic magnetic material models are derived for non-oriented materials, while e.g. laminated transformers are grain oriented. The grains are oriented to improve the magnetic properties for magnetization along the strip rolling direction. Therefore, a viscose-based magnetodynamic model is proposed by Zirka [290–292], which is able to model anisotropy of grain oriented materials. The viscose model includes the excess losses based on the so called flux switching model [193]. This model is applicable as an extension for any static hysteresis model [294].

In this chapter, the modeling of dynamic ferromagnetic material behavior is based on the statistical loss theory, which has been introduced in [44, 80] and further elaborated in [296]. The statistical loss theory is first discussed and the analysis is used to deduct the excess loss component from the total losses. This excess loss constant is applied to describe the instantaneous dynamic magnetic field strength, by the field separation formulation in Section 6.2. Eventually, the full dynamic magnetic material model is derived, which consists of the scalar Preisach model, as discussed in the previous chapter, and the dynamic analysis presented in Section 6.3. The theory is experimentally verified by a comparison to measurements performed on three laminated ring samples of Vacoflux 50-10, Vacoflux 50-35 and M800-50A. Finally, dynamic simulations with a 3d FEM and a complex impedance method are discussed and compared to measurements. The contributions of this chapter have been presented in [271, 274–276, 278].

6.1 Statistical loss theory

The statistical loss theory is valid for sinusoidal flux density waveforms only and is based on the separation of the losses into three components [26], i.e. static hysteresis losses, P_h , classical losses, P_{cl} , and excess losses, P_{ex} . The total losses are given by [15, 144]

$$P_T(f) = P_h(f) + P_{cl}(f) + P_{ex}(f) \quad (6.1)$$

where the analysis is performed in the frequency domain. As discussed in Section 3.5, the measurement instrument, the MPG-200, controls the excitation current such that the measured voltage and consequently the magnetic flux density are sinusoidal. Therefore, these measurements can be used directly for the derivation of the loss components of the statistical loss theory.

6.1.1 Static hysteresis losses

The static hysteresis losses are modeled for a range of peak magnetic flux densities, \hat{B} , and is given by

$$P_h(f) = K_h \hat{B}^a f \quad (6.2)$$

where K_h and a are constants, which are fitted to the measured hysteresis losses at various peak magnetic flux densities. To obtain the static hysteresis losses measurements have been performed at a low frequency, f , typically below one Hertz. In this work, the static hysteresis losses are measured for a number of symmetric B - H loops with a limited change of the magnetic flux density, as discussed in Section 3.5. Hence, the energy losses per cycle, $W_h = f^{-1}P_h(f)$, is measured. The fitting constants of the statistical loss model are then obtained for the measured energy losses for a range of maximum magnetic flux densities, as

$$W_h = K_h \hat{B}^a. \quad (6.3)$$

6.1.2 Classical eddy current losses

The classical losses are derived in general form from the Maxwell equations in Section 6.3. Notice that the statistical loss model only holds for laminated materials in which the skin effect can be neglected, as discussed in Section 6.3.2. The eddy current losses are obtained as

$$P_{cl}(f) = \frac{\pi^2 \sigma d^2}{6} f^2 \hat{B}^2 \quad (6.4)$$

where σ is the electric conductivity of the material and d is the lamination thickness.

6.1.3 Excess losses

The excess losses are assigned to the domain wall motion, which is hard to obtain directly from measurements. Therefore, the excess loss term is usually obtained by subtraction of the other two terms from the total measured losses. The excess losses are given by [28]

$$P_{ex}(f) = 8.64 \sqrt{\sigma G S V_0} f^{1.5} \hat{B}^{1.5} \quad (6.5)$$

where $G = 0.1357$ is a dimensionless coefficient due to eddy current damping, S is the cross-section area of the lamination and V_0 is a fitting parameter with

Table 6.1: Coefficients for the statistical loss model.

| Symbol | Vacoflux 50 | | M800-50A | Unit |
|----------|----------------------|----------------------|-----------------------|-------------|
| | 0.10 mm | 0.35 mm | | |
| σ | $2.273 \cdot 10^6$ | $2.273 \cdot 10^6$ | $4.348 \cdot 10^6$ | S/m |
| K_h | $1.62 \cdot 10^{-2}$ | $1.49 \cdot 10^{-2}$ | $2.446 \cdot 10^{-2}$ | - |
| a | 1.332 | 1.344 | 1.706 | - |
| K_{ex} | 2.40 | 2.84 | 0.061 | $AV^{-0.5}$ |

units, $A \cdot m^{-1}$, and is amongst others contributed to the grain size, the crystallographic texture and residual stresses [28]. Because this contribution has to be fitted to the measurement anyhow, the term $8.64\sqrt{\sigma GSV_0}$ is substituted by K_{ex} (in units of $A \cdot V^{-0.5}$).

Finally, the total losses in laminated magnetic materials are described as function of the frequency and peak magnetic flux density by

$$P_T(f) = K_h \hat{B}^a f + \frac{\pi^2 \sigma d^2}{6} f^2 \hat{B}^2 + K_{ex} f^{1.5} \hat{B}^{1.5}. \quad (6.6)$$

The coefficients of each of the contributions in the statistical loss model are obtained from the measured losses, with the least square fitting routine in Matlab. The results are given in Table 6.1 for all three laminated materials.

6.1.4 Experimental verification

The static and dynamic magnetic material losses are measured for a sinusoidal magnetic flux density and are obtained per cycle for both, the quasi-static and dynamic measurements. The measurements are performed on laminated ring samples of Vacoflux 50-10, Vacoflux 50-35 and M800-50A. The large variety in the magnetic properties of the evaluated material samples results in a comprehensive evaluation of the applied simulation method.

The measured static hysteresis loss is equal to the stored magnetic energy, given by (2.13). The measured hysteresis loss compared to both, the static energy loss per cycle of the statistical loss theory (6.3), and to the modeled losses with the generalized scalar Preisach model, as presented in previous chapter. The results of the statistical loss model and the Preisach model are shown in Figs. 6.1, 6.2 and 6.3 for Vacoflux 50-10, Vacoflux 50-35 and M800-50A, respectively. Besides the measured and modeled losses, the absolute discrepancy, ϵ (in mJ/kg), is shown between both models and the measurements.

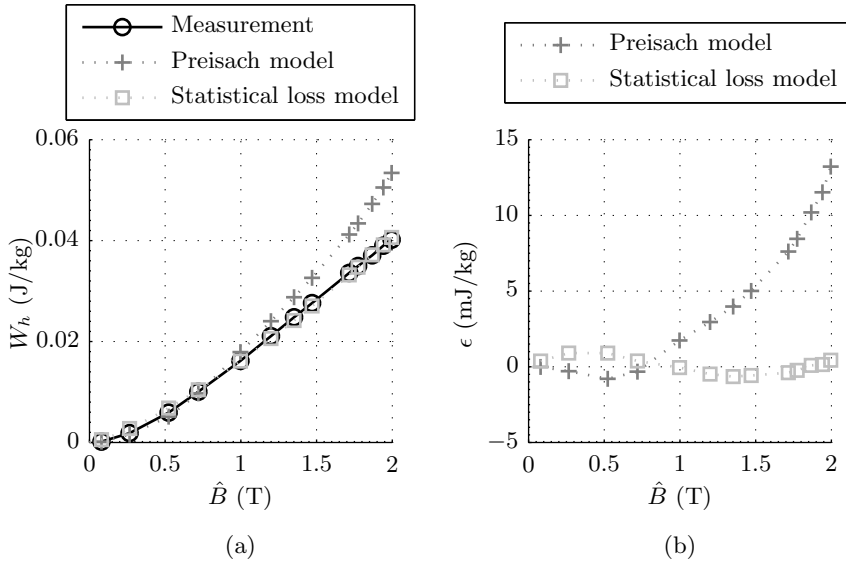


Fig. 6.1: Static hysteresis loss obtained with the Preisach model and the statistical loss model compared to measurements (Vacoflux 50-10) (a), and the error between the modeled and measured losses (b).

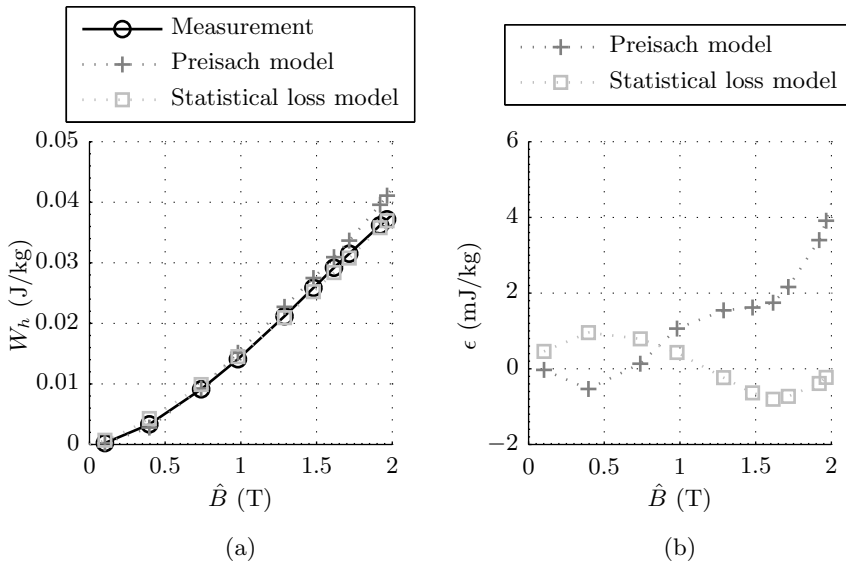


Fig. 6.2: Static hysteresis loss obtained with the Preisach model and the statistical loss model compared to measurements (Vacoflux 50-35) (a), and the error between the modeled and measured losses (b).

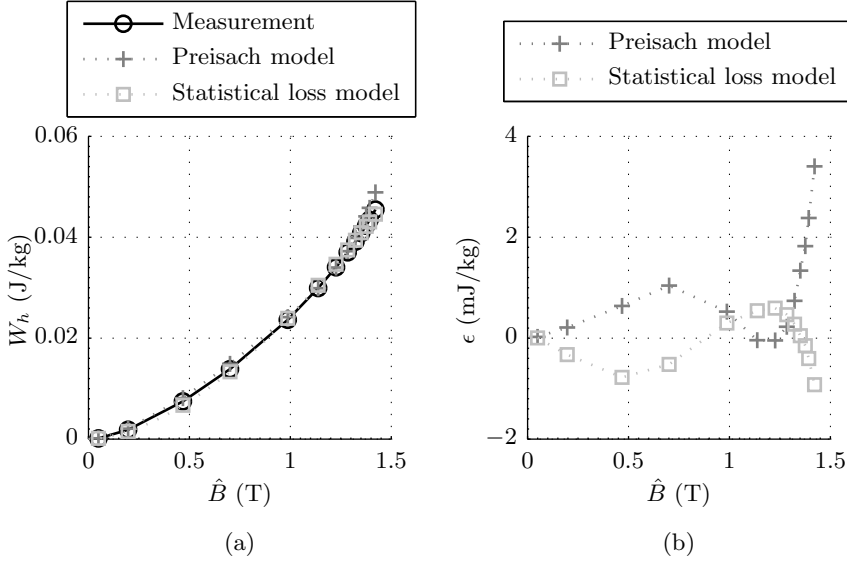


Fig. 6.3: Static hysteresis loss obtained with the Preisach model and the statistical loss model compared to measurements (M800-50A) (a), and the error between the modeled and measured losses (b).

For all three materials, the discrepancy between the statistical loss model and the generalized Preisach model is similar for low magnetic flux densities. However, the difference between the measurement and the Preisach model increases when the saturation magnetization of the material is approached. Especially for Vacoflux 50-10, the modeling error is larger for higher magnetic flux densities, as also shown in Fig. 5.19 of previous chapter. This is a direct result of the mismatch between the optimized distribution function and the magnetic constitutive relation of the ferromagnetic material.

The dynamic analysis of the statistical loss model is verified for frequencies between 40 and 400 Hz. For the dynamic measurements, the power losses in W/kg are obtained by either the magnetic energy (2.13) or coenergy (2.16) in J/kg. This stored magnetic energy of a single hysteresis loop is multiplied by the excitation frequency as

$$P = \frac{f}{\rho_m} \oint B \cdot dH = \frac{f}{\rho_m} \oint H \cdot dB \quad (6.7)$$

where ρ_m is the mass density of the specific material.

The measured dynamic magnetic material losses are compared to the modeled losses with the statistical loss model for various peak magnetic flux densi-

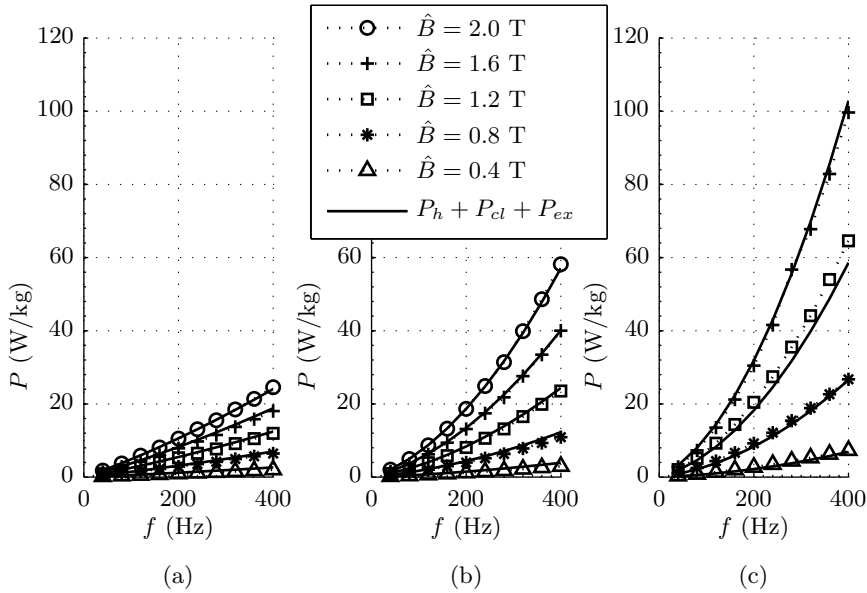


Fig. 6.4: Dynamic hysteresis losses, measured (\circ , $+$, \square , $*$, \triangle) and modeled with the statistical loss model for various peak magnetic flux densities on three toroidal samples of Vacoflux 50-10 (a), Vacoflux 50-35 (b) and M800-50A (c).

ties, $0.4 \leq \hat{B} \leq 2.0$ T, for both Vacoflux 50 materials, and $0.4 \leq \hat{B} \leq 1.6$ T, for M800-50A, as shown in Fig. 6.4(a)-(c), respectively. The analysis shows that a good agreement is obtained for each peak magnetic flux density over the whole frequency range with the statistical loss model. The thin lamination thickness of Vacoflux 50-10 decreases the eddy currents significantly, which results in lower dynamic losses at higher frequencies. It is obvious from Fig. 6.4 that the high-frequency losses of Vacoflux 50-35 and M800-50A are approximately two times and four times higher than the losses of Vacoflux 50-10, respectively.

Besides the total losses, each loss component is obtained with the statistical loss theory. In Fig. 6.5 each loss component is shown for all three materials at an excitation frequency of 320 Hz. An excitation of 320 Hz excitation is selected, because this is the frequency at which the dynamic analysis is performed on the E-core reluctance actuators in Chapter 7. The differences between the three materials shows clearly the eddy current reduction for thin laminations. The classical eddy current loss component is minimal for Vacoflux 50-10 ($\approx 7\%$), while this component is the major contributor for the losses of M800-50A ($\approx 70\%$) with 0.5 mm laminations.

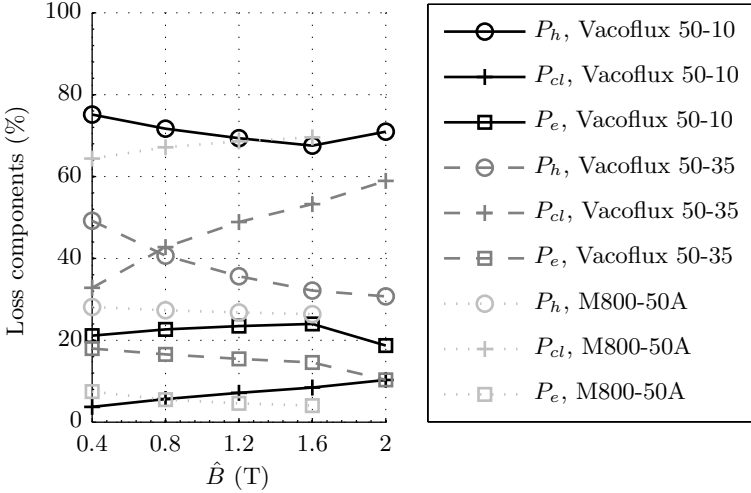


Fig. 6.5: Dynamic hysteresis loss components as percentage of the total losses obtained with the statistical loss model for the three materials, and an excitation frequency of 320 Hz.

6.2 Field separation for instantaneous modeling

The field separation method is applied to obtain the instantaneous magnetic field strength from the modeled magnetic flux density, which is necessary for the real-time analysis of arbitrary current excitations. The field separation method is equivalent to the previously discussed loss separation with the statistical loss theory (6.1). The power losses given by (6.7) can be rewritten in the time domain as [25, 86]

$$P(t) = \frac{f}{\rho_m} \int_0^T H(t) \frac{dB_m(t)}{dt} dt \quad (6.8)$$

where T is one period of the measured $B-H$ loop, and $B_m(t)$ is the instantaneous mean magnetic flux density in the cross-section of the lamination. Combining this with (6.1) gives

$$P(t) = \frac{f}{\rho_m} \int_0^T (H_h(t) + H_{cl}(t) + H_{ex}(t)) \frac{dB_m(t)}{dt} dt. \quad (6.9)$$

Hence, the effective magnetic field strength $H(t)$ is separated in three field strengths, corresponding with each of the loss components [293, 294]

$$H(t) = H_h(t) + H_{cl}(t) + H_{ex}(t) \quad (6.10)$$

where the $H_h(t)$ is calculated using the Preisach model. The classical field $H_{cl}(t)$ is given for laminated materials by

$$H_{cl}(t) = \sigma_{fe} \frac{d^2}{12} \frac{dB_m(t)}{dt} \quad (6.11)$$

which is derived in general form in Section 6.3.1 and for laminated materials in Section 6.3.2. The excess field is derived from (6.5) and (6.9) as [80, 296]

$$H_{ex}(t) = K_{ex,inst} \delta \left| \frac{dB_m(t)}{dt} \right|^{0.5} \quad (6.12)$$

where $K_{ex,inst} = K_{ex}/4.25057$ to satisfy that, by substituting (6.12) in (6.10), the excess losses in the frequency domain result in (6.5), and where

$$\delta = \text{sign} \left(\frac{dB_m}{dt} \right) = \begin{cases} +1 & \text{if } \frac{dB_m}{dt} > 0 \\ -1 & \text{if } \frac{dB_m}{dt} < 0 \end{cases} \quad (6.13)$$

Although, the excess loss constant is also dependent on the magnetic flux density [291, 292, 296], because the value of V_0 in (6.5) is dependent on the magnetic flux density [80], it is considered sufficient to model the excess field with the material dependent constant, $K_{ex,inst}$.

6.3 Eddy current model for magnetic materials

The instantaneous dynamic magnetic field strength component due to eddy currents is firstly derived in general form. This analysis is subsequently applied for laminations and permanent magnets. The skin effect is discussed and the simulation procedure of the dynamic material model in combination with the scalar Preisach model is described. Finally, the simulation results are compared to measurements performed on a laminated toroid. Both, the dynamic losses are examined and the instantaneous magnetic flux density at various excitation frequencies.

6.3.1 Rectangular shaped ferromagnetic material

The eddy currents in a ferromagnetic structure are obtained from the combination of Ampère's law (2.1) and Faraday's law (2.3) in the quasi-static form. These equations are combined with the electrical (2.7) and magnetic (2.5) constitutive relations, to obtain the eddy currents in a non-laminated, rectangularly-shaped, magnetic material. A bidirectional alternating magnetic

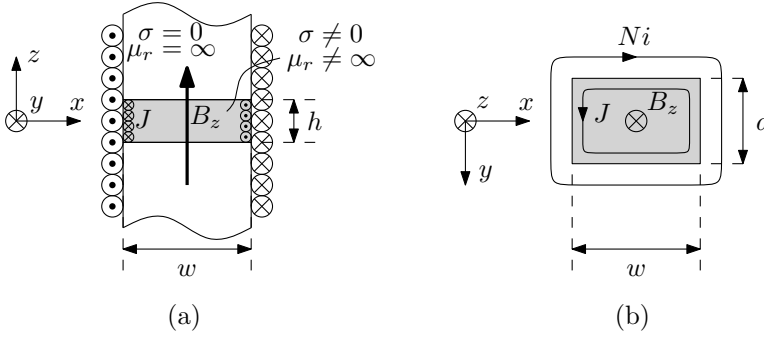


Fig. 6.6: Illustration of the magnetic flux density and the currents in a cross-sectional view through the center of a rectangular ferromagnetic material, for the x - z plane at $y = 0$ (a), and for the x - y plane at $z = 0$ (b).

flux density is induced by an external coil around the magnetic structure, as shown in Fig. 6.6. The rectangular part under consideration is hypothetically placed in an ideal magnetic circuit between two poles with an infinite magnetic permeability and zero electric conductivity.

The magnetic flux density and current density in a rectangular ferromagnetic material, are illustrated in the cross-sectional view of Fig. 6.6(a). The cross-section through the ferromagnetic material in the x - y plane is illustrated in Fig. 6.6(b). The dimensions of the rectangular magnetic material in the x -, y - and z -directions are w , d and h , respectively. In the analysis, it is assumed that the eddy currents in the material have a rectangular shape.

Given that the time-varying magnetic flux density in this problem is only directed in the z -direction, it is obtained from Faraday's law (2.3) combined with the constitutive relation (2.7) that the eddy currents are only present in the x - y plane

$$\frac{\partial J_x(y, t)}{\partial y} - \frac{\partial J_y(x, t)}{\partial x} = \sigma \frac{\partial B_z(x, y, t)}{\partial t} \quad (6.14)$$

where J_x and J_y are the current densities in the ferromagnetic material. The magnetic flux density, $B_z(x, y, t)$, at a certain time instant is illustrated in Fig. 6.7(a), which is the resultant of the source field and the magnetic flux density due to the eddy currents. According to Ampère's law, the total current in the x - and y -directions is equal, such that

$$\int_0^{\frac{d}{2}} |J_x(y, t)| dy \Big|_{x=0} = \int_0^{\frac{w}{2}} |J_y(x, t)| dx \Big|_{y=0} . \quad (6.15)$$

Under the condition that the skin effect can be neglected, it follows from (2.1, 2.3, 2.7) that the eddy current density is linearly distributed in the x - and y -directions, as shown in Fig. 6.7(b). The current density is written as

$$J_x(y, t) = y \frac{2\hat{J}_x(t)}{d} \Big|_{x=0} \quad \text{and} \quad J_y(x, t) = -x \frac{2\hat{J}_y(t)}{w} \Big|_{y=0} \quad (6.16)$$

where $\hat{J}_x(t)$ and $\hat{J}_y(t)$ are the peak current densities at the boundary of the ferromagnetic material. It follows from (6.15) and (6.16) that

$$\frac{d\hat{J}_x}{2} = \frac{w\hat{J}_y}{2} \quad \text{and hence,} \quad \hat{J}_x = \frac{w}{d}\hat{J}_y. \quad (6.17)$$

Taking the derivative of J_x and J_y (6.16) with respect to y and x , respectively, and substituting the result in (6.14) gives

$$\frac{2\hat{J}_x(t)}{d} + \frac{2\hat{J}_y(t)}{w} = \sigma \frac{\partial B_z(x, y, t)}{\partial t}. \quad (6.18)$$

Subsequently, using (6.17) and (6.16) the current density in the x - and y -directions is derived as

$$J_x(y, t) = \frac{\sigma}{1 + \frac{d^2}{w^2}} y \frac{\partial B_z(x, y, t)}{\partial t} \Big|_{x=0} \quad (6.19)$$

and

$$J_y(x, t) = -\frac{\sigma}{1 + \frac{w^2}{d^2}} x \frac{\partial B_z(x, y, t)}{\partial t} \Big|_{y=0}. \quad (6.20)$$

Additionally, a mean magnetic flux density is assumed throughout the cross-section of the ferromagnetic material, such that

$$\mathbf{B}(x, y, t) = B_{z,m}(t) \quad (6.21)$$

where $B_{z,m}$ is the mean magnetic flux density at the x - y plane, pointed in the z -direction. Consequently, the magnetic field strength is shown in Fig. 6.7(c). It follows from Ampère's law that the current density is given by

$$J_x = \frac{\partial H_z}{\partial y}, \quad \text{and,} \quad J_y = -\frac{\partial H_z}{\partial x}. \quad (6.22)$$

Hence, the magnetic field strength is quadratically related to the position, because the current density is assumed to be linearly distributed. Using (6.19)

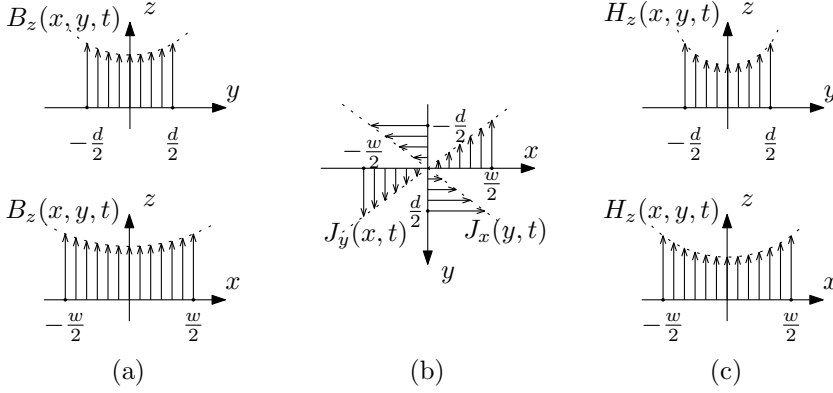


Fig. 6.7: Graphical representation of the distribution of the magnetic flux density (a), the current density (b), and the magnetic field strength (c), at the cross-sections in the middle of the rectangular material sample as shown in Fig. 6.6.

and (6.20), the magnetic field strength due to the derived eddy current densities is given by

$$H_{z,J_x}(t) = \frac{\sigma}{1 + \frac{d^2}{w^2}} \int_0^y y \frac{\partial B_{z,m}(t)}{\partial t} dy \quad (6.23)$$

$$H_{z,J_y}(t) = \frac{\sigma}{1 + \frac{w^2}{d^2}} \int_0^x x \frac{\partial B_{z,m}(t)}{\partial t} dx. \quad (6.24)$$

The sum of both magnetic field strengths, results in

$$H_{z,J_{x,y}}(t) = \frac{\sigma}{w^2 + d^2} \frac{dB_{z,m}(t)}{dt} \frac{1}{2} \left(w^2 \left(\frac{d^2}{8} - \frac{y^2}{2} \right) + d^2 \left(\frac{w^2}{8} - \frac{x^2}{2} \right) \right) \quad (6.25)$$

which is the decreasing magnetic field strength due to the eddy currents, where the magnetic field strength throughout the material is given by

$$H_z(t) = H_{z,b}(t) - H_{z,J_{x,y}}(t) \quad (6.26)$$

where $H_{z,b}$ is the magnetic field strength on the boundary of the ferromagnetic material. Finally, the mean magnetic field strength in the cross-section area of the material is obtained by the surface integral over (6.26) and substituting (6.25)

$$\begin{aligned} H_{z,m}(t) &= \frac{1}{d} \frac{1}{w} \int_{-\frac{d}{2}}^{\frac{d}{2}} \int_{-\frac{w}{2}}^{\frac{w}{2}} H_z(t) dx dy \\ &= H_{z,b}(t) - \frac{w^2 d^2}{w^2 + d^2} \frac{\sigma}{12} \frac{dB_{z,m}(t)}{dt}. \end{aligned} \quad (6.27)$$

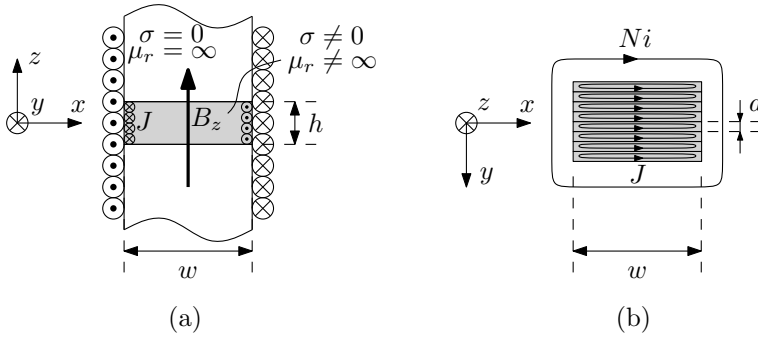


Fig. 6.8: Illustration of the magnetic flux density and the currents in a cross-sectional view through the laminated iron, for the x - z plane at $y = 0$ (a), and for the x - y plane at $z = 0$ (b).

6.3.2 Laminated material

The previous analysis of the eddy currents in a rectangularly-shaped ferromagnetic material can be simplified for thin laminations. As illustrated in Fig. 6.8, the lamination thickness, d , is much smaller than the width, w . Therefore, the eddy currents are only dependent on the lamination thickness, as can be derived from (6.27) for $w \rightarrow \infty$ [97, 98]. Hence, the mean magnetic field strength in the laminated material is given by

$$H_{m,fe}(t) = H_b(t) - \sigma_{fe} \frac{d^2}{12} \frac{dB_{z,m}(t)}{dt} \quad (6.28)$$

where σ_{fe} is the conductivity of the laminated ferromagnetic material. This eddy current model is applied to the Preisach model, as discussed in Section 6.3.5.

6.3.3 Permanent magnet

In magnetic structures where permanent magnets are included to pre-bias the magnetic flux density, the eddy currents in the permanent magnet must be taken into account under dynamic excitations. Often, segmentation is applied to reduce the eddy current losses in the permanent magnets in large machines and high-speed machines [121, 128, 232]. Alternatively, ferrite magnets and bonded permanent magnets [199] could be applied, for high-frequency applications. Both, ferrites and bonded magnets have a lower electric conductivity but also a lower remanent magnetic flux density. Another alternative is to place a conducting sleeve over the permanent magnets [152, 211, 259]. The

conducting sleeve is applied to shield the permanent magnets, by limiting the high-frequency magnetic fields variations that penetrate into the magnets.

In this thesis, a pre-biased E-core reluctance actuator with a solid NdFeB permanent magnet has been investigated. The eddy currents are taken into account for the solid permanent magnet, based on the previous derivation (6.27). The eddy currents in the permanent magnet reduce the magnetic field strength similarly as for other ferromagnetic materials. Hence, the mean coercive field strength is obtained as

$$H_{m,c}(t) = H_c - \frac{w^2 d^2}{w^2 + d^2} \frac{\sigma_{PM}}{12} \frac{dB_{z,m}(t)}{dt} \quad (6.29)$$

where H_c is the static coercive field strength of the permanent magnet (2.39), σ_{PM} is the conductivity of the permanent magnet.

6.3.4 Skin effect

In the previous section, it is assumed that the eddy current density decays linearly from the boundary to the inside of the conductive material. This assumption is only valid when the skin effect can be neglected. The current density including the skin effect is given by

$$J = J_b e^{-d/\delta} \quad (6.30)$$

where J_b is the current density on the boundary, d is the depth from the boundary into the material and δ is the skin depth. The skin depth is defined as the depth below the surface of the conducting medium, where the current density is decreased to a fraction of, $1/e \approx 0.37$, with respect to the current density at the surface boundary. The skin depth is equal to

$$\delta = \sqrt{\frac{2}{2\pi f \mu \sigma}} \quad (6.31)$$

where $\mu = \mu_0 \mu_r$ is the magnetic permeability.

The reluctance actuators discussed in Chapter 7, are manufactured from laminated SiFe (M800-50A) and CoFe (Vacoflux 50). Moreover, one of the SiFe actuators has a pre-biasing NdFeB permanent magnet. The experimental verification is performed for frequencies up to 320 Hz. The skin depths for this maximum frequency, are given in Table 6.2, for the different materials of the applied reluctance actuators. The lamination thickness of Vacoflux 50 and the sizes of the permanent magnet are smaller than twice the skin depth and the thickness of M800-50A is approximately twice the skin depth at 320 Hz. Therefore, the skin effect can be neglected in the analysis, which is also verified in

Table 6.2: Material parameters of the laminated SiFe (M800-50A) and the permanent magnet (NdFeB) and the sizes within the E-core actuator.

| Parameter | Symbol | Vacoflux 50 | M800-50A | NdFeB | Unit |
|----------------|----------------|-------------------|--------------------|--------------------|------|
| Relative perm. | μ_r | 4260 | 3260 | 1.05 | - |
| Electric cond. | σ | $0.44 \cdot 10^6$ | $4.348 \cdot 10^6$ | $0.667 \cdot 10^6$ | S/m |
| Material area | $d \times w$ | 0.10×28 | 0.5×30 | 10×30 | mm |
| Skin depth | δ_{320} | 0.65 | 0.24 | 33 | mm |

[275, 278] for the E-core of M800-50A with and without permanent magnet. Nevertheless, the skin depth can be included in the analysis as described in [264].

6.3.5 Simulation procedure

The combination of the dynamic magnetic material model and the Preisach model is solved iteratively. The magnetic field strength reduction due to the eddy currents directly influences the magnetic flux density obtained with the Preisach model. Simultaneously, the time-derivative of the magnetic flux density at a certain time step influences the magnetic field strength reduction due to eddy currents, obtained with the dynamic model. Therefore, the dynamic magnetic material model is solved iteratively. The iterative solving procedure is shown in the block diagram of Fig. 6.9, which is an extension of the block diagram of the scalar Preisach model as shown in Fig. 5.18. The procedure is described as follows;

- The scalar Preisach model is identified, including the reversible and irreversible part, the distribution function and the Preisach model is again first demagnetized.
- The dynamic, measured, current input is used and an initial relative permeability is given, which is necessary for the dynamic magnetic material model.
- The magnetic field strength is obtained by the time derivative of the instant and previous magnetic flux density with the dynamic magnetic material model.
- The magnetic flux density is calculated with the Preisach model.
- The procedure is converged for a certain time step, when the relative magnetic permeability is within an range of $\epsilon = 1 \cdot 10^{-3}$, for three successive

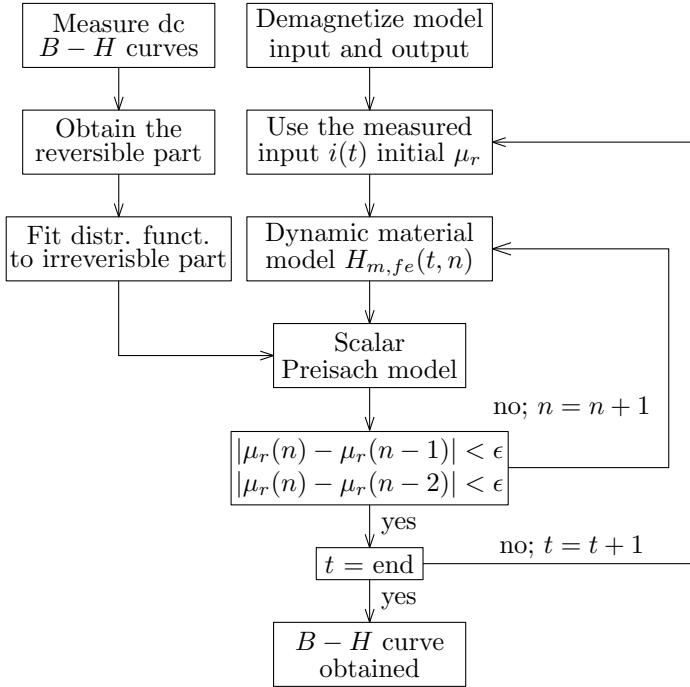


Fig. 6.9: Procedure to obtain the $B-H$ characteristics in the ferromagnetic material of a toroidal sample under ac-excitation.

iterations.

- The simulation is finalized after the last input signal and the $B-H$ characteristic is acquired.

6.3.6 Experimental verification

The instantaneous dynamic magnetic material model combined with the scalar Preisach model is experimentally verified by a comparison to the measured $B-H$ characteristics of a toroidal material sample. The simulation results are obtained using the measured magnetic field strength as model input, for three ring samples of Vacoflux 50-10, Vacoflux 50-35 and M800-50A. Measurements are performed at various frequencies and peak magnetic flux densities. From each simulated dynamic hysteresis loop, the iron losses are obtained and compared to the measured losses, as shown in Fig. 6.10. Each of these points correspond to a measurement or simulation of an instantaneous dynamic $B-H$

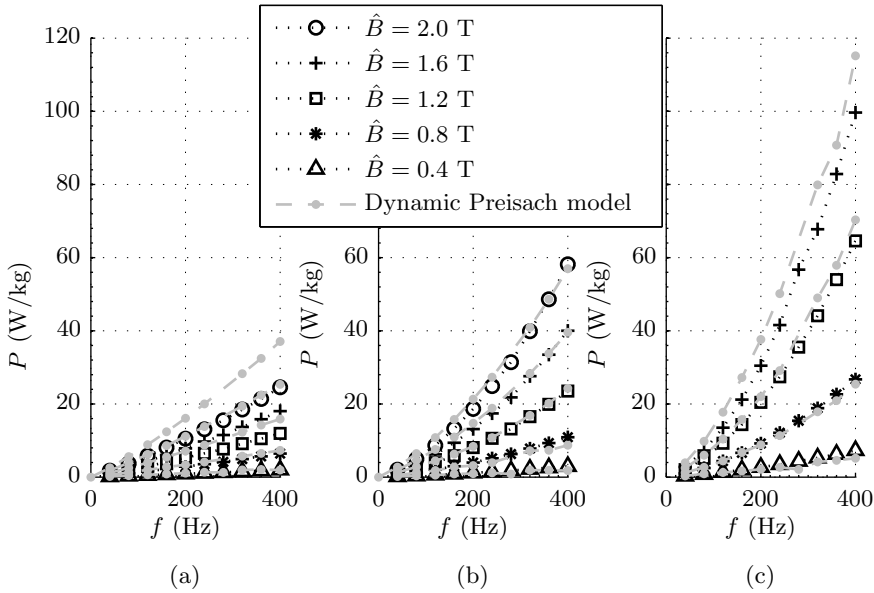


Fig. 6.10: Dynamic magnetic material model combined with the Preisach model compared to measurements with various peak magnetic flux densities on laminated toroids of Vacoflux 50-10 (a), Vacoflux 50-35 (b), and M800-50A (c).

curve.

The dynamic magnetic material model based on the Preisach model, shows good agreement with measurements for the two materials, i.e. Vacoflux 50-35 and M800-50A. A larger discrepancy has been found for the dynamic loss simulation of Vacoflux 50-10, especially for a peak magnetic flux density above 1.2 T. This discrepancy is caused by the relatively large simulation error of the static hysteresis model, which is verified in three steps. Firstly, the relatively large discrepancy of the static hysteresis model for larger loops has already been shown in Figs. 5.19 and 6.1. Secondly, the dynamic losses are relatively small for a 0.10 mm lamination thickness, as shown in Fig. 6.11(a), for an excitation of 40 and 400 Hz. Thirdly, it is shown in Fig. 6.11(b), that the simulated energy losses of the dynamic magnetic material model, increases similarly as the measured losses per cycle. However, a constant offset for each peak flux density value is observed over the full frequency range, which is caused by the static hysteresis model. In other words, besides the constant offset caused by a simulation error of the static hysteresis model, the steepness of the energy loss per cycle with respect to the frequency is similar for the dynamic model and

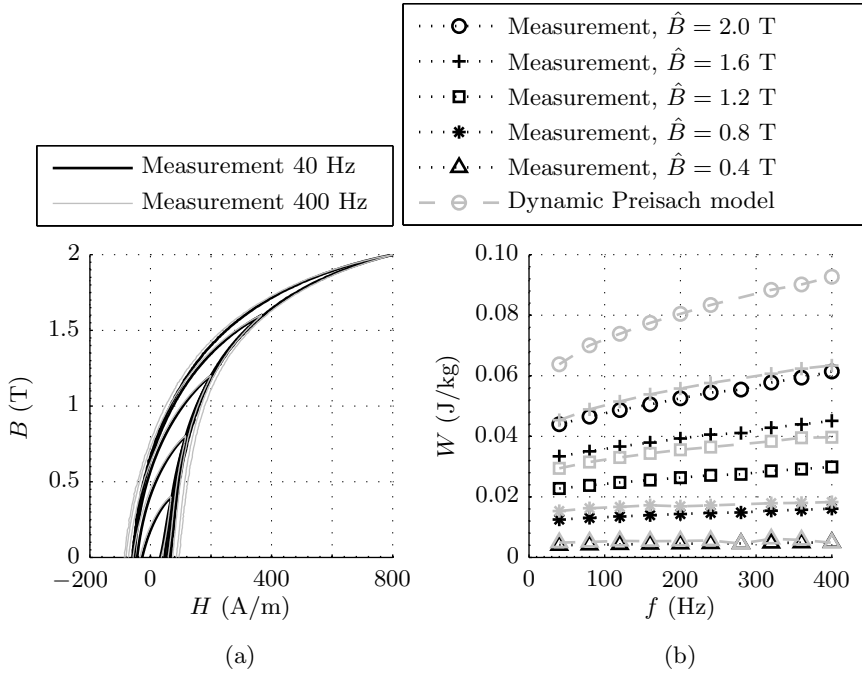


Fig. 6.11: Measured B – H curve at 40 and 400 Hz of Vacoflux 50-10 (a). The modeled dynamic magnetic material energy loss per cycle of Vacoflux 50-10 compared to measurements at for various peak magnetic flux densities (b).

the measured values.

The instantaneous discrepancy between the measured and modeled dynamic losses is also shown in Fig. 6.12 for Vacoflux 50-10, for an excitation frequency of 80, 160, 240 and 320 Hz. The difference of the remanent magnetic flux density and the coercive field strength between the simulation and the measurements at 320 Hz is equal to 39.9 % and 6.1 %, respectively. Hence, the static error of the remanent magnetic flux density is relatively large, whereas the increase of the width of the dynamic B – H loop (H_c) is predicted with a significantly better accuracy.

The dynamic Preisach model shows good agreement with measurements for Vacoflux 50-35, as is shown in Fig. 6.10(b) and Fig. 6.13. The difference of the remanence and the coercivity between the simulation and the measurements at 320 Hz is equal to 8.64 % and 7.44 %, respectively. Furthermore, the dynamic simulation of M800-50A is also in good agreement with measurements, as shown

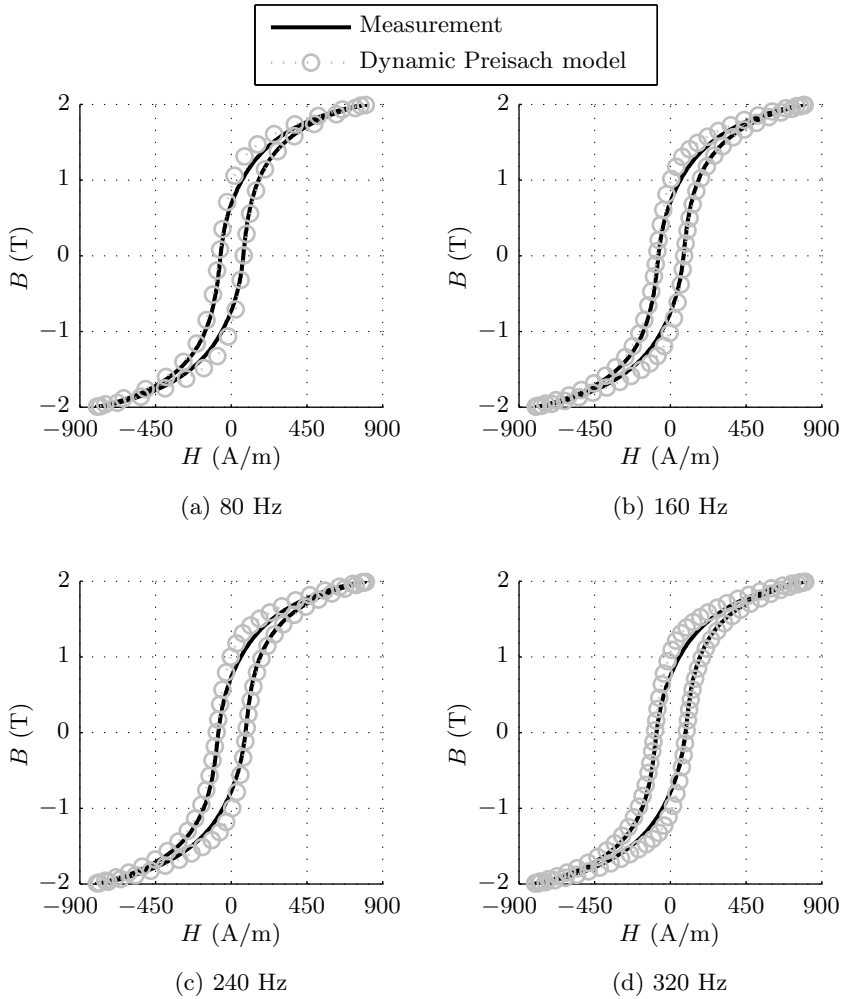


Fig. 6.12: Dynamic magnetic material model combined with the Preisach model compared to measurements on a Vacoflux 50-10 laminated toroid at four excitation frequencies (a)-(d), $f = [80, 160, 240, 320]$ Hz.

for the predicted losses in Fig. 6.10(c). The largest discrepancy of the simulated losses of M800-50A is noticeable for a peak magnetic flux density of 1.6 T in Fig. 6.10(c). This simulation error is larger, because at a magnetic flux density of 1.6 T, the maximum magnetic field strength is approximately 5000 A/m, while the saturation level of the Preisach model is equal to 600 A/m. The instantaneous modeling error of the remanence and coercivity for the 320 Hz excitation, as shown in Fig. 6.14, is equal to 7.14 % and 6.65 %, respectively.

Generally, it can be concluded that the dynamic magnetic material model performs well for a wide range of magnetic materials, ranging from the costly Vacoflux 50 with a high-saturation level, to a commonly applied and significantly less expensive material, M800-50A. The optimized distribution function applied for the Vacoflux 50-10 sample (as obtained in previous chapter), results in a larger discrepancy between the dynamic material model and measurements. For the ring samples of Vacoflux 50-35 and M800-50A the coercive field strength and remanent magnetic flux density are predicted with an accuracy below 10 % for all the simulations.

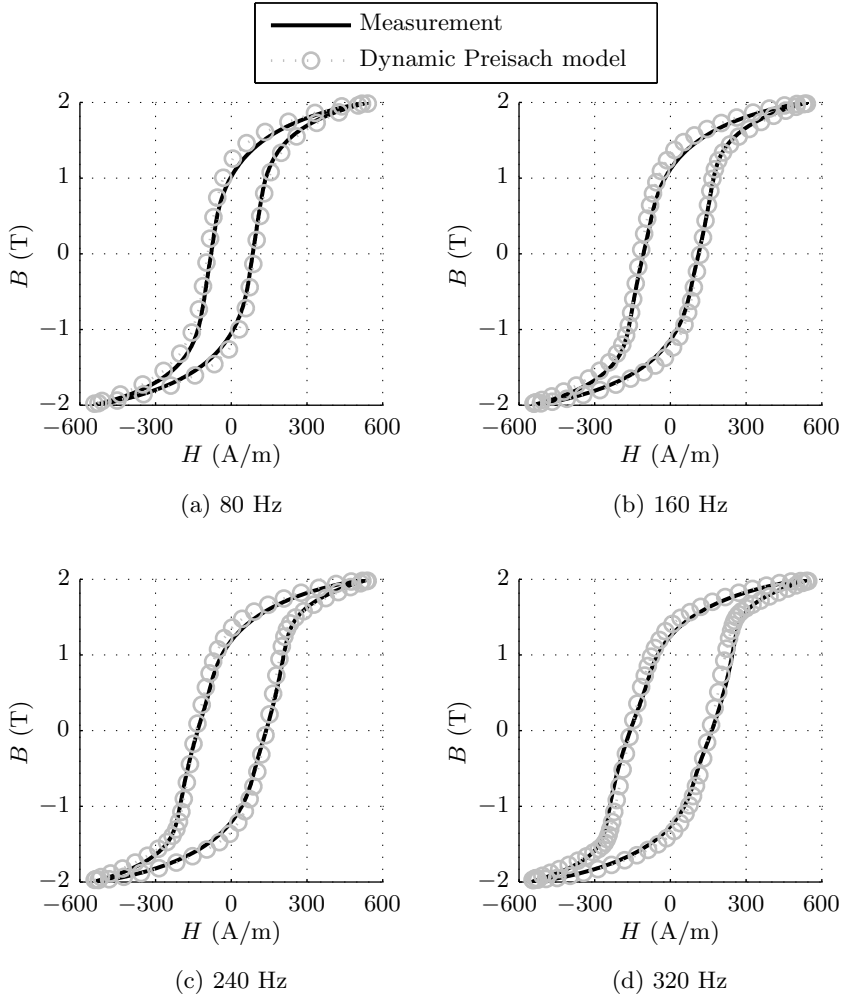


Fig. 6.13: Dynamic magnetic material model combined with the Preisach model compared to measurements on a Vacoflux 50-35 laminated toroid at four excitation frequencies (a)-(d), $f = [80, 160, 240, 320]$ Hz.

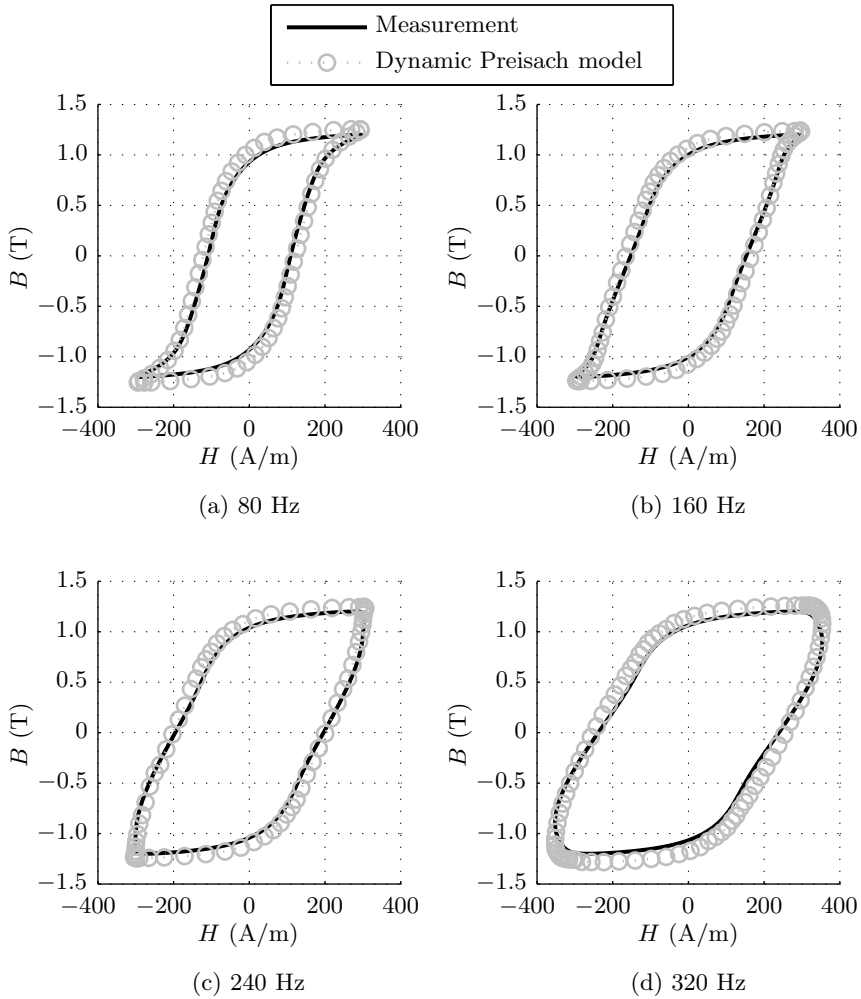


Fig. 6.14: Dynamic magnetic material model combined with the Preisach model compared to measurements on a M800-50A laminated toroid at four excitation frequencies (a)-(d), $f = [80, 160, 240, 320]$ Hz.

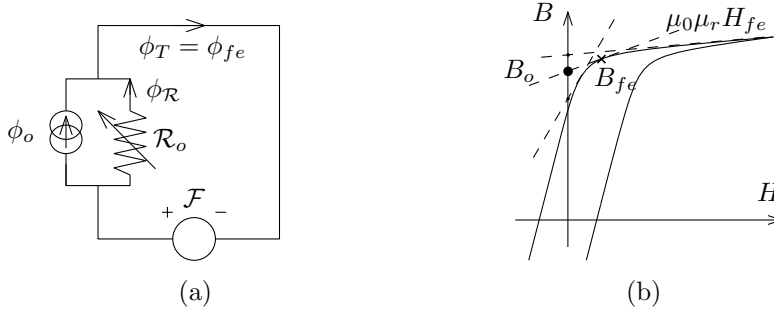


Fig. 6.15: MEC model of a ferromagnetic material including magnetic hysteresis (a), and the $B-H$ curve with the tangents (dashed) in three arbitrary working points (b).

6.4 Hysteresis modeling in reluctance actuators

The modeling of magnetic hysteresis phenomena in reluctance actuators is performed by the combination of three earlier discussed simulation methods. Firstly, the general force of the reluctance actuator is modeled with the magnetic equivalent circuit (MEC) method, as discussed in Section 2.4. Secondly, the static magnetic hysteresis effects, obtained with the Preisach hysteresis model (discussed in Chapter 5), are included in the MEC model. Thirdly, the previously discussed dynamic magnetic material model is included, to predict the instantaneous eddy currents and excess losses. All these three methods have been verified by a comparison to either measurements or FEM simulations. In this section, the combination of these three modeling methods into a MEC is discussed. The experimental verification of this combined model is presented in Chapter 7.

6.4.1 Hysteretic reluctance

In a MEC model, a hysteretic ferromagnetic materials can be modeled as a series connection of an mmf source and a reluctance or a parallel connected flux source with a reluctance. The permanent magnet is modeled by a series connection in Section 2.4. There it is assumed that the mmf source and the reluctance of the permanent magnet are constant, because the permanent magnet is used in its linear regime in the second quadrant of its $B-H$ characteristic. On the contrary, soft-magnetic materials in reluctance actuators utilize the full range of the hysteresis curve from positive to negative saturation. The ferromagnetic material is modeled with a parallel connection of a variable reluctance \mathcal{R}_o and flux source ϕ_o [12], as shown in Fig. 6.15(a).

The magnetic flux density in the iron core B_{fe} is modeled with the static Preisach model (Chapter 5) and/or with the dynamic magnetic material model (6.28). The magnetic flux density is described as [188]

$$B_{fe} = \frac{\phi_{fe}}{A_{fe}} = B_o + \mu_0 \mu_r H_{fe} \quad (6.32)$$

where A_{fe} is the cross-section area of the magnetic material and B_o is the intersection of the tangent, at the working point of the hysteresis curve, with the B -axis at $H = 0$, as shown in Fig. 6.15(b). Hence, the excitation of the flux source and the variable reluctance of the equivalent circuit are both related to the magnetic field strength as given by

$$\phi_o = B_o (H_{fe}) A_{fe} \quad (6.33)$$

$$\mathcal{R}_o = \frac{l_{fe}}{\mu_0 \mu_r (H_{fe}) A_{fe}} \quad (6.34)$$

When rate-dependent effects are modeled in laminated materials, H_{fe} is replaced by the mean magnetic field strength, i.e. $H_{m,fe}$ (6.28). In this section, the magnetic field strength in the ferromagnetic material is described as H_{fe} .

6.4.2 Hysteresis in the MEC model of a reluctance actuator

The hysteresis is incorporated in a MEC model of the pre-biased reluctance actuator as discussed in Section 2.4. The MEC model is extended with a parallel connected variable reluctance and flux source, as shown in Fig. 6.16. The total magnetic flux in the iron is now given by

$$\phi_T = \phi_{fe} = \phi_o + \phi_{\mathcal{R}} \quad (6.35)$$

where ϕ_o and $\phi_{\mathcal{R}}$ are the fluxes through the flux source and the magnetic reluctance, respectively.

The MEC model of the pre-biased E-core (2.43) as presented in Section 2.4, is expressed as

$$Ni + H_c l_{mag} = \frac{\phi_T - B_o}{\mu_0 \mu_{fe}} l_{fe} + \frac{\phi_g}{\mu_0 A_g} l_g + \frac{\phi_T}{\mu_0 \mu_{mag} A_{mag}} l_{mag} \quad (6.36)$$

using H_{fe} from (6.32). This is similarly rewritten as in (2.44)

$$Ni + H_c l_{mag} = \phi_T (\mathcal{R}_o + \mathcal{R}_{mag} + k_\phi \mathcal{R}_g) - \frac{B_o l_{fe}}{\mu_0 \mu_{fe}} \quad (6.37)$$

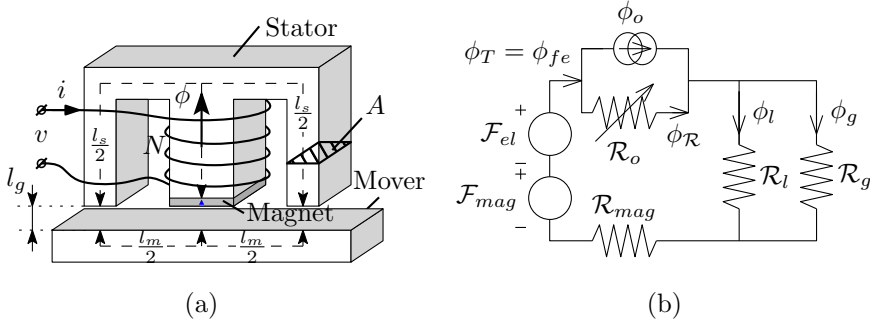


Fig. 6.16: Schematic view of a pre-biased E-core actuator (a), and the corresponding MEC model (b).

Using (6.32) and the total flux (2.45), the magnetic field strength in the iron is obtained as

$$H_{fe} = \frac{Ni + H_c l_{mag} + \frac{B_m l_{fe}}{\mu_0 \mu_{fe}}}{\mu_0 \mu_{fe} A_{fe} (\mathcal{R}_o + \mathcal{R}_{mag} + k_\phi \mathcal{R}_g)} - \frac{B_o}{\mu_0 \mu_{fe}} \quad (6.38)$$

Due to the dependency of the flux density $B_o(H_{fe})$ (6.33) and variable reluctance $\mathcal{R}_o(H_{fe})$ (6.34) on the magnetic field strength of the ferromagnetic core, the magnetic field strength is not analytically defined for a given input current. Therefore, an extra step is added to the simulation procedure to obtain the instantaneous magnetic field strength with the combined MEC model and the dynamic magnetic material model.

6.4.3 Simulation procedure

The simulation procedure to model a reluctance actuator including (dynamic) magnetic hysteresis effects, is an extension of the procedures used for the Preisach model as shown in Fig. 5.18 and the dynamic material model in Fig. 6.9. The simulation procedure consists of two iterative processes as illustrated in Fig. 6.17. The evaluated dynamic magnetic material model, as described in Section 6.3, and the interaction of the variable reluctance and the magnetic flux source of the MEC model, are solved iteratively. For stability reasons, the MEC model is iteratively solved first for the static Preisach model (which is included by a check on variable q) and subsequently the dynamic magnetic material effects are included. Similarly as in Fig. 6.9, convergence has been reached when the relative permeability is within a difference of $\epsilon = 1 \cdot 10^{-3}$, for three subsequent iterative steps.

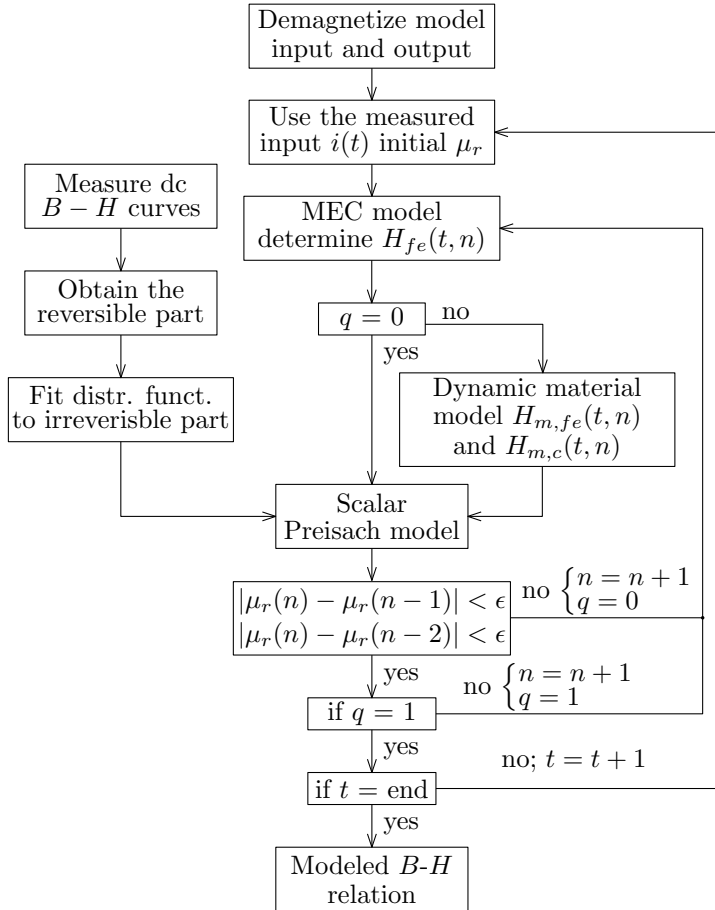


Fig. 6.17: Procedure to obtain the $B-H$ characteristics in the ferromagnetic material of the E-core reluctance actuator under an ac excitation.

The dynamic magnetic material effects are incorporated for laminated materials by the inclusion of $H_{m,fe}(t)$ from (6.28), while for the pre-biased E-core the eddy currents in the permanent magnet are incorporated with, $H_{m,c}(t)$, as given in (6.29). Finally, the force is obtained with the Maxwell stress tensor (MST) method, as explained in Section 2.3.2. The MST method is applied because it is based on the magnetic flux density in the surrounding air, which already contain the magnetic hysteresis effects as discussed in previous analysis. Additionally, it must be noted that the virtual work (VW) method, as explained in Section 2.3.1, is not applicable for obtaining the hysteretic force, as it is only valid for a lossless system.

6.5 Finite element method

Besides dynamic magnetic material phenomena, also static hysteresis is evaluated for the finite element method (FEM) in this section. Both, the static and dynamic simulations are performed with the 3d FEM (Opera 16.0) [49]. The 2d FEM has also been applied in Section 2.7 to simulate the static magnetic hysteresis in various E-core reluctance actuators, and the theory about the incorporation of magnetic hysteresis in the FEM has been introduced in Section 4.5.

The inclusion of dynamic magnetic material effects in a laminated structure is discussed. Furthermore, the FEM is experimentally verified by a comparison to static and dynamic measurements on a laminated toroid of M800-50A. Additionally, the simulation of (pre-biased) E-core reluctance actuators is discussed, of which the results on the prediction of the hysteresis in the force are compared to measurements in the following chapter.

6.5.1 Laminated structures with the 3d-FEM

To include eddy current effects in laminated magnetic materials in the FEM, it is necessary to use the 3d FEM. The simulation of individual laminations in a laminated stack, to include eddy currents in 3d FEM, simulations is rather challenging. Especially, the mesh creation for laminations with non-conductive layers in between is difficult, due to the two orders of magnitude difference between the lamination thickness and the isolating layer. Up to now, it is impossible to simulate a whole actuator with e.g. 60 individual laminations, for two reasons. Firstly, the number of mesh elements exceeds the software capabilities due to two orders of magnitude difference between the lamination thickness and the actuator dimensions. Secondly, if the mesh could be created the simulation time including dynamic hysteresis effects would at least be in the order of weeks for a single sinusoidal excitation. To be able to simulate

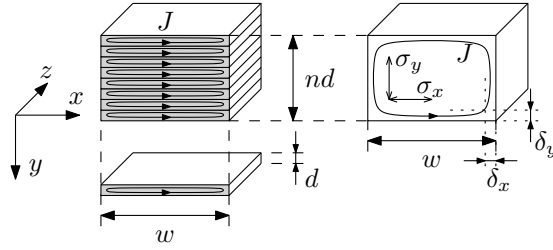


Fig. 6.18: Eddy currents in a laminated iron core and the equivalent model with an anisotropic conductivity.

eddy currents in laminated materials, an anisotropic equivalent conductivity [100] is applied for the magnetic material in the FEM simulations.

The anisotropic conductivity is derived from a lumped resistor model, which is used to obtain an equivalent conductivity in the cross-section of the ferromagnetic material. The resistors are obtained using the skin depth (6.31). The eddy currents parallel to the width and depth of the laminated material are directed in the x - and z -direction, respectively, as indicated in Fig. 6.18. The skin depth is given by

$$\delta_y = \sqrt{\frac{2}{2\pi f \mu \sigma_{x,z}}} \quad \text{and} \quad \delta_{x,z} = \sqrt{\frac{2}{2\pi f \mu \sigma_y}} \quad (6.39)$$

where y is the direction normal to the sheet, and x and z are in the plane of the sheet, as illustrated in Fig. 6.18. The specified bulk conductivity is equal to $\sigma_x = \sigma_z$, and the equivalent conductivity normal to the sheet is equal to

$$\sigma_y = \sigma_{x,z} \left(\frac{nd - 2\delta_y}{n(w + d - 2\delta_y) - w} \right)^2 \quad (6.40)$$

where d is the lamination thickness, w is the width of the sheet and n is equal to the number of sheets.

6.5.2 Experimental verification

The FEM is experimentally verified for the static simulation of minor hysteresis loops, because the hysteretic material properties applied to the FEM software, are only based on the input of the left part of the major hysteresis loop. The software uses this tabulated data to create a hysteresis model based on transplantation [176], as earlier discussed in Section 4.5.

The 3d FEM is evaluated by a comparison to dc-measurements, as shown in Fig. 6.19(a), for a maximum magnetic field strength of, $H_{max} = [50, 100, 250, 500]$

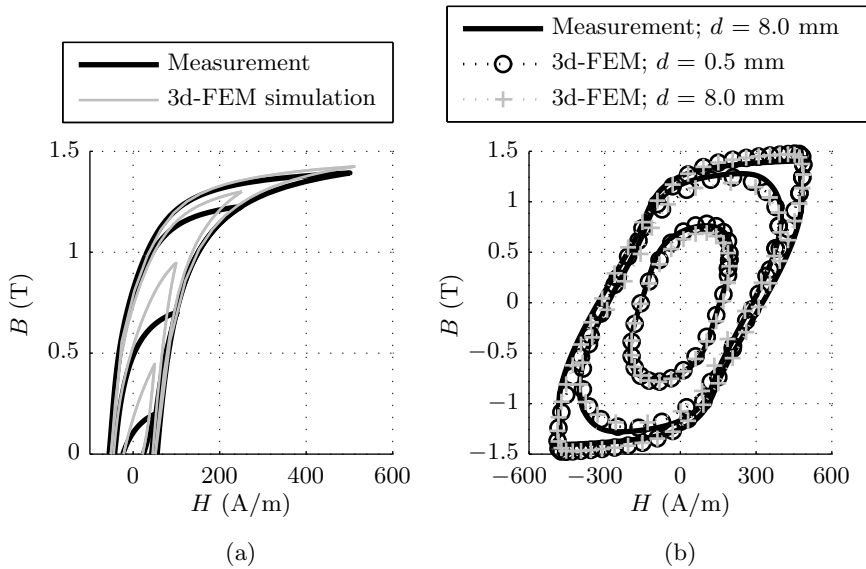


Fig. 6.19: Comparison of the simulated $B-H$ curves with the 3d FEM and the measured $B-H$ curves of M800-50A, for a dc-excitation with a maximum magnetic field strength of $H_{max} = [50, 100, 250, 500]$ A/m (a), and for a 400 Hz excitation with $H_{max} = [200, 400, 500]$ A/m (b).

A/m. It is shown that the discrepancy increases for the modeling of minor loops with smaller input extrema. This is a direct result of the limited information of the soft-magnetic material used by the software, as the hysteresis model is only based on the major hysteresis loop.

The simulation of dynamic magnetic material effects with the anisotropic conductivity is verified by a comparison between measurements on a toroid of M800-50A and simulations of two toroids with a 400 Hz excitation. The first simulated toroidal structure consists of a single lamination of 0.5 mm with a normal isotropic conductivity. The second simulated toroid consists of a non-laminated (solid) toroid with the size of the real sample, but with an anisotropic conductivity as given by (6.40). The comparison, between flux measurements on a closed toroid and the flux density obtained with both 3d FEM analyses, is shown in Fig. 6.19(b). Both simulation results are in good agreement with the measurements. The coercive field strength and remanent magnetic flux density are predicted within 10% for both simulation methods, which validates the ability to simulate laminated structures with an anisotropic conductivity.

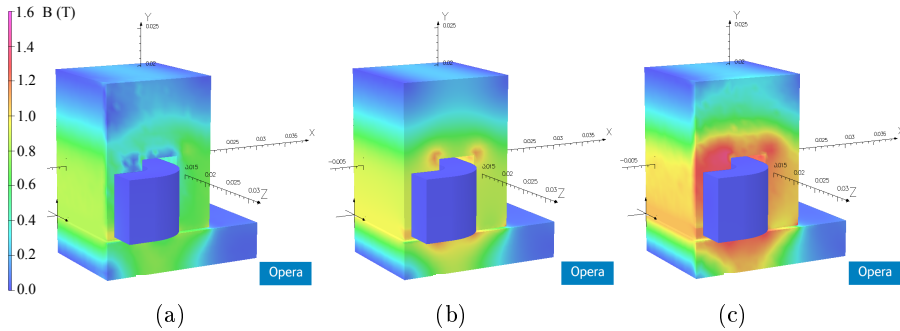


Fig. 6.20: The magnetic flux density distribution of a 3d FEM simulation of a quarter pre-biased E-core actuator with a 320 Hz excitation. For minimum current, zero current and maximum current value $[-0.7, 0.0, 0.7]$ A, for (a)-(c), respectively.

A disadvantage of this dynamic magnetic material modeling method with the 3d FEM is the inability of applying arbitrary inputs, because the anisotropic conductivity and skin depth are only determined for a fixed frequency.

6.5.3 Simulation of reluctance actuators

Besides the dynamic analysis of laminated magnetic structures, the 3d FEM is necessary to simulate the actuator topology. Especially, the airgap fringing and leakage effects are simulated using the FEM with a high-accuracy.

In Fig. 6.20 the magnetic flux density distribution of a quarter of a pre-biased E-core reluctance actuator is shown. This actuator corresponds to the pre-biased E-core reluctance actuator, which is experimentally verified in Section 7.2. The symmetry of the structure when the stator and mover are aligned, reduces the problem by a factor four, because it is sufficient to simulate only a quarter of the E-core actuator when only the position variation in the actuation direction is considered. A continuous tangential magnetic flux density is applied at the boundaries in the planes $x = 0$ and $z = 0$ to include symmetry.

The magnetic flux densities for a 320 Hz current excitation of the E-core actuator, as shown in Fig. 6.20(a)-(c), correspond with a current value of -0.7 , 0.0 and 0.7 A, respectively. It can be noted that a negative current decreases the magnetic flux density, whereas the magnetic flux density is increased for a positive current. In Fig. 6.20(b) the magnetic flux density for zero current is shown, which clearly shows the pre-biasing of the permanent magnet on the middle tooth. The nonuniform magnetic field distribution in Fig. 6.20(a) and (c), is caused by eddy currents at a 320 Hz excitation frequency, which decreases the

magnetic flux density towards the center of the actuator core, as described in Section 6.3. The accuracy of the dynamic 3d FEM simulations is compared to measurements on various E-core reluctance actuators in Chapter 7.

6.6 Complex impedance method

The dynamic complex impedance method is comparable to the static complex impedance method, as discussed in Section 4.6. The dynamic complex impedance method incorporates the dynamic behavior by including the phase delay between B and H . The amplitude and angle between the measured voltage (magnetic flux density) and the applied current (magnetic field strength) determine the permeability of the complex impedance method.

In this thesis, the phase delay of the complex permeability is stored in a look-up table for the full frequency range at which the model is applied. The phase delay is obtained from measurements and inserted in the complex permeability as given in (4.4). Hence, the complex impedance method is not a predictive method. Moreover, the model as such, cannot describe random actuator behavior, or excitations that include more than one frequency.

6.6.1 Experimental verification

The complex impedance model is compared to measurements on a laminated toroid of M800-50A, for an excitation frequency of 100 Hz and 400 Hz, as shown in Fig. 6.21(a) and (b), respectively. The simulation results show a large discrepancy for the 100 Hz excitation, which is caused by the applied non-sinusoidal magnetic field strength. A sinusoidal magnetic field strength would result in an elliptic shaped $B-H$ relation, but the measurement setup is controlled to a sinusoidal magnetic flux density, as discussed in Section 3.5, which results in the sharp loops for lower frequencies. The simulation of the magnetic flux density at a 400 Hz excitation shows that the complex impedance method performs significantly better for higher frequencies. In Fig. 6.21(b) it is shown, that the discrepancy of the complex impedance method is within 6 %, for both the remanent magnetic flux density and the coercive field strength.

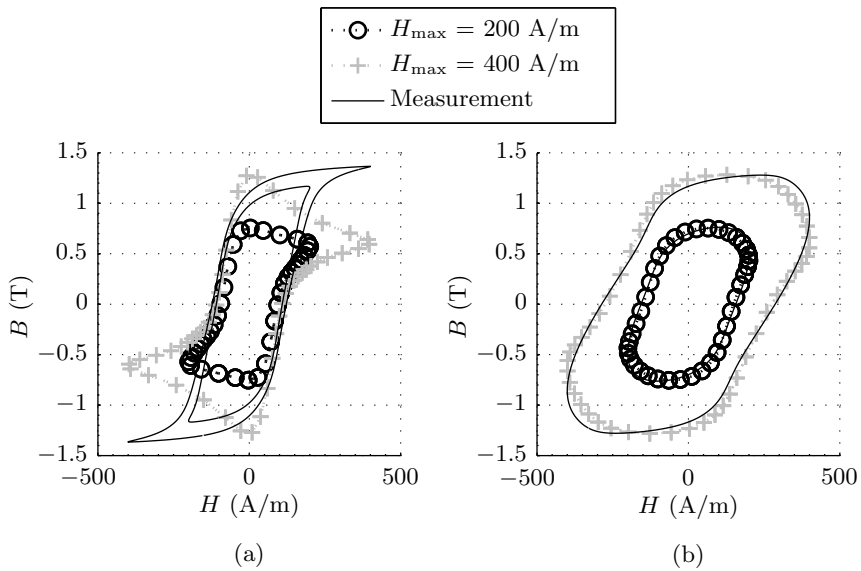


Fig. 6.21: The modeled magnetic hysteresis with the complex impedance method compared to measurements (M800-50A) for a sinusoidal voltage excitation at a frequency of 100 Hz (a), and at a frequency of 400 Hz (b).

6.6.2 Simulation of reluctance actuators

For the modeling of dynamic hysteresis effects in reluctance actuators with the complex impedance model the phase delay between the current and the force is obtained from measurements, instead of the phase delay of the magnetic flux density and the magnetic field strength. This phase delay is directly applied to a non-hysteretic MEC model of the actuator. The major difference between a closed toroid and reluctance actuators is the airgap, which is dominant in actuators. Hence, the percentage of magnetic hysteresis in the current-force characteristic is much lower than for the magnetic constitutive relation of materials (as shown in Fig. 6.21).

Furthermore, reluctance actuators are usually not continuously used up to its saturation magnetization, which results in a relatively elliptic hysteresis in the actuator core. Generally, reluctance actuators are designed for a peak-force that is much higher than the nominal force for two reasons. Firstly, the peak-force is physically restricted by the saturation of the ferromagnetic material. Secondly, the nominal temperature of the actuator limits the rms current for a specific volume and the efficiency of reluctance actuators decreases rapidly when saturation is approached. Based on these assumptions, the complex impedance method could be more applicable for reluctance actuators than for modeling magnetic materials. The accuracy of the simulation of reluctance actuators with the complex impedance model is experimentally verified by a comparison to measurements on various E-core reluctance actuators in Chapter 7.

6.7 Conclusions

The statistical loss theory is addressed and compared to measurements under various dc- and ac-excitations. Besides the statistical approach, the losses of the instantaneous $B-H$ curves are simulated with the Preisach model and compared to dc-measurements on three different material samples, i.e. Vacoflux 50-10, Vacoflux 50-35 and M800-50A. The evaluated soft-magnetic materials range from negligible dynamic losses (Vacoflux 50-10) to significant dynamic losses (M800-50A).

Besides the static hysteresis losses, the instantaneous magnetic fields are modeled for a wide frequency range of $40 \leq f \leq 400$ Hz. The dynamic simulations are based on the field separation method derived from the statistical loss theory, which incorporates the classical field and excess field components. The derivation of the classical field (due to eddy currents) in ferromagnetic materials is described and employed for both, laminated materials and solid permanent magnets. The simulation method is experimentally verified in the frequency domain by a comparison to measurements. Additionally, the instantaneous

magnetic fields are simulated and compared to measurements for several frequencies. The coercive field strength is predicted with a maximum discrepancy of 10 % for all the evaluated material samples. The remanent magnetic flux density is also modeled with an error below 10 % for Vacoflux 50-35 and M800-50A, whereas the simulated remanent magnetic flux density for Vacoflux 50-10 shows an error of 40 %, due to a discrepancy in the static hysteresis model.

The 3d FEM is examined on the prediction of the magnetic flux density for dc-excitations with various amplitudes, and for an excitation frequency of 400 Hz for the M800-50A ring sample. The 3d FEM shows good agreement with the measurements at 400 Hz, whereas the modeling of static minor loops shows a relatively large discrepancy. The complex impedance method is experimentally verified by a comparison to measurements on the same M800-50A ring sample at an excitation frequency of 100 and 400 Hz. The complex impedance method only shows similar agreement with measurements at high frequencies when both, the waveforms of the magnetic flux density and magnetic field strength approach a sine wave. The dynamic 3d FEM and the complex impedance method are only applicable for a fixed excitation frequency.

Furthermore, the applicability for reluctance actuators is discussed for all three modeling methods, which are examined on the prediction of the magnetic hysteresis in the force in the following chapter.

Experimental verification

This chapter concerns the experimental verification of the three modeling methods, as discussed in previous chapters, which have been applied to determine the force of three reluctance actuators by incorporation of magnetic hysteresis phenomena. Experimental verifications of magnetic hysteresis models for determining the hysteretic force of reluctance actuators have been earlier presented in [129, 178, 220, 224, 225]. In [129], a parametric hysteresis operator has been proposed for control of reluctance actuators, which has been obtained from the measured current-force characteristic. In [178], a static Preisach model has been applied for an E-core actuator manufactured of soft-magnetic powder material (Anchor Steel TC-80). Hence, the dynamic effects are neglected for the open-loop actuator model. In [220], magnetic hysteresis effects are modeled for an electromagnet with the Jiles-Atherton model and the static Preisach model. The inverse of both models is evaluated for the feedforward control of the electromagnet for low-frequency excitations. It is concluded that, “the Preisach model works more smoothly within the control framework and performs more robust for the given task.” In [224], a discrete Preisach model implementation is proposed for the control of an electromagnet, which is extended to an airgap-dependent model in [225]. All these implementations of hysteresis models for reluctance actuators are discussed from a control point of view, based on measured actuator performance. None of the methods describe the combination of electromagnetic actuator models and the ferromagnetic material phenomena, as presented in this thesis.

Three modeling methods are experimentally verified by force measurements on three E-core reluctance actuators. The three presented modeling methods are

the dynamic magnetic material model combined with the generalized Preisach model and the MEC model, the 3d FEM, and the complex impedance method. The combined Preisach model with the MEC model is verified for all the measurements. It should be noted that this modeling method only incorporates static flux density measurements of the considered ferromagnetic materials as model input for the simulation of the instantaneous force of the three reluctance actuators. The complex impedance model is only applicable for sinusoidal excitations, and the 3d FEM is only examined for the dynamic analysis of the two silicon-iron reluctance actuators.

One of the E-core reluctance actuators is manufactured of CoFe (Vacoflux 50-10), which has a high saturation magnetization, as discussed in Section 3.4. The other two E-core reluctance actuators are manufactured of SiFe (M800-50A). One of both SiFe actuators is pre-biased with a permanent magnet, which significantly enhances the force range. Each of the actuators is discussed separately in the following sections. The force measurements are performed on two measurement instruments which are discussed in combination with the specific actuator(s) they are applied for. The contributions of this chapter have been presented in [269, 274–276, 278].

7.1 E-core actuator of cobalt-iron

One of the E-core reluctance actuators is manufactured of a laminated stack of cobalt-iron (CoFe). More specifically, the CoFe is Vacoflux 50 with a lamination thickness of 0.10 mm. In this thesis, the material is called Vacoflux 50-10, which has a specified saturation magnetization of 2.35 T, as given in Table 3.1. The dynamic material losses are negligible because of the thin laminations, which has been experimentally verified by measurements on a ring sample in Chapter 6. Therefore, the CoFe E-core actuator is only examined for low-frequency excitations. Additionally, various force profiles are evaluated to verify the generalized Preisach model on the accuracy of the prediction of minor loops and to investigate the history dependency of the force of reluctance actuators. The measurement instrument has a high accuracy and a large force range and is further discussed in next section.

The examined CoFe E-core reluctance actuator is shown in Fig. 7.1. The stator and mover are embedded in a non-magnetic stainless steel fixture, which can be mounted to the measurement system. The two outer cables (1 and 3) are internally connected to the actuator coils, which can be separately excited to compensate for torque disturbances. Nevertheless, in this work both coils are connected in series. The cable in the middle (2) is connected to a thermal sensor to monitor the actuator temperature during the measurements.

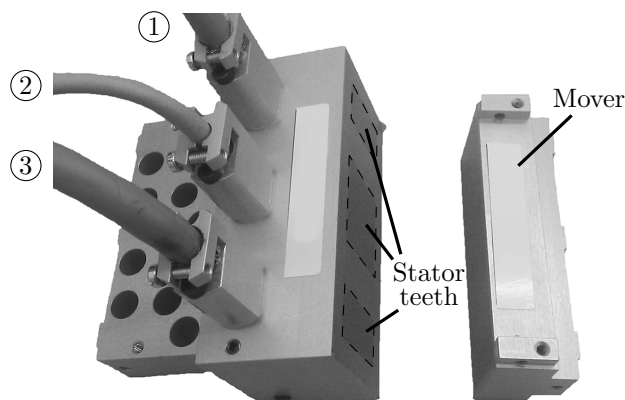


Fig. 7.1: A photo of the CoFe (Vacoflux 50-10) E-core reluctance actuator.

7.1.1 Measurement instrument

A photo of the measurement system, used to obtain the force of the CoFe reluctance actuator, is shown in Fig. 7.2(a) and a schematic illustration of the most important parts is shown in Fig. 7.2(b). This measurement system, also called actuator test-rig, measures the force of the actuator in one degree of freedom (1-DoF) only. The measurement system consists of two masses of approximately 5 kg each, which are supported by air-bearings. One is called the long-stroke mass and the other the short-stroke mass. The long-stroke mass represents the disturbance of a long-stroke actuator stage of a semiconductor lithography system, as discussed in Chapter 1. The E-core reluctance actuator functions as an unidirectional magnetic bearing between the long-stroke and short-stroke actuator stage.

The measurement instrument positions the masses by two thoroughly identified linear voice-coil actuators. When both masses are kept in position, the forces produced by the voice-coil actuators are identical to the force produced by the E-core actuator under test. The system is controlled with a position feedback controller using nanometer accurate optical encoders. The feedback controller of the measurement system has a sample frequency of 8.2 kHz. Additionally, a non-hysteretic, sixth-order, polynomial fit of the measured force of the E-core reluctance actuator is applied as feedforward force input for the voice-coil actuators.

The position variation (tracking error) of both masses is monitored during the measurement, which corresponds with the airgap variation of the reluctance actuator under test. The measured force of the E-core actuator is post-processed

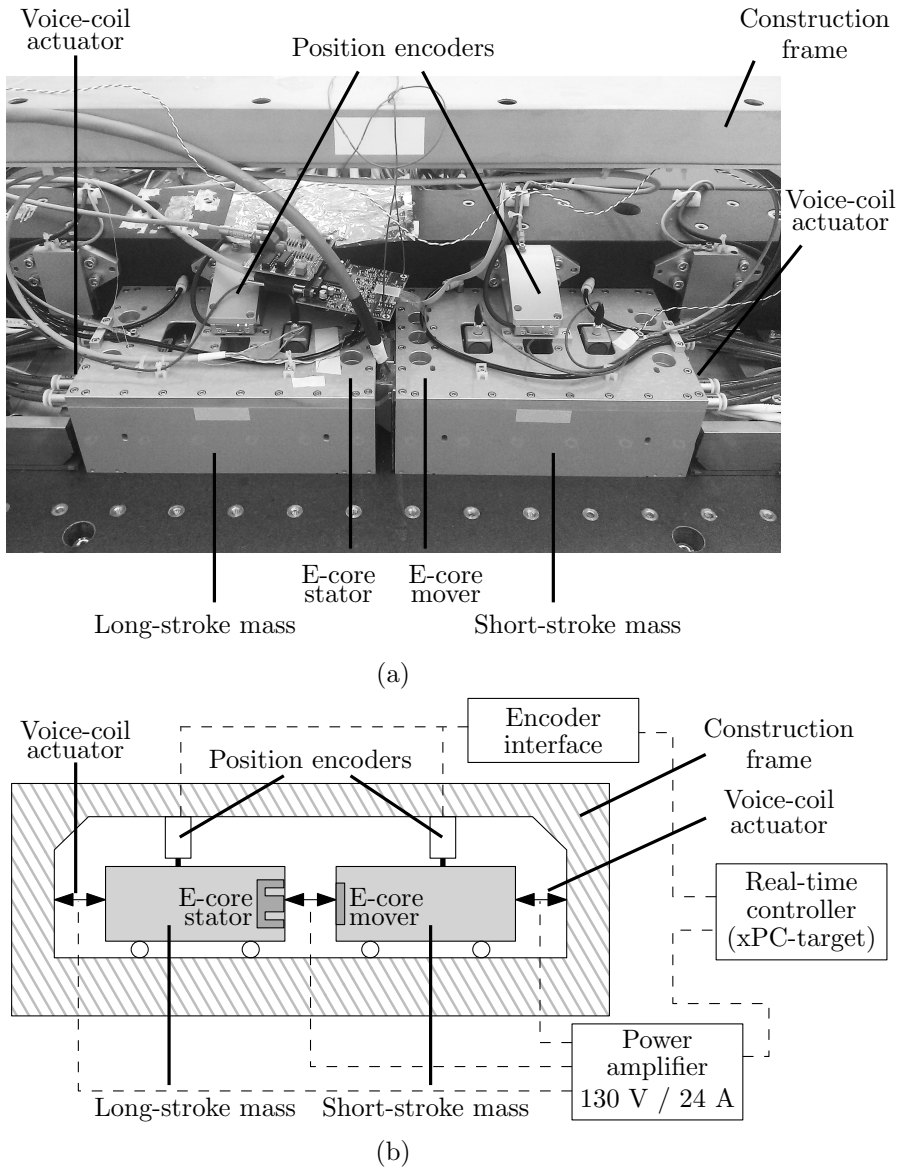


Fig. 7.2: The 1-DoF actuator test rig applied for force measurements of the CoFe E-core actuator, a photo (a), and an illustration (b), as also shown in [130].

to compensate for the measured airgap variation. The force difference due to a position variation is derived from the reluctance force obtained with the virtual work method (Section 2.3) for the magnetically linear case, as given in (2.24). By taking the derivative with respect to the airgap length, l_g , the force error of the measured force, $F_{z,meas}$, is obtained as

$$dF_z = -2 \frac{F_{z,meas}}{l_g} dl_g \quad (7.1)$$

and hence, the reluctance force with tracking error compensation is obtained as

$$F_z = F_{z,meas} \left(1 - \frac{2}{l_g} dl_g \right) \quad (7.2)$$

where dl_g is the measured tracking error.

Another measurement inaccuracy is introduced by the temperature dependent elongation of the CoFe stator, which is included in the model to correct for minor airgap deviations. The elongation coefficient of Vacoflux 50 is given as $\alpha_L = 11 \cdot 10^{-6} \text{ K}^{-1}$, which is used to obtain the elongation of the stator teeth, ΔL , as

$$\Delta L = \alpha_L \Delta T l \quad (7.3)$$

where $\Delta T = T_{core} - T_0$ and l is the length of the material, which is equal to the tooth length of the E-core actuator in this case. T_{core} is the temperature of the stator of the actuator and T_0 is the room temperature, which is kept constant at 22°C in the measurement environment. For example, at an airgap length of 0.5 mm, a temperature difference of 10°C results in an elongation of approximately 10 μm , which corresponds with a force difference of 4.5 %.

7.1.2 Simulation results of the cobalt-iron E-core actuator

Three different current excitations are applied to the CoFe E-core reluctance actuator, i.e. a 1 Hz sinusoidal signal, an arbitrary sequence with a period of 1 second, and a current excitation that shows the dependency of the hysteresis in the reluctance force on the history of the current excitation. The first two measurements are performed at a practically minimum airgap of 0.5 mm to maximize the hysteretic phenomena in the soft-magnetic material and, hence, also in the reluctance force. The third force measurement is performed at an airgap of 0.8 mm.

Each modeling method is evaluated on the prediction of the hysteresis in the reluctance force in the remainder of this chapter. The models are judged on

two aspects for the sinusoidal excitations. Firstly, the relative error of the force is examined, given by

$$\Delta F = \frac{\max(F_{meas} - F_{model})}{\max(F_{meas}) - \min(F_{meas})} \cdot 100\% \quad (7.4)$$

which is the percentage of the maximum instantaneous difference between the measured force, F_{meas} , and modeled force, F_{model} , with respect to the measured force range.

Secondly, the prediction of the amount of magnetic hysteresis in the force is evaluated by the analysis of the loop-eye present in the force, similarly as in Section 2.7. The hysteresis in the force is graphically shown by the subtraction of the non-hysteretic force obtained with the proposed analytical MEC model of the reluctance actuator. This results in loops for which the maximum opening is called the loop-eye, and corresponds with the error of the force when it is predicted with a non-hysteretic actuator model. The relative discrepancy between the measured loop-eye, eye_{meas} , and the modeled height of the loop-eye, eye_{model} , is evaluated and is obtained as

$$\Delta_{eye} = \frac{eye_{meas} - eye_{model}}{eye_{meas}} \cdot 100\% \quad (7.5)$$

which is a measure for the discrepancy of the modeled hysteresis in the force with respect to the measured amount of magnetic hysteresis in the force.

The simulation results are subsequently compared to measurements for the three current excitations applied to the CoFe E-core reluctance actuator. The discrepancies of the simulation results are discussed afterwards.

Sinusoidal current excitation

The sinusoidal current-force relation is shown in Fig. 7.3(a). The measured current force relation is compared to the static Preisach model implementation combined with the magnetic equivalent circuit (MEC) method. Additionally, a non-hysteretic MEC model is shown, which is also applied for the complex impedance model. The magnetic hysteresis in the reluctance force is visualized by subtracting the non-hysteretic MEC model from the measured and modeled force. The resulting loop-eyes, representing the instantaneous magnetic hysteresis in the reluctance force, are shown in Fig. 7.3(b). The evaluated loop-eye is indicated for the measured hysteretic force in Fig. 7.3(b).

The relative accuracy of the simulated hysteresis in the reluctance force is expressed by the maximum discrepancy of the actuator force and a loop-eye error, which are $\Delta F = 0.42\%$ and $\Delta_{eye} = -91.3\%$, respectively, for the Preisach

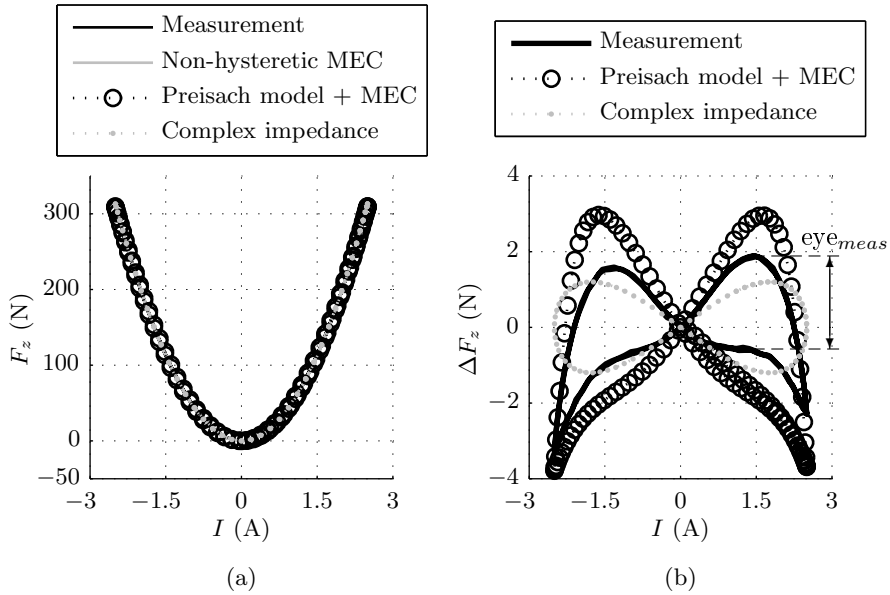


Fig. 7.3: Comparison of the simulated and measured force of the CoFe E-core reluctance actuator for a 1 Hz sinusoidal current excitation at an airgap of 0.50 mm (a), and the corresponding force error due to magnetic hysteresis (b).

models, as given in Table 7.1. The negative loop-eye error means that the hysteresis in the reluctance force is overestimated.

The relative force error of the complex impedance model is related to the non-linearity of the magnetic material in the actuator. The loop-eye error is relatively low, $\Delta_{\text{eye}} = 7.3\%$, because this is obtained from the measured phase delay between the squared current and the force.

It can be obtained from Fig. 7.3(b), that the magnetic permeability decreases for higher currents resulting in the tips of the loop-eye. The non-hysteretic actuator model and, hence, also the complex impedance model do not incorporate any nonlinear material properties, whereas the Preisach model does incorporate the nonlinear and hysteretic material properties. Therefore, the Preisach model shows a similar shape of the hysteresis in the force.

Table 7.1: Discrepancy between the simulation methods and the force measurements on the CoFe E-core actuator for a 1 Hz sinusoidal excitation.

| Method | ΔF (%) | Δ_{eye} (%) |
|----------------------|----------------|---------------------------|
| Preisach model + MEC | 0.42 | -91.3 |
| Complex impedance | 0.73 | 7.3 |

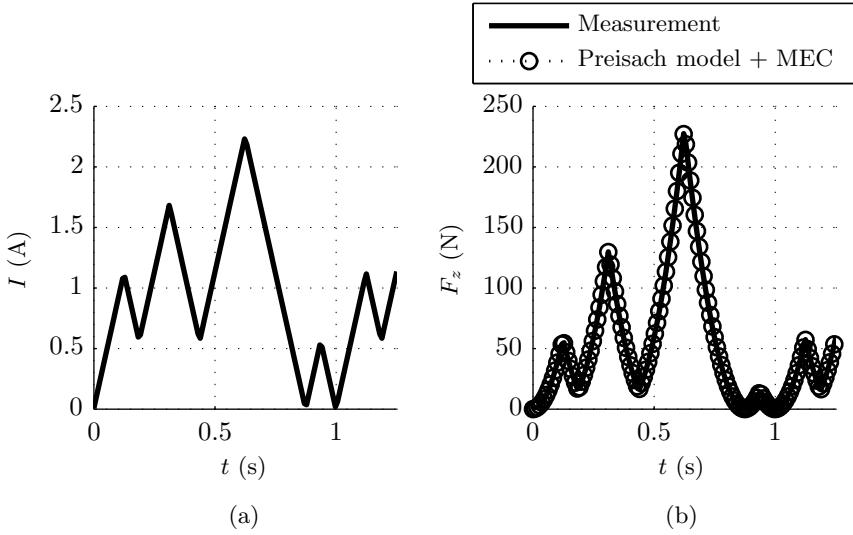


Fig. 7.4: The applied saw-tooth current excitation (a), and the corresponding measured and simulated force (b), at an airgap of 0.50 mm.

Arbitrary current excitation

Besides the sinusoidal current excitation, a more arbitrary excitation is applied to the CoFe E-core reluctance actuator. A saw-tooth-shaped input current is applied, as shown in Fig. 7.4(a). This saw-tooth current is applied to evaluate the simulation of minor hysteresis loops in the force. This saw-tooth excitation is periodically applied with a period of one second. The measured and simulated force are shown in Fig. 7.4(b). In contradiction to the sinusoidal excitation, only a positive current is applied and, hence, only the upper half of the $B-H$ curve of the magnetic material is used.

Similar to the analysis of the sinusoidal excitation, the non-hysteretic actuator model is subtracted from both the measured force and the modeled force, as

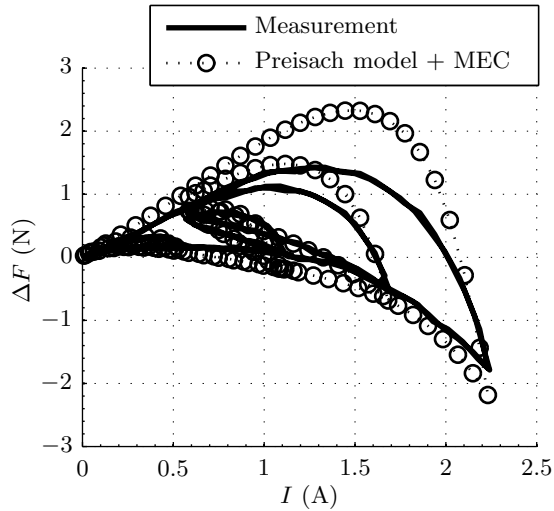


Fig. 7.5: Comparison of the simulated and measured force error due to magnetic hysteresis for a saw-tooth current excitation with a period of one second, for the CoFe E-core reluctance actuator at an airgap of 0.50 mm.

shown in Fig. 7.5. This figure clearly shows the similarity between the measured hysteresis in the force and the simulated force with the combined Preisach model and MEC model. Equivalently to the results of the sinusoidal excitation, the hysteresis in the force is overestimated with a maximum discrepancy of 1 N, which is caused by the same reasons given previously. The maximum absolute force error is 0.43 % at a current excitation of approximately 1.5 A.

History dependency of the force

The reluctance actuator modeling method including magnetic hysteresis is also experimentally verified for the analysis of the history dependency of the reluctance force of the CoFe E-core actuator. The excitation current of the E-core actuator is chosen such that a minor loop is formed due to a sinusoidal current with an amplitude of 0.5 A and an offset of 1.5 A. This minor loop is formed after a peak excitation of 3.5 A. Subsequently, the same sinusoidal current input with offset is applied after a negative peak current of minus 3.5 A, as shown in Fig. 7.6(a). The corresponding measured and simulated force are shown in Fig. 7.6(b). A distinction is made between the so called decreasing branch and the increasing branch, which correspond with the current input decreasing from the positive peak value to the negative one, and from the negative to the

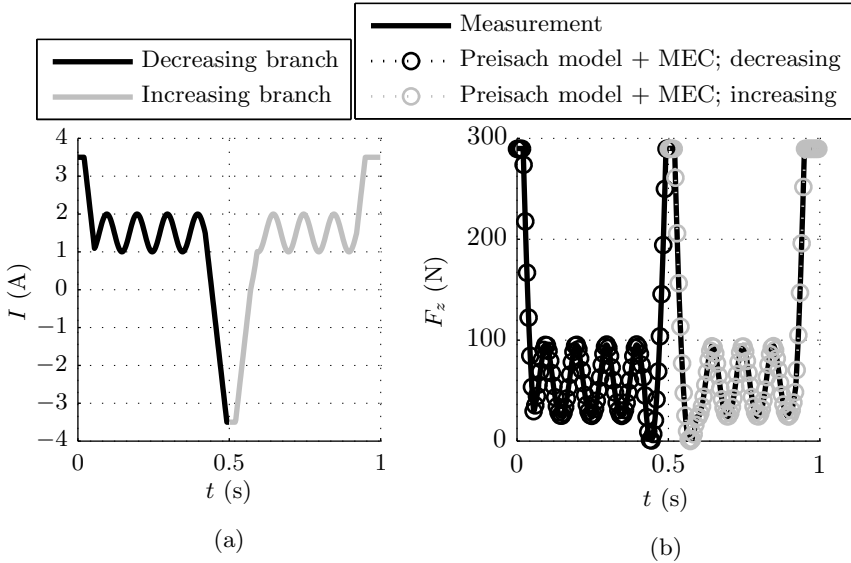


Fig. 7.6: The applied current excitation to analyze the history dependency of the CoFe E-core actuator (a), and the corresponding measured and simulated force (b), at an airgap of 0.80 mm.

positive peak value, respectively.

The measured and simulated force error due to magnetic hysteresis are shown in Fig. 7.7(a), with a zoomed view around the minor loops in Fig. 7.7(b). It can be noted from these figures, that the minor loops simulated with the combined Preisach and MEC model, are similar as the measured ones, although, the loop eye of the simulated hysteresis in the force is larger, similarly as in Figs. 7.3(b) and 7.5. Nevertheless, Fig. 7.7 clearly shows that the history dependency of the force is dependent on the previous peak values of the input. The difference between the measured minor loops is approximately 0.5 N, which corresponds with 0.17 % of the peak force.

Additionally, it can be concluded from the measured minor loops in the reluctance force, as shown in Fig. 7.7(b), that no significant accommodation occurs. Hence, this validates the conclusions in Sections 3.3 and 5.2 that accommodation is not significantly present in the force.

Besides the hysteresis in the force, the magnetic hysteresis in the actuator core has been simulated with the combined Preisach and MEC model. The simulated magnetic hysteresis in the soft-magnetic actuator core is shown in Fig. 7.8(a), as well as the $B-H$ relation measured on the ring sample of

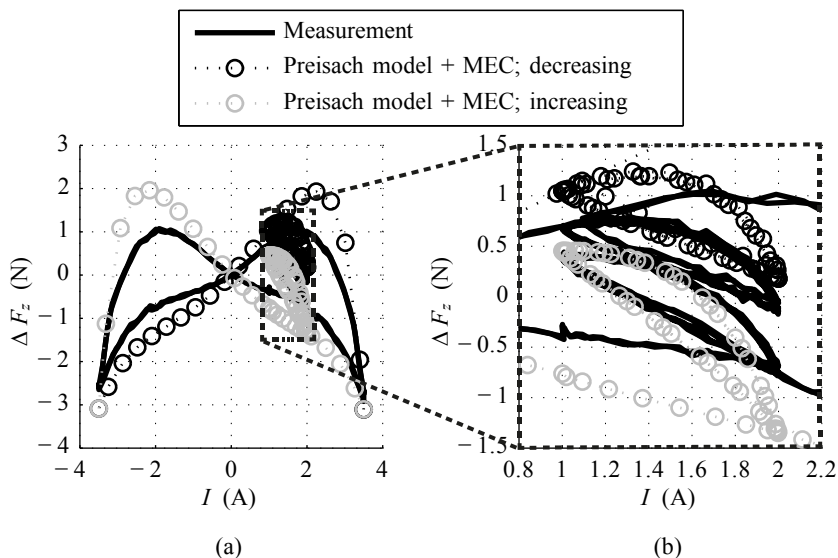


Fig. 7.7: Comparison of the simulated and measured force error due to magnetic hysteresis (a), and a zoomed (magnified) view around the two minor loops (b), for the current excitation as shown in Fig. 7.6(a), at an airgap of 0.80 mm.

Vacoflux 50-10, both with a maximum magnetic field strength of approximately 150 A/m. The two minor loops are formed as a result of the current excitation as shown in Fig. 7.6(a). Also in the zoomed view of the simulated $B-H$ characteristic in the core of the actuator, as shown in Fig. 7.8(b), the history dependency can be clearly observed by the difference in the average magnetic field strength of the minor loops.

Discussion

It can be concluded from the previous analysis that the Preisach model combined with the static MEC model predicts the shape of the hysteresis in the force with a good similarity for all three of the applied current excitations. However, the determined hysteresis in the force is overestimated with approximately 1 N, which results in a relative force error of $\Delta F = 0.42\%$ and a relative loop-eye error of $\Delta_{\text{eye}} = -91.3\%$. This discrepancy can be attributed to three causes:

- Firstly, a difference between the measured ring sample and the soft-

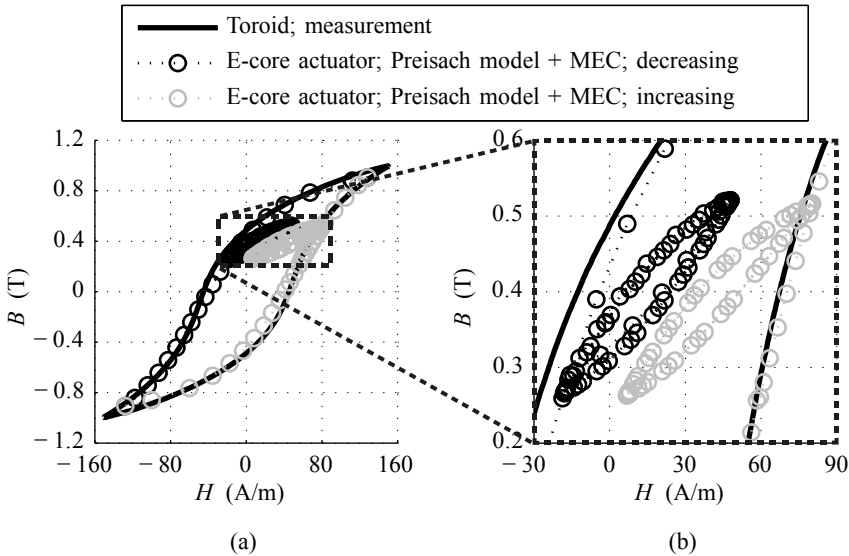


Fig. 7.8: A comparison of the B – H characteristic of the material modeled with the Preisach model in the core of the E-core actuator and a measured B – H characteristic in the laminated toroid Vacoflux 50-10 (a), and a zoomed (magnified) view around the two minor loops (b) (for the current excitation shown in Fig. 7.6(a)).

magnetic material in the actuator. The material samples are different because the material of the reluctance actuator is not from the same batch as the ring sample. The ring sample is manufactured in April 2014, but the actuator in June 2009. The differences of the magnetic material properties are typically caused by the cutting edges of the EDM process, the cutting temperature (the temperature difference between the cutting surface and the interior of the material), and the annealing time and temperature after rolling, as explained in Chapter 3. Additionally, the effects of the cutting edges in the ring sample are significantly higher than for the E-core actuator, since the actuator teeth have a larger cross-section area. Furthermore, even two ring samples which have been simultaneously manufactured show a difference in the B – H characteristic. These two toroids, which are both manufactured of Vacoflux 50-10, show a difference in the measured magnetic flux density of 55.6 mT for a minor loop with a peak magnetic field strength of 150 A/m, which is similar to the minor loop that occurs in the core of the E-core actuator, as shown in Fig. 7.9.

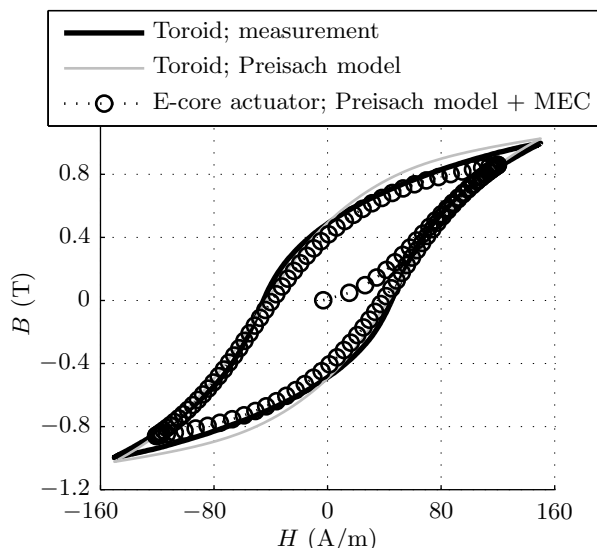


Fig. 7.9: A comparison of the $B-H$ characteristic of the material modeled with the Preisach model in the core of the E-core actuator corresponding with the excitation shown in Fig. 7.3 and the measured and modeled $B-H$ characteristic in the laminated toroid Vacoflux 50-10 similar as in Fig. 5.19.

- Secondly, a mismatch between the Preisach distribution function and the measured $B-H$ characteristic, as observed in Chapter 5 and which has been shown in Fig. 5.19. This is further investigated for the force measurement on the CoFe actuator with the sinusoidal current excitation. The magnetic flux density in the actuator core, modeled with the Preisach model, is compared to the measured $B-H$ characteristic, as shown in Fig. 7.9. It is shown that the modeled magnetic field strength in the CoFe E-core actuator varies approximately between $+120$ and -120 A/m. In this figure, the modeled $B-H$ curve in the actuator core, is also compared to the measured and modeled minor loops of the earlier investigated toroid of Vacoflux 50-10 with a peak magnetic field strength of 150 A/m. It is shown that the shape of the modeled curve is slightly different from the measured loops. The modeled hysteresis loop of the ring sample with a maximum magnetic field strength of 150 A/m overestimates the measured magnetic hysteresis loop with maximum 0.12 T, which results in an overestimation of the hysteresis in the reluctance force.
- Thirdly, the fact that only a single hysteresis operator is used for the modeling of the mover and stator core. Although the material has a high

magnetic permeability, the magnetic flux density in the material is to some extent inhomogeneous.

Considering these three plausible causes for the discrepancy of the predicted magnetic hysteresis in the reluctance force of the CoFe E-core reluctance actuator, it is arguable if it is fair to have an actuator model only based on the measured $B-H$ characteristic of a ring sample from a different batch. Nevertheless, since the major goal of this thesis is to investigate the accuracy of the force prediction of reluctance actuators from a physical electromagnetic perspective, only the measured magnetic material characteristics are used as model input for the previous and remaining analysis of the hysteresis in the force of reluctance actuators. However, for the control of a reluctance actuator after manufacturing, the magnetic material model can be adjusted to improve the prediction of the force of the reluctance actuator. The adjustment of the applied material model concerns the optimization of four variables in the Preisach distribution function based on the performed force measurements.

7.2 E-core actuators of silicon-iron

The other two E-core actuators are manufactured of laminated stacks of silicon-iron (SiFe). The SiFe is non-grain-oriented with a lamination thickness 0.50 mm (M800-50A) with a specified saturation magnetization of 2.0 T, as given in Table 3.1. One of the actuators is pre-biased with a permanent magnet on the middle tooth. Measurements are performed for frequencies up to 320 Hz on both SiFe E-core actuators, because the dynamic magnetic material effects of M800-50A are evidently present, as shown in Chapter 6. The force measurements are performed with a high-bandwidth piezoelectric load cell as discussed in next section.

The stators of the two E-core reluctance actuators are shown in Figs. 7.10(a) and (b). Both actuators have the same stator core and, hence, both actuators have a shorter middle tooth length, such that a permanent magnet can be placed on it. A NdFeB permanent magnet is applied with a measured remanent magnetic flux density and coercivity of 1.17 T and 978.5 kA/m, respectively. Consequently, the unbiased reluctance actuator is not optimally used, because the middle airgap is significantly larger than the airgap between the outer teeth and the mover. For both SiFe actuators, the force measurements are performed for a fixed airgap of 0.28 mm between the outer teeth and the mover. The stator is mechanically fixed to the frame of the measurement instrument and the mover of the actuator is fixed to the load cell.

The usage of the pre-biasing permanent magnet results, on the one hand, in an offset of the magnetic flux density in the soft-magnetic material, which in-

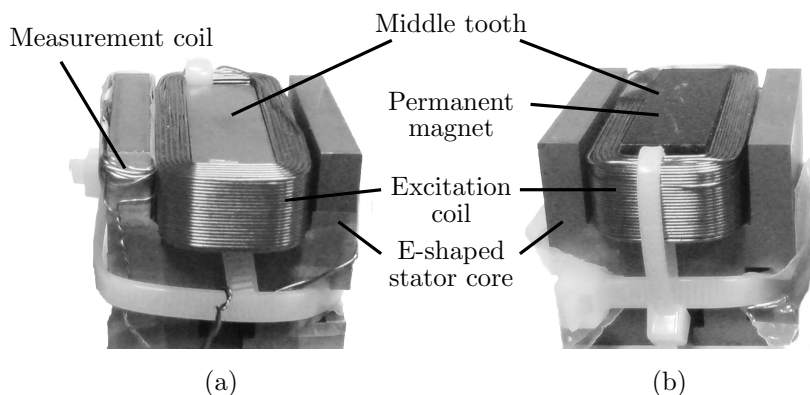


Fig. 7.10: The stator of two SiFe E-core actuators. The unbiased actuator, without permanent magnet on the middle tooth (a), and the pre-biased actuator, with permanent magnet on the middle tooth (b).

troduces a static stiffness of the reluctance actuator. On the other hand, the permanent magnet enhances the force range of the actuator and, the actuator is used in a more linear actuator regime considering the current-force characteristic. The full working range of the pre-biased actuator is shown in Fig. 7.11. This figure is obtained with the non-hysteretic MEC model, which corresponds with model 1, as discussed in Section 2.4. It shows the force profile in the actuation direction for a variable airgap and a variable current, which is significantly different than the approximately quadratic force profile of an unbiased actuator. Nevertheless, the pre-biasing permanent magnet only introduces an offset in the force, as shown in Fig. 2.8 in Section 2.6. The force of both SiFe actuators is examined for a smaller force range than for the CoFe E-core actuator but a much frequency range is taken into account.

7.2.1 Measurement instrument

The measurement instrument consists of a piezoelectric load cell with a charge amplifier and an aluminum frame (in which the load cell and actuator are mounted). A schematic illustration of the force measurement instrument in combination with a current amplifier and an integrator of the magnetic flux, is shown in Fig. 7.12.

The force measurements are performed with the piezoelectric load cell (Kistler type 9272) because it has a high rigidity and, hence, a high natural frequency [93, 145]. Similar load cells are regularly applied for force and torque mea-

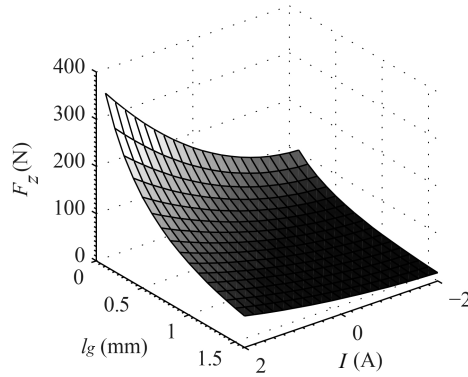


Fig. 7.11: Calculated force of the pre-biased E-core actuator with variable current and variable airgap.

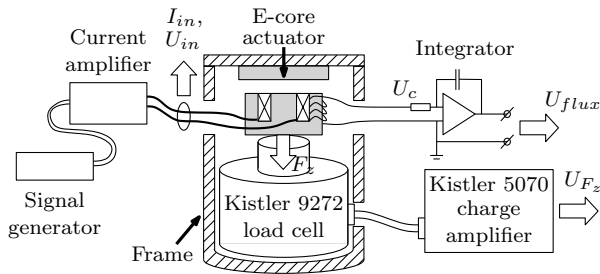


Fig. 7.12: Measurement instrument (load cell, frame and charge amplifier), the E-core reluctance actuator, the current amplifier and the integrator of the magnetic flux.

measurements of drilling and cutting machines due to the linearity over a large amplitude range [10, 210]. Other commonly used passive load cells are the strain gauge/gage [111] and hydrostatic sensor. However, both have lower bandwidth, lower strain sensitivity (factor 1000) and lower rigidity [93], which results in a larger airgap variation.

Generally, a disadvantage of piezoelectric a load cell is the inability to measure statically over a longer period of time. Hence, only steady-state ac measurements are evaluated. Moreover, ferroelectric hysteresis is present in a piezoelectric element [83, 95, 223, 281], which is comparable to ferromagnetic hysteresis in a reluctance actuator. However, the Kistler load cell uses the charge-force relation, which is non-hysteretic [83, 95], because it is an electrical equivalent of the magnetic flux-force relation for reluctance actuators.

Besides the force measurement, the magnetic flux in one of the actuator teeth is measured with a coil. This coil is located around the left tooth of the E-core reluctance actuator, as shown in Fig. 7.10(a). The magnetic flux density is obtained from the measurement coil according to (3.4), as discussed in Section 3.5, similarly as the magnetic flux density is obtained in ferromagnetic toroids. The phase delay of the measured flux with respect to the measured current and force are used in this analysis to distinguish the phase delay of the measurement instrument from the phase delay of dynamic magnetic material effects. The measured flux is not directly used for obtaining the force, because the flux-force relation is dependent on the airgap length and the positioning of the measurement coil, while the phase delay of the flux is independent of both geometric properties. Moreover, the accuracy of the non-hysteretic actuator model as presented in Section 2.4, shows better agreement with the force measurements than the force calculated from the measured flux.

Considering high-frequency measurements (up to 320 Hz), the phase response of the measurement instrument should be identified, because the measurement instrument introduces a delay. This phase delay of the measurement instrument is similar to the phase delay caused by eddy currents, although these phase delays are originated from a different source. The identification of the measurement instrument is performed with a iron-less voice-coil actuator with a ferrite permanent magnet, in which the eddy currents are limited [269], as discussed in Section 3.4. The measured phase response of the measurement instrument obtained with the voice-coil actuator is shown in Fig. 7.13. The measured phase response is modeled with a second-order low-pass filter and from each measurement of both E-core actuators the delay is determined between the measured force and magnetic flux. It can be seen in Fig. 7.13 (a) and (b) that the modeled phase response corresponds relatively good with both measurements.

The modeled phase delay is used to compensate for the phase delay of the measurement instrument. The difference is obtained between the directly measured magnetic hysteresis in the force and the actual hysteretic force after phase compensation of the measurement instrument. In Fig. 7.14(a) the difference is shown for the unbiased E-core actuator and in Fig. 7.14(b) for the pre-biased reluctance actuator. It is shown that the actual force error due to magnetic hysteresis of both actuators is approximately half the measured hysteretic loop-eye for a current excitation of 320 Hz.

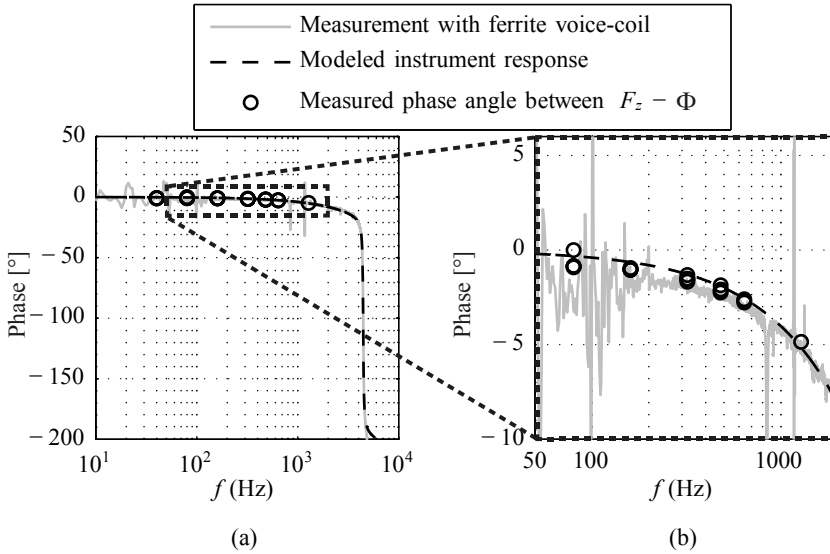


Fig. 7.13: The modeled phase delay compared to the measured phase delay of the measurement instrument (a), and a zoomed (magnified) view of the phase delay between 100 and 2000 Hz (b).

7.2.2 Simulation results of the unbiased E-core actuator

The measurement results of the unbiased E-core reluctance actuator are compared to the three dynamic reluctance actuator models which are discussed in Chapter 6, i.e. the Preisach model combined with the dynamic magnetic material model and the MEC model, the 3d FEM and the complex impedance method. The comparison on the prediction of the magnetic hysteresis in the reluctance force is shown in Fig. 7.15(a), and the loop-eyes due to magnetic hysteresis are shown in Fig. 7.15(b) for an airgap of 0.28 mm and a sinusoidal excitation with a frequency of 320 Hz. The modeling methods are examined on the maximum force error (7.4) and on the prediction of the amount of magnetic hysteresis present in the force, which is judged by the size of the loop-eye (7.5). The modeling accuracy of each method is summarized in Table 7.2.

From Fig. 7.15(b) it can be observed that the predicted dynamic magnetic hysteresis is overestimated by the 3d FEM, while the combination of the Preisach model and the MEC model shows better agreement with the measurements. The overestimation of the dynamic magnetic hysteresis by the 3d FEM results in a relatively large force error, i.e. $\Delta F_{3dFEM} = 1.4 \%$, whereas the mean current-force characteristic corresponds fairly well with the measured force.

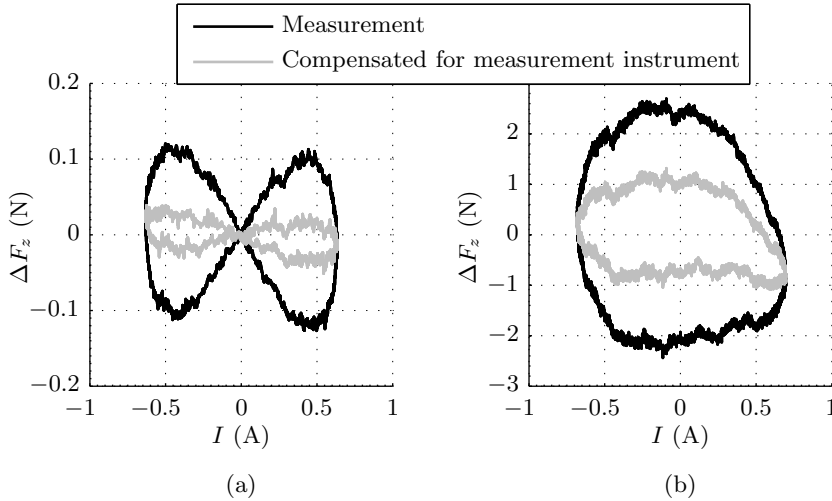


Fig. 7.14: The measured loop-eye and the loop-eye after phase compensation of the force measurement instrument, for the unbiased E-core actuator (a), and the pre-biased E-core actuator (b). Both measurements are performed for an excitation frequency of 320 Hz at an airgap of 0.28 mm.

Table 7.2: Accuracy of the simulation methods compared to the force measurements of the unbiased E-core actuator, for a 320 Hz excitation.

| Method | ΔF (%) | Δ_{eye} (%) | T_{sim} |
|----------------------|----------------|---------------------------|------------------|
| 3d FEM | 1.4 | -172 | 39 h |
| Preisach model + MEC | 0.7 | -63 | 2.1 s |
| Complex impedance | 0.5 | 28 | 31 ms |

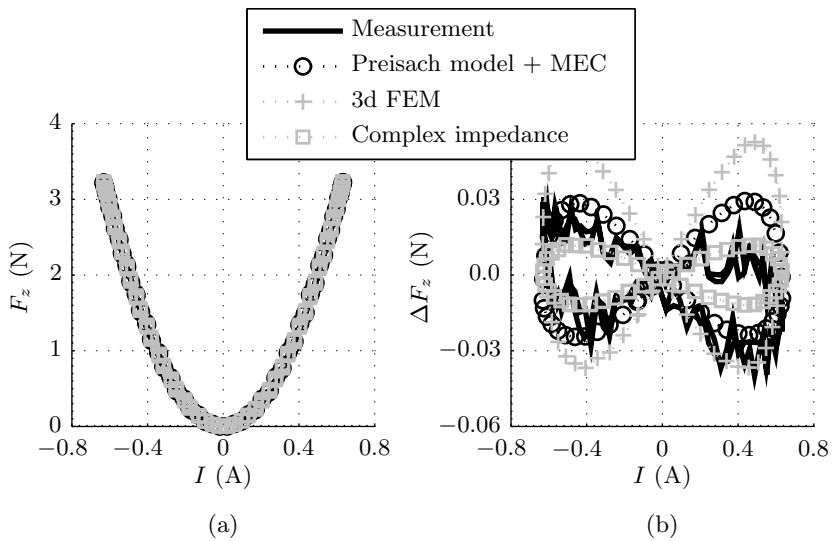


Fig. 7.15: Comparison of the simulated and measured force of the unbiased SiFe E-core reluctance actuator (a), and the force error due to magnetic hysteresis (b), for a 320 Hz sinusoidal current excitation at an airgap of 0.28 mm.

The difference between the predicted and the measured loop-eye is the largest for the 3d FEM, which overestimates the dynamic magnetic hysteresis with, $\Delta_{eye,3dFEM} = -172\%$. This is due to the fact that the software package includes only the major magnetic hysteresis loop, which results in relatively large discrepancies for low current excitations (small minor loops), similarly to the simulation results shown earlier in Fig. 6.19(a).

The combination of the Preisach model and the dynamic MEC model shows better agreement with the measurements, which is mainly caused by a smaller overestimation of the minor hysteresis loops in the soft-magnetic core material of the actuator. The approximated difference between the measured and modeled loop-eyes is $\Delta_{eye,PrM} = -63\%$, which results in a maximum force error of 0.7%. This maximum force error occurs at a current of +0.4 A. Due to asymmetry of the measured force a larger force error appears for a positive current. Moreover, the measurement noise is relatively high for this small force range, which results in a less reliable comparison than the more accurate measurement of the CoFe E-core actuator and the pre-biased actuator discussed in the following section.

The complex impedance method uses the measured phase delay between the force and magnetic flux and, hence, the height of the loop-eye shows the most correspondence with the measurement. Moreover, modeling the force with the complex impedance method improves the non-hysteretic actuator model by a factor of two, as the force error of the complex impedance method is, $\Delta F_{CIM} = 0.5\%$.

Another approach to validate the modeling methods is the analysis of the magnetic flux density in the SiFe stator core. As discussed before, the magnetic flux is measured by the measurement coil, as shown in Fig. 7.10(a). This measured magnetic flux density in the ferromagnetic material is compared to both, the modeled flux density with the 3d FEM and the combined Preisach model with the MEC model. The modeled and measured magnetic flux density is shown in Fig. 7.16(a). In Fig. 7.16(b) a zoomed view is shown, which corresponds with the first positive peak of Fig. 7.16(a). It is shown that both modeling methods overestimate the measured magnetic flux density by approximately 9%. This difference can be caused by the inaccuracy of the measurement with a distributed coil of only ten turns around one of the outer teeth, whereas the leakage and fringing fluxes are only partly measured with a significant uncertainty. Nevertheless, the 3d FEM and the combined Preisach model with the MEC model correspond reasonably well, which validates that only one iron reluctance in the MEC model is sufficient to model the mean magnetic flux density in the bulk of the actuator.

Lastly, the simulation times of the three modeling methods are given in Table 7.2. The 39 hours simulation time of the 3d FEM corresponds with the simulation of two periods of a sinusoidal current excitation in 209 steps. The

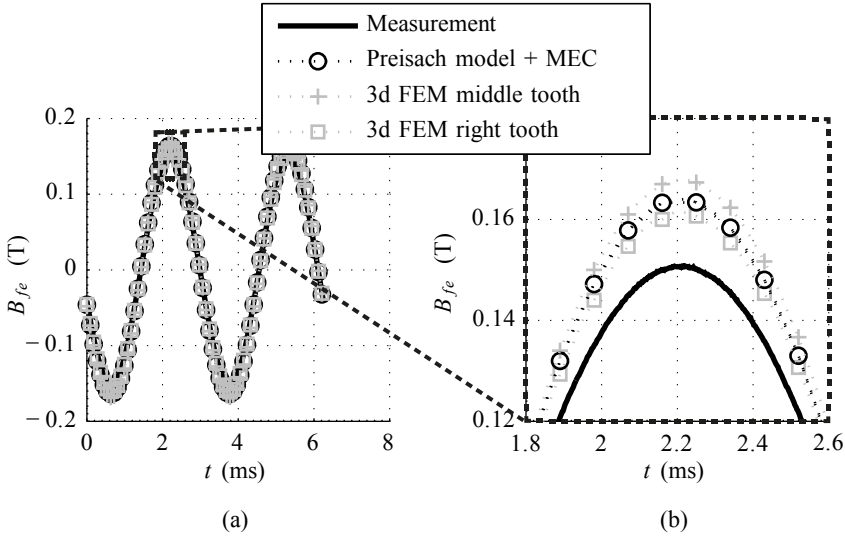


Fig. 7.16: Comparison of the measured and the simulated magnetic flux density in the stator core of the reluctance actuator (a), and a zoomed (magnified) view at one of the peaks of the sequence (b).

simulation time of the Preisach model combined with the dynamic MEC model is only 2.1 seconds for 209 steps, which is dependent on the convergence of the dynamic model. The complex impedance method in combination with the non-hysteretic MEC model takes only 31 milliseconds.

7.2.3 Simulation results of the pre-biased E-core actuator

The modeling methods are also experimentally verified for the pre-biased SiFe reluctance actuator. The force range and measured force of the pre-biased E-core actuator are shown in Fig. 7.17. The inclusion of the permanent magnet enhances the force range of the E-core actuator by a factor of 30 with respect to the unbiased actuator for the same current excitation. Moreover, it can be seen from the hysteretic 3d FEM simulation that significant saturation occurs for a current excitation above approximately 2.2 A at an airgap of 0.28 mm. Hence, the actual force range of this actuator for a current of ± 2 A is approximately 300 N. The magnetic hysteresis in the reluctance force is modeled and simulated for a sinusoidal current excitation with a peak value of 0.69 A. The corresponding force range is approximately 100 N as shown in Fig. 7.18(a).

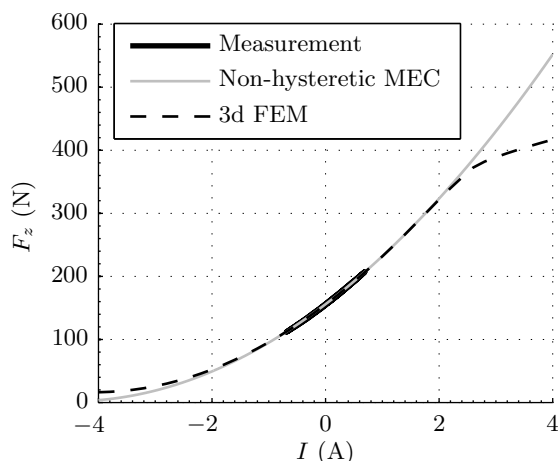


Fig. 7.17: Force of the pre-biased E-core reluctance actuator simulated for the total force range, at an airgap of 0.28 mm.

The simulated and measured magnetic hysteresis in the reluctance force for a 320 Hz excitation are visualized by the loop-eyes, as shown in Fig. 7.18(b). The relative discrepancy of the force (7.4), the loop-eye error (7.5), and the simulation time, T_{sim} , are given in Table 7.3 for each modeling method. Two periods of a sinusoidal current excitation are simulated, which corresponds for the 2d- and 3d FEM analysis with 100 and 126 time samples, respectively, whereas 242 samples are used as model input for the Preisach model and the complex impedance method.

The 2d FEM simulation shows a narrow loop-eye ($\Delta_{eye,2dFEM} = 88\%$) which is caused by neglecting eddy currents in the analysis and additionally, the slope of the current-force relation is different which is caused by neglecting the end effects. The simulation time of the transient 2d FEM analysis (73 minutes) is reasonable compared to the 3d FEM simulation time of 33 hours. The 3d FEM simulation including magnetic hysteresis and eddy currents shows good agreement with the measurements, showing a relative force error of 0.8 % with a loop-eye error of $\Delta_{eye,3dFEM} = 4.5\%$.

A comparable model accuracy is achieved with the Preisach model combined with the dynamic material and MEC model, which shows a force error of $\Delta F_{PrM} = 1.1\%$ and a loop-eye error of $\Delta_{eye,PrM} = 4.2\%$. It should be noted that this modeling method only incorporates static flux density measurements of the considered ferromagnetic material as model input for the simulation of

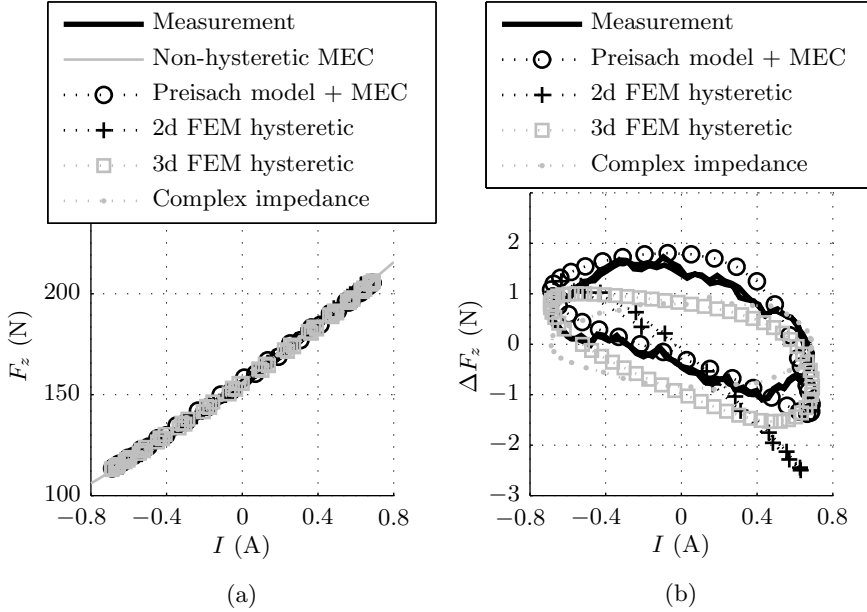


Fig. 7.18: Comparison of the simulated and measured force of the pre-biased SiFe E-core reluctance actuator (a), and the force error due to magnetic hysteresis (b), for a 320 Hz sinusoidal current excitation at an airgap of 0.28 mm.

Table 7.3: Accuracy of the simulation methods compared to the force measurements of the pre-biased E-core actuator, for a 320 Hz excitation.

| Method | ΔF (%) | Δ_{eye} (%) | T_{sim} |
|----------------------|----------------|---------------------------|------------------|
| 2d FEM | 1.9 | 88 | 1.2 h |
| 3d FEM | 0.8 | 4.5 | 33 h |
| Preisach model + MEC | 1.1 | -4.2 | 1.8 s |
| Complex impedance | 0.9 | 9.5 | 0.1 ms |

the instantaneous force of the reluctance actuator including dynamic material effects for a current excitation of 320 Hz. Moreover, the simulation time of 1.8 seconds is reasonably faster than for the FEM.

The relative force error of the complex impedance method is 0.9 %, which is directly related to the static MEC model describing the non-hysteretic actuator behavior. The loop-eye error of the complex impedance method is 9.5 %, which is in reasonable agreement with the measurements. It should be noted that this model is not predictive, because the phase delay is directly obtained from flux measurements. The calculation time is significantly shorter than for the other methods, but the model is not applicable for random current excitations and the accuracy will decrease for large excitations that approach the saturation magnetization of the specific material, as shown in Section 6.6.

7.3 Conclusions

In this chapter, the influence of static and dynamic magnetic hysteresis phenomena on the force of three E-core reluctance actuators has been examined with three simulation methods and a comparison to force measurements. A generalization of the Preisach model with the dynamic MEC model, 3d FEM simulations, and a complex impedance method combined with a static MEC model are evaluated on the prediction of magnetic hysteresis in the reluctance force. The discrepancies of the simulation results with respect to the force measurements are given in Table 7.4, for all three E-core reluctance actuators.

Firstly, it can be concluded from this analysis that the Preisach model combined with the MEC model shows good agreement with the measurements considering the relative force error, ΔF , similarly as the other simulation methods. A larger variation is observed in the loop-eye errors of the combined Preisach model and MEC model. A relatively large discrepancy is shown for the CoFe and the unbiased SiFe E-core actuators. For the unbiased SiFe actuator the large discrepancy is majorly caused by the significant measurement noise and the asymmetry of the measured force which results in a less reliable comparison than for the other actuators. The relatively large discrepancy between the simulated and measured loop-eye of the CoFe actuator can be attributed to three reasons, (i) there is a difference between the measured ring sample and the soft-magnetic material in the actuator, (ii) there is a mismatch between the Preisach model and the measured $B-H$ characteristic of the material sample, and (iii) there is only a single hysteresis operator used for the modeling of the mover and stator core of the reluctance actuator. The difference between the measured material sample and the material in the actuator core is expected to have the most influence on the simulation accuracy. This hypothesis is also in agreement with the analysis of the (dynamic) simulations of the pre-biased

Table 7.4: Discrepancy of the simulation methods with respect to the force measurements of the three E-core actuators.

| Actuator | Method | Preisach model | | CIM |
|--------------------|---------------------------|----------------|--------|---------|
| | | and MEC | 3d FEM | and MEC |
| CoFe | ΔF (%) | 0.42 | - | 0.73 |
| | Δ_{eye} (%) | -91.3 | - | 7.3 |
| SiFe unbiased | ΔF (%) | 0.7 | 1.4 | 0.50 |
| | Δ_{eye} (%) | -63 | -172 | 28 |
| SiFe pre-biased | ΔF (%) | 1.1 | 0.8 | 0.9 |
| | Δ_{eye} (%) | -4.2 | 4.5 | 9.5 |

E-core actuator, since the measured material sample in that case was obtained from the same batch as the actuator core, and the cross-section area of the outer actuator teeth is similar in size as the cross-section area of the ring sample. In case the $B-H$ characteristic of the material of the manufactured actuator core is uncertain, the distribution function of the Preisach model could be adjusted to model the hysteresis effects in the force of the actuator more accurately.

Secondly, the 3d FEM simulation shows a large discrepancy with the measured loop-eye of the unbiased SiFe actuator. This discrepancy is attributed to the inaccuracy of the simulation of minor hysteresis loops, since the force amplitude and, hence, also the variation of the magnetic flux density in the actuator core, are relatively low for these measurements. The FEM uses only data points of the major hysteresis loop as model input for the ferromagnetic material and, hence, a larger discrepancy is observed for the modeling of minor hysteresis loops, as also shown in previous chapter. The simulation with the 3d FEM shows good agreement with the measurements for the pre-biased SiFe actuator, for both the relative discrepancy of the force and the loop-eye. The 2d FEM is only evaluated for the pre-biased SiFe E-core actuator, and shows reasonable agreement with the measured force taking into account that the end-effects of the actuator are neglected and no dynamic material effects can be incorporated.

Thirdly, the complex impedance method (CIM) combined with the MEC model shows relatively good agreement with the measurements for all three E-core actuators, because the phase delay (used to incorporate magnetic hysteresis) is obtained from the measured current and force of the actuator. The discrepancy of the relative force is majorly dependent on the applied MEC model, and the size of the loop-eye is a result of the phase delay applied to the model. It should be noted that the complex impedance method is only applicable for sinusoidal current excitations.

Finally, it should be noted that there is a large variation in the simulation times of the three modeling methods. The simulation time of two periods of the 3d FEM is very time computationally expensive, i.e. between 30 and 40 hours, whereas the simulation time of the Preisach model with dynamic MEC method is approximately 2 seconds. The complex impedance method is the fastest model with a simulation time in the order of milliseconds.

Conclusions and Recommendations

This thesis concerns the modeling of nonlinear and hysteretic phenomena in reluctance actuators from an electromagnetic perspective. The ferromagnetic material in reluctance actuators enhances the force density by guiding the magnetic fields towards the airgap, where the change of energy with position is relatively high. Consequently, a high force density is achieved which is desired to increase the acceleration of actuation systems. However, the hysteretic phenomena in the magnetic materials and the nonlinear actuator behavior result in research challenges for high-precision applications, especially for semiconductor lithography systems where nanometer accurate positioning is required. This research bridges a gap between the modeling of physical properties of ferromagnetic materials and the modeling of electromagnetic actuation systems. The conclusions related to the research objectives, as stated in Section 1.2, are addressed subsequently in this chapter. Furthermore, recommendations for further research are given.

8.1 Conclusions

The conclusions are divided in three subsections. Firstly, the most dominant reluctance actuator properties are discussed which should be incorporated in the electromagnetic model. Secondly, the selection of appropriate modeling methods is discussed. Finally, a conclusion is given on the experimental verification of the applied modeling methods. In all three subsections, the modeling of reluctance actuators and the modeling of magnetic materials are separately evaluated.

8.1.1 Formulation and assessment of the reluctance actuator properties to be modeled

The assessment of reluctance actuator properties that should be incorporated in the modeling of reluctance actuators is subdivided into two categories. Firstly, the electromechanical properties of reluctance actuators are discussed, and secondly, the magnetic material properties are assessed. Lastly, the relevant actuator properties to be modeled are summarized.

Electromechanical properties

The nonlinearity of the force in the actuation direction with respect to current and position is the most significant contributor for model inaccuracies. The modeling of the parasitic force of the reluctance actuator due to misalignment of the stator and the mover is also important. These parasitic forces can be reduced significantly by an appropriate actuator design. When the parasitic forces are not minimized in the design, these forces should be incorporated in the model of the actuation system, as the forces result in undesired cross-coupling between actuators, while the specific actuator cannot compensate for these forces by itself.

Magnetic material properties

It is necessary to incorporate the measured nonlinear magnetic material properties of a material sample in the reluctance actuator model. It is important to obtain these measurements from a material sample that is from the same batch and which is manufactured in the same production process as the actuator, because the material properties are significantly changed due to manufacturing. Annealing of the magnetic material restores the magnetic properties of material samples, but annealing is not possible when an isolated laminated stack is glued before it is cut.

The dynamic magnetic material properties are significantly present for laminated materials of 0.35 mm and above, whereas the dynamic effects are insignificant for a lamination thickness of 0.10 mm. The non-congruency, accommodation and magnetostriction properties of magnetic materials have been considered insignificant compared to the general magnetic hysteresis effects. Vector hysteresis has not been considered either, since its influence is assumed to be small in the applied non-grain oriented (NGO) materials.

It can be concluded from the 2d FEM analysis that the absolute amount of the hysteresis in the force and the hysteresis losses are directly related to the peak value of the magnetic flux density in the bulk of the actuator. Based on these two observations, it is also concluded that it should be sufficient to model the hysteresis in the force with a single hysteresis operator and hence, also for this reason the inclusion of vector hysteresis is unnecessary.

The amount of static hysteresis in the force is between 0.5 and 1.0 % of the peak force for the four evaluated actuator topologies. The actuators with a higher force density, and consequently, a large magnetic flux density variation in the actuator core, experience more magnetic hysteresis in the force. The magnetic hysteresis in the cross-talk is negligible in comparison with the hysteresis in the force in the actuation direction.

By summarizing the discussed reluctance actuator properties, that should be incorporated in the actuator model for high-precision reluctance actuators, the following procedure is defined:

- Model the force in the actuation direction, which is nonlinear with current and position;
- Measure the quasi-static nonlinear magnetic material properties to obtain the magnetic permeability, the saturation magnetization and the magnetic hysteresis;
- Model the following hysteresis properties: the history dependency, the wiping-out property, and minor loops (reversal curves);
- Model dynamic magnetic material effects in reluctance actuators when an excitation frequency above 100 Hz is considered, at least for a lamination thickness of 0.35 mm or above.

8.1.2 Selection of models for the determination of the instantaneous force of high-precision reluctance actuators

Based on the formulated reluctance actuator properties to be modeled, various modeling methods are evaluated on their applicability for modeling high-precision reluctance actuators. The modeling methods are discussed on their ability to model the electromechanical reluctance actuator properties and/or the magnetic material phenomena.

8.1.2(a) Evaluation of electromechanical actuator modeling methods

Various electromagnetic modeling techniques are qualitatively compared on their suitability for the modeling of reluctance actuators. An analytical and a numerical modeling method are selected. The analytical magnetic equivalent circuit (MEC) method and a commercially available FEM are selected, which can both be extended to incorporate magnetic hysteresis phenomena in its analysis. The MEC model can predict the force in the actuation direction with an accuracy such that only the force error due to magnetic hysteresis remains. Modeling the parasitic force of reluctance actuators is ineffective with the MEC method for two reasons. Firstly, numerical methods, such as the FEM or the boundary element method (BEM) are necessary to obtain the airgap reluctances. Secondly, the MEC model approaches the complexity of the mesh of a FEM to achieve a sufficient accuracy.

8.1.2(b) Evaluation of magnetic material modeling methods

A literature review has been performed to qualitatively evaluate magnetic material models on their applicability for reluctance actuators. The evaluated modeling methods are the Preisach model, the Jiles-Atherton model, the play and stop model, the positive-feedback model, the FEM, and the complex impedance method. Additionally, the Stoner-Wohlfarth model, the Coleman-Hodgdon model and Takács model have shortly been discussed. These modeling methods have been qualitatively compared based on the following criteria:

- The ability to be combined with existing reluctance actuator modeling methods;
- The ability to have arbitrary current excitations as model input;
- The ability to incorporate rate-dependent magnetic material effects.

The Preisach model has been selected to model the hysteretic magnetic material phenomena, because it can be combined with the analytic MEC model just as

the play model and stop model. Furthermore, because of the long history and the numerous improvements of the Preisach model, this model has been selected to be used for magnetic hysteresis modeling in reluctance actuators.

The FEM has also been evaluated because it is one of the few commercially available FEM that can include magnetic hysteresis in its analysis. In addition, arbitrary current excitations and rate-dependent effects can be incorporated. An anisotropic electric conductivity has been proposed for the simulation of eddy currents in laminated materials. However, the obtained anisotropic conductivity is only valid for fixed frequencies.

The complex impedance model has been selected because of its simplicity and speed. It can easily be combined with the non-hysteretic MEC model, but it is only applicable for sinusoidal current excitations as it is implemented here with a constant phase delay per excitation frequency.

8.1.3 Experimental verification of the modeling methods

The selected modeling methods have been experimentally verified by a comparison to measurements. The measurements are divided into two parts which are discussed subsequently. It concerns the measurement of the magnetic flux density in soft-magnetic material samples and the measurement of the force of various reluctance actuators.

8.1.3(a) Verification of three hysteresis modeling methods on various magnetic materials

The three selected modeling methods have been evaluated on their ability to predict static and dynamic magnetic hysteresis phenomena in ferromagnetic materials. The generalized scalar Preisach model has been extensively elaborated for modeling ferromagnetic materials. Four Preisach distribution functions have been optimized to model the $B-H$ characteristics of three different soft-magnetic materials, i.e. CoFe (Vacoflux 50), SiFe (M800-50A) and stainless steel (AISI 430). These materials have various lamination thicknesses, i.e. two CoFe samples with 0.10 mm and 0.35 mm laminations (Vacoflux 50-10 and Vacoflux 50-35), the SiFe sample has 0.50 mm laminations, and the stainless steel sample is a solid ring with a cross-section area of $4 \times 5 \text{ mm}^2$.

The simulation results of the generalized Preisach model have been compared to quasi-static measurements. The maximum discrepancies between the measured and modeled instantaneous magnetic flux density in the ring samples of Vacoflux 50-10, Vacoflux 50-35, M800-50A and AISI 430 have been obtained as 11.2 %, 5.9 %, 4.4 % and 12.5 %, respectively. The rms errors of the simulated

magnetic flux density of three hysteresis loops are at least a factor of three lower than the maximum discrepancies, for all material samples.

Besides the static magnetic hysteresis model, the magnetic flux density has been simulated with the combination of the generalized Preisach model and the dynamic field separation method, with which the eddy current and excess field components have been obtained. This combined simulation method has been compared to the losses of numerous measured $B-H$ curves at various frequencies and peak magnetic flux densities. This comparison is performed for the three laminated ring samples, i.e. Vacoflux 50-10, Vacoflux 50-35 and M800-50A. The difference of the loss prediction with respect to the measurements is below 20 % for Vacoflux 50-10 and below 10 % for Vacoflux 50-35 and M800-50A.

In addition, the instantaneous magnetic flux density has been simulated for various excitation frequencies up to 320 Hz. The remanent magnetic flux density and the coercive field strength of the dynamic simulation method have been modeled with a discrepancy below 10 % for Vacoflux 50-35 and M800-50A, whereas the discrepancy of the magnetic field strength and the remanent magnetic flux density for Vacoflux 50-10 is below 10 % and 40 %, respectively. The relatively large simulation error for Vacoflux 50-10 is caused by a discrepancy in the static hysteresis model, on account of a mismatch between the material characteristics and the evaluated Preisach distribution functions.

Rate-dependent hysteresis effects have also been simulated with the 3d FEM and the complex impedance method. The laminated ring samples have been modeled with the FEM by an anisotropic conductivity. The remanent magnetic flux density and the coercive field strength are predicted with a maximum error of 10 % with the 3d FEM for three peak magnetic flux densities at an excitation frequency of 400 Hz. The complex impedance method shows only similar agreement with measurements at high frequencies, when both the wave-forms of the magnetic field strength and magnetic flux density are approximately sinusoidal.

8.1.3(b) Verification of the determination of the instantaneous force of three E-core actuators

The magnetic hysteresis in the reluctance force of three E-core reluctance actuators have been measured on two measurement instruments. Static force measurements have been performed on a CoFe E-core reluctance actuator (manufactured of Vacoflux 50-10), and dynamic force measurements have been performed on two SiFe E-core actuators (manufactured of M800-50A), one of which is pre-biased with a permanent magnet. The force measurements have been compared to the three proposed simulation methods for reluctance actuators,

i.e. the Preisach model combined with a dynamic MEC model, the 2d/3d FEM and a complex impedance model combined with a static MEC model. These three modeling methods are thoroughly discussed.

It has been shown that the combined Preisach model and MEC model can incorporate the most dominant magnetic hysteresis phenomena (the history dependency, minor loops and dynamic effects) in the simulation of the force of reluctance actuators. The simulated relative force error and the shape of the hysteresis in the force shows good agreement with the force measurements, similarly as for the FEM. The magnetic hysteresis in the force is simulated with the Preisach model, which only includes the static $B-H$ characteristics of the measured material samples as model input. The amount of magnetic hysteresis in the force of the CoFe reluctance actuator is overestimated, which can be attributed to three reasons:

- There is a difference between the measured ring sample and the soft-magnetic material in the actuator;
- There is a mismatch between the Preisach model and the measured $B-H$ characteristic of the material sample;
- There is only a single hysteresis operator used for the modeling of the mover and stator core of the reluctance actuator.

The first reason is expected to have the most influence on the results, because the material of the measured ring sample and the CoFe reluctance actuator are from different batches, since the E-core actuator has been manufactured approximately 5 years earlier. Additionally, the influence of the manufacturing process (in this case EDM) has a large impact on the magnetic material properties, as has been shown for an annealed and non-annealed ring sample. Considering these material uncertainties, it is arguable if it is fair to have an actuator model only based on the $B-H$ characteristic of a different material batch. The hypothesis that the material difference is the major cause of the discrepancy between the measurement and the simulation, is also in correspondence with the dynamic simulations performed on the pre-biased SiFe E-core actuator. In that case the prediction of the loop-eye (representing the hysteresis in the force) is in very good agreement with the measurements, while the measured ring sample is originated from the same batch as the actuator. However, for the control of a reluctance actuator after manufacturing, with insufficient information about the magnetic material, the Preisach model can be adjusted to improve the prediction of the magnetic hysteresis in the force.

The 3d FEM is evaluated on the prediction of the dynamic magnetic hysteresis in the force of the two SiFe reluctance actuators. The relative discrepancy of the simulated force compared to the measured force is in good agreement for both actuators. The amount of magnetic hysteresis in the force is in very good agreement for the pre-biased actuator. However, for the unbiased actuator

the loop-eye has been overestimated by approximately a factor of two. This larger discrepancy is attributed to the fact that the FEM software only uses the major hysteresis loop as model input, while the force variation and, hence, also the magnetic flux density variation have been relatively low during the measurement of the unbiased E-core actuator. This inaccurate modeling of small minor loops is also in agreement with the static simulations on a ring sample of the same material (M800-50A). It should be noted that typically a simulation of two periods of a sinusoidal excitation with the 3d FEM is very time computationally expensive, and lasts 30-40 hours.

The complex impedance method combined with the static MEC model has shown relatively good agreement on both the simulation of the force and the amount of magnetic hysteresis in the force. This is directly caused by the fact that the phase delay (used to incorporate magnetic hysteresis) has been obtained from the measured current and force of the actuators. The accuracy of the relative force is mainly dependent on the applied MEC model, which is equivalent to the static MEC model, used in combination with the Preisach model. Moreover, the complex impedance method is only applicable for sinusoidal excitations, since the phase delay is valid for a fixed frequency only.

8.2 Recommendations

During the process of performing the presented research, various directions are chosen on the never ending route of science. Consequently, various roads have been passed without exploring. The most relevant not inspected roads are addressed in the recommendations. Specifically, concerning the modeling of magnetic hysteresis and electromagnetic actuators.

8.2.1 Modeling of magnetic hysteresis

- From the evaluated magnetic material models, the recently developed positive-feedback model is considered as a model with high potential. This is an intuitive model and is based on physical material properties. An inverse hysteresis model could be implemented, which is interesting for e.g. a feedback controller or obtaining the desired voltage given a specific force profile. For the inversion of the Preisach model, the discrete Preisach model should be obtained from the Everett distribution. The discrete Preisach model could also reduce the simulation time of the hysteresis model. Besides the Preisach model, the play and stop models can be considered if research focuses on forward and inverse hysteresis modeling.

- For the control of reluctance actuators it is recommended to investigate the possibilities of fast and simple hysteresis models, such as the complex impedance model. This could be useful for applications where actuators are assigned to perform repetitive sequences or trajectories. Especially, because it has been shown that the complex impedance model performs relatively well for reluctance actuators with a sinusoidal current excitation.

8.2.2 Electromagnetic actuator modeling

- The complexity of the MEC model could be increased with a higher number of hysteretic reluctances in the ferromagnetic material, to incorporate an inhomogeneous magnetic flux density distribution. This could improve the hysteretic force prediction of reluctance actuators.
- Improve the convergence of the combined Preisach model with the dynamic magnetic material model and the MEC model. Especially, the abrupt variations of the relative permeability at the reversal points of the Preisach model cause instabilities. Hence, the simulation time can be decreased when the model converges faster.
- To obtain a more complete reluctance actuator model it could be coupled with a mechanical model that incorporates temperature, magnetostriction, accommodation, congruency, and material elongation due to the force of the actuator itself. These phenomena, occurring in magnetic materials, are approximated in this thesis to result in a maximum force error as percentage of the applied force of 0.5 % K^{-1} , 0.2 %, 0.03 %, 0.03 % and 0.04 %, respectively.
- For the analytic optimization and design of reluctance actuators with the MEC model, the leakage paths should be taken into account with a higher accuracy.

8.2.3 Actuator manufacturing

- It is recommended to incorporate magnetic material knowledge in the design of reluctance actuators. Choosing the manufacturing processes of actuators is essential for the magnetic material properties. For the cases where annealing is not feasible, the magnetic material properties should be obtained from a material sample from the same batch, and should be subjected to the same manufacturing process.

A

Airgap permeance methods

A.1 Analytic permeance method

The analytic permeance method to include fringing effects in the airgap of reluctance actuators is based on the permeance representation introduced by Roters [221]. Although, various extensions exist, such as triangular, trapezoidal and S-shaped flux tubes [159, 197, 250], the cylindrical and spherical variants presented by Roters are considered to be sufficient, because only the force of reluctance actuators in the actuation direction is analyzed in this thesis.

The two dimensional representation of the airgap model as shown in Fig. 2.5 is described in three dimensions for the examined reluctance actuators. An illustration of the corresponding flux tubes are shown in Fig. A.1(a) and (b), for a part of an actuator tooth and a mover section. In this analysis, the airgap permeances are described by nine different flux tubes, as numbered in Figs. A.1(a) and (b). The nine flux tubes are separately shown in Fig. A.2 and the permeance of each flux tube is described subsequently. The dotted arrows indicate the mean flux path, ϕ , in each flux tube, which represent the average path length of the flux lines.

The first flux tube has a rectangular shape which is already described in Section 2.4. The corresponding permeance is given in (2.38) and is written for the given geometrical parameters as

$$\mathcal{P}_1 = \mu_0 \frac{wd}{l} \tag{A.1}$$

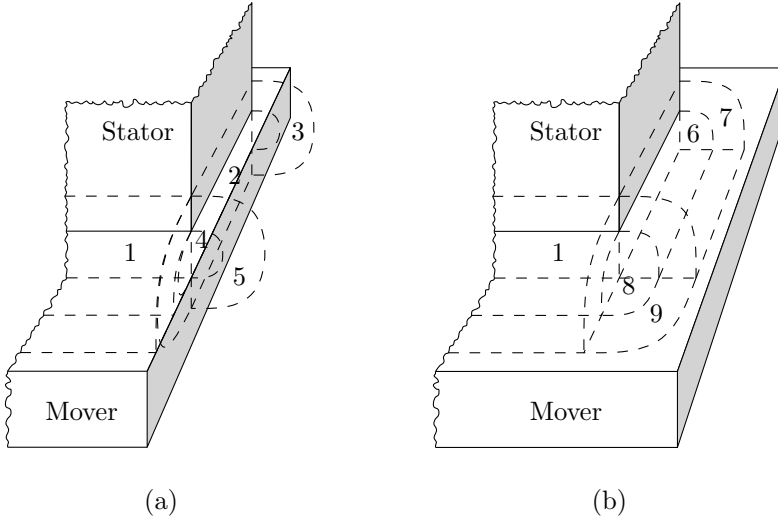


Fig. A.1: Illustration of the fringing flux tubes around a single tooth of a reluctance actuator, with equal mover width and stator width (a), and with an extended mover width compared to the stator width (b).

where w is the width, d the depth and l the length of the flux path, as illustrated in Fig. A.2(1).

The second flux tube is a half cylinder, which partly takes into account the fringing for the case when the outer surface of the mover and the stator are aligned, as shown in Fig. A.1(a). The mean length of the flux path can be considered to be equal to the length of a line drawn midway between the outer surface and the semi-circumference as shown in Fig. A.2(2). According to [221] this length is equal to $l \approx 1.22w$. The mean cross-section area is estimated by dividing the entire volume of the flux tube by its mean length, $A = \frac{\pi w^2}{8} \frac{d}{1.22w} \approx 0.322 wd$. Hence, the permeance of the second flux tube is described as

$$\mathcal{P}_2 = \mu_0 \frac{0.322wd}{1.22w} = 0.26 \mu_0 d. \quad (\text{A.2})$$

Thirdly, a half ring shaped flux tube (3) is considered. This flux tube is used to model the fluxes leaving the stator tooth from the side and entering the mover from the side, as shown in Fig. A.1(a). The flux path has a mean length of $l = \pi \frac{w+g}{4}$, and an average cross-section area of $A = d \frac{w-g}{2}$, which are combined and simplified to obtain the following airgap permeance

$$\mathcal{P}_3 = \mu_0 \frac{2d w - g}{\pi w + g} \quad (\text{A.3})$$

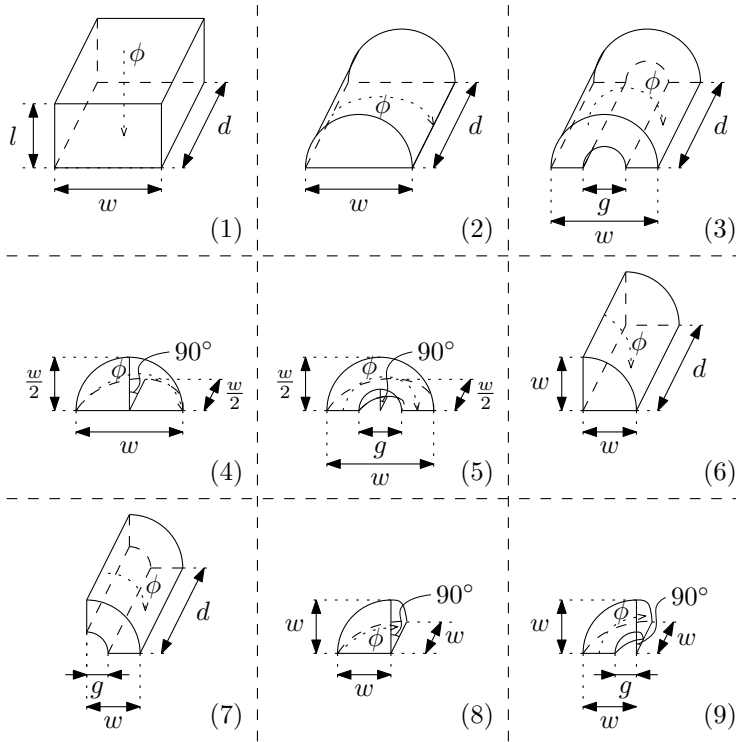


Fig. A.2: The flux tubes of which the numbers correspond with the numbers in Fig. A.1.

where g is equal to the airgap length in Fig. A.1(a).

The fourth flux tube is one quadrant of a full sphere. The mean flux line is assumed to be situated at 0.65 of the sphere radius. The mean length is graphically obtained in [221] and is approximated to be, $l \approx 1.3w$, the volume of the spherical quadrant is, $\frac{\pi}{3} \left(\frac{w}{2}\right)^3$, and hence, the average cross-section area is obtained as, $A = \frac{\frac{\pi}{3} \left(\frac{w}{2}\right)^3}{1.3w} \approx 0.1w^2$, and the resulting permeance is written as

$$\mathcal{P}_4 = \mu_0 \frac{0.1w^2}{1.3w} = 0.0775 \mu_0 w. \quad (\text{A.4})$$

The fifth flux tube is a quadrant of a spherical shell. The mean length of the flux path is equal to the length of the third (ring shaped) flux tube, $l = \pi \frac{w+g}{4}$, the volume of the spherical shell is obtained as, $\frac{\pi}{24} (w^3 - g^3)$, and subsequently the mean cross-section area is obtained as, $A = \frac{1}{6} \frac{w^3 - g^3}{w+g}$. The corresponding

airgap permeance is derived as

$$\mathcal{P}_5 = \mu_0 \frac{2}{3\pi} \frac{w^3 - g^3}{(w + g)^2}. \quad (\text{A.5})$$

The sixth flux tube is exactly one-half of path (2), and hence, its permeance is twice as large, given by

$$\mathcal{P}_6 = 0.52 \mu_0 d. \quad (\text{A.6})$$

Similarly, the flux tubes (7), (8) and (9) are identical to one-half of the flux tubes (3), (4) and (5), respectively. Therefore, the following permeance are obtained

$$\mathcal{P}_7 = \mu_0 \frac{4d}{\pi} \frac{w - g}{w + g}, \quad (\text{A.7})$$

$$\mathcal{P}_8 = 0.155 \mu_0 w, \quad (\text{A.8})$$

$$\mathcal{P}_9 = \mu_0 \frac{4}{3\pi} \frac{w^3 - g^3}{(w + g)^2}. \quad (\text{A.9})$$

A.2 Tooth contour method

The second method to obtain the airgap permeances is the tooth contour method (TCM). The TCM uses the analogy between the electric and magnetic scalar potential. The potential difference between two surfaces is obtained numerically with a electrostatic boundary element method (BEM).

The airgap permeance between two surfaces is described for the stator and mover geometry shown in Fig. A.3. The bottom surface of the stator tooth is surface S_A with the corner points $A_1 - A_4$. The top surface of the mover is divided into five subsections. The middle surface area is the reflection of the stator tooth on the mover and the other four surface areas are obtained by connecting its corner points to the corner points of the mover. In the following analysis, the right section is surface S_B with the corner points $B_1 - B_4$.

Generally, the magnetic field strength for a conservative field can written as, $\mathbf{H} = -\nabla\varphi$, where φ is the magnetic scalar potential. Using Ampère's law equivalently as in (2.35), the magnetic potential difference between points A and B is derived as

$$\int_C \mathbf{H} \cdot d\mathbf{l} = - \int_A^B \nabla\varphi \cdot d\mathbf{l} = \varphi_A - \varphi_B. \quad (\text{A.10})$$

The integral can be performed over any contour, as illustrated by the bold dashed contour, C , connecting the points A and B , as shown in Fig. A.3.

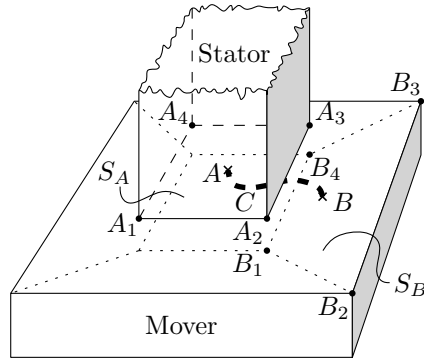


Fig. A.3: Illustration of a stator tooth and mover of a reluctance actuator, which is divided into several surface areas.

Furthermore, the analogy between magnetic and electric fields is used because it is not possible to apply a magnetic potential at a surface in a FEM simulation. The electric scalar potential, v , is related to the electric field strength as, $\mathbf{E} = -\nabla v$. The amount of electric field lines entering a surface S_B due to a potential difference from an electric charge on surface S_A , is equal to the amount of flux entering surface S_B due to magnetic charges on surface S_A .

Using (2.35-2.38), the permeance of a flux path in air can be described as

$$\mathcal{P} = \frac{\int_S \mathbf{B} \cdot d\mathbf{s}}{\int_C \mathbf{H} \cdot d\mathbf{l}} = \frac{\mu_0 \int_S \mathbf{H} \cdot d\mathbf{s}}{\varphi_A - \varphi_B}. \quad (\text{A.11})$$

The analogy between electric fields and magnetic fields shows the following equivalence

$$\frac{\int_{S_B} \mathbf{H} \cdot d\mathbf{s}}{\varphi_A - \varphi_B} \sim \frac{\int_{S_B} \mathbf{E} \cdot d\mathbf{s}}{v_A - v_B}. \quad (\text{A.12})$$

Hence, by applying an electric potential to a surface S_A , the total electric flux entering at the other surface S_B , is related to the permeance of the airgap (A.11). For a potential of 1 V at S_A the permeance between both surfaces is given by

$$\mathcal{P}_{S_A \rightarrow S_B} = \mu_0 \int_{S_B} \mathbf{E} \cdot d\mathbf{S} \quad (\text{A.13})$$

The permeances between the numerous surfaces are obtained with electrostatic simulations with a BEM. The permeances due to the combination of the various surfaces are discussed for the applied magnetic equivalent circuit (MEC) method in Section 2.4.

B

Distribution function parameters

The distribution functions for the irreversible part of the scalar Preisach model are optimized with a constrained based nonlinear optimization algorithm in Matlab as discussed in Section 5.3. Each material has a specific constitutive relation and hence, different Preisach distributions can be implemented to approximate the magnetic $B-H$ relation.

The four examined distribution functions are, the hyperbolic tangential function (5.16), the Gaussian distribution (5.17), the Cauchy-Lorentz distribution (5.18), and the Langevin function (5.19). The results of the optimization of the four distribution functions for the three evaluated materials are given in Tables B.1-B.4.

Table B.1 gives the variables of the four distribution functions and the corresponding simulation errors after a comparison to the dc-measurements of the magnetic flux density of a ring sample manufactured of Vacoflux 50-10. The analysis shows that the rms error of the Cauchy-Lorentz distribution is minimal, whereas the Langevin distribution shows an equal maximum discrepancy. The other two distribution functions show a significantly larger discrepancy.

For the distribution function optimization for the Vacoflux 50-35 material the Cauchy-Lorentz distribution shows the best agreement with the measurements. The rms error of the Langevin, Hyperbolic tangent and the Gaussian distribution is 23 %, 129 % and 151 % higher, respectively.

Table B.1: Optimized distributions for Vacoflux 50, 0.10 mm laminations, presenting the model accuracy and the parameters of the distribution function.

| Distr. funct. | ϵ_{rms} (T) | ϵ_{max} (T) | h_m (-) | h_c (-) | σ_m (-) | σ_c (-) |
|--------------------|-------------------------|-------------------------|--------------|--------------|-------------------|-------------------|
| Hyperbolic tangent | 0.062 | 0.144 | -0.0919 | 0.0922 | 0.2115 | 0.2116 |
| Gaussian | 0.067 | 0.150 | -0.0948 | 0.0956 | 0.2540 | 0.2466 |
| Cauchy-Lorentz | 0.035 | 0.134 | -0.1021 | 0.1020 | 0.0981 | 0.0995 |
| Langevin | 0.042 | 0.134 | -0.1000 | 0.1001 | 0.0571 | 0.0587 |

It can be obtained from the overview in Table B.3 that the Cauchy-Lorentz distribution approximates the measurements best for M800-50A. Both, the rms error and the maximum error are more than twice as low, compared to the Hyperbolic tangent and Gaussian distributions for M800-50A. Moreover, the errors are approximately 20 % lower than for the Langevin function.

Additionally, an optimization of the four distribution functions is performed on the dc-measurements of AISI 430. Also for this material the Cauchy-Lorentz distribution shows a higher accuracy than the other three functions. The rms error of the Langevin function is similar to that of the Cauchy-Lorentz distribution but the maximum error is 14 % higher for the Langevin function. Nevertheless, this is much better than for the Hyperbolic tangent and Gaussian function of which the rms error and maximum error is approximately 33 % and 60 %, respectively.

Considering the four optimized parameters of the distribution functions, it can be noticed that $h_m \approx -h_c$ and $\sigma_m \approx \sigma_c$, both within 3.0 % for Vacoflux 50-10, 1.1 % for Vacoflux 50-35, 0.5 % for M800-50A and within 5.5 % for AISI 430. The fact that these parameters are not equal indicates that the measured hysteresis loops, which are used for the optimization of the distribution functions, are not perfectly symmetrical.

Table B.2: Optimized distributions for Vacoflux 50, 0.35 mm laminations, presenting the model accuracy and the parameters of the distribution function.

| Distr. funct. | ϵ_{rms} (T) | ϵ_{max} (T) | h_m (-) | h_c (-) | σ_m (-) | σ_c (-) |
|--------------------|-------------------------|-------------------------|--------------|--------------|-------------------|-------------------|
| Hyperbolic tangent | 0.080 | 0.205 | -0.0934 | 0.0933 | 0.1367 | 0.1365 |
| Gaussian | 0.088 | 0.237 | -0.0934 | 0.0934 | 0.1648 | 0.1643 |
| Cauchy-Lorentz | 0.035 | 0.116 | -0.0935 | 0.0934 | 0.0663 | 0.0656 |
| Langevin | 0.043 | 0.133 | -0.0933 | 0.0932 | 0.0375 | 0.0373 |

Table B.3: Optimized distributions for M800-50A, presenting the model accuracy and the parameters of the distribution function.

| Distr. funct. | ϵ_{rms} (T) | ϵ_{max} (T) | h_m (-) | h_c (-) | σ_m (-) | σ_c (-) |
|--------------------|-------------------------|-------------------------|--------------|--------------|-------------------|-------------------|
| Hyperbolic tangent | 0.064 | 0.144 | -0.0933 | 0.0935 | 0.1345 | 0.1320 |
| Gaussian | 0.071 | 0.168 | -0.0943 | 0.0949 | 0.1627 | 0.1606 |
| Cauchy-Lorentz | 0.024 | 0.063 | -0.0882 | 0.0886 | 0.0613 | 0.0613 |
| Langevin | 0.031 | 0.079 | -0.0892 | 0.0894 | 0.0356 | 0.0349 |

Table B.4: Optimized distributions for AISI 430, presenting the model accuracy and the parameters of the distribution function.

| Distr. funct. | ϵ_{rms} (T) | ϵ_{max} (T) | h_m (-) | h_c (-) | σ_m (-) | σ_c (-) |
|--------------------|-------------------------|-------------------------|--------------|--------------|-------------------|-------------------|
| Hyperbolic tangent | 0.054 | 0.193 | -0.1670 | 0.1692 | 0.1818 | 0.1847 |
| Gaussian | 0.060 | 0.200 | -0.1690 | 0.1710 | 0.2130 | 0.2163 |
| Cauchy-Lorentz | 0.035 | 0.147 | -0.1625 | 0.1664 | 0.0917 | 0.0967 |
| Langevin | 0.037 | 0.167 | -0.1633 | 0.1662 | 0.0527 | 0.0563 |

Bibliography

- [1] A. A. M. Abdallah and L. R. Dupré, “A Rogowski-Chattock coil for local magnetic field measurements: sources of error,” *Measurement Science and Technology*, vol. 21, no. 10, p. 107003, 2010. Cited on page 58.
- [2] A. A. M. Abdallah and L. R. Dupré, “Local magnetic measurements in magnetic circuits with highly non-uniform electromagnetic fields,” *Measurement Science and Technology*, vol. 21, no. 4, p. 045109, 2010. Cited on page 58.
- [3] A. A. M. Abdallah, “An inverse problem based methodology with uncertainty analysis for the identification of magnetic material characteristics of electromagnetic devices,” Ph.D. dissertation, Ghent University, 2012. Cited on page 57.
- [4] A. A. Adly and I. D. Mayergoyz, “Experimental testing of the average Preisach model of hysteresis,” *Magnetics, IEEE Transactions on*, vol. 28, no. 5, pp. 2268–2270, 1992. Cited on page 65.
- [5] M. Al Janaideh, J. Mao, S. Rakheja, W. Xie, and C.-Y. Su, “Generalized Prandtl-Ishlinskiĭ hysteresis model: Hysteresis modeling and its inverse for compensation in smart actuators,” in *47th IEEE Conference on Decision and Control, 2008. CDC 2008*, 2008, pp. 5182–5187. Cited on pages 68 and 69.
- [6] M. Al Janaideh, S. Rakheja, and C.-Y. Su, “A generalized Prandtl-Ishlinskiĭ model for characterizing the hysteresis and saturation nonlinearities of smart actuators,” *Smart Materials and Structures*, vol. 18, no. 4, p. 045001, 2009. Cited on pages 68 and 69.
- [7] M. Al Janaideh, S. Rakheja, and C.-Y. Su, “A generalized Prandtl-Ishlinskiĭ model for characterizing rate dependent hysteresis,” in *Control Applications, 2007. CCA 2007. IEEE International Conference on*, Oct 2007, pp. 343–348. Cited on page 68.

- [8] M. Al Janaideh, C.-Y. Su, and S. Rakheja, "Development of the rate-dependent Prandtl-Ishlinskiĭ model for smart actuators," *Smart Materials and Structures*, vol. 17, no. 3, p. 035026, 2008. Cited on page 69.
- [9] O. Al Janaideh, "A stop operator-based prandtl-ishlinskii model for compensation of smart actuator hysteresis effects," 2009. Cited on pages 68 and 69.
- [10] A. Albrecht, S. S. Park, Y. Altintas, and G. Pritschow, "High frequency bandwidth cutting force measurement in milling using capacitance displacement sensors," *International Journal of Machine Tools and Manufacture*, vol. 45, no. 9, pp. 993–1008, 2005. Cited on page 158.
- [11] O. Aljanaideh, S. Rakheja, and C.-Y. Su, "A Prandtl-Ishlinskiĭ model for characterizing asymmetric and saturated hysteresis of smart material actuators," in *Intelligent Robotics and Applications*, ser. Lecture Notes in Computer Science, J. Lee, M. Lee, H. Liu, and J.-H. Ryu, Eds. Springer Berlin Heidelberg, 2013, vol. 8103, pp. 635–643. Cited on page 68.
- [12] H. Allag, A. Kedous-Lebouc, and M. E. H. Latreche, "Preisach hysteresis implementation in reluctance network method, comparison with finite element method," in *Symposium EPNC*, 2008. Cited on pages 65, 66, 98, and 131.
- [13] Y. O. Amor, M. Féliachi, and H. Mohellebi, "A new convergence procedure for the finite element computing associated to Preisach hysteresis model," *Magnetics, IEEE Transactions on*, vol. 36, no. 4, pp. 1242–1245, Jul 2000. Cited on pages 72 and 98.
- [14] P. Andrei and A. Stancu, "Identification method analyses for the scalar generalized moving Preisach model using major hysteresis loops," *Magnetics, IEEE Transactions on*, vol. 36, no. 4, pp. 1982–1989, 2000. Cited on pages 97 and 98.
- [15] K. Atallah, Z. Q. Zhu, and D. Howe, "An improved method for predicting iron losses in brushless permanent magnet dc drives," *Magnetics, IEEE Transactions on*, vol. 28, no. 5, pp. 2997–2999, Sep 1992. Cited on page 110.
- [16] D. L. Atherton, B. Szpunar, and J. A. Szpunar, "A new approach to Preisach diagrams," *Magnetics, IEEE Transactions on*, vol. 23, no. 3, pp. 1856–1865, May 1987. Cited on page 65.
- [17] B. Azzerboni, E. Cardelli, G. Finocchio, and F. La Foresta, "Remarks about Preisach function approximation using Lorentzian function and its identification for nonoriented steels," *Magnetics, IEEE Transactions on*, vol. 39, no. 5, pp. 3028–3030, 2003. Cited on page 98.

- [18] A. F. Bakker, B. C. A. Dirkx, and M. van Lent, "Design of a micrometer precision stage in a laser cutter machine," in *ASPE Proceedings*, Oct 2005. Cited on page 18.
- [19] J. Bao, B. L. J. Gysen, N. H. Vrijsen, R. L. J. Sprangers, and E. A. Lomonova, "Optimization of the force density for medium-stroke reluctance actuators," in *Proceedings of IEEE International Electric Machines Drives Conference, IEMDC 2013*, 2013, pp. 1458–1465. Cited on page 18.
- [20] J. Bao, N. H. Vrijsen, B. L. J. Gysen, R. L. J. Sprangers, and E. A. Lomonova, "Optimization of the force density for medium-stroke reluctance actuators," *Industry Applications, IEEE Transactions on*, In press. Cited on page 18.
- [21] V. Basso, G. Berlotti, A. Infortuna, and M. Pasquale, "Preisach model study of the connection between magnetic and microstructural properties of soft magnetic materials," *Magnetics, IEEE Transactions on*, vol. 31, no. 6, pp. 4000–4005, 1995. Cited on page 65.
- [22] J. P. A. Bastos, N. Sadowski, J. Viane Leite, N. Jhoé Batistela, K. Hoffmann, G. Meunier, and O. Chadebec, "A differential permeability 3-D formulation for anisotropic vector hysteresis analysis," *Magnetics, IEEE Transactions on*, vol. 50, no. 2, pp. 341–344, Feb 2014. Cited on page 79.
- [23] L. H. Bennett, F. Vajda, U. Atzmony, and L. J. Swartzendruber, "Accommodation study of a nanograin iron powder," *Magnetics, IEEE Transactions on*, vol. 32, no. 5, pp. 4493–4495, Sep 1996. Cited on page 51.
- [24] L. Bernard, X. Mininger, L. Daniel, G. Krebs, F. Bouillault, and M. Gabsi, "Effect of stress on switched reluctance motors: A magneto-elastic finite-element approach based on multiscale constitutive laws," *Magnetics, IEEE Transactions on*, vol. 47, no. 9, pp. 2171–2178, Sep 2011. Cited on page 48.
- [25] G. Bertotti, "Physical interpretation of eddy current losses in ferromagnetic materials. I. Theoretical considerations," *Journal of Applied Physics*, vol. 57, no. 6, pp. 2110–2117, 1985. Cited on pages 109 and 116.
- [26] G. Bertotti, "General properties of power losses in soft ferromagnetic materials," *Magnetics, IEEE Transactions on*, vol. 24, no. 1, pp. 621–630, 1988. Cited on pages 64, 109, and 110.
- [27] G. Bertotti, "Dynamic generalization of the scalar Preisach model of hysteresis," *Magnetics, IEEE Transactions on*, vol. 28, no. 5, pp. 2599–2601, Sep 1992. Cited on pages 65 and 109.

- [28] G. Bertotti, *Hysteresis in magnetism for physicist, materials scientists, and engineers*. Academic Press, 1998, vol. 1. Cited on pages 41, 42, 44, 46, 71, 80, 109, 111, and 112.
- [29] G. Bertotti and I. D. Mayergoyz, *The Science of Hysteresis*. Elsevier Academic Press, 2006, vol. 1. Cited on pages 42, 45, 47, 50, 51, 80, and 90.
- [30] H. Bleuler, “A survey of magnetic levitation and magnetic bearing types,” *JSME international journal, Vibration, control engineering, engineering for industry*, vol. 35, no. 3, pp. 335–342, Sep 1992. Cited on page 18.
- [31] S. Bobbio, G. Milano, C. Serpico, and C. Visone, “Models of magnetic hysteresis based on play and stop hysterons,” *Magnetics, IEEE Transactions on*, vol. 33, no. 6, pp. 4417–4426, Nov 1997. Cited on pages 68 and 69.
- [32] S. Boukhtache, B. Azoui, and M. Féliachi, “A novel model for magnetic hysteresis of silicon-iron sheets,” *The European Physical Journal Applied Physics*, vol. 34, pp. 201–204, 2006. Cited on page 67.
- [33] R. Bozorth, *Ferromagnetism*, ser. An IEEE Press Classic Reissue. Wiley, 1993. Cited on pages 43 and 48.
- [34] L. Brillouin, “Les moments de rotation et le magnétisme dans la mécanique ondulatoire,” *Journal de Physique et le Radium*, vol. 8, no. 2, pp. 74–84, Feb 1927. Cited on pages 67, 70, and 98.
- [35] M. Brokate and J. Sprekels, *Hysteresis and Phase Transitions*. Springer, 1996. Cited on pages 68 and 69.
- [36] H. Butler, “Position control in lithographic equipment,” *Control Systems, IEEE*, vol. 31, no. 5, pp. 28–47, Oct 2011. Cited on pages 3, 10, and 31.
- [37] E. Cardelli, E. Della Torre, and A. Faba, “Numerical modeling of hysteresis in Si-Fe steels,” *Magnetics, IEEE Transactions on*, vol. 50, no. 2, pp. 329–332, Feb 2014. Cited on page 79.
- [38] E. Cardelli and A. Faba, “A benchmark problem of vector magnetic hysteresis for numerical models,” *Magnetics, IEEE Transactions on*, vol. 50, no. 2, pp. 1049–1052, Feb 2014. Cited on page 79.
- [39] C. J. Carpenter, “Magnetic equivalent circuits,” *Electrical Engineers, Proceedings of the Institution of*, vol. 115, no. 10, pp. 1503–1511, Oct 1968. Cited on page 18.
- [40] G. W. Carter, *The electromagnetic field in its engineering aspects*. Bungay, Suffolk: Richard Clay and Company Ltd., 1954. Cited on page 13.

- [41] P. J. J. H. Casteren, D. T. E. H. van and E. A. Lomonova, “3-D numerical surface charge model including relative permeability: The general theory,” *Magnetics, IEEE Transactions on*, vol. 50, no. 11, 2014. Cited on page 19.
- [42] J. J. Cathey, *Electric machines*, ser. McGraw-Hill Series in Electrical and computer Engineering. McGraw-Hill Education, 2001. Cited on pages 11 and 15.
- [43] *User manual*, Flux 11.2 ed., Cedrat, Meylan, Cedex, Dec 2013. Cited on page 72.
- [44] T. Chevalier, A. Kedous-Lebouc, B. Cornut, and C. Cester, “A new dynamic hysteresis model for electrical steel sheet,” *Physica B: Condensed Matter*, vol. 275, no. 1-3, pp. 197–201, 2000. Cited on page 110.
- [45] S. Chikazumi, *Physics of Magnetism*, ser. Wiley Series on the science and technology of materials. Wiley, 1964. Cited on pages 70 and 98.
- [46] K. Chwastek, “Modelling offset minor hysteresis loops with the modified Jiles-Atherton description,” *Journal of Physics D: Applied Physics*, vol. 42, no. 16, p. 165002, 2009. Cited on page 67.
- [47] K. Chwastek, “Modelling magnetic properties of MnZn ferrites with the modified Jiles-Atherton description,” *Journal of Physics D: Applied Physics*, vol. 43, no. 1, p. 015005, 2010. Cited on page 67.
- [48] K. Chwastek, J. Szczygłowski, and W. Wilczyński, “Modelling dynamic hysteresis loops in steel sheets,” *COMPTEL: The International Journal for Computation and Mathematics in Electrical and Electronic Engineering*, vol. 28, no. 3, pp. 603 – 612, 2009. Cited on page 67.
- [49] *Vector Fields Software*, Opera version 16.0 ed., Cobham Technical Services, Kidlington, Oxford, 2013. Cited on pages 19, 64, 73, and 135.
- [50] J. M. D. Coey, *Magnetism and Magnetic Materials*. Cambridge University Press, 2010. Cited on pages 9, 44, 47, and 49.
- [51] P. Cogež, M. Graef, B. Huizing, R. Mahnkopf, H. Ishiuchi, N. I. S. Choi, J. H. Choi, C. H. Diaz, Y. C. See, P. Gargini, T. Kingscott, and I. Steff, “International technology roadmap for semiconductors,” ITRS, Tech. Rep., 2013. Cited on pages 1, 2, and 3.
- [52] B. Coleman and M. L. Hodgdon, “On a class of constitutive relations for ferromagnetic hysteresis,” *Archive for Rational Mechanics and Analysis*, vol. 99, no. 4, pp. 375–396, Dec 1987. Cited on pages 75 and 98.

- [53] J. C. Compter, "Electro-dynamic planar motor," *Precision Engineering*, vol. 28, no. 2, pp. 171 – 180, 2004. Cited on page 3.
- [54] J. C. Compter, E. A. Lomonova, and J. Makarovic, "Direct 3-D method for performance prediction of a linear moving coil actuator with various topologies," *IEE Proceedings - Science, Measurement and Technology*, vol. 150, pp. 183–191(8), Jul 2003. Cited on page 19.
- [55] D. R. Cornejo, M. L. Bue, V. Basso, G. Bertotti, and F. P. Missell, "Moving Preisach model analysis of nanocrystalline SmFeCo," *Journal of Applied Physics*, vol. 81, no. 8, pp. 5588–5590, 1997. Cited on page 79.
- [56] G. Crevecoeur, P. Sergeant, L. R. Dupré, L. Vandenbossche, and R. van de Walle, "Analysis of the local material degradation near cutting edges of electrical steel sheets," *Magnetics, IEEE Transactions on*, vol. 44, no. 11, pp. 3173–3176, Nov 2008. Cited on page 56.
- [57] B. D. Cullity, *Introduction to magnetic materials*, ser. Addison-Wesley series in metallurgy and materials. Addison-Wesley Pub. Co., 1972. Cited on pages 42, 45, 70, and 98.
- [58] B. D. Cullity and C. D. Graham, *Introduction to Magnetic Materials*. Wiley, 2009. Cited on page 98.
- [59] L. Daniel, "An analytical model for the effect of multiaxial stress on the magnetic susceptibility of ferromagnetic materials," *Magnetics, IEEE Transactions on*, vol. 49, no. 5, pp. 2037–2040, May 2013. Cited on page 56.
- [60] D. Davino, A. Giustiniani, and C. Visone, "Fast inverse Preisach models in algorithms for static and quasistatic magnetic-field computations," *Magnetics, IEEE Transactions on*, vol. 44, no. 6, pp. 862–865, Jun 2008. Cited on page 66.
- [61] B. J. H. de Bruyn, N. H. Vrijsen, J. W. Jansen, and E. A. Lomonova, "Requirements for 3d magnetostriction measurement instruments," in *Proceedings of the the Sixteenth Biennial IEEE Conference on Electromagnetic Field Computation, CEFC 2014*, Annceny, France, 25-28 May 2014. Cited on pages 49 and 93.
- [62] M. de Wulf, L. Vandeveld, J. Maes, L. R. Dupre, and J. A. A. Melkebeek, "Computation of the Preisach distribution function based on a measured Everett map," *Magnetics, IEEE Transactions on*, vol. 36, no. 5, pp. 3141–3143, 2000. Cited on page 95.
- [63] F. Delince, A. Nicolet, F. Henrotte, A. Genon, and W. Legros, "Influence of hysteresis on the behaviour of coupled finite element-electric circuit

- models,” *Magnetics, IEEE Transactions on*, vol. 30, no. 5, pp. 3383–3386, Sep 1994. Cited on pages 65 and 72.
- [64] E. Della Torre, “Effect of interaction on the magnetization of single-domain particles,” *Audio and Electroacoustics, IEEE Transactions on*, vol. 14, no. 2, pp. 86–92, Jun 1966. Cited on pages 64, 65, and 79.
- [65] E. Della Torre, J. Oti, and G. Kádár, “Preisach modeling and reversible magnetization,” *Magnetics, IEEE Transactions on*, vol. 26, no. 6, pp. 3052–3058, 1990. Cited on page 79.
- [66] E. Della Torre and G. Kádár, “Hysteresis modeling: II. accommodation,” *Magnetics, IEEE Transactions on*, vol. 23, no. 5, pp. 2823–2825, Sep 1987. Cited on pages 51 and 65.
- [67] E. Della Torre and F. Vajda, “Properties of accommodation models,” *Magnetics, IEEE Transactions on*, vol. 31, no. 3, pp. 1775–1780, May 1995. Cited on page 65.
- [68] E. Dlala, J. Saitz, and A. Arkkio, “Inverted and forward Preisach models for numerical analysis of electromagnetic field problems,” *Magnetics, IEEE Transactions on*, vol. 42, no. 8, pp. 1963–1973, 2006. Cited on page 66.
- [69] C.-I. Dobrotő and A. Stancu, “What does a first-order reversal curve diagram really mean? a study case: Array of ferromagnetic nanowires,” *Journal of Applied Physics*, vol. 113, no. 4, 2013. Cited on page 66.
- [70] R. Dong and Y. Tan, “A modified Prandtl-Ishlinskiĭ modeling method for hysteresis,” *Physica B: Condensed Matter*, vol. 404, no. 8-11, pp. 1336 – 1342, 2009. Cited on page 68.
- [71] P. M. M. Duhem, *The Evolution of Mechanics*, ser. Genesis and Method Series. Springer, 1980 (Original edition: L’*évolution de la mécanique*, Joainin, Paris, 1903). Cited on page 75.
- [72] L. R. Dupré, “Elektromagnetische karakterisatie van niet-georiënteerd elektroblik,” Ph.D. dissertation, RUG. Faculteit Toegepaste Wetenschappen, 1995. Cited on pages 67, 93, and 95.
- [73] L. R. Dupré, G. Bertotti, V. Basso, F. Fiorillo, and J. A. A. Melkebeek, “Generalisation of the dynamic Preisach model toward grain oriented Fe-Si alloys,” *Physica B: Condensed Matter*, vol. 275, no. 1-3, pp. 202 – 206, 2000. Cited on pages 79 and 109.
- [74] L. R. Dupré, O. Bottauscio, M. Chiampi, F. Fiorillo, M. Lo Bue, J. A. A. Melkebeek, M. Repetto, and M. Von Rauch, “Dynamic preisach modelling of ferromagnetic laminations under distorted flux excitations,” *Magnetics*,

- IEEE Transactions on*, vol. 34, no. 4, pp. 1231–1233, Jul 1998. Cited on page 109.
- [75] L. R. Dupré, O. Bottauscio, M. Chiampi, M. Repetto, and J. A. A. Melkebeek, “Modeling of electromagnetic phenomena in soft magnetic materials under unidirectional time periodic flux excitations,” *Magnetics, IEEE Transactions on*, vol. 35, no. 5, pp. 4171–4184, 1999. Cited on pages 67 and 109.
- [76] L. R. Dupré, J. J. Gyselinck, and J. A. A. Melkebeek, “Complementary finite element methods in 2D magnetics taking into account a vector Preisach model,” *Magnetics, IEEE Transactions on*, vol. 34, no. 5, pp. 3048–3051, Sep 1998. Cited on page 72.
- [77] L. R. Dupré and J. A. A. Melkebeek, “Electromagnetic hysteresis modelling: from material science to finite element analysis of devices,” *International Compumag Society Newsletter*, vol. 10, no. 3, pp. 4–15, 2003. Cited on page 79.
- [78] L. R. Dupré, R. Van Keer, and J. A. A. Melkebeek, “On a magnetodynamic model for the iron losses in non-oriented steel laminations,” *Journal of Physics D: Applied Physics*, vol. 29, no. 3, p. 855, 1996. Cited on page 109.
- [79] L. R. Dupré, R. Van Keer, and J. A. A. Melkebeek, “Generalized scalar Preisach model for grain oriented materials excited along arbitrary directions,” *Journal of Applied Physics*, vol. 89, no. 11, pp. 7245–7247, Jun 2001. Cited on page 109.
- [80] L. R. Dupré, R. Van Keer, and J. A. A. Melkebeek, “Modelling the electromagnetic behaviour of sife alloys using the Preisach theory and the principle of loss separation,” *Mathematical Problems in Engineering*, vol. 7, no. 2, pp. 113–128, 2001. Cited on pages 110 and 117.
- [81] L. R. Dupré, R. Van Keer, and J. A. A. Melkebeek, “A 2D finite element procedure for magnetic field analysis taking into account a vector Preisach model,” *Journal of Mathematical Problems in Engineering*, vol. 3, pp. 267–286, 1997. Cited on page 72.
- [82] A. A. Eielsen, “Topics in control of nanopositioning devices,” Ph.D. dissertation, Norwegian University of Science and Technology, Trondheim, Nov 2012. Cited on page 75.
- [83] A. A. Eielsen, J. T. Gravdahl, and K. Y. Pettersen, “Adaptive feed-forward hysteresis compensation for piezoelectric actuators,” *Review of Scientific Instruments*, vol. 83, no. 8, 2012. Cited on page 158.

- [84] D. H. Everett, "A general approach to hysteresis. Part 4. an alternative formulation of the domain model," *Transactions of the Faraday Society*, vol. 51, pp. 1551–1557, 1955. Cited on page 95.
- [85] F. Fiorillo, *Measurement and characterization of magnetic materials*, ser. Elsevier series in electromagnetism. Elsevier Academic Press, 2004. Cited on pages 52, 53, and 57.
- [86] F. Fiorillo and A. Novikov, "An improved approach to power losses in magnetic laminations under nonsinusoidal induction waveform," *Magnetics, IEEE Transactions on*, vol. 26, no. 5, pp. 2904–2910, Sep 1990. Cited on page 116.
- [87] F. Fiorillo, "Measurements of magnetic materials," *Metrologia*, vol. 47, no. 2, p. S114, 2010. Cited on pages 56 and 57.
- [88] E. P. Furlani, *Permanent magnet and electromechanical devices - materials, analysis, and applications*. United States of America: Academic Press, 2001. Cited on pages 17 and 18.
- [89] J. Füzi, "Experimental verification of a dynamic hysteresis model," *Physica B: Condensed Matter*, vol. 343, no. 1 - 4, pp. 80 – 84, 2004. Cited on pages 97, 98, and 100.
- [90] D. C. Gall and L. G. A. Sims, "On the theory and measurement of the magnetic properties of iron," *Electrical Engineers, Journal of the Institution of*, vol. 74, no. 449, pp. 453–468, May 1934. Cited on page 74.
- [91] W.-C. Gan, N. C. Cheung, and L. Qiu, "Position control of linear switched reluctance motors for high-precision applications," *Industry Applications, IEEE Transactions on*, vol. 39, no. 5, pp. 1350–1362, Sep 2003. Cited on page 18.
- [92] L. Gaul, M. Kögl, and M. Wagner, *Boundary Element Methods for Engineers and Scientists*, ser. Engineering Online Library. Springer, 2003. Cited on page 18.
- [93] G. Gautschi, *Piezoelectric sensorics: force, strain, pressure, acceleration and acoustic emission sensors, materials and amplifiers*. Springer, 2002. Cited on pages 157 and 158.
- [94] P. Ge and M. Jouaneh, "Generalized Preisach model for hysteresis non-linearity of piezoceramic actuators," *Precision Engineering*, vol. 20, no. 2, pp. 99–111, 1997. Cited on page 65.
- [95] G. Gu and L. Zhu, "High-speed tracking control of piezoelectric actuators using an ellipse-based hysteresis model," *Review of Scientific Instruments*, vol. 81, no. 8, 2010. Cited on pages 74 and 158.

- [96] G. Gu and L. Zhu, "Modeling of rate-dependent hysteresis in piezoelectric actuators using a family of ellipses," *Sensors and Actuators A: Physical*, vol. 165, no. 2, pp. 303–309, 2011. Cited on page 74.
- [97] J. J. Gyselinck, "Twee-dimensionale dynamische eindige-elementen-modellering van statische en roterende elektromagnetische energieomzetters," Ph.D. dissertation, Universiteit Gent, 2000. Cited on pages 95 and 121.
- [98] J. J. Gyselinck, L. Vandeveld, J. A. A. Melkebeek, P. Dular, F. Henrotte, and W. Legros, "Calculation of eddy currents and associated losses in electrical steel laminations," *Magnetics, IEEE Transactions on*, vol. 35, no. 3, pp. 1191–1194, May 1999. Cited on page 121.
- [99] B. Hague, *Electromagnetic problems in electrical engineering*. H. Milford, 1929. Cited on page 18.
- [100] P. Hahne, R. Dietz, B. Rieth, and T. Weiland, "Determination of anisotropic equivalent conductivity of laminated cores for numerical computation," *Magnetics, IEEE Transactions on*, vol. 32, no. 3, pp. 1184–1187, May 1996. Cited on pages 73 and 136.
- [101] J. Han and C. Moraga, "The influence of the sigmoid function parameters on the speed of backpropagation learning," in *From Natural to Artificial Neural Computation*. Springer Berlin Heidelberg, 1995, vol. 930, pp. 195–201. Cited on page 97.
- [102] R. G. Harrison, "A physical model of spin ferromagnetism," *Magnetics, IEEE Transactions on*, vol. 39, no. 2, pp. 950–960, Mar 2003. Cited on pages 64 and 70.
- [103] R. G. Harrison, "Variable-domain-size theory of spin ferromagnetism," *Magnetics, IEEE Transactions on*, vol. 40, no. 3, pp. 1506–1515, May 2004. Cited on page 70.
- [104] R. G. Harrison, "Physical theory of ferromagnetic first-order return curves," *Magnetics, IEEE Transactions on*, vol. 45, no. 4, pp. 1922–1939, Apr 2009. Cited on page 70.
- [105] R. G. Harrison, "Positive-feedback theory of hysteretic recoil loops in hard ferromagnetic materials," *Magnetics, IEEE Transactions on*, vol. 47, no. 1, pp. 175–191, Jan 2011. Cited on pages 70 and 71.
- [106] R. G. Harrison, "Modeling high-order ferromagnetic hysteretic minor loops and spirals using a generalized positive-feedback theory," *Magnetics, IEEE Transactions on*, vol. 48, no. 3, pp. 1115–1129, 2012. Cited on pages 63, 68, 70, 71, and 98.

- [107] R. G. Harrison, “Calculating the spontaneous magnetization and defining the Curie temperature using a positive-feedback model,” *Journal of Applied Physics*, vol. 115, no. 3, 2014. Cited on page 70.
- [108] P. Henrici, *Applied and Computational Complex Analysis, Discrete Fourier Analysis, Cauchy Integrals, Construction of Conformal Maps, Univalent Functions*, ser. Applied and Computational Complex Analysis. Wiley, 1993. Cited on page 18.
- [109] F. Henrotte, A. Nicolet, F. Delince, A. Genon, and W. Legros, “Modeling of ferromagnetic materials in 2D finite element problems using Preisach’s model,” *Magnetics, IEEE Transactions on*, vol. 28, no. 5, pp. 2614–2616, Sep 1992. Cited on pages 65 and 72.
- [110] M. L. Hodgdon, “Applications of a theory of ferromagnetic hysteresis,” *Magnetics, IEEE Transactions on*, vol. 24, no. 1, pp. 218–221, 1988. Cited on pages 63 and 75.
- [111] K. Hoffmann, *An introduction to measurements using strain gages: with 172 figures and tables*. Hottinger Baldwin Messtechnik GmbH, 1989. Cited on page 158.
- [112] S. A. J. Hol, J. Huang, W. Zhou, M. Koot, H. Vermeulen, J. van Eijk, and R. Munnig-Schmidt, “Highly accurate passive actuation system,” in *Proceedings of the 13th euspen International Conference*, Berlin, May 2013. Cited on page 3.
- [113] R. Hoogendijk, “Control of flexible motion systems using frequency response data,” Ph.D. dissertation, Eindhoven University of Technology, Jul 2014. Cited on page 3.
- [114] D. Howe, “Magnetic actuators,” *Sensors and Actuators A: Physical*, vol. 81, no. 1-3, pp. 268–274, 2000. Cited on page 18.
- [115] E. Ilhan, M. F. J. Kremers, E. T. Motoasca, J. J. H. Paulides, and E. A. Lomonova, “Spatial discretization methods for air gap permeance calculations in double salient traction motors,” *Industry Applications, IEEE Transactions on*, vol. 48, no. 6, pp. 2165–2172, Nov 2012. Cited on page 19.
- [116] E. Ilhan, J. J. H. Paulides, L. Encica, and E. A. Lomonova, “Tooth contour method implementation for the flux-switching PM machines,” in *Electrical Machines (ICEM), 2010 XIX International Conference on*, Sep 2010, pp. 1–6. Cited on page 24.

- [117] *Magnetic materials - Part 6: Methods of measurement of the magnetic properties of magnetically soft metallic and powder materials at frequencies in the range 20 Hz to 200 kHz by the use of ring specimens*, International Electrotechnical Commission Std. 60 404-6, 2003. Cited on page 57.
- [118] *Magnetic materials - Part 1: Classification*, International Electrotechnical Commission (IEC) Std. 60 404-1, 2000. Cited on page 52.
- [119] R. V. Iyer and X. Tan, "Control of hysteretic systems through inverse compensation," *Control Systems, IEEE*, vol. 29, no. 1, pp. 83–99, Feb 2009. Cited on page 69.
- [120] J.-P. Jastrzembski and B. Ponick, "Design of a conveyor directly driven by a hybrid linear motor following FEM and reluctance network approach," in *Linear Drives for Industry Applications (LDIA 2011)*, In Proceedings of The Eighth International Symposium on, 2011. Cited on page 18.
- [121] T.-C. Jeong, W.-H. Kim, M.-J. Kim, K.-D. Lee, J.-J. Lee, J.-H. Han, T.-H. Sung, H.-J. Kim, and J. Lee, "Current harmonics loss analysis of 150-kW traction interior permanent magnet synchronous motor through co-analysis of $d-q$ axis current control and finite element method," *Magnetics, IEEE Transactions on*, vol. 49, no. 5, pp. 2343–2346, May 2013. Cited on page 121.
- [122] D. C. Jiles, "Frequency dependence of hysteresis curves in conducting magnetic materials," *Journal of Applied Physics*, vol. 76, no. 10, pp. 5849–5855, 1994. Cited on page 109.
- [123] D. C. Jiles and D. L. Atherton, "Theory of ferromagnetic hysteresis (invited)," *Journal of Applied Physics*, vol. 55, no. 6, pp. 2115–2120, Mar 1984. Cited on pages 63, 64, 67, and 98.
- [124] D. C. Jiles and D. L. Atherton, "Theory of ferromagnetic hysteresis," *Journal of Magnetism and Magnetic Materials*, vol. 61, no. 1-2, pp. 48–60, 1986. Cited on pages 64 and 98.
- [125] J.-M. Jin, *The Finite Element Method in Electromagnetics*, 2nd ed. Wiley-IEEE Press, 2003. Cited on page 18.
- [126] G. Kádár and E. Dellar Torre, "Hysteresis modeling: I. non-congruency," *Magnetics, IEEE Transactions on*, vol. 23, no. 5, pp. 2820–2822, Sep 1987. Cited on pages 50, 65, and 91.
- [127] G. Kádár, "On the Preisach function of ferromagnetic hysteresis," *Journal of Applied Physics*, vol. 61, no. 8, pp. 4013–4015, 1987. Cited on pages 65, 67, and 91.

- [128] H. Katagiri, Y. Kawase, T. Yamaguchi, K. Kishida, and K. Morinaga, "Characteristics analysis of IPM motor applied by voltage source using 3-D finite element method with prismatic elements," *COMPEL - The International Journal for Computation and Mathematics in Electrical and Electronic Engineering*, vol. 31, no. 5, pp. 1379–1385, 2012. Cited on page 121.
- [129] A. Katalenic, J. de Boeij, H. Butler, and P. P. J. van den Bosch, "Linearization of a current-driven reluctance actuator with hysteresis compensation," *Mechatronics*, vol. 23, no. 2, pp. 163–171, 2013. Cited on page 143.
- [130] A. Katalenic, "Control of reluctance actuators for high-precision positioning," Ph.D. dissertation, Eindhoven University of Technology, Apr 2013. Cited on page 146.
- [131] M. Kersten, "Zur theorie der koerzitivkraft," *Zeitschrift für Physik*, vol. 124, no. 7-12, pp. 714–741, 1948. Cited on page 67.
- [132] M. A. Krasnosel'skiĭ, A. V. Pokrovskiĭ, and M. Niezgodka, *Systems with hysteresis*, ser. Nauka, Moscow (1983). Springer, 1989. Cited on pages 63, 64, 65, 68, 69, and 79.
- [133] M. F. J. Kremers, J. J. H. Paulides, E. Ilhan, J. L. G. Janssen, and E. A. Lomonova, "Relative permeability in a 3D analytical surface charge model of permanent magnets," *Magnetics, IEEE Transactions on*, vol. 49, no. 5, pp. 2299–2302, May 2013. Cited on page 19.
- [134] A. Krings, S. Nategh, O. Wallmark, and J. Soulard, "Influence of the welding process on the performance of slotless PM motors with SiFe and NiFe stator laminations," *Industry Applications, IEEE Transactions on*, vol. 50, no. 1, pp. 296–306, Jan 2014. Cited on page 56.
- [135] D. C. J. Krop, "Integration of dual electromagnetic energy conversions," Ph.D. dissertation, Eindhoven University of Technology, Sep 2013. Cited on pages 18, 19, and 25.
- [136] D. C. J. Krop, L. Encica, and E. A. Lomonova, "Analysis of a novel double sided flux switching linear motor topology," in *Electrical Machines (ICEM), 2010 XIX International Conference on*, Sep 2010, pp. 1–5. Cited on pages 19 and 24.
- [137] D. C. J. Krop, J. W. Jansen, and E. A. Lomonova, "Analysis and design of a tubular linear PM motor with integrated contactless energy transfer," in *IECON 2011 - 37th Annual Conference on IEEE Industrial Electronics Society*, Nov 2011, pp. 1752–1757. Cited on page 18.

- [138] A. Ktena, D. I. Fotiadis, P. D. Spanos, and C. V. Massalas, "A Preisach model identification procedure and simulation of hysteresis in ferromagnets and shape-memory alloys," *Physica B: Condensed Matter*, vol. 306, no. 1-4, pp. 84–90, 2001, proceedings of the Third International Symposium on Hysteresis and Micromagnetics Modeling. Cited on page 101.
- [139] V. A. Kuznetsov and P. Brochet, "Numerical modelling of electromagnetic process in electromechanical systems," *COMPEL: The International Journal for Computation and Mathematics in Electrical and Electronic Engineering*, vol. 22, no. 4, pp. 1142–1154, 2003. Cited on pages 19 and 23.
- [140] E. Lamprecht and R. Graf, "Fundamental investigations of eddy current losses in laminated stator cores created through the impact of manufacturing processes," in *Electric Drives Production Conference (EDPC), 2011 1st International*, Sep 2011, pp. 29–35. Cited on page 55.
- [141] E. Lamprecht, M. Homme, and T. Albrecht, "Investigations of eddy current losses in laminated cores due to the impact of various stacking processes," in *Electric Drives Production Conference (EDPC), 2012 2nd International*, Oct 2012, pp. 1–8. Cited on page 55.
- [142] L. Landau and E. Lifshits, "On the theory of the dispersion of magnetic permeability in ferromagnetic bodies," *Physikalische zeitschrift der Sowjetunion*, vol. 8, pp. 153–169, 1935. Cited on pages 45 and 70.
- [143] P. Langevin, "Magnétisme et théorie des électrons," *Annales de chimie et de physique*, vol. 5, pp. 70–127, 1905. Cited on pages 63, 67, 70, and 98.
- [144] J. D. Lavers, P. Biringer, and H. Hollitscher, "A simple method of estimating the minor loop hysteresis loss in thin laminations," *Magnetics, IEEE Transactions on*, vol. 14, no. 5, pp. 386–388, Sep 1978. Cited on page 110.
- [145] C. Lee, T. Itoh, R. Maeda, and T. Suga, "Characterization of micro-machined piezoelectric PZT force sensors for dynamic scanning force microscopy," *Review of Scientific Instruments*, vol. 68, no. 5, pp. 2091–2100, May 1997. Cited on page 157.
- [146] J. V. Leite, A. Benabou, N. Sadowski, Y. L. Menach, S. Clenet, and P. A. Da Silva, "Implementation of a vector hysteresis model in 2D finite element analysis: Study of a RSST with anisotropic sample," *International Journal of Applied Electromagnetics and Mechanics*, vol. 28, no. 1, pp. 41–47, Jan 2008. Cited on page 72.

- [147] P. J. Leonard, D. Rodger, T. Karagular, and P. C. Coles, "Finite element modelling of magnetic hysteresis," *Magnetics, IEEE Transactions on*, vol. 31, no. 3, pp. 1801–1804, May 1995. Cited on page 72.
- [148] B. Lequesne, "Fast-acting, long-stroke solenoids with two springs," *Industry Applications, IEEE Transactions on*, vol. 26, no. 5, pp. 848–856, 1990. Cited on page 18.
- [149] B. Lequesne, "Permanent magnet linear motors for short strokes," in *Industry Applications Society Annual Meeting, 1992., Conference Record of the 1992 IEEE*, vol. 1, Oct 1992, pp. 162–170. Cited on page 18.
- [150] B. Lequesne, "Bistable electromechanical valve actuator," Patent US4779582 A, 1988, US Patent 4,779,582. Cited on page 18.
- [151] J. I. Levine, *Magnetic Materials: Research, Technology and Applications*. Nova Science Publishers, Inc., 2009. Cited on pages 63 and 64.
- [152] W. Li, H. Qiu, X. Zhang, and R. Yi, "Influence of copper plating on electromagnetic and temperature fields in a high-speed permanent-magnet generator," *Magnetics, IEEE Transactions on*, vol. 48, no. 8, pp. 2247–2253, Aug 2012. Cited on page 121.
- [153] S. Lim and S. Min, "Design optimization of permanent magnet actuator using multi-phase level-set model," *Magnetics, IEEE Transactions on*, vol. 48, no. 4, pp. 1641–1644, Apr 2012. Cited on page 31.
- [154] S. Lim, T. Yamada, S. Min, and S. Nishiwaki, "Topology optimization of a magnetic actuator based on a level set and phase-field approach," *Magnetics, IEEE Transactions on*, vol. 47, no. 5, pp. 1318–1321, 2011. Cited on page 31.
- [155] L. Liu, K. K. Tan, S. Chen, C. S. Teo, and T. H. Lee, "Discrete composite control of piezoelectric actuators for high-speed and precision scanning," *Industrial Informatics, IEEE Transactions on*, vol. 9, no. 2, pp. 859–868, May 2013. Cited on page 65.
- [156] D. A. Lowther and P. P. Silvester, *Computer-aided design in magnetics*. Springer-Verlag, 1986. Cited on pages 16 and 17.
- [157] C. Mack, *Fundamental Principles of Optical Lithography: The Science of Microfabrication*. Wiley, 2008. Cited on page 2.
- [158] E. Madelung, *Über Magnetisierung durch schnellverlaufende Ströme und die Wirkungsweise de Rutherford-Marconischen Magnetdetektors*. J. A. Barth, 1905. Cited on page 63.

- [159] J. Makarovic, E. A. Lomonova, and J. C. Compter, "Innovative actuator with two controlled degrees of freedom for precision technology applications," in *Power Electronics and Drives Systems, 2005. PEDS 2005. International Conference on*, vol. 2, Nov 2005, pp. 1177–1183. Cited on pages 19, 23, and 181.
- [160] M. Marracci, B. Tellini, R. Giannetti, and S. L. Martinez, "Experimental analysis of magnetic accommodation properties via the use of complex trajectories," in *IEEE Instrumentation and Measurement Technology Conference, I2MTC 2010*, May 2010, pp. 167–171. Cited on page 51.
- [161] T. Matsuo and M. Miyamoto, "Dynamic and anisotropic vector hysteresis model based on isotropic vector play model for nonoriented silicon steel sheet," *Magnetics, IEEE Transactions on*, vol. 48, no. 2, pp. 215–218, Feb 2012. Cited on page 68.
- [162] T. Matsuo and M. Shimasaki, "Representation theorems for stop and play models with input-dependent shape functions," *Magnetics, IEEE Transactions on*, vol. 41, no. 5, pp. 1548–1551, May 2005. Cited on page 68.
- [163] T. Matsuo, Y. Terada, and M. Shimasaki, "Stop model with input-dependent shape function and its identification methods," *Magnetics, IEEE Transactions on*, vol. 40, no. 4, pp. 1776–1783, Jul 2004. Cited on page 69.
- [164] J. C. Maxwell, "On the physical lines of force," *The London, Edinburgh and Dublin Philosophical Magazine and Journal of Science*, vol. 4, 1861. Cited on page 9.
- [165] J. C. Maxwell, "A dynamic theory of the electromagnetic field," *Philosophical Transactions of the Royal Society of London*, pp. 459–512, 1864. Cited on page 9.
- [166] J. C. Maxwell, *A treatise on electricity and magnetism*. Oxford: Clarendon press, 1873. Cited on pages 9 and 63.
- [167] I. D. Mayergoyz, "Hysteresis models from the mathematical and control theory points of view," *Journal of Applied Physics*, vol. 57, no. 8, pp. 3803–3805, Apr 1985. Cited on page 64.
- [168] I. D. Mayergoyz, "Mathematical models of hysteresis," *Magnetics, IEEE Transactions on*, vol. 22, no. 5, pp. 603–608, 1986. Cited on pages 65 and 79.
- [169] I. D. Mayergoyz, *Mathematical models of hysteresis*. Springer-Verlag, 1991. Cited on pages 65, 68, 79, 80, 83, 88, 92, and 95.

- [170] I. D. Mayergoyz, *Mathematical Models of Hysteresis and their Applications: Second Edition*, ser. Electromagnetism. Elsevier Science, 2003. Cited on page 97.
- [171] I. D. Mayergoyz and G. Friedman, “Generalized Preisach model of hysteresis,” *Magnetics, IEEE Transactions on*, vol. 24, no. 1, pp. 212–217, 1988. Cited on pages 65, 79, and 93.
- [172] R. A. McCurrie, *Ferromagnetic materials: structure and properties*. Academic, 1994. Cited on pages 52 and 53.
- [173] R. T. Merrill and M. W. McElhinny, *The earth’s magnetic field: its history, origin, and planetary perspective*, ser. International Geophysics. Elsevier Science, 1984. Cited on page 9.
- [174] R. Merry, M. Uyanik, R. van de Molengraft, R. Koops, M. van Veghel, and M. Steinbuch, “Identification, control and hysteresis compensation of a 3 DOF metrological AFM,” *Asian Journal of Control*, vol. 11, no. 2, pp. 130–143, 2009. Cited on page 75.
- [175] G. Miano, C. Serpico, L. Verolino, and C. Visone, “Comparison of different hysteresis models in FE analysis of magnetic field diffusion,” *Magnetics, IEEE Transactions on*, vol. 31, no. 3, pp. 1789–1792, May 1995. Cited on page 72.
- [176] A. M. Michaelides, J. Simkin, P. Kirby, and C. P. Riley, “Permanent magnet (de-) magnetization and soft iron hysteresis effects: A comparison of FE analysis techniques,” in *COMPEL: The International Journal for Computation and Mathematics In Electrical and Electronic Engineering, 2010*, vol. 29, no. 4, 2010, pp. 1090–1096. Cited on pages 73 and 136.
- [177] R. Mitsuoka, T. Mifune, T. Matsuo, and C. Kaido, “A vector play model for finite-element eddy-current analysis using the Newton-Raphson method,” *Magnetics, IEEE Transactions on*, vol. 49, no. 5, pp. 1689–1692, May 2013. Cited on page 72.
- [178] S. Mittal and C.-H. Menq, “Hysteresis compensation in electromagnetic actuators through Preisach model inversion,” *Mechatronics, IEEE/ASME Transactions on*, vol. 5, no. 4, pp. 394–409, 2000. Cited on pages 65 and 143.
- [179] D. Miyagi, D. Otome, M. Nakano, and N. Takahashi, “Measurement of magnetic properties of nonoriented electrical steel sheet at liquid nitrogen temperature using single sheet tester,” *Magnetics, IEEE Transactions on*, vol. 46, no. 2, pp. 314–317, Feb 2010. Cited on page 47.

- [180] S. Miyairi and T. Kataoka, "A basic equivalent circuit of the hysteresis motor," *Electrical Engineering Japan (USA)*, vol. 85, pp. 41–50, 1965. Cited on page 74.
- [181] M. Moallem and G. E. Dawson, "An improved magnetic equivalent circuit method for predicting the characteristics of highly saturated electromagnetic devices," *Magnetics, IEEE Transactions on*, vol. 34, no. 5, pp. 3632–3635, Sep 1998. Cited on page 24.
- [182] A. M. F. Mood, F. A. Graybill, and D. C. Boes, *Introduction to the theory of statistics*, ser. McGraw-Hill series in probability and statistics. McGraw-Hill, 1973. Cited on page 98.
- [183] F. C. Moon, *Magneto-solid mechanics*, ser. Wiley-Interscience publication. Wiley, 1984. Cited on pages 17, 42, 44, 48, and 49.
- [184] G. E. Moore, "Cramming more components onto integrated circuits," *Proceedings of the IEEE*, vol. 86, no. 1, pp. 82–85, Jan 1998. Cited on page 1.
- [185] G. E. Moore, "Progress in digital integrated electronics [Technical literature, Copyright 1975 IEEE. Reprinted, with permission. Technical Digest. International Electron Devices Meeting, IEEE, 1975, pp. 11-13.]," *Solid-State Circuits Society Newsletter, IEEE*, vol. 20, no. 3, pp. 36–37, Sep 2006. Cited on page 1.
- [186] G. E. Moore, "Lithography and the future of Moore's law," *Proc. SPIE*, vol. 2438, pp. 2–17, 1995. Cited on page 1.
- [187] A. Mor and S. Gavril, "Eddy current effects on the asynchronous performance of the hysteresis machine," *Journal of the Franklin Institute*, vol. 314, no. 2, pp. 77–93, 1982. Cited on page 74.
- [188] D. M. Munoz, "Design, modelling and control of electrical machines," Ph.D. dissertation, Lund University, Lund, Sweden, 2004. Cited on page 132.
- [189] P. J. Nahin, *Oliver Heaviside: The Life, Work, and Times of an Electrical Genius of the Victorian Age*, ser. Oliver Heaviside. Johns Hopkins University Press, 2002. Cited on pages 9 and 10.
- [190] K. Nakamura, S. Fujio, and O. Ichinokura, "A method for calculating iron loss of an SR motor based on reluctance network analysis and comparison of symmetric and asymmetric excitation," *Magnetics, IEEE Transactions on*, vol. 42, no. 10, pp. 3440–3442, Oct 2006. Cited on page 19.
- [191] L. Néel, "Energie des parois de bloch dans les couches minces," *Comptes Rendus Acad. Sci.*, vol. 241, pp. 533–536, 1955. Cited on page 45.

- [192] S. Nitu, C. Nitu, G. Tuluca, and G. Dumitrescu, "Electromagnetic actuator with magnetic stored energy," *Journal of Materials Processing Technology*, vol. 181, no. 1-3, pp. 153–158, 2007, selected Papers from the 4th Japanese-Mediterranean Workshop on Applied Electromagnetic Engineering for Magnetic, Superconducting and Nano Materials. Cited on page 18.
- [193] D. Nitzan, "Computation of flux switching in magnetic circuits," *Magnetics, IEEE Transactions on*, vol. 1, no. 3, pp. 222–234, Sep 1965. Cited on page 110.
- [194] I. Nova, V. Havlicek, and I. Zemanek, "Dynamic hysteresis loops modeling by means of extended hyperbolic model," *Magnetics, IEEE Transactions on*, vol. 49, no. 1, pp. 148–151, 2013. Cited on page 98.
- [195] D. O'Kelly, "Eddy-current and hysteresis effects in rotating machines," *Proceedings of the IEEE*, vol. 116, no. 3, pp. 391–394, Mar 1969. Cited on page 74.
- [196] F. Ossart and G. Meunier, "Results on modeling magnetic hysteresis using the finite element method," *Journal of Applied Physics*, vol. 69, no. 8, pp. 4835–4837, 1991. Cited on page 72.
- [197] V. Ostovic, "Computation of saturated permanent-magnet ac motor performance by means of magnetic circuits," *Industry Applications, IEEE Transactions on*, vol. IA-23, no. 5, pp. 836–841, Sep 1987. Cited on pages 18 and 181.
- [198] T. T. Overboom, J. W. Jansen, and E. A. Lomonova, "Application of a permanent magnet biased E-core reluctance actuator in a magnetically suspended ceiling actuator," *Magnetics, IEEE Transactions on*, vol. 46, no. 6, pp. 2128–2131, Jun 2010. Cited on page 18.
- [199] T. T. Overboom, J. P. Smeets, J. W. Jansen, and E. A. Lomonova, "Design and control of a magnetically suspended ceiling actuator with infinite planar stroke," *Applied Mechanics and Materials*, vol. 416-417, pp. 492–502, Sep 2013. Cited on page 121.
- [200] J. F. Pan and N. C. Cheung, "Multi-dimensional switched reluctance motors for industrial applications," *Industrial Robot: An International Journal*, vol. 38, no. 4, pp. 419–428, 2005. Cited on page 18.
- [201] J. Pan, N. C. Cheung, and J. Yang, "High-precision position control of a novel planar switched reluctance motor," *Industrial Electronics, IEEE Transactions on*, vol. 52, no. 6, pp. 1644–1652, Dec 2005. Cited on page 18.

- [202] B. R. Patel, "Permanent magnet bistable solenoid actuator," USA Patent US4533 890 A, 1985, uS Patent 4,533,890. Cited on page 18.
- [203] J. J. H. Paulides, G. W. Jewell, and D. Howe, "An evaluation of alternative stator lamination materials for a high-speed, 1.5 MW, permanent magnet generator," *Magnetics, IEEE Transactions on*, vol. 40, no. 4, pp. 2041–2043, Jul 2004. Cited on page 110.
- [204] A. T. A. Peijnenburg, J. P. M. B. Vermeulen, and J. v. Eijk, "Magnetic levitation systems compared to conventional bearing systems," *Micro-electronic Engineering*, vol. 83, no. 4-9, pp. 1372–1375, 2006, in 2005 Proceedings of the 31st International Conference on Micro- and Nano-Engineering (MNE). Cited on page 2.
- [205] D. Petrichenko, M. Hecquet, P. Brochet, V. Kuznetsov, and D. Laloy, "Design and simulation of turbo-alternators using a coupled permeance network model," *Magnetics, IEEE Transactions on*, vol. 42, no. 4, pp. 1259–1262, 2006. Cited on pages 19, 23, and 24.
- [206] D. Petrichenko, "Calculation and simulation of turbogenerators using permeance network - optimization application," Ph.D. dissertation, École Centrale de Lille, France, May 2007. Cited on page 19.
- [207] D. A. Philips and F. Delince, "Practical use of the Preisach model from measurements to finite elements," *Magnetics, IEEE Transactions on*, vol. 29, no. 6, pp. 2383–2385, Nov 1993. Cited on pages 65 and 72.
- [208] D. A. Philips, L. R. Dupré, J. Cnops, and J. A. A. Melkebeek, "The application of the Preisach model in magnetodynamics: theoretical and practical aspects," *Journal of Magnetism and Magnetic Materials*, vol. 133, pp. 540 – 543, 1994. Cited on page 93.
- [209] D. A. Philips, L. R. Dupré, and J. A. A. Melkebeek, "Magneto-dynamic field computation using a rate-dependent Preisach model," *Magnetics, IEEE Transactions on*, vol. 30, no. 6, pp. 4377–4379, Nov 1994. Cited on page 109.
- [210] M. Piska, L. Yang, M. Reed, and M. Saleh, "Drilling efficiency and temperature elevation of three types of Kirschner-wire point," *Journal of Bone and Joint Surgery - Series B*, vol. 84, no. 1, pp. 137–140, 2002, cited By (since 1996): 11. Cited on page 158.
- [211] H. Polinder and M. J. Hoeijmakers, "Effect of a shielding cylinder an the rotor losses in a rectifier-loaded PM machine," in *Industry Applications Conference, 2000. Conference Record of the 2000 IEEE*, vol. 1, 2000, pp. 163–170 vol.1. Cited on page 121.

- [212] Z. B. Popović and B. D. Popović, *Introductory Electromagnetics*. Prentice Hall, 2000. Cited on page 16.
- [213] F. Preisach, “Über die magnetische nachwirkung,” *Zeitschrift für Physik*, vol. 94, no. 5-6, pp. 277–302, 1935. Cited on pages 63, 64, and 79.
- [214] P. Pruksanubal, A. Binner, and K. H. Gonschorek, “Determination of distribution functions and parameters for the Preisach hysteresis model,” in *17th International Zurich Symposium on EMC-Zurich 2006*, Mar 2006, pp. 258–261. Cited on pages 98 and 100.
- [215] C. Ragusa and M. Repetto, “Accurate analysis of magnetic devices with anisotropic vector hysteresis,” *Physica B: Condensed Matter*, vol. 275, no. 1-3, pp. 92–98, 2000. Cited on page 72.
- [216] L. Rayleigh, “XXV. Notes on electricity and magnetism - III. On the behaviour of iron and steel under the operation of feeble magnetic forces,” *Philosophical Magazine Series 5*, vol. 23, no. 142, pp. 225–245, 1887. Cited on pages 63 and 68.
- [217] A. Reimers and E. Della Torre, “Fast Preisach-based magnetization model and fast inverse hysteresis model,” *Magnetics, IEEE Transactions on*, vol. 34, no. 6, pp. 3857–3866, Nov 1998. Cited on page 72.
- [218] A. Reimers, I. Gyimesi, E. Della Torre, and D. Ostergaard, “Implementation of the Preisach DOK magnetic hysteresis model in a commercial finite element package,” *Magnetics, IEEE Transactions on*, vol. 37, no. 5, pp. 3362–3365, Sep 2001. Cited on page 72.
- [219] C. P. Riley, “Effect of magnetic hysteresis in solenoid valve operation,” *Sensor Letters*, vol. 11, no. 1, pp. 9–12, 2013. Cited on page 73.
- [220] S. Rosenbaum, M. Ruderman, T. Strohla, and T. Bertram, “Use of Jiles-Atherton and Preisach hysteresis models for inverse feed-forward control,” *Magnetics, IEEE Transactions on*, vol. 46, no. 12, pp. 3984–3989, 2010. Cited on page 143.
- [221] H. C. Roters, *Electromagnetic devices*, 1st ed. New York: Wiley, 1944, vol. 1. Cited on pages 18, 19, 23, 181, 182, and 183.
- [222] J. J. M. Rovers, “Multiphysical modeling of high-precision electromechanical devices,” Ph.D. dissertation, Eindhoven University of Technology, Mar 2013. Cited on page 2.
- [223] C. Ru and L. Sun, “Improving positioning accuracy of piezoelectric actuators by feedforward hysteresis compensation based on a new mathematical model,” *Review of Scientific Instruments*, vol. 76, no. 9, 2005. Cited on page 158.

- [224] M. Ruderman and T. Bertram, “Discrete dynamic Preisach model for robust inverse control of hysteresis systems,” in *Decision and Control (CDC), 2010 49th IEEE Conference on*, 2010, pp. 3463–3468. Cited on page 143.
- [225] M. Ruderman and A. Gadyuchko, “Phenomenological modeling and measurement of proportional solenoid with stroke-dependent magnetic hysteresis characteristics,” in *Mechatronics (ICM), 2013 IEEE International Conference on*, Feb 2013, pp. 180–185. Cited on page 143.
- [226] N. Sadowski, N. J. Batistela, J. P. A. Bastos, and M. Lajoie-Mazenc, “An inverse Jiles-Atherton model to take into account hysteresis in time-stepping finite-element calculations,” *Magnetics, IEEE Transactions on*, vol. 38, no. 2, pp. 797–800, Mar 2002. Cited on page 72.
- [227] N. Sadowski, M. Lajoie-Mazenc, J. P. A. Bastos, M. V. Ferreira da Luz, and P. Kuo-Peng, “Evaluation and analysis of iron losses in electrical machines using the rain-flow method,” *Magnetics, IEEE Transactions on*, vol. 36, no. 4, pp. 1923–1926, Jul 2000. Cited on page 110.
- [228] J. Saitz, “Newton-Raphson method and fixed-point technique in finite element computation of magnetic field problems in media with hysteresis,” *Magnetics, IEEE Transactions on*, vol. 35, no. 3, pp. 1398–1401, May 1999. Cited on page 72.
- [229] H. H. Saliah, D. A. Lowther, and B. Forghani, “A neural network model of magnetic hysteresis for computational magnetics,” *Magnetics, IEEE Transactions on*, vol. 33, no. 5, pp. 4146–4148, Sep 1997. Cited on page 72.
- [230] H. H. Saliah, D. A. Lowther, and B. Forghani, “Generalized material models for coupled magnetic analysis,” *Magnetics, IEEE Transactions on*, vol. 36, no. 4, pp. 1250–1253, Jul 2000. Cited on page 72.
- [231] D. Schieber, “Asynchronous performance of hysteresis motor,” *Journal of the Franklin Institute*, vol. 299, no. 6, pp. 433–447, 1975. Cited on page 74.
- [232] P. Sergeant, H. Vansompel, A. Hemeida, A. Van den Bossche, and L. R. Dupré, “A computationally efficient method to determine iron and magnet losses in VSI-PWM fed axial flux permanent magnet synchronous machines,” *Magnetics, IEEE Transactions on*, vol. In press, 2014. Cited on page 121.
- [233] N. Sidell and G. W. Jewell, “The design and construction of a high temperature linear electromagnetic actuator,” *Journal of Applied Physics*, vol. 85, no. 8, pp. 4901–4903, 1999. Cited on page 18.

- [234] E. W. Siemens, "Improvement in magneto-electric apparatus," Patent, 1874, US Patent 149797. Cited on page 9.
- [235] G. R. Slemon, "An equivalent circuit approach to analysis of synchronous machines with saliency and saturation," *Energy Conversion, IEEE Transactions on*, vol. 5, no. 3, pp. 538–545, Sep 1990. Cited on page 19.
- [236] C. P. Steinmetz, "On the law of hysteresis," *Proceedings of the IEEE*, vol. 72, no. 2, pp. 197–221, 1984, (Reprinted from the American Institute of Electrical Engineers Transactions, vol. 9 pp. 3-64, 1892). Cited on pages 63, 74, and 109.
- [237] C. P. Steinmetz and E. J. Berg, *Theory and Calculation of Alternating Current Phenomena*. Electrical world and engineer, incorporated, 1900. Cited on page 74.
- [238] E. C. Stoner and E. P. Wohlfarth, "A mechanism of magnetic hysteresis in heterogeneous alloys," *Philosophical Transactions of the Royal Society of London. Series A. Mathematical and Physical Sciences*, pp. 599–642, 1948. Cited on pages 63 and 75.
- [239] E. C. Stoner, "Ferromagnetism," *Reports on Progress in Physics*, vol. 11, no. 1, p. 43, 1947. Cited on page 41.
- [240] C. Stuebig and B. Ponick, "Determination of air gap permeances of hybrid stepping motors for calculation of motor behaviour," in *Electrical Machines, 2008. ICEM 2008. 18th International Conference on*, Sep 2008, pp. 1–5. Cited on page 19.
- [241] C. Stuebig and B. Ponick, "Comparison of calculation methods for hybrid stepping motors," *Industry Applications, IEEE Transactions on*, vol. 48, no. 6, pp. 2182–2189, Nov 2012. Cited on page 19.
- [242] W. Sturgeon, "Improved electromagnetic apparatus," *Transactions Royal Society for Encouragement of Arts, Manufactures and Commerce*, vol. 43, pp. 37–52, 1825. Cited on page 9.
- [243] K. Suzuki and B. W. Smith, *Microlithography: Science and Technology*, 2nd ed., ser. Optical science and engineering. Taylor & Francis, 2010. Cited on page 2.
- [244] Z. Szabó, I. Tugyi, G. Kádár, and J. Füzi, "Identification procedures for scalar Preisach model," *Physica B: Condensed Matter*, vol. 343, no. 1-4, pp. 142–147, 2004, proceedings of the Fourth International Conference on Hysteresis and Micromagnetic Modeling. Cited on page 95.

- [245] J. Takács, “A phenomenological mathematical model of hysteresis,” in *COMPEL: The International Journal for Computation and Mathematics in Electrical and Electronic Engineering*, 2001, vol. 20, no. 4, 2001, pp. 1002–1015. Cited on page 75.
- [246] J. Takács, *Mathematics of Hysteretic Phenomena: The $T(x)$ Model for the Description of Hysteresis*. Wiley, 2003. Cited on pages 73, 75, and 98.
- [247] N. Takahashi, S.-H. Miyabara, and K. Fujiwara, “Problems in practical finite element analysis using Preisach hysteresis model,” *Magnetics, IEEE Transactions on*, vol. 35, no. 3, pp. 1243–1246, 1999. Cited on page 66.
- [248] N. Takahashi, M. Morishita, D. Miyagi, and M. Nakano, “Examination of magnetic properties of magnetic materials at high temperature using a ring specimen,” *Magnetics, IEEE Transactions on*, vol. 46, no. 2, pp. 548–551, Feb 2010. Cited on page 47.
- [249] X. Tan and J. S. Baras, “Modeling and control of hysteresis in magnetostrictive actuators,” *Automatica*, vol. 40, no. 9, pp. 1469–1480, 2004. Cited on page 68.
- [250] Y. Tang, J. J. H. Paulides, and E. A. Lomonova, “Automated design of DC-excited flux-switching in-wheel motor using magnetic equivalent circuits,” in *Ecological Vehicles and Renewable Energies (EVER), 2014 Ninth International Conference on*, March 2014, pp. 1–10. Cited on pages 19 and 181.
- [251] R. S. Tebble and D. J. Craik, *Magnetic Materials*. Wiley, New York, 1969. Cited on page 67.
- [252] P. Tian, G. Li, and R. W. Jones, “Ellipse-based modelling of hysteresis in a smart actuator,” in *IEEE/ASME International Conference on Advanced Intelligent Mechatronics, AIM 2010*, Jul 2010, pp. 872–877. Cited on page 74.
- [253] H. F. Tiersten, *Linear piezoelectric plate vibrations: elements of the linear theory of piezoelectricity and the vibrations of piezoelectric plates*. Plenum Press, 1969. Cited on page 11.
- [254] P. M. Tyler, “Magnetic permeances between iron pole pieces,” *British Journal of Applied Physics*, vol. 13, no. 7, p. 345, 1962. Cited on page 18.
- [255] F. Vajda and E. Della Torre, “Relationship between the moving and the product Preisach models,” *Magnetics, IEEE Transactions on*, vol. 27, no. 5, pp. 3823–3826, Sep 1991. Cited on page 65.

- [256] P. J. van Bree, C. M. M. van Lierop, and P. P. J. van den Bosch, "Control-oriented hysteresis models for magnetic electron lenses," *Magnetics, IEEE Transactions on*, vol. 45, no. 11, pp. 5235–5238, Nov 2009. Cited on page 51.
- [257] B. van de Wiele, L. Vandenbossche, L. R. Dupré, and D. de Zutter, "Energy considerations in a micromagnetic hysteresis model and the Preisach model," *Journal of Applied Physics*, vol. 108, no. 10, 2010. Cited on page 65.
- [258] M. A. van den Brink, "Method of and device for repetitively imaging a mask pattern on a substrate," Patent, 1992, EP0498499-A1. Cited on page 2.
- [259] J. L. F. van der Veen, L. J. J. Offringa, and A. J. A. Vandenput, "Minimising rotor losses in high-speed high-power permanent magnet synchronous generators with rectifier load," *Electric Power Applications, IEE Proceedings -*, vol. 144, no. 5, pp. 331–337, Sep 1997. Cited on page 121.
- [260] A. van Lievenooogen, A. Toma, and U. Ummethala, "Challenges in the application of hybrid reluctance actuators in scanning positioning stages in vacuum with nanometer accuracy and mgauss magnetic stray field," in *American Control Conference (ACC), 2013*, Jun 2013, pp. 5286–5289. Cited on page 3.
- [261] T. Van Tran, J.-L. Coulomb, B. Delinchant, O. Chadebec, N. H. Vrijsen, J. W. Jansen, and E. A. Lomonova, "Hybridizing network reluctance and boundary integral methods: comparisons on an E-core actuator," in *Proceedings of Computational Magnetics, COMPUMAG 2011*, Sydney, Australia, 12-15 Jul 2011. Cited on pages 10, 19, and 29.
- [262] L. Vandenbossche, "Magnetic hysteretic characterization of ferromagnetic materials with objectives towards non-destructive evaluation of material degradation," Ph.D. dissertation, Universiteit Gent, 2009. Cited on page 56.
- [263] L. Vandenbossche, S. Jacobs, F. Henrotte, and K. Hameyer, "Impact of cut edges in magnetization curves and iron losses in e-machines for automotive traction," in *Proceedings of 25th World Battery, Hybrid and Fuel Cell Electric Vehicle Symposium & Exhibition, EVS 2010*, Schenzhen, China, Nov 2010. Cited on page 56.
- [264] H. Vansompel, P. Sergeant, and L. R. Dupré, "A multilayer 2-D-2-D coupled model for eddy current calculation in the rotor of an axial-flux PM machine," *Energy Conversion, IEEE Transactions on*, vol. 27, no. 3, pp. 784–791, Sep 2012. Cited on page 123.

- [265] B. Vaseghi, S. Rahman, and A. Knight, "Influence of steel manufacturing on J-A model parameters and magnetic properties," *Magnetics, IEEE Transactions on*, vol. 49, no. 5, pp. 1961–1964, May 2013. Cited on page 56.
- [266] J. P. M. B. Vermeulen and T. P. M. Cadee, "Challenges in next-generation substrate positioning," in *Proceedings of the EUSPEN international conference*, Delft, 2010, pp. 283–286. Cited on page 3.
- [267] A. Visintin, *Differential Models of Hysteresis*, ser. Applied Mathematical Sciences. Springer, 1994. Cited on pages 65, 68, 69, and 71.
- [268] N. H. Vrijsen, "Comparison of linear voice coil and reluctance actuators for high-precision applications," Master's thesis, Eindhoven University of Technology, Jun 2010. Cited on page 10.
- [269] N. H. Vrijsen, J. W. Jansen, J. C. Compter, and E. A. Lomonova, "Measurement method to determine the magnetic hysteresis effects of reluctance actuators by evaluation of the force and flux variation," *Review of Scientific Instruments*, vol. 84, no. 7, 2013. Cited on pages 64, 144, and 159.
- [270] N. H. Vrijsen, J. W. Jansen, and E. A. Lomonova, "Comparison of linear voice coil and reluctance actuators for high-precision applications," in *14th International Power Electronics and Motion Control Conference, EPE/PEMC 2010*, Ohrid, Macedonia, Sep 2010, pp. S3–29–S3–36. Cited on pages 3, 10, 18, and 31.
- [271] N. H. Vrijsen, J. W. Jansen, and E. A. Lomonova, "Analysis of magnetic hysteresis in a high-precision E-core reluctance actuator compared to measurements," in *Proceedings of the Fifteenth Biennial IEEE Conference on Electromagnetic Field Computation, CEFC 2012*, Oita, Japan, Nov 11-14 2012, p. 365. Cited on page 110.
- [272] N. H. Vrijsen, J. W. Jansen, and E. A. Lomonova, "Finite element analysis and Preisach hysteresis model compared to measurements on a toroid," in *Proceedings of the Sixth IEEE Young Researchers Symposium in Electrical Power Engineering : challenges in sustainable electrical energy, YRS 2012*, Delft, The Netherlands, Apr 16-17 2012, pp. 1–5. Cited on page 80.
- [273] N. H. Vrijsen, J. W. Jansen, and E. A. Lomonova, "Finite element analysis and Preisach hysteresis model of a toroid compared to measurements," in *Proceedings of IEEE Energy Conversion Congress and Exposition, ECCE 2012*, Raleigh, North Carolina, Sep 15-20 2012. Cited on pages 25, 58, 80, and 98.

- [274] N. H. Vrijsen, J. W. Jansen, and E. A. Lomonova, "Force prediction including hysteresis effects in a short-stroke reluctance actuator using a 3d-FEM and the Preisach model," in *Proceedings of the Ninth International Symposium on Linear Drives for Industry Applications, LDIA 2013*, Hangzhou, China, Jul 7-10 2013, p. 362. Cited on pages 110 and 144.
- [275] N. H. Vrijsen, J. W. Jansen, and E. A. Lomonova, "Force prediction including hysteresis effects in a short-stroke reluctance actuator using a 3d-FEM and the Preisach model," *Applied Mechanics and Materials*, vol. 416-417, pp. 187–194, Sep 2013. Cited on page 123.
- [276] N. H. Vrijsen, J. W. Jansen, and E. A. Lomonova, "Prediction of magnetic hysteresis in the force of a pre-biased E-core reluctance actuator," in *Proceedings of IEEE International Electric Machines Drives Conference, IEMDC 2013*, 2013, pp. 1450–1457. Cited on pages 110 and 144.
- [277] N. H. Vrijsen, J. W. Jansen, and E. A. Lomonova, "Comparison of magnetic hysteresis in the reluctance force of four E-core actuator topologies," in *Proceedings of the IEEE International Magnetics Conference, INTERMAG 2014*, Dresden, Germany, 4-8 May 2014, pp. 67–68. Cited on page 10.
- [278] N. H. Vrijsen, J. W. Jansen, and E. A. Lomonova, "Prediction of magnetic hysteresis in the force of a pre-biased E-core reluctance actuator," *Industry Applications, IEEE Transactions on*, vol. 50, no. 4, p. 9, Jul 2014. Cited on pages 73, 110, 123, and 144.
- [279] P. Weiss, "L'hypothèse du champ moléculaire et la propriété ferromagnétique," *Journal de Physique Théorique et Appliquée*, vol. 6, no. 1, pp. 661–690, 1907. Cited on pages 44 and 63.
- [280] *Integrated engineering software User's guide*, Winipeg, Manitoba, Canada, May 2009. Cited on page 24.
- [281] H. Xie, M. Rakotondrabe, and S. Régnier, "Characterizing piezoscanner hysteresis and creep using optical levers and a reference nanopositioning stage," *Review of Scientific Instruments*, vol. 80, no. 4, 2009. Cited on page 158.
- [282] X.-D. Xue, K. W. E. Cheng, T. W. Ng, and N. C. Cheung, "Multi-objective optimization design of in-wheel switched reluctance motors in electric vehicles," *Industrial Electronics, IEEE Transactions on*, vol. 57, no. 9, pp. 2980–2987, Sep 2010. Cited on page 18.
- [283] S. Yamada, Y. Kanamaru, and K. Bessho, "The transient magnetization process and operations in the plunger type electromagnet," *Magnetics*,

- IEEE Transactions on*, vol. 12, no. 6, pp. 1056–1058, Nov 1976. Cited on page 18.
- [284] K. Yamazaki and N. Fukushima, “Iron loss model for rotating machines using direct eddy current analysis in electrical steel sheets,” *Energy Conversion, IEEE Transactions on*, vol. 25, no. 3, pp. 633–641, Sep 2010. Cited on page 110.
- [285] F. A. A. Zaher, “An analytical solution for the field of a hysteresis motor based on complex permeability,” *Energy Conversion, IEEE Transactions on*, vol. 5, no. 1, pp. 156–163, Mar 1990. Cited on page 74.
- [286] M. R. Zakerzadeh and H. Sayyaadi, “Experimental comparison of some phenomenological hysteresis models in characterizing hysteresis behavior of shape memory alloy actuators,” *Journal of Intelligent Material Systems and Structures*, vol. 23, no. 12, pp. 1287–1309, 2012. Cited on pages 68 and 70.
- [287] S.-W. Zhao, N. C. Cheung, W.-C. Gan, J. M. Yang, and J. F. Pan, “A self-tuning regulator for the high-precision position control of a linear switched reluctance motor,” *Industrial Electronics, IEEE Transactions on*, vol. 54, no. 5, pp. 2425–2434, Oct 2007. Cited on page 18.
- [288] S. E. Zirka and Y. I. Moroz, “Hysteresis modeling based on transplantation,” *Magnetics, IEEE Transactions on*, vol. 31, no. 6, pp. 3509–3511, 1995. Cited on page 73.
- [289] S. E. Zirka, Y. I. Moroz, and E. Della Torre, “Combination hysteresis model for accommodation magnetization,” *Magnetics, IEEE Transactions on*, vol. 41, no. 9, pp. 2426–2431, Sep 2005. Cited on page 51.
- [290] S. E. Zirka, Y. I. Moroz, P. Marketos, and A. J. Moses, “Novel approach to modelling losses in electrical steel laminations,” in *The Fourth International Conference on Computation in Electromagnetics, CEM 2002*, Apr 2002. Cited on page 110.
- [291] S. E. Zirka, Y. I. Moroz, P. Marketos, and A. J. Moses, “Dynamic hysteresis modelling,” *Physica B: Condensed Matter*, vol. 343, no. 1-4, pp. 90–95, 2004, proceedings of the Fourth Intional Conference on Hysteresis and Micromagnetic Modeling. Cited on page 117.
- [292] S. E. Zirka, Y. I. Moroz, P. Marketos, and A. J. Moses, “Properties of dynamic Preisach models,” *Physica B: Condensed Matter*, vol. 343, no. 1-4, pp. 85–89, 2004, proceedings of the Fourth Intional Conference on Hysteresis and Micromagnetic Modeling. Cited on pages 110 and 117.

-
- [293] S. E. Zirka, Y. I. Moroz, P. Marketos, A. J. Moses, and D. C. Jiles, "Measurement and modeling of B-H loops and losses of high silicon nonoriented steels," *Magnetics, IEEE Transactions on*, vol. 42, no. 10, pp. 3177–3179, Oct 2006. Cited on page 116.
- [294] S. E. Zirka, Y. I. Moroz, P. Marketos, A. J. Moses, D. C. Jiles, and T. Matsuo, "Generalization of the classical method for calculating dynamic hysteresis loops in grain-oriented electrical steels," *Magnetics, IEEE Transactions on*, vol. 44, no. 9, pp. 2113–2126, Sep 2008. Cited on pages 110 and 116.
- [295] S. E. Zirka, Y. I. Moroz, E. Y. Moroz, G. A. Evdokunin, M. V. Dmitriev, and C. M. Arturi, "Principles of modeling transformer transients taking into account topology and magnetic core features," *Russian Electrical Engineering*, vol. 84, no. 1, pp. 14–20, 2013. Cited on page 19.
- [296] S. E. Zirka, Y. I. Moroz, R. G. Harrison, and K. Chwastek, "On physical aspects of the Jiles-Atherton hysteresis models," *Journal of Applied Physics*, vol. 112, no. 4, 2012. Cited on pages 67, 110, and 117.

Samenvatting

Magnetic hysteresis phenomena in electromagnetic actuation systems

De eisen en specificaties van positioneringssystemen worden continu aangescherpt. In de lithografische halfgeleiderindustrie worden hierbij de fysische grenzen opgezocht, vooral met betrekking tot de krachtdichtheid en positienauwkeurigheid van actuatorsystemen. Een hogere krachtdichtheid is nodig om het positioneringssysteem een hogere versnelling te geven. Dit kan worden vertaald naar een hogere productiesnelheid en als gevolg daarvan lagere kosten per geproduceerde computerchip. Tegelijkertijd met het verhogen van de krachtdichtheid moet de positienauwkeurigheid van het actuatorsysteem worden verbeterd om computerchips te kunnen produceren met meer rekenkracht of een hogere opslagcapaciteit. Om dit te behalen is in de nabije toekomst een positienauwkeurigheid van een fractie van een nanometer vereist.

Actuatoren gebaseerd op de Lorentzkracht zijn gedurende de afgelopen decennia meestal toegepast voor actuatorsystemen, omdat deze goede eigenschappen heeft wat betreft positienauwkeurigheid. Deze nauwkeurigheid kan worden behaald doordat de Lorentz-actuator een lineaire stroom-krachtrelatie heeft die bij benadering positieonafhankelijk is. Na jarenlange verbetering van de krachtdichtheid is het nu de verwachting dat het maximum bijna bereikt is. Daarom wordt er onderzoek gedaan naar een fysiek ander actuatorprincipe om de productiesnelheid van toekomstige actuatorsystemen te vergroten. Dit onderzoek is gericht op reluctantieactuatoren voor korte-slag-toepassingen, omdat dit type actuator een meer dan tien keer hogere krachtdichtheid kan behalen dan Lorentz-actuatoren.

De reden dat er vaak niet voor reluctantieactuatoren wordt gekozen is de niet-lineariteit van de stroom-kracht- en de positie-krachtrelaties, alsook de aanwezigheid van magnetische hysteresis en wervelstromen in de ferromagnetische materialen. Deze actuatoreigenschappen zijn erg uitdagend voor het modelleren van de actuatorkrachten. In dit proefschrift is de nauwkeurigheid van

de krachtvoorspelling van reluctantieactuatoren onderzocht vanuit een fysisch elektromagnetisch perspectief.

Er is onderzocht welke elektromagnetische modelleringstechnieken toegepast kunnen worden voor het beschrijven van de kracht van reluctantieactuatoren. De methode van magnetische equivalente circuits (MEC) en een commercieel beschikbaar eindige-elementenmethode zijn geselecteerd om de niet-lineaire positie-kracht- en stroom-krachtrelaties te modelleren. Het niet-hysteretische MEC-model is onder andere gekozen omdat het kan worden uitgebreid met een hysteretisch materiaalmodel. Het MEC-model is voldoende nauwkeurig om de kracht in de bewegingsrichting te bepalen, terwijl het meenemen van de parasitaire krachten te onnauwkeurig is. De eindige-elementenmethode is gebruikt om de actuatoren te modelleren, omdat deze methode voldoende nauwkeurigheid heeft voor de krachten in de actuatierichting en de parasitaire krachten. Verder is de eindige-elementenmethode gebruikt om te onderzoeken of de mate van homogeniteit van de magnetische fluxdichtheid effect heeft op de hoeveelheid hysteresis in de kracht. Hieruit blijkt dat de absolute hoeveelheid hysteresis in de kracht in de bewegingsrichting proportioneel is met de piekwaarde van de magnetische fluxdichtheid in het overgrote deel van de actuator. Verder is de hysteresis in de parasitaire kracht als gevolg van een verkeerde uitlijning, verwaarloosbaar vergeleken met de hysteresis in de bewegingsrichting.

De fysische eigenschappen van magnetische hysteresis in ferromagnetische materialen zijn beschouwd, inclusief de afhankelijkheid van het verleden, het uitwisselbaarheidsprincipe en de tijdsafhankelijkheid. De tijdsafhankelijkheid wordt veroorzaakt door macroscopische wervelstromen en de extra dynamische verliezen. Deze aspecten worden besproken omdat ze bepalend zijn voor de keuze van een geschikte modelleringmethode. Daarnaast zijn de belangrijkste eigenschappen van verschillende type staalsoorten beschouwd met betrekking tot de toepassing voor reluctantieactuatoren, nl. nikkel-ijzer (NiFe), silicium-ijzer (SiFe), kobalt-ijzer (CoFe), ferriet en roestvast staal. De invloeden van het uitgloeien in het productieproces zijn beschouwd en meetmethoden zijn benoemd die gebruikt kunnen worden voor de kwalificatie van ferromagnetische materialen.

Het Preisach hysteresis model is geselecteerd om de meest dominante ferromagnetische materiaaleigenschappen te beschrijven. Dit model kan het niet-lineaire hysteretische gedrag van magnetische materialen modelleren voor een willekeurige input, waarbij de afhankelijkheid van het verleden wordt meegenomen. Door de combinatie met het MEC-model wordt het materiaalgedrag meegenomen in het actuatormodel. Bovendien is een dynamisch materiaalmodel gebruikt om de tijdsafhankelijke effecten mee te nemen. Behalve het Preisach model, is ook de eindige-elementenmethode en een complex-impedantiemodel beschouwd betreffende hun modelnauwkeurigheid van het dynamische gedrag van reluctantieactuatoren.

Met het Preisach model is de magnetische fluxdichtheid gesimuleerd en vergeleken met quasi-statische metingen van drie verschillende materiaaltypen, te weten CoFe (Vacoflux 50), SiFe (M800-50A) en roestvast staal (AISI 430). Voor de gelamineerde materialen met een lameldikte van 0.10, 0.35 en 0.50 mm is ook het dynamische materiaalmodel geëvalueerd. Het maximale verschil tussen de metingen en de simulaties is 10 % voor de meeste excitaties van dc tot aan 400 Hz.

De voorspelling van de hysteresis in de kracht is vergeleken met krachtmetingen op drie E-core reluctantieactuatoren. Eén hiervan is gemaakt van CoFe en twee zijn van SiFe, waarvan er één is voorgespannen met een permanente magneet en de andere niet. De krachtmeting van de CoFe-actuator is gedaan met een testopstelling waarbij de kracht is bepaald met twee lineaire Lorentz-actuatoren. Een optische encoder met een nauwkeurigheid van een nanometer is hierbij gebruikt voor de positiebepaling, en een terugkoppelende regeling is gebruikt om de luchtspleet constant te houden. De dynamische hysteresis effecten in de kracht van de twee SiFe-actuatoren zijn gemeten met een piezo-elektrische krachtcel. De hysteresis in de krachtmetingen is vergelijkbaar met de kracht verkregen met de statische en dynamische reluctantieactuatormodellen wat resulteert in een goede voorspelling van zowel de absolute kracht als de hoeveelheid hysteresis in de kracht.

Dankwoord

Na vier jaar hard werken is het dan zover, het proefschrift is geschreven. Het heeft me soms veel energie gekost, maar door de hulp van velen is de tijd vaak ook voorbij gevlogen. Als ik tussendoor terugkeek, dan had ik vaak het gevoel dat er relatief weinig vooruitgang was geboekt. Uiteindelijk is er in vier jaar tijd toch zoveel gebeurd dat het voldoende is gebleken om er een boek over te schrijven. Hiervoor wil ik graag iedereen bedanken die hier in meer of mindere mate aan hebben bijgedragen en in het bijzonder de volgende mensen.

Elena, bedankt voor de mogelijkheid die je me hebt gegeven en het vertrouwen om deze uitdaging aan te gaan. Hoewel het, tot aan je vraag aan mij om te promoveren, nooit een van mijn persoonlijke doelstellingen was, ben ik blij dat ik deze kans heb gegrepen. Door de vele discussies met jou, maar vooral ook met Helm, ben ik tot nieuwe inzichten gekomen. De vrijheid die jullie me gaven, heeft ervoor gezorgd dat ik uiteindelijk zelf kon bepalen waar het onderzoek heen moest. Ook door de vele niet-technische gesprekken, soms buiten de gebruikelijke kantoortijden, ben ik gegroeid als persoon. De tomeloze inzet van jullie beiden heeft er voor gezorgd dat de kwaliteit van het werk steeds weer verbeterd werd. Jullie karakter en enthousiasme hebben me vaak geïnspireerd om zelf ook een stapje meer te zetten. Helm, ik wil je nog speciaal bedanken voor het herhaaldelijk verbeteren van mijn aangeleverde teksten voor papers en uiteindelijk dit proefschrift.

Mijn onderzoeksproject, 'XTreme Motion' is gebaseerd op de samenwerking tussen de industrie en vijf vakgroepen, te weten vier van de TU/e en één van de TUD. Deze samenwerking was niet met iedereen even intensief, maar de gezamenlijke werkpakketoverleggen met de control systems groep en de bijbehorende bedrijven hebben mijn onderzoek richting gegeven. Daarom wil ik Andelko, maar ook Hans, Nelis en Paul bedanken voor hun input tijdens deze discussies.

Verder ben ik erg dankbaar voor de interesse in mijn onderzoek vanuit het bedrijfsleven, welke is gebleken uit de goede opkomst in de verschillende bij-

eenkomsten. Uit deze interesse bleek ook de relevantie van het werk, wat me gedurende het onderzoek heeft gestimuleerd om verder te gaan. Daarom wil ik de betreffende organisaties bedanken, maar natuurlijk vooral de direct betrokkenen, Hans H., Hans V., Iwan, Jeroen d. B., Jeroen v. D., Sven en Wouter (ASML), John en René (Heidenhain), Bas en Korneel (Prodrive), Bart en Johan (Magnetic Innovations), en Marco (TMC). Hans Vermeulen in het bijzonder bedankt voor je inspanningen als initiator van het XTreme Motion-project. Verder wil ik John bedanken voor de begeleiding tijdens mijn periode bij Heidenhain, waarbij vooral je visie op de elektromechanica en je vele praktische oplossingen me erg hebben geïnspireerd. Gedurende mijn verblijf bij ASML hebben Iwan, Sven en Vijayendra (VJ) me regelmatig geholpen. Sven, jij vooral bedankt voor de gesprekken tijdens de lunchpauzes.

Ook wil ik mijn commissieleden bedanken, prof.dr.ir. J. Benschop, prof.dr.ir. L. Dupré, prof.dr.ir. M. Geers, dr.ir. R. Klaver en prof.dr.-ing. B. Ponick voor jullie deelname aan mijn promotiecommissie, het lezen van mijn proefschrift en bovendien de zeer waardevolle input van enkele van jullie. Luc, in het bijzonder nog bedankt voor de nuttige discussie ongeveer halverwege mijn promotieonderzoek, welke me uiteindelijk erg geholpen heeft bij het meenemen van de dynamische hysteresis effecten in mijn analyse.

Uiteraard wil ik ook mijn collega's bedanken binnen de vakgroep Electromechanics and Power Electronics, met name mijn huidige en oud-kamergenoten Jan, Jeroen, Martin, Gierri, Davy, Erik en Gabriel. Jing, Bart en Stefan, bedankt voor de goede samenwerking gedurende jullie afstudeerproject. Ondanks dat er geen proefopstelling is geweest, wil ik toch Rutger, Wim en Marijn bedanken omdat jullie klaar stonden als er iets geregeld moest worden. Monica en Nancy, bedankt voor de vele administratieve werkzaamheden. Verder wil ik alle (ex-)spelers van 'Spielen Und Erleben' bedanken voor de ontspannen uurtjes in de pauze, met in het bijzonder Timo voor de organisatie van de zaalvoetbalwedstrijden. Als laatste wil ik 'TheBruceDickinson productions' bedanken voor hun ondersteuning welke meestal L^AT_EX gerelateerd was.

Naast de technische inbreng van specialisten, waren familie en vrienden minstens zo belangrijk, wat zorgde voor een prettig evenwicht tussen werk en privé. Ik heb het altijd erg belangrijk gevonden om deze balans in mijn leven te waarborgen wat, afgezien van de weken voor de deadlines, naar mijn idee aardig gelukt is. Dit is vooral toe te schrijven aan de afleiding waar jullie allemaal voor gezorgd hebben: samenkomen bij onze (schoon)ouders (opa en oma), feestjes, verjaardagen, (zaal)voetballen, stappen, maar zeker ook niet te vergeten de afleiding van onze kleine Sander.

De persoon die ik het meest wil bedanken is mijn vrouw Suzanne, de moeder van onze zoon en zwanger van ons tweede wondertje. We zijn ondertussen alweer ruim 14 jaar samen en in deze periode heb je me altijd gesteund in mijn keuze om mezelf door te ontwikkelen. De reisjes naar conferenties en de deadlines kwamen niet altijd goed uit, maar je hebt hier nooit een probleem van gemaakt, omdat je wist dat dit belangrijk voor me was. Je bent er altijd voor me geweest, zonder jou was het nooit gelukt. Ik hou van je!

Bedankt allemaal !!!

Nilles, augustus 2014

Curriculum Vitae

Nilles Vrijsen was born on 14-06-1984 in Eindhoven, The Netherlands. After finishing his pre-university education in 2003 at Pius X college in Bladel, he studied electrical engineering at the Eindhoven University of Technology in Eindhoven. He obtained his bachelor degree in 2008. In 2010 he graduated within the group of Electromechanics and Power Electronics on the comparison of voice-coil and reluctance actuators for short-stroke high-precision applications. In 2010 he started his Ph.D. project at the same university on the modeling of magnetic hysteresis phenomena in reluctance actuators, of which the research results are presented in this dissertation. In 2013 he received the best paper award at the LDIA conference in Hangzhou, China. Since November 2014 he started his industrial career at Prodrive in Son.